REPORT DOCUMENTATION PAGE

AFRL-SR-BL-TR-98-
0136

1. AGENCY USE ONLY (Leave blank)	2. REPORT DATE	3. REPORT TYPE AND DATES COVERED
	05/31/97	Final Report 06/01/93-05/31/97

4. TITLE AND SUBTITLE	5. FUNDING NUMBERS
A Fucussed Fundamental Studey of Predicting Materials Degrdation & Fatique	F49620-93-1-0349
6. AUTHOR(S) E.Dow Whitney James H. Adair	
7. PERFORMING ORGANIZATION NAME(S) AND ADDRESS(ES) University of Florida 219 Grinter Hall Gainesville, Florida 32611	**8. PERFORMING ORGANIZATION REPORT NUMBER** 4509466-12
9. SPONSORING/MONITORING AGENCY NAME(S) AND ADDRESS(ES) Dr. Alexander Pechenik AFOSR/NI 110 Duncan Ave. Suite B115 Bolling AFB, DC 20331-8080 NA	**10. SPONSORING/MONITORING AGENCY REPORT NUMBER** P00002

11. SUPPLEMENTARY NOTES

12a. DISTRIBUTION/AVAILABILITY STATEMENT	12b. DISTRIBUTION CODE
DISTRIBUTION STATEMENT A Approved for public release; Distribution Unlimited	

13. ABSTRACT (Maximum 200 words)

SEE EXCUTIVE SUMMARY

19980205 052

DTIC QUALITY INSPECTED 4

14. SUBJECT TERMS	15. NUMBER OF PAGES
	829
	16. PRICE CODE

17. SECURITY CLASSIFICATION OF REPORT	18. SECURITY CLASSIFICATION OF THIS PAGE	19. SECURITY CLASSIFICATION OF ABSTRACT	20. LIMITATION OF ABSTRACT

FINAL REPORT
Volume I

A University Research Initiative

on

A Focused, Fundamental Study on the Environmental Degradation of Ceramic Materials in Aerospace Structures

For the Period
June 1, 1993 through May 31, 1997

Sponsored by AFOSR Grant Number F49620-93-1-1349DEF

Program Monitor: **Alexander Pechenik**
AFOSR/NI
Building 410
Bolling ABF, DC 20332-6448

Research Team Participants: From the University of Florida:

Principal Investigator: Dr. E. Dow Whitney
Co-Principal Investigator: Dr. James H. Adair
Paul H. Holloway
John J. Mecholsky, Jr.
James D. Winefordner
Benjamin Smith

From Southwest Louisiana University:
Don W. Dareing

From the University of Utah:
Dinesh K. Shetty

Executive Summary

A multidisciplinary team of investigators from the University of Florida, the University of Utah, and the University of Tennessee conducted a comprehensive, integrated study on the wear and fatigue of ceramic and metal materials for aerospace applications. The work was focused on a study of wear and fatigue in the context of the materials silicon nitride (Si_3N_4) and M-50 steel, and environments relevant to hybrid bearings in advanced turbine engines. The four year program was initiated in May, 1993 and concluded at the end of May, 1997. This document represents the fourth and final report of the program.

A fundamental approach was employed to better understand the combined effects of mechanical stress, chemical environment, and high temperatures on wear and fatigue. Individual expertise on the research team spanned the disciplines of material science, chemistry, mechanics, and physics needed to understand the tribochemical nature of wear and fatigue. The program was also strongly coupled to industry and national laboratories to better facilitate transfer of the fundamental knowledge and technology to be developed into existing military and commercial systems.

The primary objectives in the study were to: (1) develop and evaluate *ex-situ* and selected *in-situ* methods to detect wear; (2) develop a broad-based fundamental understanding of wear and wear mechanisms; (3) develop rolling contact fatigue maps for the hybrid bearing systems; (4) develop lifetime predictions for wear and rolling contact fatigue based on the *ex-situ* and *in-situ* wear detection methods; and (5) develop surface modification systems for hybrid bearing systems that either aid in wear detection or act to minimize wear damage.

During the course of the four year study, 25 technical articles were prepared for referred international journal articles (21) or referred proceedings (4) which are included in the appendices in addition to numerous presentations by the students and faculty associated with the project at various international meetings and symposia. During the course of the program at the University of Florida, 1 B.S. Honors thesis, 4 M.S. degrees (3 with thesis and one non-thesis) and 5 Ph.D. degrees were awarded with one M.S. and two Ph.D. pending at this writing. Abstracts for the theses are also provided in the appendices of the final report.

The following technical goals were achieved during the four year investigation:

1. Analytical chemistry methods were developed to monitor the wear debris in lubricants from hybrid bearings.
2. A spectroscopic method based upon UV-visible spectra was developed to monitor and predict viscosity changes during lubricant breakdown and carbonaceous sludge formation.
3. Rigorous comparisons of the performance of hybrid bearings relative to all steel and all ceramic bearings have been conducted in many of our studies, all of which demonstrate the superior performance of the hybrid bearings, particularly in adverse conditions.
4. A theory for wear mechanisms of the Si_3N_4 rolling element has been developed and tested.
5. A theory to predict bearing life based upon specific wear data generated during the program has been developed and tested.
6. Several surface modification techniques on the M50 raceway material and the Si_3N_4 rolling element including ion implantation, diamond-like-carbon and diamond, and surface compressive coatings have demonstrated that the already excellent tribological properties of the hybrid materials can be improved.

Both the main shaft bearings for the engines on the recently developed F-22 tactical fighter as well the oxygen turbo-pump on the NASA space shuttle depend upon hybrid bearings for their superior performance. There are also many additional, but often, proprietary applications for hybrid bearings where severe operating environments preclude the use of all-steel bearings. Based upon non-destructive evaluation methods and testing developed on other DoD-sponsored programs on hybrid bearings, there is little chance that

a ceramic rolling element will be passed for bearing insertion without detecting a flaw large enough to produce a spall in the operating bearing. It will be shown in the current report that the hybrid bearing materials consistently out perform the all-steel bearings whether the comparison criteria is specific wear rate, coefficient of friction, or life to failure. Furthermore, under severe conditions including no lubrication, particles suspended in the lubricant, high temperatures and humidity, and high Hertzian contact stress, the performance of the hybrid bearing is almost always superior to all steel bearing systems. The hybrid bearing combination of materials with silicon nitride rolling elements, steel raceways (M-50 steel was evaluated for the most part), and, if lubricated, a synthetic polyester lubricant had comparable or lower wear rates, coefficients of friction, and fatigue life at similar Hertzian contact stresses than all steel bearing materials.

Improvement as well as trust in the reliability of ceramic elements for continued insertion for a variety of applications including in advanced turbine engines will require advances in three areas: (1) continued critical testing and dissemination of wear mechanisms and performance comparisons between all-steel bearings and hybrid bearings, (2) a more fundamental understanding of the wear and degradation mechanisms that precede failure of hybrid bearings, particularly with respect to corrosion of the steel raceway materials and ceramic when particularly severe lubricant degradation products and environments create the possibility of corrosion-mediated spallation, and (3) new techniques that can continuously monitor the prefailure events so that the critical bearing elements can be safely replaced prior to their failure.

Regardless of the technical successes of hybrid bearings, the major barrier to wide scale implementation of ceramic rolling elements continues to be their high cost relative to all-steel systems. The high cost is of great concern if the superior performance of the hybrid bearings is to achieve a significant impact in general usage, or similar to many structural ceramics, finds only niche, value-added applications. More cost-efficient processing and surface-finishing methods, increased volume of production, and specific engineering specifications to meet acceptable, not necessarily optimal, performance requirements for the chemical and mechanical environments in operating bearings will continue to reduce the cost of ceramic bearings.

The final report is organized in a similar fashion to prior annual reports with a summary of the findings and accomplishments on each of the tasks with cited research manuscripts included in Appendices 2-38 usually as a report to be submitted to the relevant technical literature, a preprint, or as a reprint of work supported by the contract during the four project years. The abstracts of the master of science (M.S.) and doctor of philosophy (Ph.D.) degrees awarded at the University of Florida based on support from the AFOSR-sponsored project in the Departments of Chemistry and Materials and Science and Engineering are also included in the appendices.

TABLE OF CONTENTS

VOLUME I

VOLUME II

Final Report

A University Research Initiative
on
A Focused, Fundamental Study
on the
Environmental Degradation
of Ceramic Materials
in Aerospace Structures

For the Period
June 1, 1993 through May 31, 1997

Sponsored by AFOSR Grant Number F49620-93-1-0349DEF

INTRODUCTION

A multidisciplinary team of investigators from the University of Florida, the University of Southwestern Louisiana, and the University of Utah conducted a comprehensive, integrated study on the wear and fatigue of ceramic and metal materials for aerospace applications. The work is focused on a study of wear and fatigue in the context of the materials and environments relevant to hybrid bearings in advanced turbine engines. The four year program was initiated in May, 1993 and concluded at the end of May, 1997. This document represents the fourth and final report of the program.

A fundamental approach was employed to better understand the combined effects of mechanical stress, chemical environment, and high temperatures on wear and fatigue. Individual expertise on the research team spanned the disciplines of material science, chemistry, mechanics, and physics needed to understand the tribochemical nature of wear and fatigue. The program was also strongly coupled to industry and national laboratories to better facilitate transfer of the fundamental knowledge and technology to be developed into existing military and commercial systems.

The primary objectives in the study were to: (1) develop and evaluate *ex-situ* and selected *in-situ* methods to detect wear; (2) develop a broad-based fundamental understanding of wear and wear mechanisms; (3) develop rolling contact fatigue maps for the hybrid bearing systems; (4) develop lifetime predictions for wear and rolling contact fatigue based on the *ex-situ* and *in-situ* wear detection methods; and (5) develop surface modification systems for hybrid bearing systems that either aid in wear detection or act to minimize wear damage.

Despite the advances made in the development of hybrid bearings composed of Si_3N_4 bearings and M-50 raceways, their use in military applications has been limited. However, both the main shaft bearings of the recently developed F-22 tactical fighter as well oxygen turbo-pump on the NASA space shuttle depend upon hybrid bearings for their superior performance. There are also many additional, but often, proprietary applications for hybrid bearings where severe operating environments preclude the use of all-steel bearings. Based upon the nondestructive evaluation methods and testing developed on other DoD-sponsored programs for hybrid bearings, there is little chance that a ceramic rolling element will be passed for bearing insertion without being able to detect a flaw large enough to produce a spall in the operating bearing. It will be shown in the current report that the hybrid bearing materials consistently out perform the all steel bearings whether the comparison criteria is specific wear rate, coefficient of friction, or life to failure. Furthermore, under severe conditions including no lubrication, particles suspended in the lubricant, high temperatures and humidity, and high Hertzian contact stress, the performance of the hybrid bearing is almost always superior to all steel bearing systems. The hybrid bearing combination of materials with silicon nitride rolling elements, steel raceways (M-50 steel was evaluated for the most part), and, if lubricated, a synthetic polyester lubricant had comparable or lower wear rates, coefficients of friction, and fatigue life at similar Hertzian contact stresses than all steel bearing materials. Improvement as well as trust in the reliability of ceramic elements for continued insertion for a variety of applications including in advanced turbine engines will require advances in three areas: (1) continued critical testing and dissemination of wear mechanisms and performance comparisons between all steel bearings and hybrid bearings, (2) a more fundamental understanding of the wear and degradation mechanisms that precede failure of hybrid bearings, particularly with respect to corrosion of the steel raceway materials and ceramic when particularly severe lubricant degradation products and environments create the possibility of corrosion-mediated spallation, and (3) new techniques that can continuously monitor the prefailure events so that the critical bearing elements can be safely replaced prior to their failure.

Regardless of the technical successes of hybrid bearings, the major barrier to wide scale implementation of ceramic rolling elements continues to be their high cost relative to all-steel systems. The high cost is of great concern if the superior performance of the hybrid bearings is to achieve a significant impact in general usage, or similar to many structural ceramics, finds only niche, value-added applications. More cost-efficient processing and surface-finishing methods, increased volume of production, and specific engineering specifications to meet acceptable, not necessarily optimal, performance requirements for the chemical and mechanical environments in operating bearings will continue to reduce the cost of ceramic bearings.

There were five specific activities that the interdisciplinary team undertook in the research. They are: (1) Detection of bearing wear; (2) Measurement of bearing wear; (3) Determination of wear mechanisms; (4) Development of precatastrophic failure prediction; and (5) Development of methods to minimize wear of ceramic bearings. Thus, five parallel activities were conducted with overlap both in personnel and program objectives to provide the required integration and promote synergism among the program team members. A summary of the work performed on each of these activities is discussed.

The final report is organized in a similar manner to the prior reports with a summary of the findings and accomplishments on each of the tasks with cited research manuscripts included in Appendices 2-38 either as a report to be submitted to the relevant technical literature, a preprint, or as a reprint of work supported by the contract during the four project years. During the course of the four year study, 25 technical articles were prepared for referred international journal articles (21) or referred proceedings (4) which are included in the appendices in addition to numerous presentations by the students and faculty associated with the project at various international meetings and symposia. During the course of the program at the University of Florida, 1 B.S. Honors thesis (Appendix , 4 M.S. degrees (3 with thesis and one non-thesis) and 5 Ph.D. degrees were awarded with one M.S. and two Ph.D. pending at this writing.

TECHNOLOGY TRANSFER AND LINKS TO OTHER UNIVERSITIES, U.S. INDUSTRY AND NATIONAL LABORATORIES

Technology transfer and interaction with commercial organizations involved in the business of designing bearings, producing the materials to be used and using the bearings is an integral part of the project. Three annual workshops on Wear and Degradation of Materials in Aerospace Structures were held to augment technology transfer and promote constructive criticism from outside collaborators on the program. The agendas and participants of each of the three workshops are attached in Appendix 1. The exchange of information and technical know-how provided by the industrial and national laboratory partners initiated by the workshops was critical in maintaining the focus of the program, exchanging technical information and ideas and establishing communication with key industrial and national laboratory personnel to aid the project team in rapidly developing the know-how and understanding the knowledge among the partners specific to hybrid bearings.

PROGRESS ON SPECIFIC ACTIVITIES

Activity 1.0 Detection of Wear

The objective of this activity is to evaluate the detection of wear both by methods with *in-situ* wear detection potential as well as *ex-situ* techniques. The ultimate goal is to develop an understanding between wear detection schemes and impending failure as deduced in activities 2, 3, and 4. The development of solution chemistry analysis specific to the materials used in hybrid bearings was spurred by the need for techniques similar to the standard JOAP and SOAP analyses developed for lubricants and all-steel bearings in military applications. In particular, chemical analysis for the silicon nitride rolling elements required the development of chemical assay techniques to analyze both the bulk Si as well as the grain boundary materials which are typically either Mg-based or Y,Al-based depending upon the manufacturer (see Appendix 25 for a review of the processing and properties of the ceramic materials used in hybrid bearings as well as a discussion on fatigue lifetimes). Another objective of this task was to evaluate the role of a typical synthetic polyester-based lubricant that meets U.S. military specifications in hybrid bearing performance particularly when lubricant degradation begins to play a role in bearing lifetime . This activity was directed by James D. Winefordner. Publications and theses abstracts related to Activity 1 are provided in Appendices 2 through 11.

Task 1.1 Elemental Spectroscopy of Wear Debris

Inductively coupled plasma mass spectrometry (ICP-MS) is one of the few techniques capable of multielement determinations with low detection limits. However, when an organic matrix is nebulized into the ICP-MS, carbon condenses on the cooled interface cones, sooting and blocking the apertures. A second disadvantage of nebulizing organics into the ICP-MS is that carbide compounds formed in the ICP may act as molecular interferences for some elements, making it difficult or impossible to detect these elements. Electrothermal vaporization (ETV), microwave digestion, and laser ablation were chosen as a sample introduction techniques to be developed and evaluated for the silicon nitride ceramics because these techniques reduced the problems associated with conventional nebulization. When using ETV for sample introduction, the analyte was separated from the sample matrix, which made it possible to analyze oil samples while eliminating oxygen addition and reducing molecular interferences due to the organic matrix. A method was developed for the determination of Al, Mg, Fe, and Y metallo-organic compounds in lubricating oil by electrothermal vaporization inductively coupled plasma mass spectrometry (Appendices 2,3, 7-11). A pneumatically-operated graphite plug holder was added to the ETV so that the dosing hole could be plugged during the ETV heating cycle.

The detection efficiency is the number of ions reaching the Faraday detector divided by the number of atoms injected into the furnace and was 8.3×10^{-6}, 1.8×10^{-6}, 2.1×10^{-6} and 3.4×10^{-6}, respectively for Al, Fe, Mg, and Y. The detection efficiencies for the metallo-organic elements was an order of magnitude poorer than that of the aqueous elements studied in our laboratory using the same instrument. Detection limits was limited by the high level of impurities present in the blank and the poorer transport efficiency. For the determination of Mg, the detection was limited by the carbon interferent. Y was not present in the blank, therefore it has a better limit of detection. The detection limit of Y was limited by the amplifier noise.

If metallic species can be successfully dissolved in a liquid, the samples can be introduced into the ICP system via nebulization of the liquid. A variety of relevant elements have been introduced into both organic and aqueous solutions via microwave digestion (Appendix 7). Metallo-organic solutions of Al, Cr, Fe, Mg, Mo, Ni, Ti, and Y have been successfully digested, nebulized into the ICP, and the singly-charged ions measured by mass spectrometry. Metal particulates in oil matrices have been quantitatively determined using microwave digestion with ICP analyses. Linear analytical curves for the various elements have been obtained from detection limits of about 1ppb to greater than 1 ppm levels in solution. Lubricating oils collected from Rolling Contact Fatigue testers (oil from the Shetty and Adair testers were both used) have been analyzed via microwave digestion. Lower concentrations of wear products (Al and Y from grain boundary phases in the Si_3N_4 bearing balls and Fe, Ni, etc. From M-50 steel rods) were generated as a function of time for in the hybrid material test samples (Si_3N_4 bearing balls with M-50 steel rod) than the all-steel case at similar initial contact Hertzian stresses which is consistent with both specific wear rates and fatigue lifetimes determined by RCF testing in Tasks 2-3.

In laser ablation (LA), solid samples are exposed to the a high power laser beam. Thermal energy accumulates at the region of beam exposure so rapidly that thermal transport can not take place fast enough to dissipate the thermal energy. The exposed materials rupture via gaseous product generation as well perhaps some solid particulate debris. Laser ablation techniques overcome the sometimes time consuming digestion and electrothermal vaporization steps required to introduce ceramic samples into an ICP system. Laser ablation also has some limitations including the relatively high cost of lasers powerful enough to ablate ceramic materials, the exposed area that is ablated can vary from shot to shot, a composite material such as Si_3N_4 with specific grain boundary phases can ablate non-uniformly which necessitates the need for matrix-matched standards for quantitative analyses, and that laser-material interactions are not completely understood. In spite of these limitations, LA is a simple, rapid technique to introduce sample into the ICP-MS chamber. In the current study, documented in Appendices 8 through 10, laser ablation has been developed for both the surfaces of Si_3N_4 rolling elements as well as oil samples containing debris. It was shown that LA sample introduction provides more accuracy from solid samples rather than oils because of the need for matrix-matching with standards (Appendix 10). Both NIST solution standards and solid glass standards provided to be useful in determining the trace constituents in bearing materials (Appendices 9). In the current studies it was also shown that a compact and inexpensive Nd:YAG laser offers a low cost solid LA sampling option for ICP-MS, which is also available in a portable form (Appendix 8). Light scattering was also used to normalize the signals in LA-ICP-MS (Appendix 11). It was shown that the technique is useful for analyzing samples within a particular matrix and if the particle sizes are similar, but light scattering normalization of the signals is not as effective as the use of an internal standard.

Task 1.2. Analysis of the Role of Lubricant in Wear of Hybrid Bearing

In addition to the analysis of wear debris, the role of the lubricant on hybrid bearing performance was also evaluated (Appendices 4 through 6). A commercial, synthetic polyester-based lubricant was used in these studies. While the use of a commercial lubricant precludes an intimate knowledge of the base stock and additive package, it maintains the relevance and focus of the project goals with respect to hybrid bearing performance. Both the as-received lubricant and lubricant thermally degraded in a variety of conditions at 200°C to 300°C (in air, under Ar, with M-50 steel present as a catalyst, etc.) were used to evaluate the performance of hybrid bearing materials with a pin-on-disk tribometer under less than ideal conditions. These results will be reported in Task 2. The lubricants were also carefully evaluated by a variety of techniques in both University of Florida laboratories and in the Lubricant Characterization facility directed by S. Brown at Pratt&Whitney Aircraft (West Palm Beach, FL). It was shown that the commercial lubricants degradation leads to carbonaceous particulates (Appendices 4 and 5) known commonly as "sludge." While this is well known it was also shown that the determination of the concentration of the sludge via UV-visible absorption analyses enables one to produce a total lubricant degradation number when combined with more familiar analyses such as TAN (total acid number) and anti-oxidant concentration determinations. The rate of sludge particle formation was dependent on a parabolic rate law indicating the rate limiting step in sludge formation is diffusion of species from the bulk solution to the growing carbonaceous particle interface (Appendices 4 and 5). It was also shown that the change in viscosity of the lubricant can be predicted with the Einstein relationship for particulate suspensions once the concentration of sludge particles is known via analysis and deconvolution of the UV-visible absorption spectra for the degraded lubricant (Appendices 4 and 6). The implication is that compact UV-visible spectroscopy can be utilized in-situ to monitor the change in lubricant viscosity due to the formation of sludge particles.

Activity 2.0 Measurement of Wear

The objective of the second activity is to better understand the physical characteristics of the surfaces of bearings and raceways as a function of wear. John J. Mecholsky, Jr. directed this activity for the program team. Additional documents and manuscripts related to the work on this task are provided in Appendix 12 through 21.

Task 2.1 Characterization of the Microstructures and the Mechanical Properties

Processing, microstructures, and properties of the two primary silicon nitride materials that were used in the current study are summarized in Appendix 2. In Table 1 are listed the physical and mechanical properties of two commercial rolling element materials. Representative microstructures (courtesy of H.A.J. Chin of Pratt&Whitney Aircraft for sample preparation) are shown in Figures 2 and 3 in Appendix 26. The Mg-doped Si_3N_4 has more equiaxed grains with a slightly higher hardness, but lower toughness than the Y,Al-doped materials with more elongated grains.

Table 1. Physical and Mechanical Properties of Two Bearing Grade Si_3N_4 (Appendix 26)

Type of Silicon Nitride Material	Y,Al-Doped	Mg-Doped
Densification process	Pressureless Sintering + HIPing	Hot-Isostatic-Pressing
Oxide additives	Y_2O_3 and Al_2O_3	MgO
Density (g/cm^3)	3.23	3.16
Young's modulus (GPa)	308	320
Poisson's ratio	0.29	0.26
Fracture toughness (MPam$^{1/2}$)	6 - 8 $5.15 \pm 0.06^*$	4.1
Hardness (Vickers Indentation) GPa	14 -16 (at 20 kg)	16.6 (at 10 kg)
Coefficient of thermal expansion (x10^{-6} m/m°C), 20-800°C	2.9 - 3.2	2.9
Thermal conductivity (watt/m°C)	18 - 25 (at 20°C)	29.3 (at 100°C)

*Measured by the authors using short-bar technique.

One material is a direct HIPed Si_3N_4 with MgO as the additive. The other material is a pressureless sintered and posted-HIPed Si_3N_4 with Y_2O_3 and Al_2O_3 as the sintering additives. The density of the sintered HIPed silicon nitride (3.23 g/cm^3) is slightly larger than that of the direct-HIPed silicon nitride (3.15 g/cm^3) because of the different additives used. In addition to the fracture toughness values reported by the manufacturers, fracture toughness of the Y,Al-doped materials was determined by the authors in an on-going research program using the chevron-notched short-bar tests.

Silicon nitride typically has higher fracture toughness than the other non-transforming monolithic ceramics. This is attributed to the whisker-like interpenetrating morphology of the β-Si_3N_4 grains which deflect and/or bridge the crack, and thus increase the fracture resistance. In the so-called self-reinforced silicon nitrides, this unique microstructure has been further exploited to increase the fracture toughness to ~10 MPa√m. The wear behavior and rolling contact fatigue resistance of self-reinforced silicon nitrides has not been reported yet. However, it is likely that the fine-grained microstructure of the commercial bearing-grade Si_3N_4 has the advantage of obtaining better surface finish as compared to the coarse-grained self-reinforced silicon nitride materials.

The material requirements for a rolling element, in addition to high fatigue stress, include high hardness and adequate toughness to minimize the wear rate. The fatigue stress for the Si_3N_4 bearing element in a hybrid bearing is much higher than the fatigue stress for the M-50 steel raceway. It has been shown that the raceway spalls much more readily than the Si_3N_4 rolling element so long as the quality control on the ceramic rolling element has eliminated large surface or near subsurface flaws. One of the problems with an all ceramic rolling elements (i.e., both ceramic rolling element and raceway) is the high wear rates and therefore reductions in service life. Furthermore, service life for a bearing does not necessarily mean that a catastrophic failure takes place. Bearings (i.e., rolling element, raceway, and cage) are designed to have uniform and low wear rates. Under ideal conditions a bearing is replaced because the increasing gap between rolling element and raceway due to uniform wear begins to cause excessive vibration. In most hybrid bearing designs, the inner M-50 steel raceway undergoes the most stress and experiences the highest wear rate. The fatigue stress for a ceramic bearing that Mecholsky uses as part of the effort at UF is on the order of ~3-20GPa. To put this into perspective, the ~1inch bearings in the oxygen turbopump on the NASA space shuttle are designed for a maximum Hertzian contact stress of ~2GPa.

Task 2.2 Evaluation of Rolling Contact Wear and Fatigue Life of Si_3N_4

Task 2.2.1 Evaluation of the Cyclic Fatigue Life of Hybrid Bearing Materials

Full-scale bearing tests provide the most accurate data on the applicability of a bearing material. However, full-scale bearing tests are expensive and time-consuming, particularly in the case of ceramic materials. Four different methods were used to evaluate wear in hybrid bearing materials in the current study, rolling contact fatigue (RCF) testing, a cyclic fatigue test based upon a WC-Co bearing ball contacting a Si_3N_4 flat plate, a pin-on-disk system used also to measure the coefficient of friction, and a traction rig. A cost effective and expedient way to evaluate bearing materials is to use rolling-contact fatigue tests that incorporates simple geometry's of the specimens and simulates the rolling-contact. The RCF testers, however, do not reproduce the many complex test conditions encountered in a full-scale bearing test. Furthermore, Grade 5 bearing surfaces have an extensive lifetime usually beyond the scope of a graduate student career. Therefore, conditions that produce accelerated testing are generally used in RCF testing. In the current program, surface roughening, particulate suspended in the lubricant, and thermally and chemically degraded lubricants were used to evaluate wear and fatigue life.

To date, there is no established standard test for measuring RCF life. A number of test rigs have been used for evaluating the performance of bearing steels and Si_3N_4 materials. Typically, in such tests, a detector coupled with a shutdown device is used to monitor the vibration of the assembly. When a preset vibration level is exceeded, indicating the formation of a spall, surface crack, or excessive uneven wear, the test is automatically stopped and the lifetime of the test is recorded. Alternatively, tests may be suspended at different time durations to study the wear rate and mechanisms (Appendices 12,13).

In the current study, RCF tests were accelerated by the usual surface roughening of Si3N4 rods with M-50 steel bearing balls (see Appendices 12-13) and by the use of less than ideal lubricant including particulate added to the lubricant (Appendices 16-17) and the use of thermally degraded lubricant (Appendices 17-19). With roughened surfaces (R_a=0.18μm), RCF lifetimes were limited by wear on the steel bearing balls while as-polished surfaces (R_a=0.08μm) resulted in fatigue life determined by either the metal ball failing or test suspension at 100 hours (Appendices 12-13). For studies in which near ideal bearing elements ($R_a \approx$3nm) of M-50 steel rods and ceramic bearing balls were used, particles were present in the lubricant used in RCF testing. In these cases, fatigue life was dictated by contact stress fatigue on the M-50 steel rods with indenting, cutting, and plowing of the steel surfaces by the particles a secondary, but important additional effect (Appendices 16-17).

RCF testing of thermally degraded lubricants is still underway. In pin-on-disk testing with a thermally degraded lubricant, there was no distinctive effect in wear or changes in coefficient of friction due to any particular degradation product. This finding implies that wear is basically an opportunistic effect with any weak link in the material system of bearing elements and lubricant leading to enhanced wear. A correlation was found between coefficient of friction and the concentration of all of the degradation products (Appendices 18-19). Another preliminary study (Appendix 14) based on microstructural evaluation indicated that corrosion of the M-50 steel in the synthetic ester-based lubricant takes place during the course of the experiment and that relative humidity in the atmosphere plays a role in the corrosion of the steel. In general, more pitting was observed on the M-50 steel as the relative humidity was increased. A correlation between the infra-red spectra of the state of wear on the surface on the silicon nitride was also found with a semi-empirical molecular orbital calculation used to generate theoretical IR spectra as a function of Si_3N_4 cluster size. Wear surfaces correlated well to smaller cluster sizes while spectra from as-polished surfaces were more consistent with larger Si_3N_4 cluster sizes.

Task 2.2.2 Traction rig analysis of Si_3N_4 on Si_3N_4 and Si_3N_4 on M-50 steel

Rolling contact wear in ball bearings takes place within the Hertzian contact region as a result of microslippage between the balls and races. The level of microslippage depends upon the relative sliding velocity of the balls on bearing races as determined by the distance from the instantaneous axis of rotation and the contact surface. Within the contact region, the surfaces may experience various levels of microslippage. It is the sum total of this microslippage that affects wear rate, heat generation and friction torque. Traction coefficients were used to make these predictions. Technical details of these studies are provided in Appendices 20 and 21.

Bulk modulus data for graphite powder compressed up to 690 MPa (100,000 psi) was obtained and it was shown how this property can be used to predict the film thickness of graphite powder in Hertzian contact. It was shown that other powder lubricants being considered for high temperature applications can be analyzed with this method but would require the above physical properties at the specified temperature. A procedure for predicting traction coefficients for powder lubricants compressed to Hertzian contact pressures was developed by Dareing and co-workers (Appendices 21, 22, and 27). The method of analysis requires prior knowledge of physical properties of the powder lubricant under extreme pressures. The technique is based on the assumption that unconsolidated powder lubricants behave as elastic solids when compressed to Hertzian pressure levels in rolling contact regions. This assumption is supported by the classic work of P.W. Bridgman who studied the effects of extreme pressure on physical properties of several chemical substances, including graphite. Relevant physical properties are: bulk modulus, shear strength, coefficient of friction, modulus of elasticity/rigidity and Poisson's ratio. Each of these physical properties depend on the magnitude of applied compressive stress. Expected minimum film thickness of powder lubricants in Hertzian contact is also produced using bulk modulus/pressure data.

Activity 3.0 Determination of Wear Mechanisms

Wear-mechanism maps for silicon nitride in rolling contact can be useful design tools for hybrid or all-ceramic bearings. Before a wear mechanism map can be constructed, however, the various wear mechanisms of silicon nitride in rolling contact should be identified and distinguished. Several wear mechanisms have been reported in the literature, but there may be still other mechanisms that have not been identified, especially for rolling contact in oil-lubricated conditions. In oil-lubricated rolling contacts, certain chemical reactions can occur between the lubricant and the secondary phases of the silicon nitride, particularly at high temperatures. There is very little information on this subject in the literature.

RCF testers have been used primarily to investigate the fatigue failures or to compare the overall wear resistances of different materials. For wear mechanism studies, RCF testers are not as useful as sliding contact testers. For example, most RCF testers do not readily have the capability of measuring rolling friction coefficient, which is an important parameter for distinguishing different wear mechanisms. On the other hand there is very little information about how the wear behavior in sliding contact can be correlated to the wear phenomenon in rolling contact. Constructing the rolling wear mechanism maps based on RCF test data, or establishing sound correlations between sliding and rolling wear behaviors is essential for comprehensive characterization of silicon nitride for bearing applications.

The objective of this activity was to determine the mechanism(s) of failure modes of the bearings as a function of environment and stress states relevant to ceramic ball and roller bearings. The ultimate goal was to produce rolling contact fatigue mechanism maps similar to the deformation mechanism and creep mechanism maps.

Wear mechanisms of silicon nitride have been studied extensively in both sliding contact and rolling contact fatigue testing (Appendices 12-21). Mecholsky and co-workers have also designed a cyclic contact fatigue test to reproduce the cyclic loading that a bearing ball experiences during operation (Appendices 22-25). The data taken from these sources has been used to evaluate wear mechanisms particularly on the silicon nitride rolling element. Wear behaviors of silicon nitride have been investigated by a number of investigators using various testers. What is lacking however, are correlations between the laboratory-scale wear tests and the prospective full-scale applications. To establish such correlations it is important to understand the wear mechanisms of silicon nitride, particularly in rolling contact, and how the mechanisms change with variation of the environmental conditions.

Since the word "wear" implies the formation and removal of debris particles, it includes to some extent a fracture process. Several wear mechanisms, based on fracture mechanics theories, have been proposed in the literature; for example, the lateral cracking and fracture mechanism proposed by Evans et al. and the delamination wear mechanism proposed by Fleming and Suh. The lateral cracking and fracture mechanism employs the concepts of indentation fracture mechanics and takes into account the plastic deformation in brittle materials. The delamination wear mechanism focuses on the shear stress acting on a subsurface crack when abrasive motion occurs on the surface using linear elastic fracture mechanics theory. Both mechanisms involve a mechanical-type wear process with the load (P), indenter geometry, elastic modulus (E), hardness (H), and fracture toughness (K_C) of the materials as the major variables and material parameters. However, as the material processing and surface finishing techniques of Si_3N_4 rolling elements have been improved, wear of Si_3N_4 is typically mild and the mechanism is not purely mechanical, but more complicated. For example,

(1) In sliding contact studies, wear debris was found to be generated by crack (surface and subsurface) formations in the scale of microstructural features. On that scale, the continuum and elastic fracture mechanics theories are not valid and the local stresses are clearly defined.

(2) Formation of wear debris very likely involves chemical reactions at the interface. The chemical reactions can be affected by the interface temperature, humidity, and the additives in the lubricant used.

Wear mechanisms of silicon nitride have been widely studied in sliding contact. Rolling contact fatigue tests, on the other hand, have been primarily used for evaluating the fatigue lives of different grades of Si_3N_4 and demonstrating the feasibility of using Si_3N_4 as a bearing material. Information in the literature on the wear mechanisms of silicon nitride in rolling contact is limited. An extensive literature survey has been made to review the state of knowledge of the fatigue and the wear behavior of Si_3N_4 in various rolling-contact conditions (Appendix 26). The current studies into wear degradation mechanisms for brittle materials have identified three stages of wear damage (Appendices 22-24). These stages will be described below. However, before describing this damage mechanism process, the specific conditions to which the mechanisms apply have to be explained.

In discussing wear degradation due to rolling fatigue, the distinction is made between elastic processes and elastic-plastic processes. The degradation mechanisms will be different for the two cases. Wear degradation of (elastic-plastic) ductile materials will be governed mainly by the shear stresses beneath the contact region. Wear degradation in (elastic) brittle materials will be governed mainly by fracture processes due to tensile stresses outside the contact region and under the contact region at the surface. The case for brittle materials will be addressed here. In addition, there are two different behaviors that can be observed in the degradation of brittle materials which are subjected to cyclical contact, depending on the condition of the material and the shape and magnitude of the stress field. We will only address the case for a Hertzian stress field here. If the material was processed in such a way as to have bulk defects such as microcracks, pores, inclusions, etc., then most likely the damage will initiate from the subsurface and propagate to the surface. Alternatively, if the largest defect is at the surface, then Hertzian cone cracks will form outside the contact area, but the formation will occur at lower load levels than for defect free surfaces. If the processing procedures have been improved to the extent that there are no, or minimal, bulk defects, then the wear degradation process is due to a fracture process as a result of Hertzian (elastic) contact stresses.

In order to study the degradation of brittle materials due to wear processes, the load is cycled on a ball contacting a plate (Appendix 22). This test simulates the essential properties of the wear process. A WC-Co spherical ball is placed in contact with a silicon nitride material. In general, the levels of damage can be different depending on specific composition and microstructure.

The mechanisms of failure due to wear in brittle materials which have been processed to remove bulk defects and have a fine surface finish can be divided into three stages (Appendix 22-23, 26). The first (Stage I) is a roughening of the surface under the contact region due to separation of the grain boundaries. The second (Stage II) is the formation of cone cracks or partial cone cracks near the periphery of the contact region and the further degradation of the region under the contact area by grain pullout and microcrack formation. The third stage (Stage III) involves the removal of material from the region outside the contact area by connection of surface cracks.

Stage I occurs because, in most silicon nitride materials, there is a grain boundary phase which is glassy or partially glassy. This glassy phase is viscoelastic and as such will have a time delay in response to deformation. This delayed response allows tensile stresses to form at the grain boundary during the unloading cycle; on subsequent cycles, separation of the grain boundary occurs by crack formation in a tensile mode. This process results in an uplift of the surface under the contact region and appears as a roughening of the surface.

Stage II occurs because the Hertzian stress field causes high tensile stresses at the edge of the contact region, and because of the existence of cracks on the surface. These cracks can be subjected to stress corrosion processes as well. Cracks will start at the grain boundaries and propagate in a circulator trace on the surface and in a cone shape beneath the surface in a classical Hertzian cone crack formation. Simultaneously, the degradation under the contacted region is progressing because traction forces beneath the spherical indenter lead to pullout and further roughening of the surface.

Stage III is the final damage stage and involves the propagation of the cone cracks toward the surface and a connection to the surface cracks which results in removal of material from the surface. This appearance may sometime resemble what has been termed "spallation." However, we make the distinction between spallation and contact fracture damage in that spallation is generally caused by subsurface cracks which propagate to the surface and the damage described here is for Hertzian cone cracks on the surface.

In addition to the relatively conventional scanning electron microscopy analyses, the surfaces of bearing balls were examined in the as-received condition and after wear testing using the atomic force microscope (AFM) (Appendix 25). This instrument allows the detection of small deviations from the surface. The balls that were worn had a smoother surface than balls that were as-received after surface finishing. Thus, it is not the surface finish, *per se*, that contributes to the degradation, but rather grain pullout, fatigue and stress corrosion of the grain boundary phases. Pits were observed on the surfaces of these balls.

Fractal analysis was used to characterize the wear damage on balls that were subjected to wear in a four ball tester (Appendix 25). In addition, fractal analysis was performed on fracture surfaces of fatigue specimens and of laboratory control bars failed at different stress levels. All of the fracture surfaces had the same fractal dimension indicating that the fracture process was the same in "spallation" damage of balls, on fracture surfaces of rods failed in cyclic fatigue and of bars failed at low and high stress levels. Thus, this implies that the mechanisms of damage are the same. Other tests as described above have confirmed that the ball damage was not spallation, but rather a fracture process. Fracture in fatigue specimens may start for different reasons than fast fracture bars failed in flexure, but the actual propagation is the same as in the controlled laboratory tests.

This study showed that, for Si_3N_4 the fractal dimension, D*, is the same for failure surfaces created under different stress states. This fact implies that the fracture process in brittle materials could be controlled by one stress mode, such as a local Mode I stress. The existence of a relation between D* and the critical stress intensity factor K_{Ic} for Si_3N_4 further supports this supposition. Furthermore, the D* value is independent of scaling factors for an identical material and again demonstrates the fractal nature of fracture surfaces.

The information from this study implies that: (1) the fractal dimension of the fracture surface produces additional information to indicate that the brittle material failure process is governed by local bond breaking and controlled by a Mode I type stress regardless of the global stress state; (2) the fracture process in Si_3N_4 is a self-similar process from small scales to large scales, represented by its fractal dimension; (3) the relationship between D* and the material constants further implies that fracture is a fractal process; and (4) using the relation of the fractal dimension and fracture energy, we show an atomic scale process zone near the crack tip.

The reason that the fractal approach is appealing is that it not only provides a means of characterizing the material's failure surface, but also suggests a means for generation of the fracture surface. From this study, the fractal method emerges as a method with potential for identification of a failure model, and eventually will lead to an understanding of fracture and wear processes in material structures.

Activity 4.0. Development of Precatastrophic Failure Prediction

The objective of this activity is to develop and test the models generated to predict wear as a function of time. The approach and organization in this task are similar to that in Activity 3. As data is generated in Task 1, 2, and 5, the effort in this activity will take on increased emphasis. In this activity two large reviews of activities related to the hybrid bearing materials and the development of a theoretical approach for bearing service life are included in Appendices 26 and 27.

Personnel at the University of Utah and the University of Florida compiled a comprehensive review with the state of knowledge on two bearing grade Si_3N_4 materials (Appendix 26). Included in the report was the various ceramic processing steps used to make ceramic bearing materials, microstructural and physical properties including bend strength, hardness, and fracture toughness, and properties relevant to wear applications including RCF life for both hybrid and all steel bearings. The theory formulated and tested for wear and fracture of the Si_3N_4 rolling elements by Mecholsky and co-workers (Appendices 22-24) was also summarized. Directions for further development and implementation of hybrid bearings were also presented in this compilation provided in Appendix 26.

Dareing (University of Tennessee) has provided an evaluation of the performance and prediction of bearing wear for the hybrid systems (Appendix 27). The wear data was generated at the University of Utah and Florida and compiled at UF for Dareing as part of the synergy that was present among program team members. Traction data used in the calculations was generated by Dareing and his co-workers. The methodology developed by Dareing and co-workers includes prediction of heat generation, roller ball wear, and torque input for radial roller ball bearings. Performance predictions are based on the mechanism of microslippage within Hertzian contact regimes. Wear was predicted for various combinations of bearing geometry, material properties, load, surface conditions, and rotational speed. Additional details of the mathematical model and computer program are provided in Appendix 27. This development by Dareing and co-workers will greatly aid in the prediction of wear for hybrid bearings. The hybrid bearing is predicted to perform better than steel bearings with respect to heat generation, torque, coefficient of friction, and service life.

Activity 5.0. Development of Methods to Minimize Wear of Hybrid Bearings

5.1 Ti Surface Modification of M-50 (unheat-treated, soft)

Two types of surface modification techniques have been used with untreated M-50 steel: Ion implantation and reactive sputter coating. Details of the surface modifications are provided in Appendix 28. Under lubricated conditions, TiO_X showed the lowest friction coefficient of 0.04 at relative humidity of 30-35%. A possible explanation for this behavior comes from the surface chemistry. Since the TiO_X surface possesses an acidic nature, it should attract OH^- groups from the oil lubricant and form a thin layer chemically bonded to the surface. This relatively stable surface film could enhance the separation between the pin and the disc by maintaining a better lubrication under all conditions. As a result, the friction force would be reduced during the sliding test. This hypothesis needs to be confirmed by future experiments and verified by surface chemical analysis.

For the unlubricated tests, TiC_X showed a maximum friction coefficient of 0.4, which was the lowest among all the samples tested under the same conditions. Furthermore, the friction value was not significantly affected by the change in relative humidity. Hard, high modulus surface coating may result in less friction and wear by reducing the wear contact area. This effect was verified by the reduced wear mark diameter from the Si_3N_4 pin as well as a reduced wear track width on the disc. Physical separation between steel and the humid environment could contribute to the lack of an effect of humidity when the TiC_x surface modification is present.

Wear debris was collected during and after each wear test from the wear track and the ball individually. The debris was studied using scanning electron microscopy (SEM) and energy dispersive X-ray spectroscopy (EDS) analysis. Significant differences in debris composition, appearance, and quantity were observed over different surface conditions. By studying the spectral peak ratio of Fe/O and Si/O, semi-quantitative information about the debris was obtained.

For M-50 standard material, the Fe/O ratio was high and Si/O ratio was lower in debris from the pin verses from the wear tracks. This suggests that either the amount of Fe transferred to the Si_3N_4 pin surface increased or more oxidation occurred on the disc surface or both. More Si transfer to the track was observed as the wear test proceeded. For Ti implanted M-50, the Fe quantity was low in the debris at for the earlier testing period. However, the amount of Si in the debris from both ball and track increased significantly as the test proceeded. The TiC_x coated sample showed much less debris generation overall during the tests. A very small amount of Fe was detected in the debris. However, the Si quantity increased to a much higher level than that from M-50 and Ti implanted M-50.

Analysis of debris is still preliminary and much is currently in progress. However, using wear track width and pin wear mark diameter as being proportional to wear volume, TiC_x showed the least wear rate and both M-50 and Ti implanted M-50 had similar wear rates under the unlubricated conditions. A more complete analysis will be available in the future.

1. Under lubricated conditions, TiO_x provided the lowest friction coefficient of 0.04 for 3/8" diameter pin under 50g load.
2. Under unlubricated conditions, TiC_x provided the lowest friction coefficient of 0.4 for 3/8" diameter pin under 50g load.
3. Higher humidity results in higher friction coefficients for standard M-50 and Ti implanted M-50. However, TiC_x coated M-50 appears not to be affected by humidity variation.
4. Analysis shows that significant differences exist in debris composition, appearance, and quantity for different testing materials. Both pin and disc are wearing.

Task 5.2 Silane Self-Assembly Systems as Lubricious Surface Treatments

Lubricants have among the additive package, species designed to provide lubricious surfaces (Appendix 18). For example, tricresylphosphate is used to provide a lubricious agent in all steel bearing systems. Like many amphiphilic molecules the polar, phosphate head group binds to Fe sites on the steel surfaces with the relatively bulky, three aromatic rings extending into the bulk solution to provide the desired lubricious surface. Choudhary has evaluated the use of silane coupling agents using silicon as a model material. The eventual aim of this thrust is to design lubricant additives specific to the hybrid bearing materials in contrast to the lubricant additive packages developed for all steel bearings that are nonetheless used in hybrid bearing systems. Self-assembled films on Si using three different organo-silanes, η-octadecyl-triethoxysilane (OTES), η-octadecyltriethoxysilane (OTMS), and , η-octadecyltrichlorosilane (OTCS) were used to evaluate the efficacy of the self-assembled monolayers (SAM) to provide lubricious surfaces. Pin-on-disk with a SAM on a Si flat and a Si_3N_4 pin was used to determine coefficient of friction as a function of speed, pin travel, load and relative humidity. Three organo-silanes differing only with respect to the coupling moiety were used because the organization in the SAM increases in order from the chloro, methoxy, and ethoxy based coupling agents. The SAMs provided increased lubricity for speeds up to 0.5 cm/s in dry conditions, but their influence disappeared above this speed. Relative humidity increased the CoF increased, while COF determined in a synthetic lubricant was as low as 0.01. In general, SAM stability indicated by the load that a SAM was capable to withstanding while providing lubricity decreased as the organization of the SAM increased. It is believed that the SAMs based on OTES and OTMS, although more organized, are more brittle and, therefore, more subject to mechanical degradation than the more poorly organized OTCS-based SAM. The results of this work indicate it is feasible to use organo-silanes to provide a lubricious coating on silicon-based materials so long as the coating is compatible with the lubricious agent on the steel raceway. However, work is currently being designed to test whether the organo-silanes can diffuse rapidly enough from the bulk solution to the bearing surface during operation to provide a self-healing lubricious layer.

Task 5.3 Hard Coatings

The work conducted on the processing and tribological properties of hard coatings are summarized in Appendix 30-34. Both diamond-like-carbon and diamond coatings was evaluated as part of this effort. Diamonex, Inc (Allentown, PA) used chemical vapor deposition techniques to coat M-50 steel with diamond-like-carbon (DLC) coating and a form of DLC designed for higher temperatures for Adair and co-workers. The primary advantage of putting a DLC coating on the M50 steel raceway materials rather than diamond is that DLC may be deposited at temperatures much lower than those required for diamond. As a consequence, the thermal expansion mismatching, carbonization, other problems experienced in depositing diamond on steel are avoided with DLC coatings on steel. Nunez then performed the tribological testing using a pin-on-disk system to determine coefficient of friction as a function of load, relative humidity, and temperature. It was found that the CoF was relatively insensitive to load over the range of loads tested (25 to 250g loads) for the 0.25 inch ball and DLC-coated M50 steel flat used in the pin-on-disk tester while both relative humidity and temperature had profound effects on CoF. In unlubricated conditions, the CoF increased with increased relative humidity, while CoF decreased with temperature to 300°C (CoF=0.05), but increased to 0.1 and 0.3 at 400°C and 500°C, respectively. The CoF value increased from 0.05 at 35%RH to 0.05 to 0.1 at 65%RH for the Si_3N_4/DLC-M50 system. In contrast, the Si_3N_4/M50 steel pin-on-disk system had CoF values from ~0.45 for unlubricated conditions to ~0.12 with a synthetic polyester-based lubricant. Thus, the 4 micron thick DLC on the M-50 significantly reduced the CoF, particularly for unlubricated conditions. The CoF results for the various conditions were consistent with evaluations by Gardos and Ravi and Erdemer et al. that discussed the role of the surface chemistry, particularly the state of surface hydrogenation as a function of environment.

A number of reports have been generated for diamond coatings on the Si_3N_4 rolling element material as well as a general approach to control the grain size of CVD diamond films (Appendices 31-34). Films up to 5 micron thick have been reported using the particulate enhanced CVD approach based on control over the colloidal properties of abrasive diamond powders used as nuclei in the CVD growth of diamond (31-33). In Appendix 34, the use of nanometer diamond seeds permits the preparation of diamond films on Si_3N_4 with an as-grown surface roughness of R_a=24 nm in contrast to the typical diamond film surface roughness of $R_a \geq 100$nm. The surface roughness of diamond coatings is an issue in preparation because specific wear rate increases with increased roughness. Polishing diamond is possible, but polishing should be unnecessary if the surface roughness of the as-grown CVD diamond is low enough. The specific wear rate of the initially diamond-coated Si_3N_4 pin fell in between literature values for CVD diamond films polished to R_a values of ~100nm and 11nm. The experimental results verify the hypothesis that as-grown surface roughness of diamond films can be controlled by the enhanced CVD process developed at UF and that specific wear rate of a Si_3N_4 pin is a function of diamond surface roughness.

Task 5.4 Coatings the Provide Surface Compression

Low fracture toughness has always been a concern in using ceramic materials for bearing elements. Silicon nitride has slightly higher fracture toughness than other monolithic ceramics, but such toughness has to be combined with quality-controlled processing routes, fine surface finish and nondestructive evaluation in order to have consistent performance. Residual compressive stress on the surface of silicon nitride bearing elements is expected to have the advantage of higher apparent fracture toughness and damage resistance, with potential for cost savings in processing, surface finishing, and nondestructive evaluation (Appendices 35 through 37).

Surface compression has a positive effect on the RCF performance; however, several important questions must be addressed before this approach can be utilized. For example, (1) the effect of the residual surface compression on the RCF performance of CVD SiC should be examined at different levels of surface compression. It is likely that there is an optimum compressive stress for this approach since the CVD SiC will spontaneously debond at the substrate-coating interface if the surface compression is too high; (2) it is essential to eliminate subsurface defects in the CVD-SiC that can lead to catastrophic spalling; (3) can this approach be employed on CVD Si_3N_4? Currently, the deposition rate of CVD Si_3N_4 is too low to be economically viable.

Surface compression via the layered composite concept can also be implemented by a cosintering process. However, this approach is likely going to increase the manufacturing cost of ceramic bearings. Optimum surface compression plus appropriate substrate with lower material cost appear to be the key elements for the successful application of this technology.

EDUCATIONAL ACTIVITIES

During the course of the program at the University of Florida, 1 B.S. Honors thesis, 4 M.S. degrees (3 with thesis and one non-thesis) and 5 Ph.D. degrees were awarded with one M.S. and two Ph.D. pending at this writing. Abstracts for the theses are also provided in the appendices of this final report.

The concepts embodied in tribochemical interactions and tribological behavior of materials have been incorporated in the graduate curriculum at the University of Florida via modification of existing graduate courses. Dr. Adair teaches two courses, Applied Solution Chemistry and Applied Colloid and interfacial Chemistry that have incorporated relevant aspects of tribochemistry and lubricant chemistry into the curriculum. Dr. Mecholsky has also folded tribological and cyclic interactions into his graduate course on Advanced Mechanical Properties of Materials. Dr. Adair also teaches two undergraduate courses entitled Design of Engineering Ceramics and Environmental Stability of Materials while Dr. Mecholsky teaches an undergraduate course on Mechanical Behavior of Materials which incorporate tribological properties of materials as part of the learning process for undergraduate students in Materials Science and Engineering at the University of Florida.

ACKNOWLEDGMENTS

The university participants deeply appreciate the support from the Air Force Office of Scientific Research, and especially Dr. Alexander Pechnik, for the support from University Research Initiative that permitted the work reported herein to be conducted. Grateful acknowledgment is also conveyed to the Deans of the Colleges of Engineering and Liberal Arts and Sciences at the University of Florida for the matching support for graduate student stipends and equipment as well as to the Department Chairs in Materials Science and Engineering and Chemistry. Personnel in the Major Analytical Instrumentation Center at UF and, in particular, Dr. Robert E. Chodelka, Dr. Lambers, Dr. Augosto Morrone, Mr. Wayne Acree, and Mr. Richard Crockett are thanked for graduate student instruction in the panorama of analytical equipment inn MAIC including AFM, SEM, and XPS characterization.

The university participants also are grateful to the participants in the three annual workshops. The industrial partners and national laboratory personnel who participated at the annual workshops helped to maintain the focus of the work and avoid straying from the pragmatic and practical aspects of the project without compromising the scientific basis of the studies conducted. Grateful acknowledgment is especially made for the contributions of John Minor, Roger Bursey, Sue Brown, and Herb Chin of Pratt & Whitney Aircraft in West Palm Beach, Florida for their efforts to aid the university participants with their laboratory facilities, characterization equipment, know-how, and experience with hybrid bearings.

APPENDICES

APPENDIX 1, **Agendas, Attendance lists, and action items from the three Annual Workshops on Predicting Materials Degradation and Fatigue in Aerospace Structures held at the University of Florida in 1994, 1995, and 1996.**

APPENDIX 2, **M.P. Escobar, "Determination of Wear Metals in Lubricating Oil by Electrothermal Vaporization Inductively Coupled Plasma Mass Spectrometry," Abstract of Ph.D. Dissertation presented to the Graduate School, University of Florida, May 1995. Dissertation copy available upon request. J.W. Winefordner, advisor.**

APPENDIX 3, **M.P. Escobar, B.W. Smith, and J.D. Winefordner, "Determination of Metallo-Organic Species in Lubricating Oil by Electrothermal Vaporization Inductively Coupled Plasma Mass Spectrometry," Analytica Chimica Acta, 320, 11-17(1996).**

APPENDIX 4, **R. Sabia, "Physical and Chemical Interactions of Lubricants in Hybrid Bearing Systems," Abstract of Ph.D. Dissertation presented to the Graduate School, University of Florida, May 1996. Dissertation copy available upon request. J.H. Adair, advisor.**

APPENDIX 5, **R. Sabia, Herb A.J. Chin, and J.H. Adair, "A Kinetic Study of the Degradation Behavior and Mechanisms of a Synthetic Ester-Based Lubricant," submitted for publication.**

APPENDIX 6, **R. Sabia, J. Simmons, P.H. Holloway, Herb A.J. Chin, and J.H. Adair, "The Use of Optical Spectrometry to Monitor Degradation in a Synthetic Ester-Based Oil," submitted for publication.**

APPENDIX 7, **Robin A. Russell, "Determination of Metallo-Organic and Particulate Wear Metals in Lubricating Oils Associated with Hybrid Ceramic Bearings by Inductively Coupled Plasma Spectrometry," Abstract of Ph.D. Dissertation presented to the Graduate School, University of Florida, August 1997. Dissertation copy available upon request. J.D. Winefordner, advisor.**

APPENDIX 8, **S.A. Baker, B.W. Smith, and J.D. Winefordner, "Laser Ablation Coupled Mass Spectrometry with a Compact Laser Source,"** ***Spectroscopic Perspectives*****, 51[2], 1997.**

APPENDIX 9, **S.A. Baker, M.J. Dellavecchia, B.W. Smith, and J.D. Winefordner, "Analysis of silicon nitride bearings with laser ablation inductively coupled plasma mass spectroscopy," to be published in** ***Analytica Chimica Acta*****, 1997.**

APPENDIX 10, **Scott A. Baker, "Analysis of Glass, Ceramic, and Soil Samples Using Laser Ablation Inductively Coupled Mass Spectrometry," Abstract of Ph.D. Dissertation presented to the Graduate School, University of Florida, to be presented to the graduate school, May 1998. Dissertation copy available upon request. J.D. Winefordner, advisor.**

APPENDIX 11, **S.A. Baker, B.W. Smith, and J.D. Winefordner, "An Investigation of Light Scattering for Normalization of Signals in Laser Ablation Inductively Coupled Mass Spectrometry," submitted for publication.**

APPENDIX 12, **L-Y Chao And D.K. Shetty, "Wear and Fatigue Damage in Ball-on-Rod Rolling Assessed with Steel/Steel, Steel/Si_3N_4 and Si_3N_4/Si_3N_4 Contacts," to be submitted for publication.**

APPENDIX 13, **L-Y Chao And D.K. Shetty, "Wear and Fatigue Damage in Ball-on-Rod Rolling Assessed with Steel/Steel, Steel/Si_3N_4 and Si_3N_4/Si_3N_4 Contacts," ABSTRACT OF M.S. Thesis to be presented to the graduate school at the University of Utah, 1998. Thesis copy available upon request. D.K. Shetty, advisor.**

APPENDIX 14, **S. Akunuri, "Wear Characteristics of Silicon Nitride-M50 Steel Hybrid Bearing System," Abstract of M.S. Thesis presented to the Graduate School, University of Florida, July 1995. Thesis copy available upon request. J.H. Adair, thesis advisor.**

APPENDIX 15, **F. Mohammadi, J.H. Adair, E.D. Whitney, and J.K. West, "An Infrared Spectroscopy Analysis of MgO-Doped Silicon Nitride,"** ***Cer. Trans.*****, 69, 53-58 (1995). Non-thesis M.S.**

APPENDIX 16, **D.J. Mitchell, J.J. Mecholsky, Jr., and J.H. Adair, "Rolling contact fatigue and wear analysis of M50-M50 all-steel and Si_3N_4-M50 hybrid bearing rolling element systems using lubricants contaminated with Arizona test dust or single crystal α-Al_2O_3 particulate.**

APPENDIX 17, **D. J. Mitchell, R. Sabia, E.D. Whitney, and J. H. Adair, "Characterizing the Performance of Advanced Rolling Element Materials,"** ***Cer. Engr. & Sci. Proc.*****, 18[4], 85-92, (1997).**

APPENDIX 18, **R. Sabia, Herb A.J. Chin, and J.H. Adair, "Friction and Wear Properties of Silicon Nitride/M-50 Steel Sliding Couples in Degraded Ester-Based Lubricant," submitted for publication.**

APPENDIX 19, **R. Sabia, D.J. Mitchell, and J.H. Adair, "Effects of Oil Degradation on the Friction and Wear Properties of Silicon Nitride/M-50 Steel Sliding Couples,"** ***Cer. Engr. & Sci. Proc.*****, 18[3], 361-368, (1997).**

APPENDIX 20, **S. Atluri, and D. W. Dareing, "Traction Behavior and Physical Properties of Powder Graphite Lubricants Compacted to Hertzian Pressure Levels," submitted for publication.**

APPENDIX 21, **P. Cento and D. W. Dareing, "Evaluation of Ceramic Materials in Hybrid Ball Bearings," submitted for publication.**

APPENDIX 22, **Z. Chen, "Wear Mechanisms of Silicon Nitride Bearing Materials Under Contact Fatigue Stresses," Abstract of Ph.D. Dissertation presented to the Graduate School, University of Florida, May 1995. Dissertation copy available upon request. J.J. Mecholsky, advisor.**

APPENDIX 23, **Z. Chen, J. C. Cuneo, J. J. Mecholsky, Jr., and S. Hu, "Damage Processes in Si_3N_4 Bearing Material Under Contact Loading,"** ***Wear*** **198, (1996) 197-207.**

APPENDIX 24, **S. Hu, Z. Chen and J. J. Mecholsky, Jr., "On the Hertzian Fatigue Cone Crack Propagation in Ceramics," accepted for publication in *International Journal of Fracture.***

APPENDIX 25, **Z. Chen, J. J. Mecholsky, Jr., T. Joseph and C. L. Beatty, "Application of Fractal Fracture to Advanced Engine Material," in *Ceramic Materials and Components for Engines*, D.S. Yan, X.R. Fu and S.X. Shi, eds., World Scientific, Singapore, 1995, pp. 506-509.**

APPENDIX 26, **L.Y. Chao, D.K. Shetty, J.J. Mecholsky, and J.H. Adair, "Silicon Nitride in Rolling Contact Applications - Review and Assessment," J. Materials Education, 17 [5&6], 245-303 (1995).**

APPENDIX 27, **Don W. Dareing, Final Report on subcontract to the University of Tennessee, A Focused, Fundamental Study on Predicting Materials Degradation and Fatigue in Aerospace Structures, May, 1997**

APPENDIX 28, **P.H. Holloway, J. He, J.H. Adair, and W.D. Sproul, "Surface Modifications of M50-Si_3N_4 for Wear Reduction and Failure Prediction," oral presentation at the International Conference on Metallurgical Coatings and Thin Films, San Diego, CA, April, 1995.**

APPENDIX 29, **K. Choudary, "Tribology of Self-Assembled Monolayer Films on Silicon," Abstract of M.S. Thesis, University of Florida, 1997. Dissertation copy available upon request. P.H. Holloway, advisor.**

APPENDIX 30, **G.R. Nunez, "Effects of Diamond-Like-Coatings (DLC) in the Tribology of Hybrid Bearing Materials," Senior Honors Thesis, Mechanical Engineering, University of Florida, December 1994. J.H. Adair, advisor.**

APPENDIX 31, **Paul A. Demkowicz, "Colloidal Properties and Enhanced Chemical Vapor Deposition of Diamond," abstract of M.S. Dissertation presented to the Graduate School, University of Florida, May 1996. Dissertation copy available upon request. J.H. Adair, advisor.**

APPENDIX 32, **P.A. Demkowicz, S.S. Staehle, M.L. Carasso, and J.H. Adair, "Literature Review: The Colloidal Behavior and Engineering Applications of Diamond," submitted to J. Mat. Ed.**

APPENDIX 33, **M.L. Carasso, S.S. Staehle, P.A. Demkowicz, D.R. Gilbert, R.K. Singh, and J.H. Adair, "Control of the Microstructure of Polycrystalline Diamond and Related Materials via an Enhanced CVD Process, Ceramic Microstructures '96, Plenum Press, in press.**

APPENDIX 34, **P.A. Demkowicz, M.L. Carasso, D.R. Gilbert, R.K. Singh, and J.H. Adair "Colloidal Enhancement of CVD Growth of Diamond," to be submitted for publication.**

APPENDIX 35, **R. Lakshminarayanan, D.K. Shetty, and R.A. Cutler, "Toughening of Layered Ceramic Composites with Residual Surface Compression,"** ***J. Am. Ceram. Soc.*****, 79[1]79-87 (1996).**

APPENDIX 36, **R. Lakshminarayanan, D.K. Shetty, and R.A. Cutler, "Residual Stress Effects on Fracture Toughness of Layered Composites Assessed with Single-Edge-Notch - Bend (SENB) Specimens," submitted for publication.**

APPENDIX 37, **L.Y. Chao, R. Lakshminarayanan, D.K. Shetty, and R.A. Cutler, "Rolling-Contact Fatigue and Wear of CVD-SiC with Residual Surface Compression," submitted for publication.**

APPENDIX 1, Agendas, Attendence lists, and action items from the three Annual Workshops on Predicting Materials Degradation and Fatigue in Aerospace Structures held at the University of Florida in 1994, 1995, and 1996

Final Program
on
First Annual Workshop on Predicting Materials Degradation and Fatigue in Aerospace Structures.

January 7, 1994

University of Florida Reitz Union

Conference Room 349

8:00 - 8:30 AM	Registration & Continental breakfast	
8:30 - 8:45	Welcome and Introduction	Dr. Reza Abbaschian
8:45 - 9:10	Program Objectives and Management of Wear	Dr. Dow Whitney
9:10 - 9:35	Task 1 Detection of Wear	Ben Smith
9:35 - 10:00	Task 2 Measurement of Wear	Dr. Jack Mecholsky Dr. Dinesh Shetty
10:00 - 10:15	Coffee Break	
10:15 - 10:40	Task 3 Determination of Wear Mechanisms	Dr. Dow Whitney
10:40 - 11:05	Task 4 Precatastrophic Wear Prediction	Dr. Jim Adair
11:05 - 11:30	Task 5 Methods to Minimize Wear	Dr. Paul Holloway
11:30 - 11:45	Expected Results	Dr. Jim Adair
11:45 - 1:30	Lunch - Ballroom A-Reitz Union	
1:15 - 2:30	Committee Meetings	

Room 363	Detection of Wear	Dr. Jim Winefordner
Room 362	Measurement of Wear	Dr. Jack Mecholsky
Room 336	Determination of Wear Mechanisms	Dr. E. Dow Whitney
Room 334	Precatastrophic Wear Predictions	Dr. Jim Adair
Room 361	Methods to Minimize Wear	Dr. Paul Holloway

2:30 - 2:45	Coffee break
2:45 - 3:30	Committee Reports
3:30 - 5:00	Laboratory tours of MSE, Chemistry, and Major Analytical Instrumentation Center
6:00	Reception - Student Posters and Wine & Cheese - Ballroom A-Reitz Union
7:00 - 9:00	Dinner Banquet - Ballroom A-Reitz Union

ATTENDANCE LIST FOR 1994 WORKSHOP

Lewis B. Sibley
Tribology System, Inc.
225A Plank Avenue
Paoli, PA 19301
(215) 889-9088

William F. Mandler, Jr.
Enceratec
810 Brown Street
Columbus, IN 47201

Dr. James F. Dill
Mechanical Technology, Inc.
Engineering and Technology Divison
968 Albany-Shaker Road
Latham, NY 12110
(518) 785-2136

Alexander Pechenik
AFOSR/NC
110 Duncan Avenue
Suite 100
Bolling Air Force Base
Washington, DC 20332-0001
(202) 767-7749

John R. Miner
Technology Manager
Mechanical Components and Systems Programs
WEST END
Pratt & Whitney
Beeline Highway
West Palm Beach, FL 33410-9600
(407) 796-5951

Peter Chang
BIRL
Northewestern University
1801 Maple Avenue
Evanston, IL 60201
(708) 491-4108

Dr. Philip Centers
WL/POSL, Bldg. 490
1790 Loop Road N
WPAFB, OH 45433
(513) 255-6608

Dr. Kent J. Eisentraut
WL/MLBT
1790 Loop Road
WPAFB, OH 45433
(513) 255-4860

Dr. Karl Mecklenburg
WL/MLBT
1790 Loop Road
WPAFB, OH 45433
(513) 255-2465

Mike Foley
Norton Co.
Goddard Road
North Boro, MA 01532
(508) 756-9336

Dr. Leslie D. Kramer
Martin Marietta Missile Systems
PO Box 555837 MP-126
Orlando, FL 32855-5837

Y. P. Chiu
Torrington Company
59 Field Street
PO Box 1008
Torrington, CT 06790

Dinesh Shetty
University of Utah
304 EMRO
Salt Lake City, UT 84112
(801) 581-6449

Oh-Hun Kroon
Norton Advanced Ceramics
1 Goddard Road
Northboro, MA 01532
(508) 351-7944

Dr. James Adair
University of Florida
PO Box 116400
Gainesville, FL 32611
(904) 392-6594

Sreeram Akunuri
University of Florida
PO Box 116400
Gainesville, FL 32611
(904) 392-1015

Nelson Bell
University of Florida
PO Box 116400
Gainesville, FL 32611
(904) 392-1015

Cheryl Davis
University of Florida
301 CRB
Gainesville, FL 32611
(904) 392-0792

Monica Escobar
University of Florida
301 CRB
Gainesville, FL 32611
(904) 392-0792

Jun He
University of Florida
PO Box 116400
Gainesville, FL 32611
(904) 392-6664

Dr. Paul Holloway
University of Florida
PO Box 116400
Gainesville, FL 32611
(904) 392-6664

Dr. Jack Mecholsky
University of Florida
PO Box 116400
Gainesville, FL 32611
(904) 3929692

Farhad Mohammadi
University of Florida
PO Box 116400
Gainesville, FL 32611
(904) 392-1015

Robert Sabia
University of Florida
PO Box 115400
Gainesville, FL 32611
(904) 392-1015

Sherry Staehle
University of Florida
PO Box 116400
Gainesville, FL 32611
(904) 392-1015

Ben Smith
University of Florida
301 CRB
Gainesville, FL 32611
(904) 392 0792

Sridhar Venigalla
University of Florida
PO Box 116400
Gainesville, FL 32611
(904) 392-1015

Dr. Dow Whitney
University of Florida
PO Box 116400
Gainesville, FL 32611
(904) 3926687

Dr. James Windfordner
University of Florida
301 CRB
Gainesville, FL 32611
(904 392-0792

FIRST ANNUAL WEAR WORKSHOP REPORT AND RECOMMENDATIONS
January 7, 1994

TASK 1. DETECTION OF WEAR
Modifications/Suggestions
I. Analysis of other elements (Minor, Trace)
Steels (MSONEL) + Ceramics
II. Particle Size Limitations of Methods
III. New Standards
IV. Fluorinated as well as Conventional Lubricants
1. New Standards
2. Absolute vs. Standards Analysis

TASK 2. MEASUREMENT OF WEAR
I. Tests to Produce Wear
II. Measurement of Wear
III. Other Pertinent Points
1. Tests to Produce Wear
A. There are no standard tests.
B. Any existing test will measure some character of wear.
C. Tests can rank effects of variables (e.g. lubricants) in nearly the same order. (However, tests are not the same)
D. Use lubrication during tests. (Application Driven)
2. Measurement of Wear
A. Ceramic wear is difficult to measure.
B. Profilometer will provide same info.
C. Weight loss may not be meaningful.
D. Dry tests are not meaningful. Use lubrication.
3. Other Pertinent Points
A. Unintentional dynamic loading may be most important factor in wear tests.
B. Moisture is important.
C. Tests and analysis should be application driven.
D. Cleaning of balls is important.
E. NDI very important and exists.
F. Univ. contrib.= deter. of incipient damage

TASK 3 and 4. WEAR MECHANISMS AND PREDICTION OF PRECATASTROPHIC FAILURE (NOT FRACTURE)
I. Cull Freaks:
1. NDI/NDE dye penetrant. Evaluate dark field Fluorescence UV- IR microscopy
2. Acoustic ultrasound ($\geq 10\ \mu$ m) (acoustic microscope)
II. Controls for Chemical/Physical Analysis for Wear Debris
1. Large as well as small particles
III. Keep Company Samples Proprietary (generic labels)
IV. Only Use Well-Characterized
1. Oils - mineral
2. Additives - ester
3. Anti-oxidants, etc.
4. Fluorinated lubricants - required temperature range from -65°F to 700°F
5. polyphenylethers required temperature range (+40°F to 550°F)
V. Communicate with Industry/Gov't/University
1. (Phone numbers)
2. Avoid the reinventing wheel (check out what we plan to do with industry to ensure that we are covering new ground)

VI. Samples to be Generated at UF
VII. Samples/Specimen Generated by Industry/Gov't
VIII. Provide Specific Goals and Work Plans for UF Date Generation
(i.e. % RH, temp., oil, surface finish)
IX. Be sure to define the (usually) variables that are not usually well documented
(i.e. RH, water, conc. in oil)
X. Air/Fuel Ratio
XI. Are There Any Mechanisms at Partners to Transfer Know-how etc. Via Graduate Student Training?
XII. Co-ops
XIII. Fellowships, etc.
XIV. Faculty Visits
XV. Sabbaticals(?)
XVI. Florinated Fluids
XVII. Need to use freon type solvents
1. 2450 M H_Z
2. Dilution microwave -2.45 GH_Z
3. w/ Xylene Al, Mg, Y etc. in 10ppt 1-3 μm Si_3N_4 particle

TASK 5. METHODS TO MINIMIZE WEAR

I. Use hard/compressive coatings
II. Use lubricating layers
1. Solid
2. Liquid
3. Combination
III. Techniques:
1. Agree that plasma spray and similar approaches not good prospects
2. Ion implant not good for production
3. Others to consider
A. Laser ablation
B. Plasma polymerization/pyrolysis
IV. Materials
1. Hard/compressive
A. BIRL: working with C_xN_y
$TiN_x/NbN_y/MoN_z$
CrN_x/TiN_y
$Ti\text{-}AON_x$
B. Opportunity to exchange Mat'l/Charact.
BIRL<-> UF
C. UF <-> diamond coating
2. Lubrication:
A. Be aware of distinction of hard vs. lubricating layers
B. Computer programs
3. Self-generating, healing protective/lub. layers
A. Very desirable (not exactly smart).
B. Examples: SiO_z, MoS_2, DEBRI, TiO_2
C. Not a Si_3N_4 - production program
V. Environment
1. RT -? (800°F)
2. Air to Fuel/Air Mixtures
3. Humidity - very important

Final Program

on

Second Annual Workshop on Predicting Materials Degradation and Fatigue in Aerospace Structures

January 5-6, 1995

University of Florida Reitz Union

Conference Rooms B74-B75

January 5

12:00-1:30 p.m.	Registration & lunch	
1:30-1:45	Welcome and Introduction	Dr. Reza Abbaschian
1:45-2:00	Program Objectives and Management of Wear	Dr. E. Dow Whitney
2:00-2:20	Task 1 Detection of Wear	Dr. Ben Smith Dr. James Adair
2:20-3:00	Task 2 Measurement of Wear	Dr. Jack Mecholsky Dr. Dinesh Shetty
3:00-3:20	Coffee Break	
3:20-3:45	Task 2 Measurement of Wear (continued)	Dr. Don Dareing
3:45-4:05	Task 3 Determination of Wear Mechanisms	Dr. E. Dow Whitney
4:05-4:15	Task 4 Precatastrophic Wear Prediction	Dr. James Adair
4:15-4:35	Task 5 Methods to Minimize Wear	Dr. Paul Holloway Dr. James Adair
4:35-5:05	Rocket Turbo Pump Experience with Hybrid Bearings	Dr. Herb Chin Pratt & Whitney

Final Program (continued)

5:05-5:30	Experience with Nitrogen Alloyed Stainless Steels	Dr. Edgar Streit FAG Bearings
5:30-5:40	Experience with Polymer Composite Systems	Dr. Charles Beatty University of Florida
6:30-7:30	Reception and student posters Arredondo Room Reitz Union	

1995 WORKSHOP ATTENDEES

NAME	COMPANY
OFF CAMPUS	
Susan Brown	Pratt and Whitney
Harold Burrier	The Timken Company
Herbert Chim	Pratt and Whitney
Y.P. Chiu	Torrington
Don Dareing	University of Southwestern Louisiana
Dr. Kent Eisentraut	U.S. Air Force
Thomas Faegg	Thomas Optical
Mike Foley	Norton Company
Kathleen Havey	Wright Lab
Bill Mandler	Enceratec
Karl Mecklenburg	U.S. Air Force
John Minor	Fratt and Whitney
Alexander Pechenik	AFOSR/NC
Vimal Pujari	Norton Company
John Reintjes	Naval Research Lab
Dr. Peter Schmidt	Office of Naval Research
Dinesh Shetty	University of Utah
Lew Sibley	Tribology Systems
Edgar Streit	FAG
Peter Ward	MPB Corporation
Russ Yeckley	Norton Company
ON CAMPUS	
Dr. Reza Abbaschian	Materials Science
Dr. James Adair	Materials Science
Scott Baker	Chemistry
Dr. Charles Beatty	Materials Science
Zheng Chen	Materials Science
Robert Chodelka	Materials Science
Jacques Cuneo	Materials Science
Paul Demkowicz	Materials Science
Mostafa Elrahman	Materials Science
Monica Escobar	Chemistry
Craig Habeger	Materials Science
Jun He	Materials Science
Dr. Paul Holloway	Materials Science
Jeff Kerchner	Materials Science
Richard Linhart	Materials Science
Dr. John Mecholsky	Materials Science
Jamie Rhodes	Materials Science
David Rusak	Chemistry
Ben Smith	Chemistry
Sridhar Venigalla	Materials Science
Jon West	Research Park
Dr. Dow Whitney	Materials Science
Dr. Jim Winefordner	Chemistry

1995 WORKSHOP RECOMMENDATIONS

TASK 1 - DETECTION OF WEAR

J. Winefordner, Presiding

1. Bring perfluoropolyalkyl ether lubricants into program - in all applications and tests.
2. Add new metal elements to lubricant analysis including Cr, Ti, Ni, and Mo.
3. Include Cronidur 30 samples with Si_3N_4 ball bearings.
4. Analyze debris-laden oils.
5. Study particle size effects (Al_2O_3, etc.) for ETV-ICP-MS.
6. Organometallics in fluorinated lubricants behavior in ETV-ICP-MS.
7. Vaporization of small (<1 mm) Si_3N_4 balls with DC arc method.

TASKS 2 & 3 - MEASUREMENT OF WEAR

J. Mecholsky, Presiding

1. Tests and Measurement of Wear

   A. Examining only one variable during wear test may be misleading. Therefore, use several measurable characteristics (e.g., weight loss, profilimeter traces of wear track, etc.).

   B. Identify incipient wear at low stresses, i.e., realistic stresses.

   C. Identify threshold stress level, if it exists. Critically examine ways to do this.

   D. Examine worn balls or rods from bearing systems.

2. Other Pertinent Points

   A. Handling of balls is critical! The balls should be individually packaged and handled.

   B. Lubricants are important but, for now, we should select <u>one</u> "standard." (Partnership agreed to Exxon turbo oil 2380 for the time being.)

   C. Use the atomic force microscope more to examine wear tracks.

   D. It is suggested that tests be interrupted to determine if there is evidence of incipient wear.

E. Break down of films can be critical and should be addressed.

F. Tests at £ 700°F should be attempted where possible.

G. Microstructure/property correlation is essential.

TASK 5 - METHODS TO MINIMIZE WEAR

P. Holloway, Presiding

OBJECTIVES:

Minimize wear

Detect wear, impending failure

Self heal

1. Properties to be determined
   - A. Coefficient of friction
   - B. Lubrication layer retention
   - C. Thermal conductivity
   - D. High hardness
   - E. D coefficient of thermal expansion

2. Temperature ranges to be examined
   - A. Phase III - 700°F (bulk oil-in temperature)
   - B. Lower temperature - 550°F
   - C. At rolling contact - (P&W - John Minor)

3. Materials to be incorporated
   - A. Balls - Si_3N_4
   - B. Retainer - AlSi 4340/Ag Plate
- Hard retainer
   - C. Race
Base - M50, M50NiL
Pyrowear 675 (carbarized, class III super 12 stainless steel)
Cronidur - HNS, LNS

4. Lubricants to be examined

   A. Up to 700°F - Perfluoropolyalkylethers (PFPAE) + additives (WPAFB, P&W)

   B. Up to 350°F - EXXON 2380

5. Coatings to be incorporated

   A. Thin dense Cr - TDC

   B. CrN_X

   C. NbN_X

   D. DLC

   E. TiO_X, TiC_X

   F. Nanocomposite layered structures

Final Program

Third Annual Workshop on Predicting Materials Degradation and Fatigue in Aerospace Structures

January 4 and 5, 1996

University of Florida — J. Wayne Reitz Union
Room 282

<u>January 4, 1996</u>

12:00 - 1:00	Registration and Lunch — 235 Reitz Union	
1:00 - 1:15	Welcome and Introduction	Dr. Reza Abbaschian
1:15 - 1:45	Program Objectives and Management of Wear	Dr. Dow Whitney
1:45 - 2:30	Task 1 - Detection of Wear	Dr. Ben Smith Rob Sabia, Dr. Rajiv Bendale
2:30 - 3:00	Task 2 - Measurement of Wear	Dr. Jack Mecholsky
3:00 - 3:15	Coffee Break	
3:15 - 3:45	Task 2 - *continued*	Dr. Dinesh Shetty
3:45 - 4:00	Task 3 - Determination of Wear Mechanisms	Dr. Whitney
4:00 - 4:15	Task 4 - Precatastrophic Wear Prediction	Dr. Jim Adair
4:15 - 5:00	Task 5 - Methods to Minimize Wear	Dr. Paul Holloway, Dr. Adair Dr. Charles Beatty
5:00 - 5:30	Summary	Dr. Adair
6:00 - 7:00	Reception, Student Posters, Wine and Cheese — Arredondo Room, 4th Floor	
7:00 - 9:00	Banquet — Arredondo Room, 4th Floor "Experiences with Hybrid Bearings in the Oxygen Turbo Pump in the Space Shuttle"	Dr. Roger Bursey, Speaker

<u>January 5, 1996</u>

7:00 - 8:00	Continental Breakfast — 282 Reitz Union	
8:00 - 9:30	Committee Meetings	
	Room 272 Detection of Wear	Dr. Winefordner, Dr. Smith
	Room 276 Measurement of Wear	Dr. Mecholsky, Dr. Shetty
	Room 278 Methods to Minimize Wear	Dr. Holloway, Dr. Adair
9:30 - 9:45	Coffee Break	
9:45 - 10:30	Committee Reports	
10:30 - 12:00	Laboratory Tours of Materials Science and Engineering, Chemistry, and Major Analytical Instrumentation Center	

Task 1

APPENDIX 2, M.P. Escobar, "Determination of Wear Metals in Lubricating Oil by Electrothermal Vaporization Inductively Coupled Plasma Mass Spectrometry," Abstract of Ph.D. Dissertation presented to the Graduate School, University of Florida, May 1995. Dissertation copy available upon request. J.W. Winefordner, advisor.

APPENDIX 3, M.P. Escobar, B.W. Smith, and J.D. Winefordner, "Determination of Metallo-Organic Species in Lubricating Oil by Electrothermal Vaporization Inductively Coupled Plasma Mass Spectrometry," Analytica Chimica Acta, 320, 11-17(1996).

APPENDIX 4, R. Sabia, "Physical and Chemical Interactions of Lubricants in Hybrid Bearing Systems," Abstract of Ph.D. Dissertation presented to the Graduate School, University of Florida, May 1996. Dissertation copy available upon request. J.H. Adair, advisor.

APPENDIX 5, R. Sabia, Herb A.J. Chin, and J.H. Adair, "A Kinetic Study of the Degradation Behavior and Mechanisms of a Synthetic Ester-Based Lubricant," submitted for publication.

APPENDIX 6, R. Sabia, J. Simmons, P.H. Holloway, Herb A.J. Chin, and J.H. Adair, "The Use of Optical Spectrometry to Monitor Degradation in a Synthetic Ester-Based Oil," submitted for publication.

APPENDIX 7, Robin A. Russell, "Determination of Metallo-Organic and Particulate Wear Metals in Lubricating Oils Associated with Hybrid Ceramic Bearings by Inductively Coupled Plasma Spectrometry," Abstract of Ph.D. Dissertation presented to the Graduate School, University of Florida, August 1997. Dissertation copy available upon request. J.D. Winefordner, advisor.

APPENDIX 8, S.A. Baker, B.W. Smith, and J.D. Winefordner, "Laser Ablation Coupled Mass Spectrometry with a Compact Laser Source," *Spectroscopic Perspectives*, 51[2], 1997.

APPENDIX 9, S.A. Baker, M.J. Dellavecchia, B.W. Smith, and J.D. Winefordner, "Analysis of silicon nitride bearings with laser ablation inductively coupled plasma mass spectroscopy," to be published in *Analytica Chimica Acta*, 1997.

APPENDIX 10, Scott A. Baker, "Analysis of Glass, Ceramic, and Soil Samples Using Laser Ablation Inductively Coupled Mass Spectrometry," Abstract of Ph.D. Dissertation presented to the Graduate School, University of Florida, to be presented to the graduate school, May 1998. Dissertation copy available upon request. J.D. Winefordner, advisor.

APPENDIX 11, S.A. Baker, B.W. Smith, and J.D. Winefordner, "An Investigation of Light Scattering for Normalization of Signals in Laser Ablation Inductively Coupled Mass Spectrometry," submitted for publication.

APPENDIX 2, M.P. Escobar, "Determination of Wear Metals in Lubricating Oil by Electrothermal Vaporization Inductively Coupled Plasma Mass Spectrometry," Abstract of Ph.D. Dissertation presented to the Graduate School, University of Florida, May 1995. Dissertation copy available upon request. J.W. Winefordner, advisor.

Abstract of Dissertation Presented to the Graduate School
of the University of Florida in Partial Fulfillment of the
Requirements for the Degree of Doctor of Philosophy

DETERMINATION OF WEAR METALS IN LUBRICATING OIL BY ELECTROTHERMAL VAPORIZATION INDUCTIVELY COUPLED PLASMA MASS SPECTROMETRY

By

Monica Paola Escobar

May 1995

Chairperson: James D. Winefordner
Major Department: Chemistry

The inductively coupled plasma mass spectrometer (ICP-MS) is one of the few techniques capable of multielement determinations with low detection limits. ICP-MS is an almost ideal technique for the analysis of lubricating oils due to its many advantages, which include broad linear dynamic range, multielemental analysis, rapid acquisition of mass spectra, and low detection limits. However, there is a serious problem when an organic matrix is nebulized into the ICP-MS. Carbon condenses on the cooled interface cones, sooting and blocking the apertures. This is prevented by adding a small amount of oxygen (2 - 10%) to the carrier gas so that all the carbon is oxidized and volatilized. Too little oxygen will result in clogging of the interface and too much will result in rapid deterioration of the orifice. A second disadvantage of nebulizing organics into the ICP-MS is that carbide compounds formed in the ICP

may act as molecular interferences for some elements, making it difficult or impossible to detect these elements.

Electrothermal vaporization (ETV) was chosen as a sample introduction technique because it eliminates several of the problems associated with conventional nebulization. When using ETV with ICP-MS, the graphite furnace vaporizes the sample, and it is then transported to the ICP where it is ionized. Each step can then be optimized separately, adding several advantages to the technique: analysis of small sample volumes, high sample transport efficiency, even higher sensitivity, and separation of the analyte from the sample matrix, which leads to the ability to analyze samples in organic, high acid, and high solid matrices. This makes it possible to analyze oil samples while eliminating oxygen addition and reducing molecular interferences due to the organic matrix.

This dissertation describes the development of a method for the determination of wear metals in lubricating oils by electrothermal vaporization inductively coupled plasma mass spectrometry. Hardware modifications were made to the ETV to improve transport efficiency to the ICP. These included the addition of a graphite plug holder, a new ETV-tubing interface, a new sample transfer valve, and a modification to the sample introduction glassware. The technique was then characterized using aqueous solutions of the analytes of interest with sodium chloride and palladium nitrate added as sample carriers. Finally, a method was developed for the detection of Al, Mg, Fe, and Y metallo-organic compounds in an oil matrix.

APPENDIX 3, M.P. Escobar, B.W. Smith, and J.D. Winefordner, "Determination of Metallo-Organic Species in Lubricating Oil by Electrothermal Vaporization Inductively Coupled Plasma Mass Spectrometry," Analytica Chimica Acta, 320, 11-17(1996).

ELSEVIER

Analytica Chimica Acta 320 (1996) 11–17

ANALYTICA CHIMICA ACTA

Determination of metallo-organic species in lubricating oil by electrothermal vaporization inductively coupled plasma mass spectrometry

Monica P. Escobar [1], Benjamin W. Smith, James D. Winefordner *

Department of Chemistry, University of Florida, Gainesville, FL 32611, USA

Received 19 June 1995; revised 25 September 1995; accepted 10 October 1995

Abstract

Inductively coupled plasma mass spectrometry (ICP-MS) is one of the few techniques capable of multielement determinations with low detection limits. However, when an organic matrix is nebulized into the ICP-MS, carbon condenses on the cooled interface cones, sooting and blocking the apertures. A second disadvantage of nebulizing organics into the ICP-MS is that carbide compounds formed in the ICP may act as molecular interferences for some elements, making it difficult or impossible to detect these elements. Electrothermal vaporization (ETV) was chosen as a sample introduction technique because it reduced the problems associated with conventional nebulization. When using ETV for sample introduction, the analyte was separated from the sample matrix, which made it possible to analyze oil samples while eliminating oxygen addition and reducing molecular interferences due to the organic matrix. We have developed a method for the determination of Al, Mg, Fe, and Y metallo-organic compounds in lubricating oil by electrothermal vaporization inductively coupled plasma mass spectrometry. A pneumatically-operated graphite plug holder was added to the ETV so that the dosing hole could be plugged during the ETV heating cycle.

Keywords: Electrothermal vaporization; Inductively coupled plasma-mass spectrometry; Wear metals; Organo-metallic species; Lubricating oils

1. Introduction

There is a strong interest in replacing metallic ball bearings with those made of silicon nitride (Si_3N_4), for a wide variety of applications. The determination of wear-related trace elements in the lubricating fluids used with these bearings is important in the development of models concerning the mechanisms of wear for these materials. The routine determination of wear debris may also serve as an indication for optimization of engine maintenance procedures.

The composition of wear debris provides insight into how the bearings are wearing as well as wear information about other engine components. The routine testing of lubricants used in engines is also important for diagnostic purposes, including preventive maintenance by indicating when oil changes,

* Corresponding author.

[1] Present address: Procter and Gamble Pharmaceuticals, P.O. Box 191, Norwich, NY 13815, USA.

SSDI 0003-2670(95)00556-0

component replacement, and engine overhauls are required. The wear metal debris can be metallic (from mechanical wear), oxidized (from oxidative corrosion), or metallo-organic (from chemical corrosion). Therefore, it is important to use an analytical technique that will detect dissolved species to millimeter-sized particles.

Electrothermal vaporization (ETV) is an excellent sample introduction technique for inductively coupled plasma mass spectrometry (ICP-MS) analysis with organic samples. It requires only a small sample volume and has rapid sample changeover. Most importantly, the organic matrix may be removed and vented to atmosphere by using a carefully programmed ETV temperature ramp, reducing the level of carbide interferents and preventing the clogging of the sampling cone of the mass spectrometer. For this reason, oxygen addition for organic matrix ashing is normally not required. However, very little research has been reported in this area. A brief review of previous work involving metals in organic samples by ETV-ICP-MS follows.

Hall et al. [1] were the first to use ETV-ICP-MS for the determination of metal in organic material. They determined gold in isobutyl methyl ketone (IBMK), a solvent commonly used for the extraction of geological samples. The authors used a laboratory-built glass domed ETV. They vented the organic matrix during the drying step before vaporizing the Au into the ICP. They had favorable results, with a 3% R.S.D. and a detection limit for gold of 8 pg/ml.

Osborne [2] determined elemental as well as organic mercury in petroleum samples. He used a modified Perkin Elmer HGA 500 furnace coupled to a Sciex 250 ICP-MS. Post-furnace addition of oxygen to the carrier gas was used to ash the organic matrix. The ETV parameters used were a vaporization step at 2650°C and a cleanout step at 2700°C. No statistical difference was found between the determination of elemental and organic Hg. A comparison was also made of the Hg signal obtained when the organic mercury compound was dissolved in different length alkanes (C_5–C_{32}); it was found that the Hg signal decreased as the carbon chain length was increased. The best results were obtained with a carbon length of 12 or lower. The precision was between 5.9–13% R.S.D. for the shorter chains and 70 and 55% R.S.D. for C_{28} and C_{32}, respectively; the detection limit was 3 ppb Hg in pentane. The decrease in Hg signal with increasing chain length was attributed to the increased plasma loading because of the increased energy demands for longer carbon chains and the spatial distribution of the Hg which was not confined to the plasma axis. The author also noted an increase in the wear of the interface cones due to the additional oxygen. Richner and Wunderli [3] used ETV-ICP-MS to differentiate between organic and inorganic chlorine. A Sciex Elan 5000 and ETV-600 were used, along with platform graphite tubes. Oxygen gas flow at 20 ml/min was added to the furnace carrier argon to ash the organic matrix. The ETV ramp temperature program consisted of a drying step at 140°C, an initial vaporization step at 400°C to vaporize the organic Cl, and a second vaporization step at 2650°C to vaporize the inorganic Cl. The main application of this method was in the determination of polychlorinated biphenyls (PCBs) in waste oils. The precision of the method for Cl was 10–20% R.S.D., with detection limits of 0.5–9 μg/g for different PCBs. However, PCBs containing less than three Cl atoms could not be detected, even at 50 μg/g. The authors attributed this to the high volatilities of these compounds. They concluded that the Cl compounds were being vaporized during the drying step, accounting for the loss of signal. Because the method could not distinguish between PCBs and other organic Cl compounds, it was suggested that it should be used only as a rapid screening technique for the determination of PCBs in waste oils.

Manninen [4] used ETV-ICP-MS for the determination of extractable organic chlorine (EOCl). EOCl is the portion of total organic chlorine which is separated from a sample by using an organic solvent extraction procedure. A Fisons PlasmaQuad PQ II with a Fisons ETV Mk III instrument was used for the analysis. The furnace heating was as follows: the drying step was at 100°C, the ashing temperature was 1000°C, and the vaporization temperature was 2600°C. The furnace was not vented during drying or ashing, and no oxygen was added to ash the organic matrix; carbon build-up was observed on the interface cones. Several chlorinated compounds were studied, including *p*-chloroanisol, pentachlorophenol, trichloroethene, and *o*-chlorobenzoic acid. Chlorine was determined in ethyl acetate with a detection limit of 10 ng. The precision was 5% R.S.D. for standards and from 5 to 30% R.S.D. for real samples.

The goal of the present research has been to develop analytical methodologies for the quantitative analysis of both minor and trace elements present as soluble metallic species and as wear particles in lubricating oils. Our initial approach has been the application of ETV-ICP-MS to the quantitation of metallo-organic species present in lubricating oils. The elemental species chosen (Al, Mg, Fe and Y) are considered to be critical in detecting wear in Si_3N_4–steel bearing systems.

2. Experimental

2.1. Reagents

Single element metallo-organic standards of Al, Mg, Fe, and Y at 500 μg/g in base oil (Johnson Matthey, Ward Hill, MA) were diluted in xylene (Low Trace Metal Grade, Mallinckrodt, Chesterfield, MS) to make solutions of 20% oil by weight/volume (20 g oil/100 ml total volume) in xylene. Base oil was used to provide enough oil to make up 20% oil and to prepare analytical blanks. A multielement metallo-organic standard in oil which contained 21 elements at 10 ppm (wt.) (S-21, Conostan, Ponca City, OK) and Standard Reference Material 1084a (wear metals in oil, 100 ppm, NIST, Gaithersburg, MD) were diluted in a similar way. Blanks for these standards were prepared from base oil obtained from each source. Solutions of NaCl (99.9%, Puratronic grade, Johnson Matthey, Ward Hill, MA) were prepared in methanol (Optima grade, Fisher Scientific, Pittsburgh, PA).

2.2. Apparatus

The inductively coupled plasma mass spectrometer used for this work was a Finnigan MAT SOLA equipped with the SOLA ETV accessory. The electrothermal vaporizer was modified by the installation of a pneumatic graphite plug holder for the dosing hole. It was important that the organic matrix from the oil samples not enter the plasma to prevent sooting and blocking of the interface apertures. The best way to accomplish this was to vaporize the organic matrix at a low temperature before vaporizing the analyte. A pneumatic plug holder was constructed so that the graphite tube could be vented through the dosing hole and then plugged during the heating cycle.

2.3. Instrument optimization

The optimization of instrumental parameters was difficult with a 'dry' plasma. A constant signal was required to tune the instrument, or adjust the voltage settings on the mass spectrometer to obtain a maximum signal. A constant signal was also required to optimize the placement of the plasma torch position over the sampling orifice. Many researchers have tuned the lenses using a wet plasma, or nebulizing a standard solution, then removing the nebulizer and spray chamber after optimization and hooking up the ETV interface [1,5–11]. A few researchers have tuned with a wet plasma, then continued to nebulize blank water throughout the ETV runs in order to minimize changes in the ion lens settings [12,13]. Several researchers have tuned on a signal from an element slowly vaporized from the furnace, such as mercury [14–16]. One group tuned on the ^{12}C signal generated from a blank ETV firing or from CO_2 present as an impurity in the argon gas supply, then tuned on the Cd signal generated from its slow vaporization off of the furnace [17,18]. Several other researchers have tuned on the signal present from a spectral feature in the plasma, such as Ar_2 [14] or ArH [19]. Tuning on the signal from an element vaporized from the furnace was difficult because a stable signal was difficult to generate, and adjustment of the torch position using a spectral feature was impossible because species such as Ar_2 were present throughout the plasma.

In our laboratory, tuning was accomplished using nitrogen added to the ETV carrier gas flow. House nitrogen was connected to the auxiliary mass flow controller on the ETV. Using this controller, N_2 gas was slowly bled into the main ETV argon gas flow to the plasma. A nitrogen gas flow of 10–30 ml/min added to the 1 l/min argon flow produced enough signal at mass 14 or 28 to detect with the Faraday plate detector. Without the added nitrogen flow, no signal was observed on the Faraday detector. Nitrogen was present throughout the plasma. However, during the tuning procedure, the nitrogen concentration was higher in the central channel than throughout the rest of the plasma. Therefore, the torch was finely adjusted over the sampling cone orifice. Initial adjustments were made using a wet plasma, nebulizing a standard tuning solution of 2 ppm Al, Mg, Cd, Pb, and In, once every one to two weeks. The nebulizer was then removed and the ion lenses were then tuned using nitrogen at mass 14 (N^+) or 28 (N_2^+), or argon at mass 40, depending upon the mass of the analyte of interest. This method worked well because a constant signal could be maintained for as long as necessary.

The ETV parameters were optimized for each element, except carrier flow, which was kept constant at 1 l/min, as this was the flow needed to puncture the plasma and form the central channel. The ETV vaporization temperature was optimized by measuring three injections of the same concentration for a series of temperatures. The peak intensities and precision for each set of runs were compared, and the temperature that gave the highest intensity, with good precision (< 15% R.S.D.), was chosen as the optimum vaporization temperature.

2.4. Procedure

A 10 μl aliquot of organic standard was introduced into the graphite furnace through the dosing hole with a 25 μl gas-tight Hamilton syringe (Model 1702, Hamilton, Reno, NV). The furnace program was then initiated through the computer, and the graphite plug holder was actuated at the appropriate time with the aide of a stopwatch. Each new plug was conditioned twice by consecutive blank firings to remove any impurities in the graphite, and the plug was replaced daily. At the time set by the operator in the software program, the sample valve was actuated by the computer so that the ETV carrier argon flow was diverted from the ICP. The mass spectrometer scanned from 8 to 12 s for each run. The parameters were set for a dwelltime of 50 ms per channel with 64 channels per atomic mass unit. The Faraday plate detector was used for all runs as the signal intensity was too high for the electron multiplier detector. The SOLA software had no means of performing single ion monitoring; in order to monitor only one mass throughout the length of the ETV ramp, the mass analyzer had to be manually switched to the "local" mode using the switch on the front control panel of the mass spectrometer once the ETV run was initiated and the mass of interest was selected. Limits of detection were calculated based on the 3σ criteria using the standard deviation of a series of blank injections as the measure of blank noise. [20].

3. Results and discussion

3.1. Matrix modification

Promising results have been obtained using NaCl as a carrier for the determination of aqueous standards in ETV-ICP-MS [21]. However, NaCl in aqueous solution and in methanolic solution were both found to be unsuccessful as a carrier for metals in organic solvents because of splattering in the former case and poor precision (15–70% R.S.D.) in both cases. Fortunately, the carbon in the organic solvents proved to be sufficient as a carrier for the metals of interest.

3.2. Measurement of metallo-organic Al

The best ETV conditions were found to be those in Table 1. By insertion of the 1200°C ashing step with a 1 s–20°C rest time prior to the vaporization step, it was possible to avoid a spectral interferent (possibly CHN^+) from the organic matrix and to achieve a %R.S.D. ≈ 14 for a 0.5 ng organo-aluminum sample.

The proposed mechanism for the two-step ETV program was that at the first vaporization tempera-

Table 1
ETV temperature program for metallo-organic aluminum

Temperature (°C)	Ramp time (s)	Hold time (s)
350	35	30
1200	2	2
20	1	1
2400	1	2
20	2	5

ETV valve delay: 59 s; ETV scan delay: 4 s.

ture (2 s at 200°C), the furnace temperature was not held long enough for steady-state conditions. Therefore, some of the organic matrix vaporized but not the Al. If this step was held for a longer period of time (7 s instead of 2 s), the signal of the second peak (at 2400°C) started to decrease while the intensity of the first peak increased. This was most likely due to the metallo-organic Al being vaporized at the 1200°C step. The 20°C rest step simply separated the two signals in time, while providing a short time for recondensation of the analyte to occur in the graphite tube.

The proposed mechanism which involves a portion of the organic matrix functioning as the sample carrier was verified as follows. The oil was not completely vaporized in the furnace during the first vaporization step which was verified by observing the green C_2 emission in the ICP and by monitoring the C_2 signal at mass 24 during the second vaporization step. Kantor [22] described the use of organic species as carriers. Citric acid has also been used successfully as a carrier [21]. Additional proof that the organic matrix was acting as a carrier involved varying the volume of a 300 ppb Mg sample and measuring each volume three times while monitoring the Mg signal. The results in Fig. 1 show that the signal did not increase linearly. The increased transport efficiency with larger amounts of matrix is consistent with the organic species being the carrier.

Calibration curves for metallo-organic Al in 20% base oil in xylene were linear from the detection limit to the highest mass (50 ng) run. The correlation coefficient (R) was 0.999 for peak intensity versus Al mass. The correlation coefficient for peak area vs. Al mass was 0.994. The limit of detection for the peak height data was 200 pg, and the limit of detection for the peak area data was 400 pg. Poorer precision was obtained for peak area (< 20% R.S.D.) than for peak height (< 10% R.S.D.). The poorer precision was probably the result of the incomplete separation of the spectral interferent (CHN^+) from the Al signal. This did not affect the peak values significantly, as the interferent appeared as a shoulder on the peak. The detection limit was blank-limited. It was impossible to obtain a cleaner oil and xylene blank because most organic solvents are purified for organic content, not metal content. The linear response extended to 50 ng, where the Faraday detector was saturated. However, the Faraday detector could have been set to less sensitive settings to extend the detection range up to two orders of magnitude.

3.3. Measurement of metallo-organic Fe

The optimum ETV program used for Fe is shown in Table 2. The valve was opened during the 20°C rest time to limit the organic vapor being transferred to the ICP. The ashing temperature was lower for Fe than Al. Since the metallo-organic compounds in the

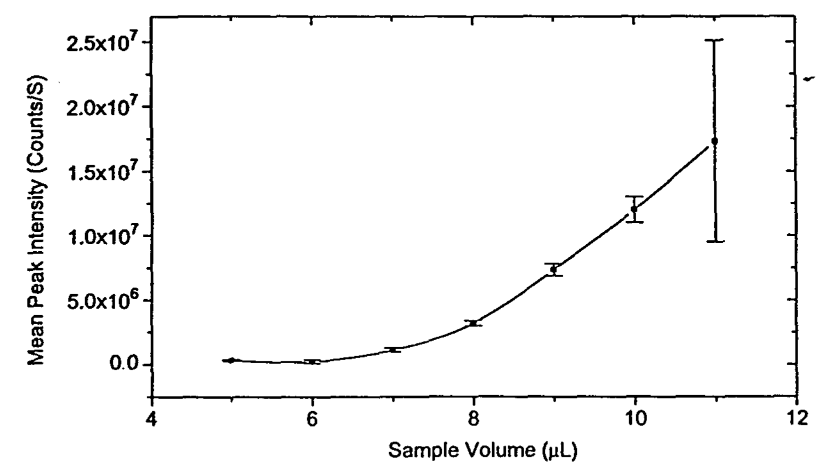

Fig. 1. Effect of sample volume on organometallic Mg signal (300 ng/ml Mg).

base oil standards are proprietary, it is not known if the Fe compound was indeed more volatile than the Al compound. At ashing temperatures higher than 900°C, the analyte peak started to decrease because of Fe loss during the ashing step. The analytical curve using the Fe ETV program was linear from the detection limit to 150 ng. The detection limit was 130 pg, and the R value was 0.999. The detection limit was once again blank-limited. The precision was generally less than 10% R.S.D., except for the two lower concentrations, which were between 15 and 25% R.S.D. The upper limit of linear response, 150 ng, was limited by saturation of the Faraday plate detector at the most sensitive setting.

3.4. Measurement of metallo-organic Mg

Mg was especially difficult to measure in an organic matrix because C_2 is an interferent at the same mass. This posed an even greater challenge because carbon particulates were acting as the analyte carrier. A small percentage (2–15%) of oxygen was bled into the furnace during the drying and ashing steps to ash the carbon. Much of the carbon was removed, as observed by the decrease in the carbon signal. However, the precision of the Mg suffered, with 50% R.S.D. being typical. This was attributed to the loss of the carrier, namely the organic matrix. Sodium chloride in methanol was also unsuccessful as a carrier for Mg. Therefore, NaCl addition and oxygen ashing were not used.

The optimized ETV program for metallo-organic Mg is show in Table 3. A series of calibration standards were measured, resulting in linear calibration curves from the detection limit to 10 ng. The R value was 0.99, which was slightly poorer than that for Al or Fe. The precision was also poorer, ranging from 3 to 27% R.S.D. The detection limit was 200 pg and was limited by the C_2 interferent.

Table 2
Optimum ETV program for Fe

Temperature (°C)	Ramp time (s)	Hold time (s)
350	35	30
900	1	2
20	1	1
2600	1	2
20	2	5

ETV valve delay: 68 s; ETV scan delay: 1 s.

Table 3
Optimum ETV program for Mg

Temperature (°)	Ramp time (s)	Hold time (s)
350	35	30
1200	1	2
20	1	2
2600	1	3
20	2	2

ETV valve delay: 66 s; ETV scan delay: 2 s.

3.5. Measurement of metallo-organic Y

The detection of yttrium by ETV-ICP-MS was much more difficult than for Fe, Mg and Al. Several matrix modifiers, including NaCl and $Pd(NO_3)_2$ were evaluated but poor recoveries were obtained. Although freon or other halogen containing gases could have been used, the environmental hazards associated with their use eliminated them from further consideration. Sulfur hexafluoride was evaluated because it provided a source of fluorine required for volatilization. The optimum vaporization temperature for yttrium was 2700°C. Peak tailing increased with SF_6 flow rate, because of the formation of SF_3, with the same mass as Y, in the plasma. However, by keeping the SF_6 flow rate at about 30 ml/min or less, peak tailing was negligible. The detection limits obtained, using SF_6, ranged from 5 to 60 pg and the precision from 6 to 45%. We observed that the precision improved markedly if the SF_6 was not flowing during the atomization step. Therefore, prior to use, furnace tubes were preconditioned by flowing SF_6 at 10 ml/min continuously while the furnace was cycled through three temperature program cycles. After this treatment, good performance for Y was observed for about 50 ETV program cycles. Using this approach, a limit of detection of 70 pg was obtained, limited by detector noise. The precision was 15%. There was no interference from SF_3 observed using the Faraday detector. Studies are currently underway to determine the mechanism of the SF_6 action.

4. Conclusions

The detection efficiency is the number of ions reaching the Faraday detector divided by the number of atoms injected into the furnace and was 8.3×10^{-6}, 1.8×10^{-6}, 2.1×10^{-6} and 3.4×10^{-6}, respectively for Al, Fe, Mg, and Y. The detection efficiencies for the metallo-organic elements was an order of magnitude poorer than that of the aqueous elements studied in our laboratory using the same instrument. Detection limits were limited by the high level of impurities present in the blank and the poorer transport efficiency. For the determination of Mg, the detection was limited by the carbon interferent. Y was not present in the blank, therefore it had a better limit of detection. The detection limit of Y was limited by the amplifier noise.

Acknowledgements

We thank Paul Hart for building the pneumatic graphite plug holder. The authors gratefully acknowledge the Air Force Office of Scientific Research (F49620-93-1-0349) for support of this research.

References

[1] G.E.M. Hall, J.C. Pelchat, D.W. Boomer and M.J. Powell, Anal. At. Spectrom., 3 (1988) 791.
[2] S.P. Osborne, Appl. Spectrosc., 44 (1990) 1044.
[3] P. Richner and S.J. Wunderli, Anal. At. Spectrom., 8 (1993) 45.
[4] P.K.G. Manninen, J. Anal. At. Spectrom., 9 (1994) 209.
[5] E.H. Bailey, A.J. Kemp and K.V. Ragnarsdottir, J. Anal. At. Spectrom., 8 (1993) 551.
[6] C.J. Park, J.C.V. Loon, P. Arrowsmith and J.B. French, Anal. Chem., 59 (1987) 2191.
[7] R.E. Sturgeon, S.N. Willie, J. Zheng, A. Kudo and D.C. Gregoire, J. Anal. At. Spectrom., 8 (1993) 1053.
[8] M.M. Lamoureux, D.C. Gregoire, C.L. Chakrabarti and D.M. Goltz, Anal. Chem., 66 (1994) 3208.
[9] M.M. Lamoureux, D.C. Gregoire, C.L. Chakrabarti and D.M. Goltz, Anal. Chem., 66 (1994) 3217.
[10] N. Shibata, N. Fudagawa and M. Kubota, Anal. Chem., 63 (1991) 636.
[11] D.C. Gregoire and R.E. Sturgeon, Spectrochim. Acta., 48B (1993) 1347.
[12] T. Hirata, T. Akagi, H. Shimizu and A. Masuda, Anal. Chem., 61 (1989) 2263.
[13] R. Tsukahara and M. Kubota, Spectrochim. Acta., 45B (1990) 779.
[14] J.M. Carey, E.H. Evans, J.A. Caruso and W.L. Shen, Spectrochim. Acta., 46B (1991) 1711.
[15] D.C. Gregoire, J. Anal. At. Spectrom., 3 (1988) 309.
[16] R.J.B. Hall, M.R. James, T. Wayman and P. Hulmston, in K.E. Jarvis, A.L. Gray, I. Jarvis and J. Williams (Eds.), Plasma Source Mass Spectrometry, Royal Society of Chemistry, Cambridge, 1990, pp. 145–154.
[17] P.G. Whittaker, T. Lind, J.G. Williams and A.L. Gray, Analyst, 114 (1989) 675.
[18] A.R. Date and Y.Y. Cheung, Analyst, 112 (1987) 1531.
[19] N. Shibata, N. Fudagawa and M. Kubota, Spectrochim. Acta., 47B (1992) 505.
[20] G. Long and J.D. Winefordner, Anal. Chem., 55 (1983) 712A.
[21] R.D. Ediger and S.A. Beres, Spectrochim. Acta., 47B (1992) 907.
[22] T. Kantor, Spectrochim. Acta., 43B (1988) 1299.

APPENDIX 4, R. Sabia, "Physical and Chemical Interactions of Lubricants in Hybrid Bearing Systems," Abstract of Ph.D. Dissertation presented to the Graduate School, University of Florida, May 1996. Dissertation copy available upon request. J.H. Adair, advisor.

Abstract of Dissertation Presented to the Graduate School
of the University of Florida in Partial Fulfillment of the
Requirements for the Degree of Doctor of Philosophy

PHYSICAL AND CHEMICAL INTERACTIONS OF LUBRICANTS
IN HYBRID BEARING SYSTEMS

By

Robert Sabia

May, 1997

Chairman: James H. Adair
Major Department: Materials Science and Engineering

Experiments designed to evaluate the effects of oil degradation on bearing performance were carried out on a commercial synthetic lubricant (MIL-L-23699) at temperatures between 200-300°C. Characterization included analysis of coking and preliminary analysis using UV/VIS spectroscopy as a technique for oil monitoring. Tribological experiments were performed using a pin-on-disk test machine with yttria/alumina doped silicon nitride and M-50 steel test materials with hardness and surface finish indicative of bearing grade materials. Results showed a general increase in friction with decreasing oil condition, and results from wear testing showed no correlation with oil condition.

A kinetic study of the effects of various environmental parameters on oil degradation was performed at 250°C. Environmental parameters included testing in oxidative and non-oxidative environments and investigating the presence of M-50 steel as a catalyst material at both low and high relative humidity. Analysis included changes in the rates of degradation for the various environmental parameters, as well as analysis of

antioxidant removal and subsequent effects on the formation of high molecular weight degradation products. Results showed that the presence of M-50 steel acted to increase the rate of oil degradation while high humidity lowered the rate of degradation. Water was also found to be a primary degradation products. From the beneficial affect of high humidity and from the generation of water as a byproduct, the mechanism for the formation of high molecular weight degradation products is proposed to be a polycondensation reaction. Furthermore, diffusion is proposed to be rate limiting for this process .

An investigation into the use of ultraviolet/visible absorption spectrometry as a technique for oil monitoring was carried out on oil samples generated at 250°C. Analysis included determining the mechanism for spectral changes and determining effects of environmental parameters on associated changes. Results showed spectral changes with degradation to be the result of changes in intensity for absorption peaks which represented the base stock and degradation products. The behavior of these absorption peaks followed the Beer-Lambert law and can be used to represent the concentration of degradation product.

APPENDIX 5, R. Sabia, Herb A.J. Chin, and J.H. Adair, "A Kinetic Study of the Degradation Behavior and Mechanisms of a Synthetic Ester-Based Lubricant," submitted for publication.

KINETIC STUDY ON THE DEGRADATION BEHAVIOR AND MECHANISMS OF A SYNTHETIC ESTER-BASED LUBRICANT

Robert Sabia,[*1] Herbert A.J. Chin,[2] and James H. Adair[*1]
[1]University of Florida
Materials Science and Engineering
Gainesville, FL 32611
[2]Pratt & Whitney Aircraft
West Palm Beach, Fl 33410

*Member, Society of Tribologists and Lubrications Engineers

ABSTRACT

Individual effects of thermal, thermal-oxidative, and tribochemical degradation mechanisms on a conventional synthetic ester-based lubricant (MIL-L-23699C) have been studied. Degraded oil samples were generated under experimental conditions performed in the presence of oxidative and non-oxidative environments, high and low humidities, and the presence of or lack of M-50 steel as a catalyst material. All experiments were performed at 250°C and samples were collected as a function of time. Samples were characterized for total acid number, antioxidant content, water content, viscosity, spectrometry, and molecular weight. Molecular weight peak analysis was performed assuming Gaussian distributions. Results were compared to determine influences of the aforementioned variables on the rate of formation of higher molecular weight species in the synthetic oil. From these results, and from experiments performed on condensed vapors collected during the degradation runs, influences of each variable on the depletion of antioxidant and generation of high molecular weight species are shown.

KEY WORDS

Degradation, Humidity, Lubrication, Oxidation.

INTRODUCTION

Current understanding of the degradation behavior of the lubricants used for gas turbine jet engines is limited. The individual effects of each variable encountered during engine operation has not been completely investigated. Of the kinetic studies which have been reported, test systems have been simplified by limiting studies to one additive mixed into one base stock. For conventional lubricants which are blends of multiple additives and base stocks, results from simplified tests may not be representative with effects of competing degfradation mechanisms not taken into account. Interest in oil degradation behavior stems from the effects of thermal, thermal-oxidative, and tribochemical degradation mechanisms, as well as the influences of high humidity environments.

Current Understanding of Degradation Mechanisms

Under current bearing applications where bulk lubricant operating temperatures range between 75-150°C, boundary and elastohydrodynamic contact temperatures can reach 250-350°C due to frictional heating (1-2). Chemical reactions, which normally are nonexistent or of low reaction rate, can be accelerated under these temperature conditions (3). When operating for extended time at temperatures over 200°C, most commercial ester-based lubricants oxidize, polymerize, or evaporate (4). The most common mechanisms for the degradation of these ester-based lubricants are thermal and thermal-oxidative degradation mechanisms, as well as tribochemical degradation mechanisms (5).

Thermal and Oxidative Degradation

Both thermal and thermal-oxidative degradation processes consist of a free radical chain mechanism (1,6-8). In these processes, free radicals are generated through either a hydroperoxide radical mechanism, a carbon-carbon scission mechanism, or both. These free radicals then act to polymerize other lubricant constituents by starting reaction chains via abstraction of hydrogen atoms from parent molecules (9). Free radical chain propagation is the most detrimental oil degradation mechanism. This type of degradation is in part controlled by the addition of antioxidant additives.

Antioxidant Behavior

Oxidation degradation is minimized in synthetic ester-based lubricants by the addition of oxidation inhibitors referred to as antioxidants. Antioxidant additives act to eliminate this free radical chain propagation mechanism by donating a proton to the free radicals, therefore rendering them inactive. The antioxidant molecule then becomes a free radical which is self stabilized through resonance (7,8).

Tribochemical Degradation Mechanisms

Metallic surfaces and debris have been shown to play an increasing role in ester based lubricant breakdown above 180°C by increasing the rate of degradation (1-2,5,9-11). These metallic surfaces can act as catalysts, either inhibiting or promoting oil degradation. Organometallics, oxides, and inorganic compounds all form upon reaction between metal surfaces, oil constituents, and contaminants, acting in the same manner as catalysts (1,9). Reactions with metallic debris can be more serious than those with metal surfaces due to higher activity of the debris (9). Ceramic surfaces are less active and have been shown to form passivation layers (11). These passivation layers are generated by reaction with water absorbed in the oil and water vapor generated as a combustion product (13). For ceramics, reactions with oil constituents are limited by the passivation films unless the rate of wear is faster than the rate of reaction. In this manner, the formation of oxide and oxynitride films on silicon nitride can produce lower coefficients of friction and wear rates in hybrid and ceramic bearings (3,14-16). However, oxide films formed on metal surfaces result in junction growth (15). Oxide debris collect around the contact regions and do not lower the coefficient of friction.

Previous Kinetic Studies

Although many kinetic studies have been reported for the determination of individual effects on specific lubricant additives, one report is of particular note. A pressurized Penn State microoxidation tester was used by Hunter et al. to determine the kinetic behavior and optimal concentration of an antioxidant additive (7). Experiments were performed using various mixing ratios of the antioxidant phenyl-alpha-naphthylamine (PANA) in the polyol ester trimethylolpropane triheptanoate. The micro-oxidation test consisted of placing a thin film of oil onto a metal catalyst surface in a pressure controlled environment with flowing gas at temperatures below 200°C. Tested samples were studied for molecular weight changes using gel permeation chromatography (GPC). Results showed that removal of the lower molecular weight peak which represented the PANA coincided with slight increases in the generation of higher molecular weight species. Furthermore, the rate of generation for the higher molecular weight species increased significantly after complete removal of the PANA. These results are of particular interest due to the fact that antioxidant concentration was monitored and related to the direct formation of higher molecular weight species.

Hunter et al. (7) demonstrated how the depletion of antioxidant directly affects oil degradation. However, results were presented for one environment without changing test variables and are therefore limited in determining how a particular additive or oil base stock could be improved. If the individual degradation effects of each variable faced in an operating turbine engine could be determined, both oils and additives could be engineered for improved performance with respect to a specific degradation mechanism, rather than with respect to competing mechanisms.

The most significant limitation in determining ways for improving lubricant performance is the lack of understanding in the individual effects of variables encountered during engine operation. The object of this chapter is to determine how thermal degradation, thermal-oxidative degradation, high humidity, and the presence of the M-50 steel catalyst effect oil degradation. Of particular emphasis will be antioxidant depletion and the formation of high molecular weight species.

MATERIALS AND METHODS

In order to determine the individual effects of thermal, thermal-oxidative, and tribochemical degradation mechanisms, a series of experiments was designed and performed under varying environments. As shown in Table 1, a total of eight experiments were performed while varying atmosphere, humidity, and the presence of M-

50 steel surfaces. For each test, 750 ml of as-received synthetic ester-based oil (MIL-L-23699C) was placed in a Pyrex beaker on a hot plate. The hot plate was connected to a constant temperature controller. The thermocouple from the controller was covered with a glass capillary tube, sealed at one end before being placed into the oil bath to avoid catalytic degradation created by the thermocouple probe. Gas flow was supplied to the oil bath using a flow meter set to 0.83 L/min and a glass dispersion tube placed into the bath. Finally, the beaker was wrapped in fiberglass insulation to aid in temperature control. In this manner, the oil was completely isolated from metallic surfaces which might act as catalysts. The hot plate was set to the highest setting and the temperature controller was set to 250°C, resulting in a heating rate of approximately 225°C/hour.

In accordance with Table 1, gas flow supplied to each experiment was either compressed argon, resulting in an inert (non-oxidative) atmosphere which allows for thermal degradation without oxidative degradation, or compressed air which would promote both thermal and oxidative degradation. Samples of M-50 steel were supplied as catalyst surfaces for the designated tests in the form of 1/4" diameter bearing balls placed in the oil bath at the beginning of each experiment. The resulting ratio of available surface area to oil was 3.6 mm^2/ml, which was kept constant for each of the appropriate tests. For tests performed under low humidities, gas flow for both compressed argon and air was determined with an on-line sensor (Implant Sciences Corporation, Wakefield, MA 01880) as ≤12%. For the tests performed under high humidity, a liquid bubbler filled with distiller water was placed between the flow meter and the oil bath. The resulting relative humidities for the gas flow entering the bath were 85% for argon and 92% for air.

To analyze the kinetic aspects of the degradation processes, 50 ml samples were taken during each experiment using a glass pipette. Sample times recorded from initial heatup were 3, 5, 7, 9, and 13 hours heat treatment time. Each sample was stored in a glass bottle with a Teflon lined lid to protect the oil samples from the environment and to prevent absorption of water, which might lead to further degradation.

Analysis of the oil constituents and degradation byproducts which evaporated during these tests was performed by collecting the vapors at various times during test OX12NC. Collection was performed using a vacuum pump which pulled vapors from the beaker through Teflon tubing and into a condenser tube cooled by liquid nitrogen. After vapors were collected, the condenser tube was removed from the liquid nitrogen and sealed to prevent condensation not associated with the test.

In order to determine the effects of degradation on a physical property of the oil samples, viscosity tests were performed using a variable speed rheometer (Brookfield RVDV III, Brookfield Engineering Laboratories, Inc., Stoughton, MA 02072) with a 0.8° cone angle between shear rates of 0.75 and 450 s^{-1}. Experiments were performed at 40±0.1°C using a constant temperature water bath, therefore producing results which can be directly compared with military specifications. Water content of the oil samples was determined using coulometric Karl Fisher titration (Accumet 150 Controller and 110KF Titration Module, Fisher Scientific, Pittsburgh, PA 15219).

The extent to which oil degradation had occurred for each sample was determined using a number of analytical techniques. Antioxidant concentration for each sample was determined using a Remaining Useful Lubricant Life Evaluation Rig (RULLER) (9), and the extent to which degradation had occurred was determined from the total acid number

(TAN) (17). For TAN experiments, exceptions from the ASTM designation were the use of aqueous based buffers and titration to pH 11, the later of which allowed all acidic groups of equivalent and higher strength than phenolics (pKa=10) to be base neutralized. These techniques are used in combination to predict when an oil is likely to degrade and the extent to which degradation has occurred.

Chemical analysis of the tested samples and condensed vapors was performed spectroscopically using transmission FTIR (20SXB with Omnic™ Software, Nicolet Instrument Company, Madison, WI 53711) with KRS-5 salt crystals for sample mounting and a circular fluid cell for dilute samples, with nitrogen as the purge gas. This technique allowed for the partial analysis of chemical changes in the oil samples through observation of changes in the characteristic absorption peaks.

In order to determine the differences in rates of degradation resulting from thermal and thermal-oxidative degradation mechanisms, as well as the influences of catalytic surfaces and high humidity environments, molecular weight analysis was performed on the oil samples and the collected vapors. Size exclusion chromatography, also known as gel-permeation chromatography (GPC), was performed using an ultraviolet/visible (UV/VIS) wavelength detector (Waters™ Chromatography Division, Millipore Corporation, Milford, MA 01757). A pre-filter and 50-1K, 5K-10K, 20K-300K and 100K-1000K molecular weight range columns (Phenogel, Phenomenex, Torrence, CA 90501) were used to determine the molecular weight distribution of each sample, with tetrahydrofuran as the solvent carrier. The columns were calibrated between 92 and 870,000 MW using polystyrene molecular weight standards and toluene. Approximately 20-30 mg of each sample was mixed with 10 ml of tetrahydrofuran and filtered three times through a 0.22 μm Teflon filter before injection. The flow rate was set to 0.4 ml/min, and the injection volume was 20 μl. UV/VIS data for the oil samples was processed at a constant wavelength of 216 nm. Data was calibrated against the polystyrene standards to generate molecular weight distributions from the measured elution times. In order to accurately compare results from each run, all data was corrected by normalizing the areas under each data curve. Evaluation of changes in peak intensities and locations was performed using peak separation and analysis software (Peakfit™ V 4.0, Jandel Scientific Software, San Rafael, CA 94901) assuming a Gaussian distribution.

RESULTS AND DISCUSSION

Results of characterization testing performed on the experiments described in Table 1 are separated according to rheological analysis, chemical analysis, molecular weight analyses, and peak analysis of the molecular weight distributions. Analysis of condensed volatile was performed in order to determine the low molecular weight degradation products. Results for rates of degradation and the formation of particulates are presented for each test series.

Rheological Analysis

As a first step in determining the extent to which degradation in the oil samples had occurred, viscosity data was plotted versus test time for each series of experiments (Figure 1(a)). All results yielded Newtonian behavior without a Bingham yield point, thus the data reflects average viscosity changes for the tested shear rates. Viscosity changes for the tests performed in inert (non-oxidative) environments gradually increased to 23-30% change for the 13 hour test samples. Results for tests performed in oxidative environments showed higher rates of viscosity change, with the final 13 hours test samples reflecting viscosity changes above 100%. Of the tests performed in oxidative environments, the tests which included the M-50 steel catalyst showed greater changes than those without catalyst. Furthermore, high humidity environments resulted in lower changes in viscosity. Effects of catalyst (M-50 steel) and high humidities were not shown to affect viscosity changes for the tests performed in non-oxidative environments.

Chemical Analysis

Determination of the extent to which degradation has occurred in the test samples began with analysis of the antioxidant content. Results from RULLER experiments are shown in Figure 1(b), plotted with antioxidant concentration as a function of test time. Antioxidant levels for samples tested in inert (non-oxidative) atmospheres gradually decreased at approximately identical rates to concentrations between 54-57% for the 13 hour test samples. Results for experiments run in oxidative environments indicate that humidity and the presence of a catalyst affected the depletion of antioxidant in much the same way as with increasing viscosity changes shown in Figure 1(a). Degradation experiments performed with catalyst material showed increased rates of antioxidant depletion, whereas experiments performed in high humidity environments showed decreasing rates of antioxidant depletion. For the tests performed in oxidative environments, the antioxidant concentrations leveled out between 35 and 40% for the 9 hours test samples. Results show that significant degradation occurs before the 40% antioxidant concentration is met.

Further analysis of the condition of the samples was determined using total acid number (TAN). Figure 1(c) shows TAN results plotted versus time. Molality (M) values associated with the TAN are also presented, showing the concentration of base neutralized acid sites. Results showed that the extent to which degradation had occurred in the various tests followed the same trends as with viscosity and antioxidant changes. Results for tests performed in non-oxidative environments showed TAN values increased to approximately 0.45 mg KOH (0.008 mg oil). Since TAN values are not considered significant until above 1.0, these results show small amounts of degradation for the experiments performed in non-oxidative environments, with no evidence of catalyst or humidity effects. For the samples performed in oxidative environments, TAN values rose above 2.9 for the 13 hour test samples. Greater amounts of degradation were shown for experiments performed with M-50 steel catalyst, and the experiments performed in high humidity environments exhibited lower amounts of degradation.

FTIR analysis of the as-received sample, seen in Figure 2, shows strong absorption peaks between 2850-3000 cm^{-1} as well as the 1465 cm^{-1} peak reflects C-H absorption. The strong peak at 1743 cm^{-1} for the as received oil reflect one or more carbonyl peaks for ester structures within the base oil. The variety of lower intensity peaks between 1000-1465 cm^{-1}, which include the C-C(=O)-O (lactone) and the O-C-C peaks, are not distinguishable (18). As for changes in the spectra of the oil samples as a function of test time, results showed broadening of the carbonyl peak (1743 cm^{-1}) which could not be attributed to any one mechanism. Possibilities included transesterification, the formation of ketones, and the formation of carboxylic acids. With increasing test time, changes in peak ratios occurred between thehydrocarbon and carbonyl vibration peaks, as well as the peaks in the fingerprint region of the spectrum. For the results of longer test time samples from oxidative environments, a hydroxyl peak appeared in the range 3300-3700 cm^{-1}, suggesting the formation of either carboxylic acids, alcohols, or water.

Molecular Weight Analysis

Although results from viscosity, antioxidant, and TAN testing suggest trends in the degradation behavior of the oil system under various test conditions, these results only reflect chemical and physical responses to degradation. The results do not describe or explain the kinetics of the individual degradation mechanisms. In order to better understand the influences of the individual mechanisms on the rate of degradation, molecular weight analysis was performed.

Size exclusion chromatography results are presented for the IN12NC test samples in Figure 3. A total of six peaks were found for the as-received oil sample, with molecular weights of 215, 267, 432, 662, 863, and 1292. In order to determine how the molecular weight distributions change as a function of test time, peak separation and analysis ($r^2 \geq 0.996$) was performed using Gaussian curve fitting for each of the tests. Changes in the molecular weight distributions varied for each test series: For both test series, decreases in intensities were observed for the four lowest MW peaks. Increases in intensities were observed for the two highest peaks. The peaks which undergo the greatest changes are the 1292 MW and 267 MW peaks.

Peak Analysis

The significance of the changes for the 1292 MW and 267 MW peaks can be understood from the observation of a number of correlations. Figure 4(a) shows viscosity changes versus the formation of high molecular weight species reflected by increasing area in the 1292 MW peak. Two fitted curves are presented, one for the data points from tests performed in non-oxidative environments and the other for data points representing oxidative testing. The two curves deviate at approximately 25% viscosity change and 55% peak area, showing dramatic increases in peak area for the test performed in oxidative environments. Further comparisons were made for TAN results plotted against the 1292 MW peak area, as shown in Figure 4(b). Again two fitted curves are presented, one for each test environment. Changes in peak area increased dramatically for the oxidative environment data at TAN values above 0.8 and 55% peak area. The increases in peak area as a function of both viscosity and TAN values initially began at the same approximate peak area of 55%. This suggests that the viscosity changes are a direct result of the oil degradation as indicated by the TAN results. Fitted curves for data from the experiments performed in oxidative environments are represented by $y = 5.11 \cdot 10^{-6} \cdot x^{3.95}$ and $y = 5.43 \cdot 10^{-7} \cdot x^{3.66}$ for viscosity changes and TAN values respectively.

Similar correlations were made with changes in intensities for the 267 MW peak. As shown in Figure 5(a), decreases in peak height directly correlate with decreasing antioxidant content along the curve $y = 33.04 \cdot x^{0.23}$. Since the minimum molecular weights **(no repeated units)** for the base stock esters pentaerythritol and 1,1,1-trimethylolpropane are 374 amd 302 respectively, the 267 MW peak can be attributed to the antioxidant(s). However, the results do not give insight as to the relationship of the 267 MW peak with para-alphanapthylamine (219 MW) and di-octylphenylamine (381 MW), the antioxidant additives used in these oils.

A second correlation for the 267 MW peak is shown in Figure 5(b), where peak height is plotted versus changes in viscosity. These results show that viscosity increased at a constant rate to 25% change, reflected by a 10% height in the 267 MW peak, before increasing significantly. This shows that increasing viscosity was not dependent on the removal of a low molecular weight species (as is one possibility), but rather completely dependent on the depletion of the antioxidant. Furthermore, Figure 5(b) shows that the effectiveness of the antioxidant is lost when the 267 MW peak height has dropped to approximately 10%, thus correlating with Figure 5(a) to an antioxidant concentration between 55-60% as determined by the RULLER technique.

Results for the test series performed in oxidative atmospheres yielded dissimilar results. Initial rates of decreasing 267 MW peak height are not the same, as high humidity environments decreased the rate in which the peak changed, while the presence of the catalyst material increased the rate at which the peak was removed. This trent is consistent with results shown in Figure 1, where viscosity, TAN, and antioxidant concentration data showed identical trends with respect to catalyst and humidity. The depletion of antioxidant, increase in TAN values, and the increase in viscosity were accelerated by the presence of catalyst, and hindered by high humidity for the experiments performed in oxidative environments.

Analysis of the Volatiles

Transmission FTIR showed the second species to be either an ester, ketone, or carboxylic acid (see Figure 6(a)). As with the previously mentioned results for the oil samples, the only peaks which could be identified were those representing hydrocarbon and carbonyl vibrations. For vapor samples which were collected as a function of test time, spectra for this species did show changes in peak ratios. However, the significance of these changes could not be determined due to the fact that identification of this compound has not been confirmed.

Analysis of the condensed vapors from the OX12NC test showed the evaporation of at least two distinct chemical species which spontaneously phase separated, with the denser phase incorporating more than 75% of the liquid volume. Analysis of the first species was performed using FTIR with a circular fluid stage and results compared to those for deionized water. As seen in Figure 6(b), the hydroxyl peaks located between 3000-3500 and at 1635 cm^{-1} are identical for both spectra. Minor peaks are located between 2800-3000 cm-1, representing vibrational characteristics of a C-H stretch (18). This suggests that the sample might contain small amounts of alcohol. Since special care was taken to ensure that no condensation would occur between sampling and cooling of the condenser tube, these results show that water is a degradation product for the synthetic oil.

Molecular weight tests performed on a mixture of both species show changes in peak heights and locations. As seen in Figure 7, the 3 hour sample consisted of species with similar molecular weights to those of the as-received oil sample. For the 7 hour test sample, the lower molecular weight peaks shift. These results show original species of the oil are evaporating at the 250°C test conditions. Furthermore, volatile degradation products are generated and not detected in the oil samples. These molecular weight results also suggest that the antioxidant (or a degradation product of the antioxidant) is one of the volatiles.

In order to confirm the formation of water as a volatile degradation product, coulometric Karl Fisher was performed. The as-received oil sample had a water content of 566 ppm. Water content initially fell during the first hours of oil testing, but leveled off or increased for higher test times. This confirms the FTIR results which showed water to be a degradation product. Results for the tests performed in non-oxidative environments showed no obvious correlations between test conditions and times, as water content fluctuated between 325-575 ppm. Results for samples from the oxidative test environments showed that the water content initially fell below 400 ppm, before gradually increasing at rates which were increased by the presence of high humidities and catalyst materials. Final water content values for the oxidative test environments ranged between 327 ppm for the OX12NC test and 538 ppm for the OX92C test. Although both catalyst and high humidity increased water content and therefore seem to increase water generation, results for viscosity, total acid number, and antioxidant content testing presented in Figure 1 show that the high humidity environments slow the thermal-oxidative degradation process. This behavior cannot be used to qualify the types of reactions which generate this behavior (hydrolysis of the ester resulting in water consumption and condensation resulting in water generation are possible reactions), but simply shows the effects of water on antioxidant content.

A mechanism for the lower degradation rate for oil samples tested under high humidity environments can now be proposed. Water vapor which is absorbed by the oil acts to hinder the formation of the high molecular weight degradation products by slowing the reaction which depleted the antioxidant, thus delaying the chemical and physical changes associated with extreme oil degradation.

Rate of Degradation

The effects humidity and catalyst presence have on the actual rate of degradation can be determined. The degree of degradation was generated for peak 1 results using the following:

$$\text{Growth Factor} = \text{Mean Molecular Weight} \times \text{Peak Area Fraction} \qquad (1)$$

Rate of degradation was then determined by plotting growth factor versus test time for each test series performed in an oxidative environment (Figure 8(a)). Since the growth factor is a representation of the concentration of high molecular weight degradation product, the linear relationship for each test with time indicates that the 1292 MW peak is represented by multilple species and that the formation of the degradation products follows a high order kinetic reaction (2nd or higher) (19). Table 2 lists linear correlation coefficients ($r^2 \geq 0.985$) and slopes for each test series. With high order kinetic reactions, the slope m of the concentration is related to the rate constant by the following equation:

$$m = 2 \cdot k \qquad [2]$$

The rate constant k is dependant on concentration of degradation products with respect to one another. Since the exact order of the kinetic reactions cannot be determined without knowing concentration of the degradation products, the rate constant cannot be determined.

In order to interpret how the formation of high molecular weight species affects lubricant performance, the interactions of the molecular weight species found in the 1292 MW peak must be related with viscosity results. Since all viscosity measurements reflected Newtonian behavior, the Einstein equation, Eq. (3), for particle content can be investigated as a plausible explanation for changes in both optical and viscoelastic behaviors (20).

$$\eta^* = \eta_o \cdot (1 + \frac{5}{2} \cdot \phi) \tag{3}$$

The η^* refers to the experimental viscosity, η_o refers to the as-received viscosity, and ϕ refers to the percent particle volume of the system. In Figure 8(b), the calculated particle content is shown to correlate with changes in the high molecular weight degradation product represented by the growth factor. This correlation suggests that the degradation products are acting as particulate species with respect to physical changes shown by the viscosity results. The fitted curve for Figure 8(b) follows the parabolic relation $y = 0.036 - 1.82 \cdot x + 4.51 \cdot x^2$ and has a correlation coefficient of r^2=0.99.

In order to understand the kinetic information generated and presented using the growth factor (Eq. (1)), a review of rate determining and limiting mechanisms by Overbeek was incorporated (21). In his article, Overbeek gave definitions for rate of reactions when diffusion is and is not rate determining. Information was presented in terms of mean particle size and particle size distribution. In order to apply this information to the present work, calculations were made to estimate the particle size of the high molecular weight degradation products by calculating the radius of gyration (22):

$$r_g = \frac{l \cdot \sqrt{\dfrac{MW}{M_o}}}{\sqrt{6}} \tag{4}$$

The r_g is the radius of gyration, l refers to the bond length, chain MW is molecular weight, and M_o is monomer molecular weight. Since the repeating units for the base ester structures are ethylene and since the standard used to calibrate the GPC columns were polystyrene, the monomer weight of polyethylene (M_o=28) and bond length for polystyrene (l=0.53 nm), these values were used for the calculations to estimate the radius of gyration for the high molecular weight degradation products.

Figure 8(b) plots changes in the mean molecular weight values for the high molecular weight degradation product versus changes in the molecular weight distributions of the fitted Gaussian peaks taken to by the full width half maximum values. The estimated values for radius of gyration which correspond to the molecular weight changes are also presented, where $MW \sim r_g^2$. As shown during the initial stage of oil degradation (prior to antioxidant removal), changes in particulate size do not correlate with changes in particle size distribution and thus no information can be determined as for the rate limiting effects. After the antioxidant is removed (corresponding on Figure 8(b) to a mean molecular weight value of approximately 1300 MW), changes become linear. This relationship indicates the availability of rate determining information after antioxidant is depleted. From Figure 8(a), mean molecular weight (and thus particle radius squared) changes linearly with time, thus following the relationship:

$$a^2 = k \cdot t + b \tag{5}$$

where a refers to the particle size and k and b are constants. Integration of Eq. (5) shows that changes in mean molecular weight (particle size) follows the kinetic relation:

$$\frac{da}{dt} = k' \cdot a^{-1} \tag{6}$$

where k' is a constant. In accordance with the work presented by Overbeek, Eq. (6) follows the relation for diffusion limiting growth:

$$\frac{da}{dt} = \frac{D \cdot (c_\infty - c_o) \cdot V}{a^n} \tag{7}$$

where D is the diffusion coefficient, V is molar volume, $(c_\infty - c_o)$ is the change in concentration, and n can be 2, 1, 0, and -1. These result thus show that once the antioxidant is removed, degradation in the oil system is diffusion limited.

CONCLUSIONS

Results for tests designed to separate the individual effects of thermal and thermal-oxidative degradation mechanisms, as well as to determine the influence of high humidity and the effectiveness of M-50 steel as a catalyst material were performed at 250°C. For tests carried out in inert (non-oxidative) environments, the presence of the M-50 steel catalyst and high humidity did not significantly affect the rate of antioxidant removal. Furthermore, these results were not accompanied by significant changes in viscosity and TAN values, thus the limited effect of thermal degradation mechanisms on oil degradation for the various environments has been determined.

Results for tests performed in oxidative environments yielded dissimilar results. The presence of the M-50 catalyst material increased and high humidity decreased changes in viscosity, antioxidant content, total acid number, and molecular weight peak area/height ratios. These results show that the combined effects of oxidative and thermal degradation act to increase the total degradation of the oil significantly more than for thermal degradation alone.

Analysis of volatiles recovered from the degradation tests were analyzed using FTIR and GPC. Results show water to be a degradation product. Although qualitiative influences on specific reactions (e.g., hydrolysis and condensation reactions) could not be determined, the effect of adsorbed water was shown to lower the rate of antioxidant removal.

Changes in concentration of the high molecular weight degradation products have been shown to follow a high order kinetic reaction. The order of the reaction can not be determined without more specific information on the degradation species. As for the physical changes in the oil, a direct correlation between the formation of high molecular weight species and viscosity was found using the Einstein equation for Newtonian fluids containing small particles. In this manner, the high molecular weight species are shown to act as particulate materials with respect to the physical behavior of the oil.

Further information on the nature of the oil degradation reaction was determined by relating changes in molecular weight to changes in particle size and distribution of the high molecular weight degradation product. Although no direct conclusions could be drawn for the oil system prior to antioxidant depletion, the knowledge of how free radicals act to degrade oil and how antioxidants act as scavengers to eliminate the free radicals suggests that variations in mean molecular weight and MW distribution are the result of a continuously changing concentrations of free radicals resulting in a low rate of degradation. Results showed that after the antioxidant was depleted, the reaction to form high molecular weight degradation products was diffusion limited.

ACKNOWLEDGMENTS

The authors gratefully acknowledge the support of the Air Force Office of Scientific Research Grant Number F49620-93-12-0349DEF in partial support of this work. The authors would also like to thank Michael Zamorra, Dr. Jim Kunetz and Ahmad R. Hadba of the University of Florida Department of Materials Science and Engineering for experimental assistance. The authors would also like to thank Pratt & Whitney for laboratory and equipment use in the West Palm Beach location.

REFERENCES

(1) Klaus, E.E., "Status of New Directions of Liquid Lubricants," in New Directions in Materials, Wear, and Surface Interactions, Tribology in the 80's, William R. Loomis, ed., Noyes Publications, (1985), pp. 354-375.

(2) Klaus, E.E., Duda, J.L., and Wu, W.T., "Lubricated Wear of Silicon Nitride," Lubrication Engineering, 47, 8, pp. 679-684, (1991).

(3) Gee, M.G., "Wear Testing and Ceramics," Journal of Engineering Tribology, 208, pp. 153-166, (1994).

(4) Ajayi, O.O., Erdemir, A., Hsieh, J.H., Erck, R.A., and Fenske, G.R., "Combined Solid and Liquid Lubrication of Silicon Nitride under Boundary Conditions," Lubrication Engineering, 48, 7, pp. 584-591, (1992).

(5) Hsu, S.M., Ku, C.S., and Pei, P.T., "Oxidative Degradation Mechanisms of Lubricants," in Aspects of Lubricant Oxidation, ASTM STP 916, W.H. Stadtmiller and A.N. Smith, eds., American Society for Testing and Materials, Philadelphia, (1986), pp. 27-48.

(6) Bakunin, V.N., and Parenago, O.P., "A Mechanism of Thermo-Oxidative Degradation of Polyol Ester Lubricants," Journal of Synthetic Lubrication, 9, 2, pp. 127-143, (1992).
(7) Hunter, M., Klaus, E.E., and Duda, J.L., "A Kinetic Study of Antioxidant Mechanisms," Lubrication Engineeering, 49, 6, pp. 492-498, (1993).
(8) Schnabel, W., Polymer Degradation Principles and Practical Applications, Macmillan Publishing Co. Inc, New York, (1981).
(9) Kauffman, R.E., "On-Line and Off-Line Techniques for Monitoring the Thermal and Oxidative Degradations of Aircraft Turbine Engine Oils - Part I: Laboratory Evaluations," Lubrication Engineering, 51, 11, pp. 914-921, (1995).
(10) Jones, W.R., "The Furture for Liquid Lubricants and Additives, Thermal and Oxidative Stabilities of Liquid Lubricants," in New Directions in Lubrication, Materials, Wear, and Surface Interactions, Tribology in the 80's, Ed. Loomis, W.R., Noyes Publications, Park Ridge, NJ, (1985), pp. 810-813.
(11) Gates, R.S., and Hsu, S.M., "Effect of Selected Chemical Compounds on the Lubrication of Silicon Nitride," Tribology Transactions, 34, pp. 417-425, (1991).
(12) Kauffman, R.E., Saba, C.S., Rhine, W.E., and Eisentraut, K.J., "Chemical Nature of Wear Debris," ASLE Transactions, 28, 3, pp. 400-406, (1985).
(13) Danyluk, S., Park, D.S., and McNallan, M., "Scanning Electron Microscopy of Tribochemical Films on Si_3N_4 to H_2O at High Temperatures," Ultramicroscopy, 37, pp. 239-246, (1991).
(14) Cranmer, D.C., "Wear Surface Analysis of Silicon Nitride," Lubrication Engineering, 44, 12, pp. 975-980, (1988).
(15) Kato, K. "Tribology in Ceramics," Wear, 136, pp. 117-133, (1990).
(16) Park, D.S., Danyluk, S., and McNallan, M.J., "Influence of Tribochemical Reaction Products on Friction and Wear of Silicon Nitride at Elevated Temperatures in Reactive Environments," Journal of the American Ceramic Society, 75, 11, pp. 3033-3039, (1992).
(17) ASTM Designation F664-89, Americal Society for Testing Materials, Swarthware, PA, pp. 218-224.
(18) Silverson, R.M., Bassler, G.C., and Morrill, T.C., Spectrometric Identification of Organic Compounds, John Wiley & Sons, New York (1991).
(19) Steinfeld, J.I., Francisco, J.S., and Hase, W.L., Chemical Kinetics and Dynamics, Prentice Hall, New Jersey, (1989).
(20) Einstein, A., Investigations on the Theory of the Brownian Movement, Dover Publications, Inc., USA, (1956).
(21) Overbeek, J.Th.G., "Monodisperse Colloidal Systems, Fascinating and Useful," Advances in Colloid and Interface Science, 15, pp. 251-277, (1982).
(22) Hiemenz, P.C., Polymer Chemistry, Marcel Dekker Inc., New York, (1984).

Table 1. List of degradation experiments for the kinetic study.

Test ID	Temperature	Atmosphere	Humidity	Catalyst
IN12NC	250°C	inert	<12 %	None
IN12C	250°C	inert	<12 %	M-50
IN85NC	250°C	inert	~85 %	None
IN85C	250°C	inert	~85 %	M-50
OX12NC	250°C	oxidative	<12 %	None
OX12C	250°C	oxidative	<12 %	M-50
OX92NC	250°C	oxidative	~92 %	None
OX92C	250°C	oxidative	~92 %	M-50

Table 2. List of correlation coeffiencents and slopes for plot of Growth Factor versus test time shown in Figure 8(a).

Test ID	Correlation Coefficient (r^2)	Slope (m)
IN12NC	0.997	56.43
IN12C	0.985	53.60
IN85NC	0.993	57.84
IN85C	0.992	54.28
OX12NC	0.994	84.09
OX12C	0.998	87.25
OX92NC	0.996	79.94
OX92C	0.996	77.74

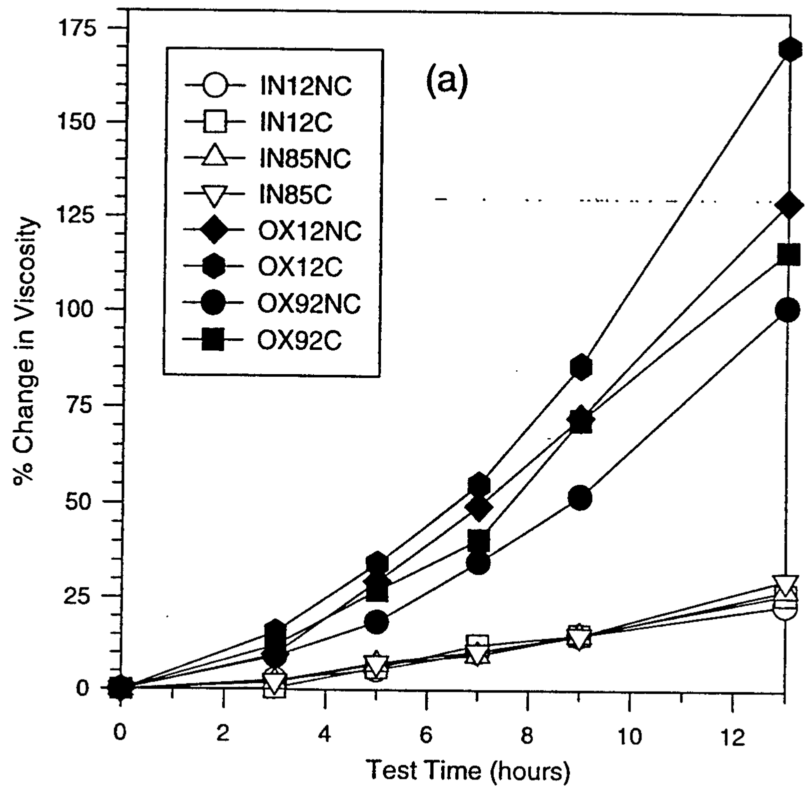

(a)
IN12NC
IN12C
IN85NC
IN85C
OX12NC
OX12C
OX92NC
OX92C
% Change in Viscosity
Test Time (hours)
0
25
50
75
100
125
150
175
0
2
4
6
8
10
12

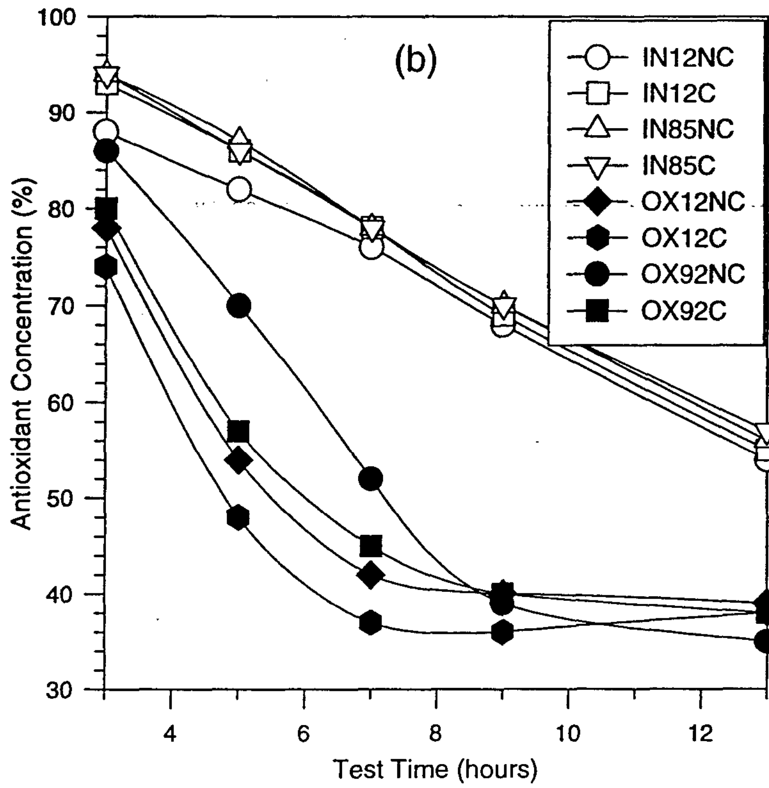

(b)
IN12NC
IN12C
IN85NC
IN85C
OX12NC
OX12C
OX92NC
OX92C
Antioxidant Concentration (%)
100
90
80
70
60
50
40
30
4
6
8
10
12
Test Time (hours)

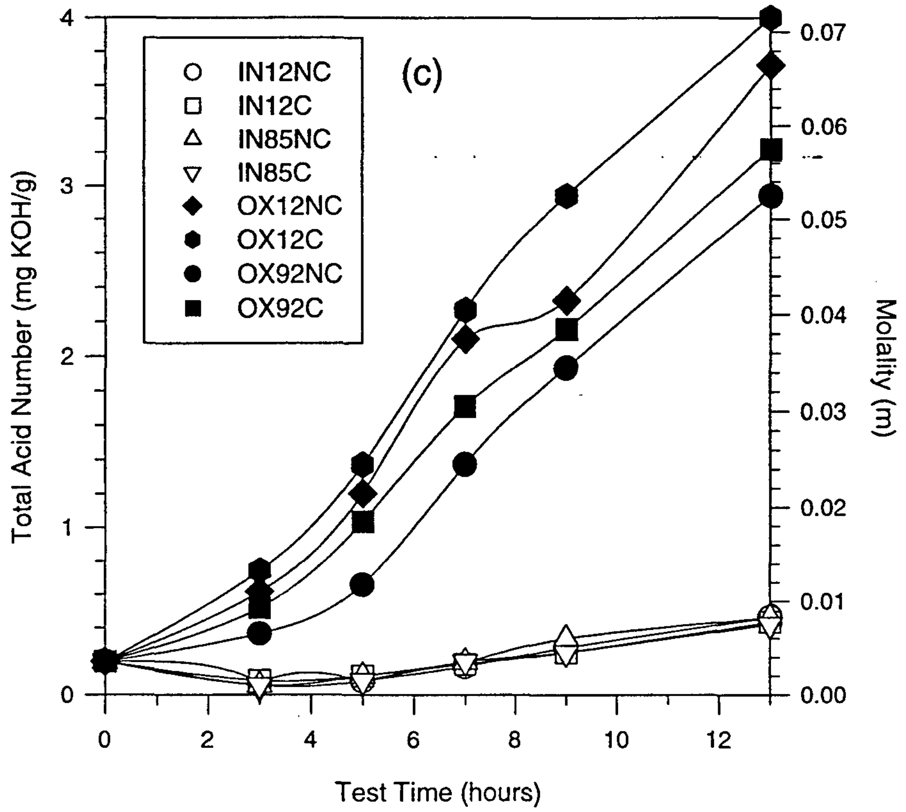

Figure 1. (a) Changes in viscosity as a function of test time for all test series, (b) changes in antioxidant content as a function of test time for all test series, and (c) changes in total acid number as a function of test time. Oxidative test environments yield significant changes in both chemical and physical aspects of oil condition. The presence of M-50 steel sufaces is shown to increase degradation, and high humidity is shown to decrease degradaion.

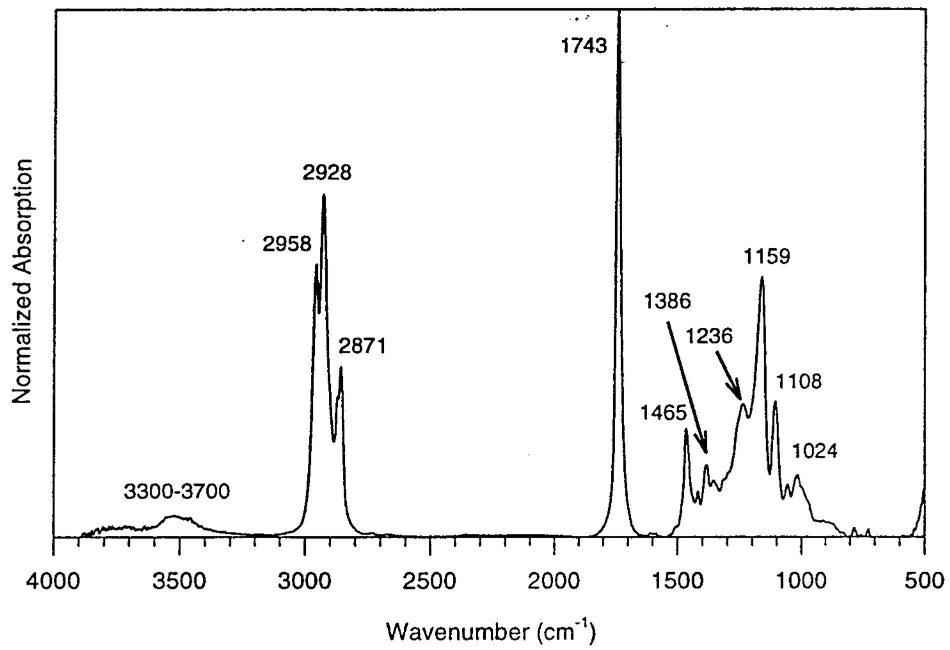

Figure 2. FTIR spectra for the 13 hours sample from test OX12NC. Peaks located between 2850-3000 cm-1 represent C-H stretch. and the 1743 cm-1 peak represents an ester carbonyl C=O stretch peak. Peaks between 1000-14000 cm-1 represent C-O stretch from esters.

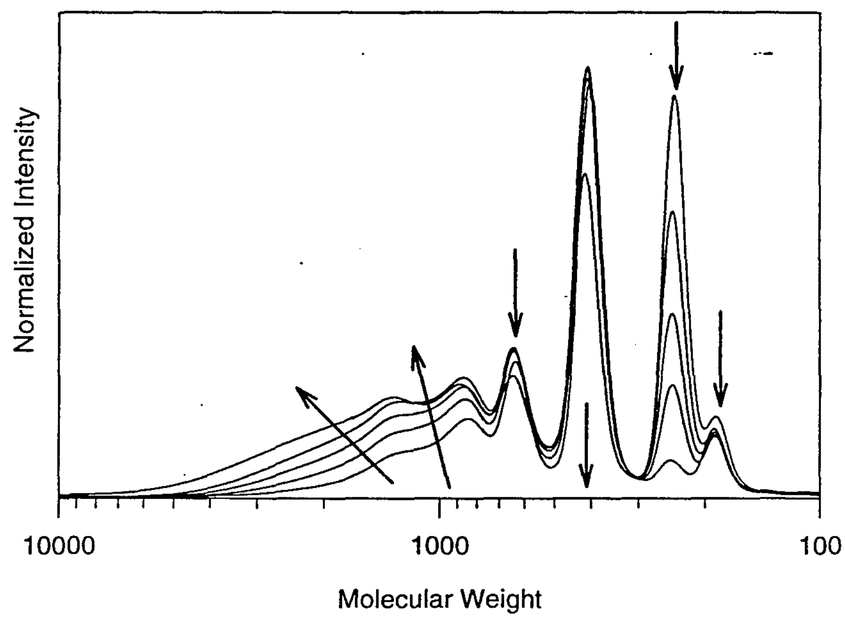

Figure 3. Molecular weight chromatogram curves for test IN12NC. Low and high MW peaks decrease and increase in intensity respectively with increasing test time.

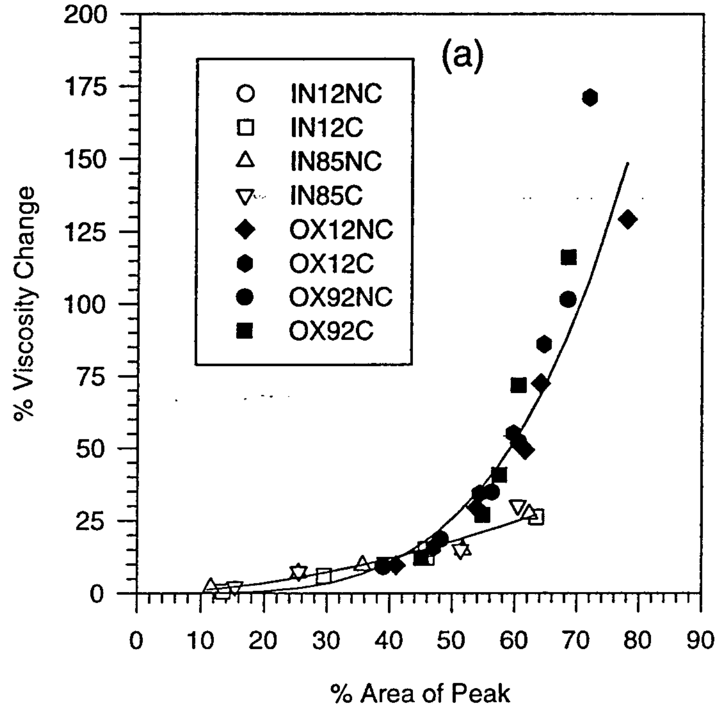

(a)
IN12NC
IN12C
IN85NC
IN85C
OX12NC
OX12C
OX92NC
OX92C
% Viscosity Change
% Area of Peak
0
25
50
75
100
125
150
175
200
0
10
20
30
40
50
60
70
80
90

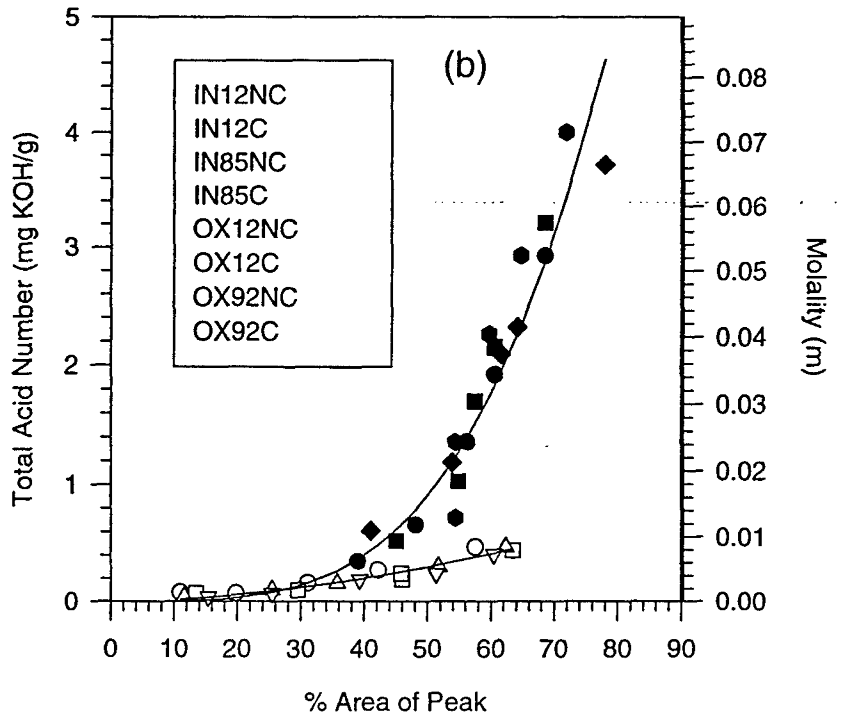

Figure 4. (a) Viscosity changes versus changes in percent area of the 1292 MW peak. Plotted lines correspond to oxidative environments ($y = 5.11 \cdot 10^{-6} \cdot x^{3.95}$) with r^2=0.82 and non-oxidative environments ($y = 0.019 \cdot x - 1.75$) with r^2=0.94. (b) Changes in total acid number versus changes in percent area for the 1292 MW peak. Plotted lines correspond to oxidative environments ($y = 5.43 \cdot 10^{-7} \cdot x^{3.66}$) with r^2=0.75 and non-oxidative environments ($y = 2.95 \cdot 10^{-4} \cdot x^{1.77}$) with r^2=0.92.

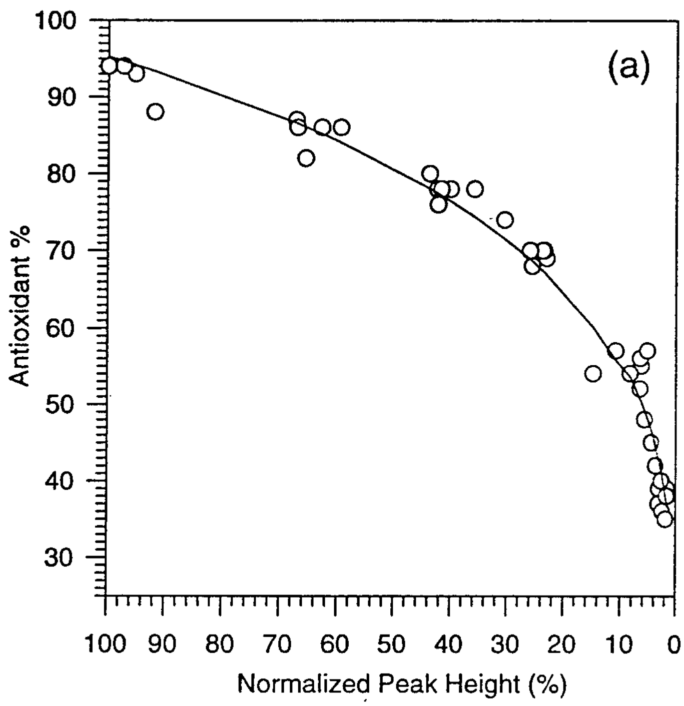

(a)
Antioxidant %
100
90
80
70
60
50
40
30
100 90 80 70 60 50 40 30 20 10 0
Normalized Peak Height (%)

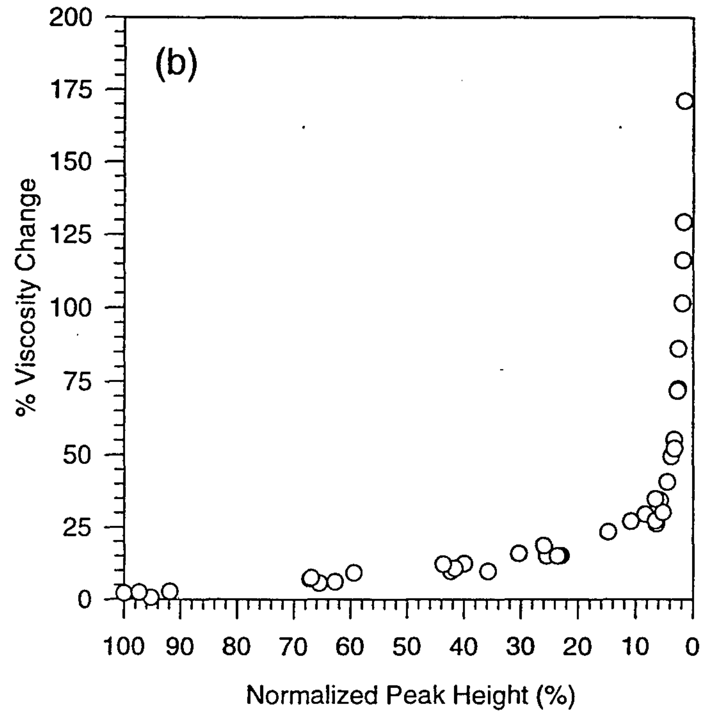

Figure 5. (a) Changes in antioxidant content versus normalized height for the 267 MW peak. Fitted line reflects $y = 33.04 \cdot x^{0.23}$ with r^2=0.98. (b) Changes in viscosity versus normalized height for the 267 MW peak. Results show viscosity to increase significantly after removal of the 267 MW antioxidant peak, corresponding with a 40-45% antioxidant context by RULLER measurements.

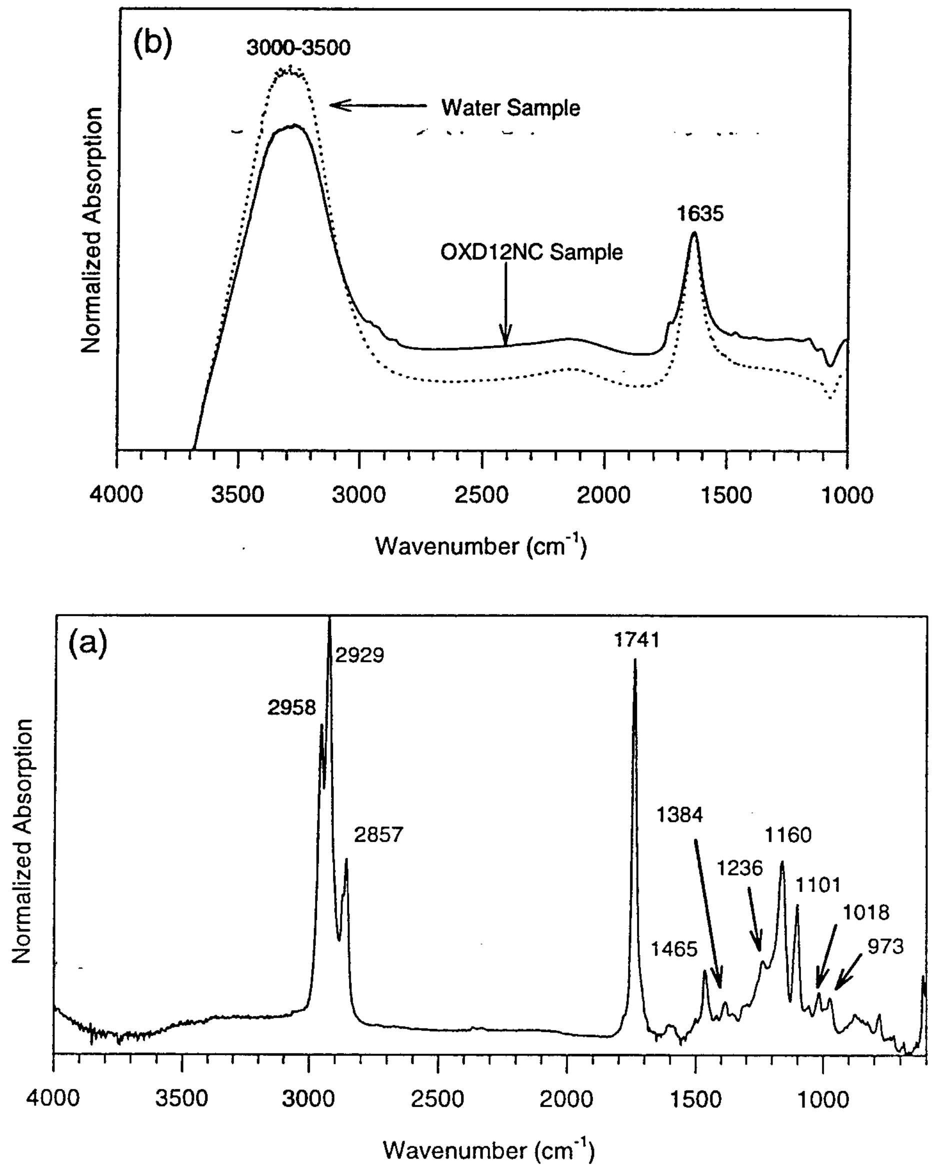

Figure 6. FTIR spectrums for volatile phases condensed from test OX12NC. Results show that the less dense phase (a) contains an ester, and the more dense phase (b) consists of a water solution.

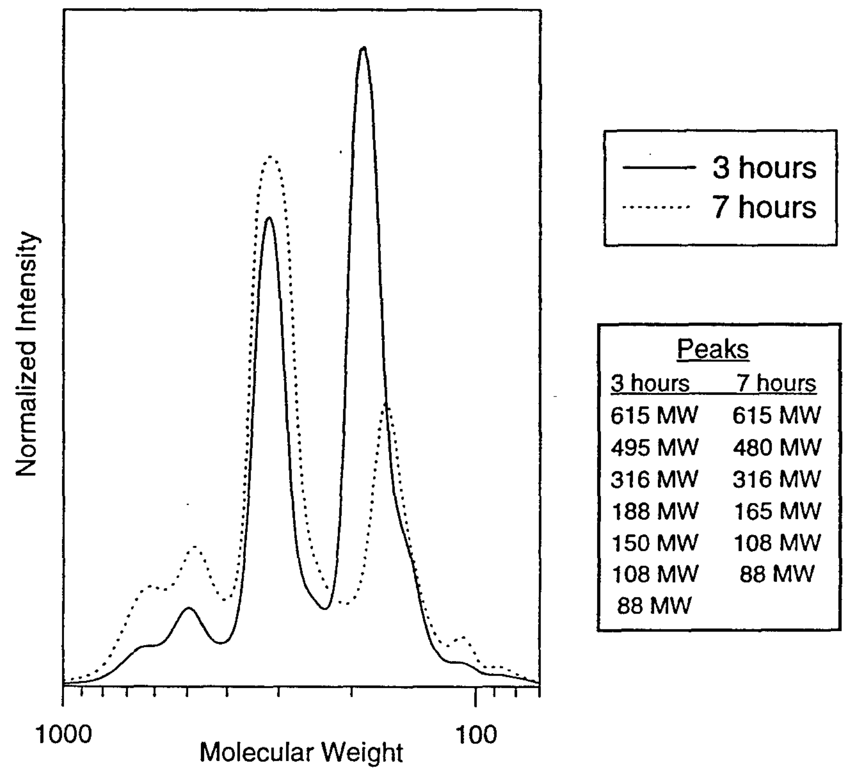

Figure 7. Molecular weight distibution for condensed volatiles from test OX12NC at 3 and 7 hour test times. Collection of 188 MW species suggests the volatilization of antioxidant.

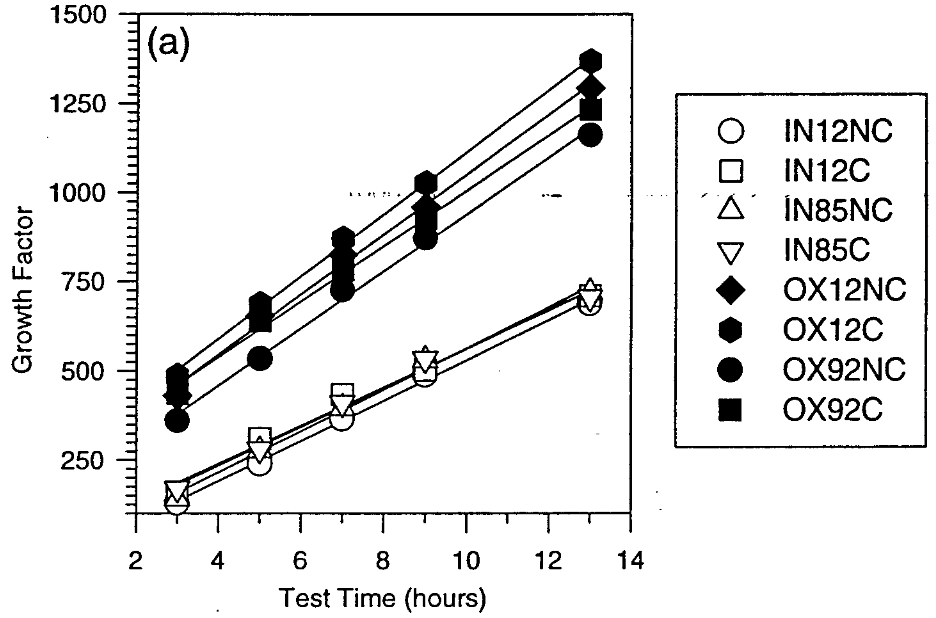

(a)
Growth Factor
1500
1250
1000
750
500
250
2
4
6
8
10
12
14
Test Time (hours)
IN12NC
IN12C
IN85NC
IN85C
OX12NC
OX12C
OX92NC
OX92C

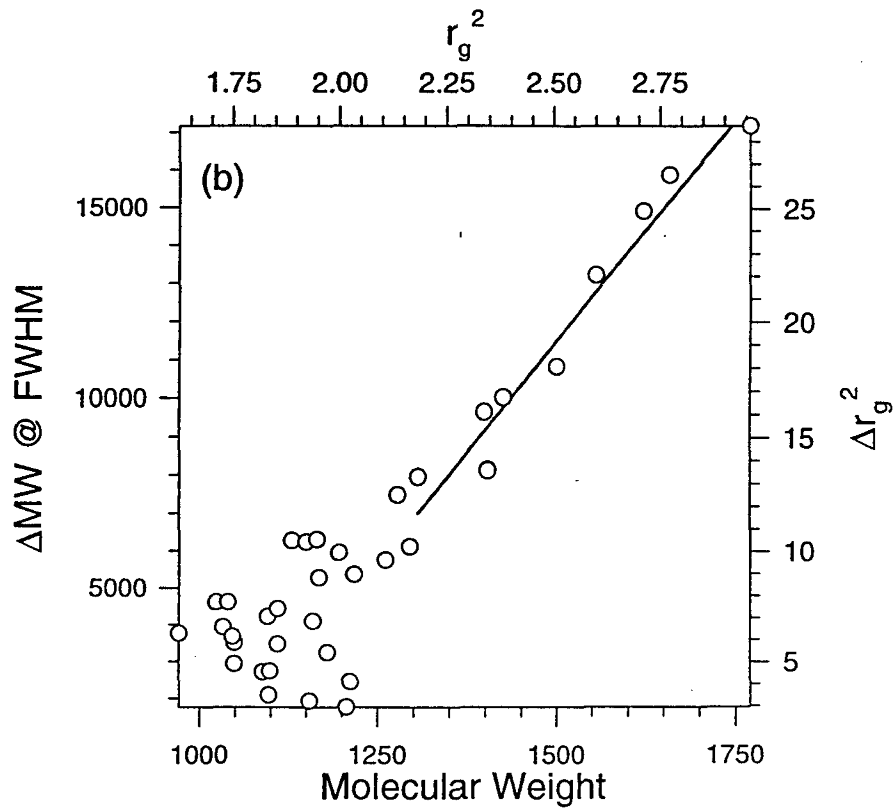

Figure 8. (a) Rate of growth for high molecular weight degradation species showing a linear relationship between the high MW degradation product and test time, thus representing a higher order kineatic reaction. (b) Changes in molecular weight distribution versus molecular weight and corresponding radius of gyration values for the high MW degradation product shows the reaction to be diffusion limited after antioxidant depletion.

APPENDIX 6, R. Sabia, J. Simmons, P.H. Holloway, Herb A.J. Chin, and J.H. Adair, "The Use of Optical Spectrometry to Monitor Degradation in a Synthetic Ester-Based Oil," submitted for publication.

THE USE OF UV/VIS SPECTROMETRY TO MONITOR SYNTHETIC ESTER-BASED LUBRICANT DEGRADATION

Robert Sabia,*[1] Kevin Powers,[1] Joseph H. Simmons,[1] Paul H. Holloway,[1]
Herbert A.J. Chin,[2] and James H. Adair*[1]
[1]University of Florida
Materials Science and Engineering
Gainesville, FL 32611
[2]Pratt & Whitney Aircraft
West Palm Beach, Fl 33410

*Member, Society of Tribologists and Lubrications Engineers

ABSTRACT

The optical adsorption of synthetic ester-based oil samples has been investigated as a technique to monitor the degradation of oil. Degraded oil samples were generated at 250°C under various environmental conditions. Samples were characterized using viscosity, total acid number, antioxidant content, molecular weight, and ultraviolet/visible absorbance spectrometry. This information was used to determine the relationship between absorption data and oil degradation, and to determine the feasibility of utilizing this technique as a means of oil monitoring. Results show that changes in optical adsorption peaks from the as-received oil track chemical changes associated with oil degradation. The behavior of the degraded oil adsorption peaks are shown to follow the Beer-Lambert law and thus reflect concentration of degradation product.

KEY WORDS

Optical, Degradation, Lubrication, Friction, Wear.

INTRODUCTION

An important goal in monitoring lubricant degradation is the development of an *in-situ* method in which component failure can be predicted and therefore avoided. Analysis of the synthetic ester-based oils used with bearing systems associated with advanced turbine jet engines is critical in attaining this goal for two reasons. First and foremost, many of the oil lubricants used for gas turbine engines offer variable performance characteristics due to variations in basestock chemistry. In concert with the variable performance conditions which lubrication systems encounter due to differences in factors such as seal integrity, the actual lubricant can dictate lifetime performance of the hybrid bearing system. Second, analysis of the oil systems offers a unique opportunity to allow for *in-situ* monitoring of the oil condition by means of sampling and analysis, or by real-time analysis during operation.

Oil Monitoring Techniques

In order to determine the condition of an engine's oil system at any given time, a select number of techniques are chosen. These test methods typically fall into two categories: the analysis of basic fluid parameters and off-line monitoring techniques.

Basic Fluid Parameters

As a first look at the extent of degradation in used oil samples, two basic techniques are used. To determine the extent to which degradation has affected the physical condition of the oil, viscosity testing is employed. To determine the extent to which the oil has chemically degraded, total acid number (ASTM 664-89) is used. Total acid number (TAN) is a technique in which a small amount of the oil sample is dissolved in solvents and titrated using 0.1N alcoholic KOH. The amount of KOH solution needed to titrate the oil sample to a specific pH represents the concentration of base neutralized acidic sites on the various oil constituents and degradation products.

Off-line Techniques

Over the past decade, a number of techniques have been developed to determine the condition of degraded oil samples. Through the investigations of Kauffman et al., one particular technique has earned recognition. This technique is referred to as the Remaining Useful Lubricant Life Evaluation Rig (RULLER) (1-3). A small sample of degraded oil is dissolved in a solvent and tested using a voltametric method to determine the antioxidant concentration in the oil sample. Taking into account the fact that the lubricant begins to degrade before the antioxidant content is completely depleted, the percent of antioxidant remaining is related to the remaining useful life of the used oil sample.

Ultraviolet/Visible Absorption Spectrometry

Ultraviolet and visible (UV/VIS) spectrometry is a commonly used technique for the identification of organic compounds (4-6). Absorbance of a particular molecule occurs when two criteria are met. The difference between two energy levels for a given macromolecule must be exactly equal to the energy associated with an incoming wavelength, and one energy level must contain an electron and the other a vacant electronic state, as seen in Eq. (1):

$$\Delta E = h \cdot v = E_1 - E_2 \qquad (1)$$

where h is Plank's constant (6.63×10^{-34} J·s), ν is frequency (s^{-1}), and E_1 and E_2 refer to the initial and final energies of the macromolecule, respectively. Measurements are typically made between 200 and 900 nm, with added information available at larger wavelengths in the near-infrared region (NIR).

Qualitative analysis with UV/VIS spectrometry can be difficult. The vast numbers of absorbing species for each wavelength make the task of identification difficult without knowledge of the exact structures present (4). Application of ultraviolet spectroscopy (at short wavelengths) is limited due to the large number of species which absorb in this region. Molecules must contain chromophoric groups in order to absorb, which include (poly)enes, molecules with aromatic rings, and molecules with carbonyl groups (5).

Once an absorption peak is related to the presence of a given species, quantitative analysis using UV/VIS spectrometry is possible using the Beer-Lambert law as seen in Eq. (2) (4-5).

$$A = \log_{10}(\frac{I_O}{I}) = \varepsilon \cdot c \cdot l \qquad (2)$$

A is the absorbance, I_0 is the intensity of the incident light (quanta/second), I is the intensity of the transmitted light (quanta/second), ε is the molar absorptivity or extinction coefficient ($liters \cdot mol^{-1} \cdot cm^{-1}$ or $m^3 \cdot kg^{-1} \cdot m^{-1}$), c is the concentration, and l is the optical path length. This equation yields a linear relationship between the concentration and absorptivity of a given species. While A in the Beer-Lambert equation represents the peak height at the absorbance maximum, a more accurate measure of concentration is obtained by replacing A with total integrated Intensity.

Objective

The absorption behavior of degraded oil samples in the ultraviolet and visible regions of the electromagnetic spectrum will be determined to evaluate this technique as a means for *in-situ* oil monitoring. Referred to as UV/VIS absorption spectrometry, this technique offers a unique opportunity in chemical analysis due to the fact that tests are quick and sensors can be manufactured to relatively small sizes. Results from preliminary work (7) yielded a linear relation between total loss edge values and changes in viscosity. This linear relationship held for oil samples degraded to various times at different temperature treatments (210-300°C), showing total loss edge values to be independent of temperature variations. As a result, degradation of oil samples for this study will be limited to environmental variables only.

MATERIALS AND METHODS

In order to determine the potential of using UV/VIS absorption spectrometry for oil monitoring, a series of oil degradation experiments was performed at 250°C under various environmental conditions. As shown in Table 1, a total of eight experiments were performed while varying atmosphere, humidity, and the presence of M-50 steel surfaces. For each test, 750 ml of as-received synthetic oil (MIL-L-23699) were placed in a Pyrex beaker on a hot plate. The hot plate was connected to a constant temperature controller. The thermocouple from the controller was covered with a glass capillary tube sealed at one end, then placed into the oil bath. Gas flow was supplied to the oil bath using a flow meter set to 0.83 L/min and a glass dispersion tube placed into the bath. Finally, the beaker was wrapped in fiberglass insulation to aid in temperature control. In this manner, the oil was completely isolated from metallic surfaces which might act as catalysts. The hot plate was set to the highest setting and the temperature controller was set to 250°C, resulting in a heating rate of approximately 225°C/hour.

In accordance with Table 1, gas flow supplied to each experiment was either compressed argon, resulting in a relatively inert (non-oxidative) atmosphere which would allow for thermal degradation with minimum oxidative degradation, or compressed air which would promote both thermal and oxidative degradation. Samples of M-50 steel were supplied as catalyst surfaces for the designated tests in the form of 1/4" diameter bearing balls placed in the oil bath at the beginning of each of the experiments. The resulting ratio of available surface area to oil was 3.6 mm^2/ml, which was kept constant for each of the appropriate tests. For tests performed under low humidities, water content for both compressed argon and air was determined with an on-line sensor (Implant Sciences Corporation, Wakefield, MA 01880) to be ≤12% RH. For the tests performed under high humidity, a liquid bubbler filled with distiller water was placed between the flow meter and the oil bath. The resulting relative humidities for the gas flow entering the bath were 85% for argon and 92% for air.

In order to analyze changes in oil condition with test time, 50 ml samples were taken during each experiment using a glass pipette. Sample times recorded from initial heatup were 3, 5, 7, 9, and 13 hours. Each sample was stored in a glass bottle with a Teflon lined lid to protect the oil samples from the environment and to prevent absorption of water, which might lead to further degradation.

In order to determine the effects of degradation on the physical behavior of the oil samples, viscosity tests were performed using a variable speed rheometer (Brookfield RVDV III, Brookfield Engineering Laboratories, Inc., Stoughton, MA 02072) with a 0.8°

cone angle. Experiments were performed at 40±0.1°C using a constant temperature water bath, thereby producing results comparable with military specifications.

The extent to which oil degradation had occurred for each sample was determined using a number of analytical techniques. Antioxidant concentration for each sample was determined using a Remaining Useful Lubricant Life Evaluation Rig (RULLER) (1-3) and the extent to which degradation had occurred was determined from the total acid number (TAN) (8). For TAN determination, there were two modifications to the ASTM procedure, the use of aqueous based buffers and titration to pH 11. These techniques are used in combination to predict when an oil is likely to degrade and the extent to which degradation has occurred.

In order to observe the formation of high molecular weight degradation products, size exclusion chromatography, also known as gel-permeation chromatography (GPC), was performed using an ultraviolet/visible (UV/VIS) wavelength detector (Waters™ Chromatography Division, Millipore Corporation, Milford, MA 01757). A pre-filter and 50-1K, 5K-10K, 20K-300K and 100K-1000K molecular weight range columns (Phenogel, Phenomenex, Torrence, CA 90501) were used to determine the molecular weight distribution of each sample, with tetrahydrofuran as the solvent carrier. The columns were calibrated between 92 and 870,000 MW using polystyrene molecular weight standards and toluene. Approximately 20-30 mg of each sample was mixed with 10 ml of tetrahydrofuran and filtered three times through a 0.22 μm Teflon filter before injection. The flow rate was set to 0.4 ml/min, and the injection volume was 20 μl. UV/VIS data for the oil samples was processed at a constant wavelength of 216 nm. Data were calibrated against the polystyrene standards to generate molecular weight distributions from the measured elution times. In order to accurately compare results from each run, all data was corrected by normalizing the areas under each data curve. Evaluation of changes in peak intensity and location of the high molecular weight degradation products was performed using peak separation and analysis software (Peakfit™ V 4.0, Jandel Scientific Software, San Rafael, CA 94901) assuming Gaussian distributions.

Further tests were performed on these oil samples using UV/VIS spectrometry. Using a portable UV/VIS spectrometer (Ultrospec III, Pharmacia LKB Biochrom LTD, Cambridge, England), oil samples were placed in a constant path length cell and analyzed for transmittance with ±0.1% accuracy covering the ultraviolet and visible regions of the electromagnetic spectrum between 200 and 900 nm. In order to determine the total loss edge for each sample, the tangent of each spectra was generated and the intercept of the tangent to the x-axis was determined. Further analysis was performed in the near infrared spectrum by measuring absorbance characteristics of the oil samples using a high performance UV/VIS/NIR spectrometer (Lambda 9 UV/VIS/NIR Spectrometer, Perkin-Elmer Corporation, Norwalk, CT 06856) with ±0.1% accuracy between 350 and 2000 nm (2 μm). In order to analyze the absorption behavior of the degrading oil and to determine if the Beer-Lambert law was followed for the absorption behavior of concentrated samples, the 13 hour sample from test OX12NC was diluted in as-received oil and appropriately analyzed.

RESULTS AND DISCUSSION

Oil samples used in this study were generated by degrading a conventional synthetic turbine oil (MIL-L-23699) under various environmental conditions as shown in Table 1 and previously reported by Sabia et al. (9) Characterization was performed using rheological measurements at 40°C, total acid number, antioxidant content using RULLER measurements, and molecular weight analysis using a UV/VIS detector at 216 nm. The absorption characteristics of the oil samples was determined using UV/VIS/NIR spectrometry.

Sample Characterization

Results from viscosity measurements performed at 40°C showed all oil samples to yield Newtonian behavior without Bingham yield points. Oil viscosity (23.3 cP for the as-received sample) increased with increasing test time for each series of experiments, with more dramatic increases in viscosity changes for those experiments performed in oxidative environments (>100% maximum change) compared to non-oxidative environments (25-30% maximum change). The presence of the M-50 steel catalyst caused more extreme changes in viscosity and the effect of high humidity produced less extreme changes in viscosity, particularly for those samples tested in oxidative environments. (9)

Results for total acid number and antioxidant content changes as a function of test time and environment showed changes similar to those for viscosity. As test time proceeded, the extent to which degradation had occurred increased, as indicated by increasing TAN values. The potential for continued degradation also increased, as indicated by decreasing antioxidant content. Variations in the rate of changes in TAN and antioxidant content with respect to catalyst and humidity were consistent with those for viscosity changes. (9) Maximum changes for the 13 hour test samples yielded TAN and antioxidant values of 0.45 and 55% respectively for non-oxidative environments, and 4.0 and <40% respectively for oxidative test environments.

Molecular weight analysis performed on the oil samples showed the formation of a high molecular weight species above 1300 MW. With increasing test time, peak area determined by Gaussian curve fitting increased while maintaining the same mean molecular weight. Upon depletion of the antioxidant, peak analysis showed continual growth in peak area to be accompanied by an increasing shift in mean molecular weight. In order to incorporate changes in both peak area and mean molecular weight of the degradation product, a growth factor has been generated:

$$\text{Growth Factor} = \text{Mean Molecular Weight} \times \text{Peak Area Fraction} \tag{3}$$

Total Loss Edge Analysis

In order to determine if the oil samples in this report exhibit the same linear relationship between total loss edge values and changes in viscosity as discussed for the preliminary work (7), transmittance measurements were performed between 200 and 900 nm. As shown in Figure 1 for samples from tests IN12NC, the transmittance behavior of the oil samples decreased and the loss edge increased to higher wavelengths as test time proceeded. Values for total loss edge were determined by extending the tangent for each spectra to the zero percent transmittance intercept. Total loss edge (TLE) values for all eight test series are plotted versus corresponding changes in viscosity in Figure 2. For the samples generated in non-oxidative environments, a linear relationship between the TLE values and viscosity changes is shown with a slope of 8.11. For samples generated in oxidative environments, the initial increase in TLE values with increasing viscosity follows the same linear relationship as for samples tested in non-oxidative environments (m=8.11) until approximately 675 nm and 25% viscosity change, above which the viscosity begins to increase at a greater rate following the curve $y = 482.91 \cdot x^{0.10}$ (with correlation coefficient, r^2=0.96). For the as-received sample, a TLE value of 390 nm shows that the pristine oil does not correlate with the linear relation observed during the initial stages of degradation.

Deviations for experiments performed in oxidative environments from the linear relationship found for the non-oxidative environments can be explained by observing the chemical changes in the oil samples shown by total acid number (TAN) and antioxidant concentration changes. Figure 3(a) shows TAN values plotted against changes in antioxidant content for all test series. As degradation proceeded, antioxidant content fell below 40% and leveled off. Since TAN values are not considered significant until above 1.0, Figure 3(a) shows that extensive oil degradation initiated when the antioxidant content fell below approximately 60%. Knowing the antioxidant concentration level at which significant degradation began (i.e. at the onset of antioxidant depletion), the plot of antioxidant content versus viscosity change (Figure 3(b)) can now be used to determine the corresponding viscosity change. A 60% antioxidant content corresponds to a 25% change in viscosity, the same value at which total loss edge began to deviate in Figure 2. Once the antioxidant level fell below approximately 60%, significant chemical changes occurred in the oil until approximately 40% antioxidant, at which point the chemical changes were accompanied by significant physical changes as indicated by the viscosity results. This region between 60-40% antioxidant content and 25-50% viscosity change is considered to be the region in which changes in antioxidant content with lubricant degradation become critical. Thus, comparing these results with Figure 2, the TLE values accurately correspond to the physical changes in the oil samples until the antioxidant level reaches the critical concentration.

Absorption Behavior of the Degraded Oil Samples

In order to understand the correlation between total loss edge values and physical degradation effects reflected by viscosity changes, the absorption behavior of the oil samples generated for this study must be determined. This was accomplished using a high performance ultraviolet/visible spectrometer which was capable of detecting absorption characteristics in the near infrared spectra region. Samples were tested to higher wavelengths within the infrared region in order to discern between absorption and scattering effects in the oil. The absorption behavior shifted in the same manner as the transmittance results shown in Figure 1: As degradation proceeded, both absorbance and loss edge shift to higher wavelengths.

In order to determine if optical spectra changes for the oil samples were the result of absorption rather than scattering, portions of the 13 hour sample from test OX12NC were diluted in as-received oil to concentrations shown in Table 2. These solutions were mixed and then tested using the high performance UV/VIS/NIR spectrometer. The results are shown in Figure 4(a). The absorbance of the solutions increased and loss edge shifted to higher wavelengths with increasing concentration, as indicated by the arrow.

The changes in absorption behavior have been attributed to the presence of three absorption peaks, located at 355, 415 and 500 nm and referred to as peaks 1 though 3 respectively. Peaks were fitted for Gaussian shapes as shown in Figure 4(b). Peak 1 is initially highly absorbing and decreases in intensity as concentration of the degraded oil increases. Peaks 2 and 3 initially are not strongly absorbing, but increase in absorbance with increasing concentration of the degraded oil. In Figure 4(b), the most absorbing peak for the indicated concentration is identified. For dilutions of 2.09% and below, peak 1 at 355 nm is dominant and thus dictates the location of the total loss edge (extrapolated to an absorption value of 5 corresponding to 0 transmittance). For concentrations of 9.45% and above, peak 2 is most absorbing and dictates the location of the loss edge. These results show that the absorbance spectra (and associated total loss edge values) will reflect the extent of oil degradation, but only after a certain amount of degradation has occurred and a large enough concentration of degradation species exist. Evident from these results is the explanation as to why the as-received oil sample does not correspond with the linear relationship observed during the initial stages of degradation between TLE values and viscosity changes: The initial TLE value for the as-received sample reflects the absorption behavior of the base ester and does not reflect degradation until the absorbance of peaks 1 and 2 decrease and increase respectively to the point in which peak 2 predominates.

Absorption Behavior and Degradation Product Concentration

Results of changes in the absorption behavior of the degraded oil sample diluted in as-received oil (shown in Figure 4) suggests that absorption characteristics are directly related to the concentration of the degradation products. In order to test this hypothesis, the Beer-Lambert law (Eq. (2)) for this oil system was evaluated. Changes in peak area as a function of concentration were calculated from fitted Gaussian distributions and used for absorbance values (listed in Table 2). Figure 5 shows changes in absorbance peak area as a function of concentration for peaks 2 and 3. Both peaks yield linear results, and thus confirm to the Beer-Lambert law.

Results shown in Figure 5 yielded slopes for both peaks which are approximately equal (m= 4.1 and 4.2 for peaks 2 and 3 respectively), suggesting the possibility that both peaks are due to the same degradation product. In order to determine if the absorbing species are the high molecular weight products observed in gel permeation chromatography (GPC) analysis, the absorbance characteristics for test samples from all eight degradation experiments must be determined. Figure 6(a) shows the absorption characteristic for peak 2 area ($y = 0.86 \cdot x^{1.34}$) and peak 3 ($y = 0.14 \cdot x^{1.68}$) plotted versus changes in peak area for the high molecular weight degradation product. Both absorption peaks follow the same general trend until approximately 45% peak area, at which the absorbance values for peak 3 undergo positive deviation with respect to peak 2. To understand the significance of this change in absorbance behavior, Figure 6(b) shows the changes in peak area for the high molecular weight species versus changes in viscosity for the oil samples. At values of approximately 45%, peak 3 area for experiments performed in oxidative environments deviate from the initially linear relationship between peak 2 area and viscosity change. This deviation signifies the onset of physical changes which result from extreme oil degradation. Relating this data to the results for absorbance changes in Figure 6(a) show that deviations for both plots occur at 45%, thus signifying that the absorbance characteristics for peak 2 and 3 do not reflect the same behavior.

Degradation Product Concentration Versus Particle Volume

From the absorbance information generated for the oil samples, relative concentration of the absorbing species can be determined by normalizing the absorbance area for a given peak with respect to the most degraded test sample. Although this normalization method does not allow for determination of the extinction coefficient associated with the absorbing species, the method does allow for a general description of the extent to which the quantity of degradation product affects the overall absorbance properties of the test samples. Further comparisons can be made with the physical changes associated with oil degradation by treating the high molecular weight degradation product as particulates. Since all viscosity measurements reflected Newtonian behavior, the Einstein equation, Eq. (4), for particle content can be investigated as a plausible cause for both optical and viscoelastic behaviors (10-11).

$$\eta^* = \eta_o \cdot \left(1 + \frac{5}{2} \cdot \phi\right) \tag{4}$$

The η^* refers to the experimental viscosity, η_o refers to the as-received viscosity, and ϕ refers to the percent particle volume of the system. Assuming that viscosity changes in the oil samples are the result of high molecular weight degradation products acting as particulate species, the estimated particle content determined using Eq. (4) may be compared with absorbance data. Figure 7 shows the relationship between particle volume as calculated using Eq. (4) and the relative concentration of the degradation species determined for absorbance peaks 2 (a) and 3 (b). Particle volume calculations yielded maximum values of 0.69%. Concentrations associated with the absorption peaks show linear relationships, with slope and correlation coefficients of m=1.34 and r^2=0.93 for peak 2 and m=1.55 and r^2=0.92 for peak 3. The differences in slopes may in fact signify that the two absorbance peaks do not reflect the same behavior. Furthermore, the linear relationships shown in Figure 7 support the hypothesis that the high molecular weight degradation products behave as particulate species to increase viscosity in the degraded oil.

Association of Absorbance Peaks

Identification of the absorbing species reflected by peaks 1 through 3 has not been accomplished. Possible degradation products for synthetic oil systems and the lack of absorption information on each product makes identification impossible at this time. However, knowing that absorption peaks 1 and 2 are in the ultraviolet spectra, that only compounds with chromophoric groups (e.g., poly(enes) and species with carbonyl and aromatic rings) absorb in this region, and that ester compounds are the primary constituent (>90%) in the as-received oil allows for a general association of the probable absorbing species. Since peak 1 decreases and peak 2 increases, peak 1 can be attributed to the original base esters, which decrease in concentration during reaction to form degradation products, and peak 2 can be attributed to the high molecular weight degradation product which contains carbonyl groups.

Comparison of Peak Area and Total Loss Edge Analysis

This work has shown that using total loss edge (TLE) values to predict the physical changes associate with oil degradation is plausible, and that the TLE values actually reflect the absorbance behavior of peaks associated with the base ester and degradation products. Although analysis of the absorption peaks has also been shown to be an accurate method for observing oil condition, information from both absorption peaks area and TLE values will now be compared to determine which technique is more representative of the state of degradation in the oil.

Since the absorbance behavior of peaks 2 and 3 have been shown in Figure 5 to conform to the Beer-Lambert law, the area under each absorbance curve can be related to the concentration of degradation product. The rate of product generation follows a high order kinetic reaction (9). To confirm the same behavior for the absorptivity of peaks 2 and 3, Figure 8 shows a linear relationship between absorbance and test time. Values for correlation coefficients and slopes are shown in Table 3. Comparison of this data with the results for growth factor analysis shows lower correlation coefficients for the absorption peaks, an indication of less accurate measurements which is attributed to human error involved in absorbance peak fitting. Further comparison of slope values shown in Table 3 yield linear correlation coefficients ≥0.92, confirming that the absorbance peak information accurately reflects the concentration of high molecular weight degradation products.

In order to compare the total loss edge (TLE) technique with absorbance peak results, changes in TLE values are plotted versus test time for all eight test series in Figure 9. Results for absorbance peak analysis (Figure 8) show that both peaks 2 and 3 reflect linear growth versus test time, whereas TLE values shown in Figure 9 do not hold a linear relationship. This comparison shows that the TLE values do not accurately represent the absorption data and therefore is not indicative of changes in degradation product concentration. Furthermore, initially high rates of TLE change with test time are attributed to the fact that the TLE values initially reflect base ester absorbance properties and do not reflect degradation until the concentration of degradation species is significant.

Direct comparison of total loss edge values with results for the two absorbance peaks is shown in Figure 10. Data follows the relations $y = 190.59 \cdot x^{0.16}$ for peak 2 and $y = 273.68 \cdot x^{0.14}$ for peak 3. Values of absorbance peaks increase at higher rates with increasing degradation in comparison to TLE values. This shows that the sensitivity of the TLE technique in measuring extent of degradation is lost as more severe degradation occurs. Also evident is the fact that changes in absorbance values for peak 2, although proportional to peak 3 (Figure 5), are greater with respect to peak 3 and therefore more sensitive to small changes in degradation behavior.

CONCLUSIONS

This paper has presented data supporting the use of absorbance characteristics of synthetic ester-based oil samples to determine degradation behavior and oil condition. Two techniques have been investigated: the use of absorbance changes characteristic of the base esters and degradation products, and the use of total loss edge (TLE) values determined by the changes in absorbance peak intensities. The investigations were centered on oil samples generated at 250°C under various environments.

The changes in absorbance spectra for the oil samples were shown to be the result of changes in the behavior of three absorption peaks located at 355, 415, and 500 nm. Total loss edge values determined for the oil samples are a direct reflection of the absorbance peak which predominates for a given sample. As degradation proceeded, the 355 nm peak decreased in intensity and is thus attributed to the base esters. The absorbance of the 415 and 500 nm peaks increased with increasing degradation, and these peaks are attributed to the degradation products. As degradation proceeds, TLE values are dominated by the 355 nm peak and thus represent the base esters until the absorptivity of the degradation products predominate, at which point the TLE values are dominated by the 415 and 500 nm peaks and increase at a roughly linear rate with time. However, comparison of TLE values with absorbance changes for these three peaks has shown that changes in peak area are more representative and sensitive to changes in degradation behavior.

Further relations have been shown between the formation of the high molecular weight degradation products and changes in the absorption characteristics of peaks at 415 and 500 nm. The 415 nm peak has been attributed to an absorbance characteristic of the degradation product which reflects concentration, whereas the 500 nm peak has been attributed to an absorbance characteristic which represents product concentration and size. By relating the formation of the high molecular weight products to the formation of particulate species using the Einstein relationship for viscosity given in Eq. (4), results have shown that the relative concentration of degradation products correlated with the formation of particulate species.

In reference to using these techniques for monitoring oil condition and the extent to which degradation has proceeded, values for both the 415 and 500 nm absorbance peaks have been shown to correlate with concentration for the high molecular weight degradation product. Information gained from absorbance results can be used to relate concentration and estimate mean molecular weight for the degradation products based on UV-visible spectrometry.

ACKNOWLEDGMENTS

The authors gratefully acknowledge the support of the Air Force Office of Scientific Research Grant Number F49620-93-12-0349DEF. Thanks are also given to Michael Zamorra, Dr. Jim Kunetz and Ahmad R. Hadba of the University of Florida Department of Materials Science and Engineering for their assistance with the characterization. The authors would also like to thank Pratt & Whitney for laboratory and equipment use in the West Palm Beach location.

REFERENCES

(1) Kauffman, R.E., "Developement of a Remaining Useful Life of a Lubricant Evaluation Technique. Part III: Cyclic Voltammetric Methods," Lubrication Engineering, 45, 11, 709-716, 1995.

(2) Kauffman, R.E., "On-Line and Off-Line Techniques for Monitoring the Thermal and Oxidative Degradations of Aircraft Turbine Engine Oils - Part I: Laboratory Evaluations," Lubrication Engineering, 51, 11, 914-921, 1995.

(3) Kauffman, R.E., "Remaining Useful Life Measurements of Deisel Engine Oils, Automotive Engine Oils, Hydraulic Fluids, and Greases Using Cyclic Voltammetric Methods," Lubrication Engineering, 51, 3, 223-229, 1995.

(4) "Materials Characterization," Metals Handbook Ninth Edition, 10, American Society for Metals, 1986.

(5) Rabek, J.F., "Experimental Methods in Polymer Chemistry, " John Wiley & Sons, New York, 1980.

(6) Silverson, R.M., Bassler, G.C., and Morrill, T.C., "Spectrometric Identification of Organic Compounds," John Wiley & Sons, 1991.

(7) Sabia, R., Mitchell, D., Chin, A.J., and Adair, J.H., "Effects of Oil Degradation on the Friction and Wear Properties of Silicon Nitride/M-50 Steel Sliding Couples," *Submitted to the Society for Tribologists and Lubrication Engineers.*

(8) ASTM Designation F664-89, Americal Society for Testing Materials, Swarthware, PA, pp. 218-224.

(9) Sabia, R., Chin, A.J., and Adair, J.H., "A Kinetic Study on the Degradation Behavior and Mechanisms of a Synthetic Ester-Based Lubricant," *Submitted to the Society for Tribologists and Lubrication Engineers.*

(10) Einstein, A., "Investigations on the Theory of the Brownian Movement, " Dover Publications, Inc., USA, 1956.

(11) Hunter, R.J., "Foundations of Colloid Science Volume I," Oxford University Press Inc., New York, 1993.

Table 1. List of degradation experiments used for UV/VIS spectrometry testing.

Test ID	Temperature	Atmosphere	Humidity	Catalyst
IN12NC	250°C	inert (Ar)	<12 %	None
IN12C	250°C	inert (Ar)	<12 %	M-50
IN85NC	250°C	inert (Ar)	~85 %	None
IN85C	250°C	inert (Ar)	~85 %	M-50
OX12NC	250°C	oxidative (Air)	<12 %	None
OX12C	250°C	oxidative (Air)	<12 %	M-50
OX92NC	250°C	oxidative (Air)	~92 %	None
OX92C	250°C	oxidative (Air)	~92 %	M-50

Table 2. List of concentrations (weight percent) and normalized absorbance peak areas (given in percent change) for OX12NC 13 hour test sample diluted in as-received oil.

Concentration (weight %)	Area Peak 1 (355 nm)	Area Peak 2 (415 nm)	Area Peak 3 (500 nm)
0.36%	-28%	86%	200%
0.54%	-32%	136%	220%
0.66%	-40%	157%	300%
0.85%	-44%	176%	520%
2.09%	-50%	597%	900%
4.95%	NA	1610%	2650%
9.45%	NA	3189%	4100%
29.12%	NA	7400%	6900%
50.00%	NA	13,058%	14,900%
75.00%	NA	19,637%	19,900%
100.00%	NA	23,584%	21,900%

Table 3. List of correlation coefficients and slopes for linear regression analysis performed on absorbance versus time plots shown in Figure 11.

Test ID	Peak 2: r^2	Peak 2: Slope	Peak 3: r^2	Peak 3: Slope
IN12NC	0.998	265.2	0.980	68.1
IN12C	0.998	245.9	0.951	67.7
IN85NC	0.982	286.2	0.931	82.2
IN85C	0.991	298.6	0.970	77.7
OX12NC	0.975	571.0	0.957	186.5
OX12C	0.960	779.0	0.949	184.2
OX92NC	0.990	602.1	0.970	152.0
OX92C	0.987	669.3	0.952	192.6

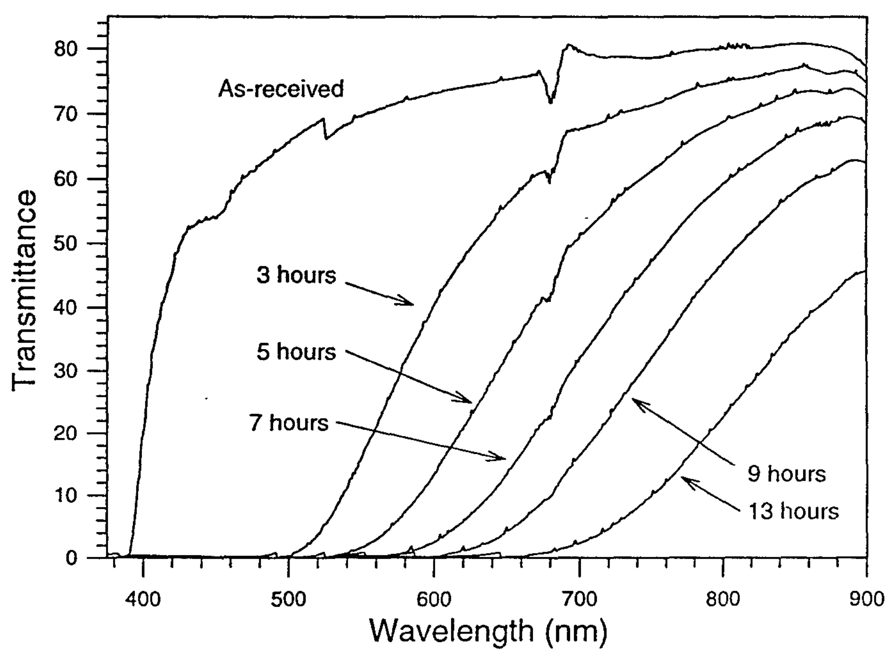

Figure 1. UV/VIS spectra for tests IN12NC, plotted as transmittance versus Wavelength. Results show a decrease in transmittance and a shift of the total loss edge to high wavelengths with decreasing oil condition.

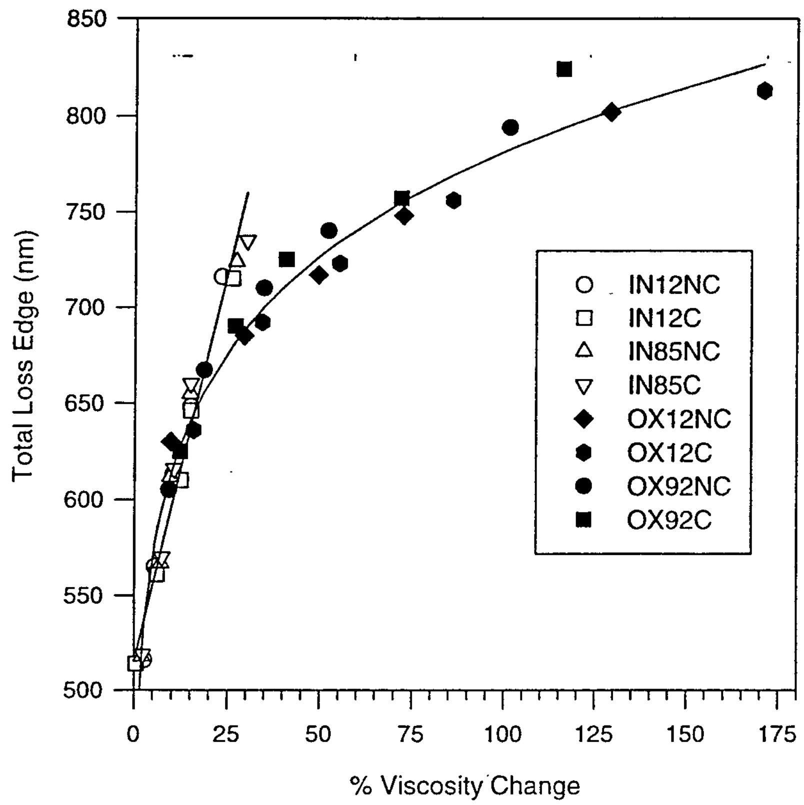

Figure 2. Total loss edge versus changes in viscosity. Lines reflect oxidative ($y = 482.91 \cdot x^{0.10}$) and non-oxidative environments ($y = 8.11 \cdot x + 515.13$) with correlation coefficients of r^2=0.96. Results show deviations in total loss edge behavior for samples tested in oxidative and inert atmospheres.

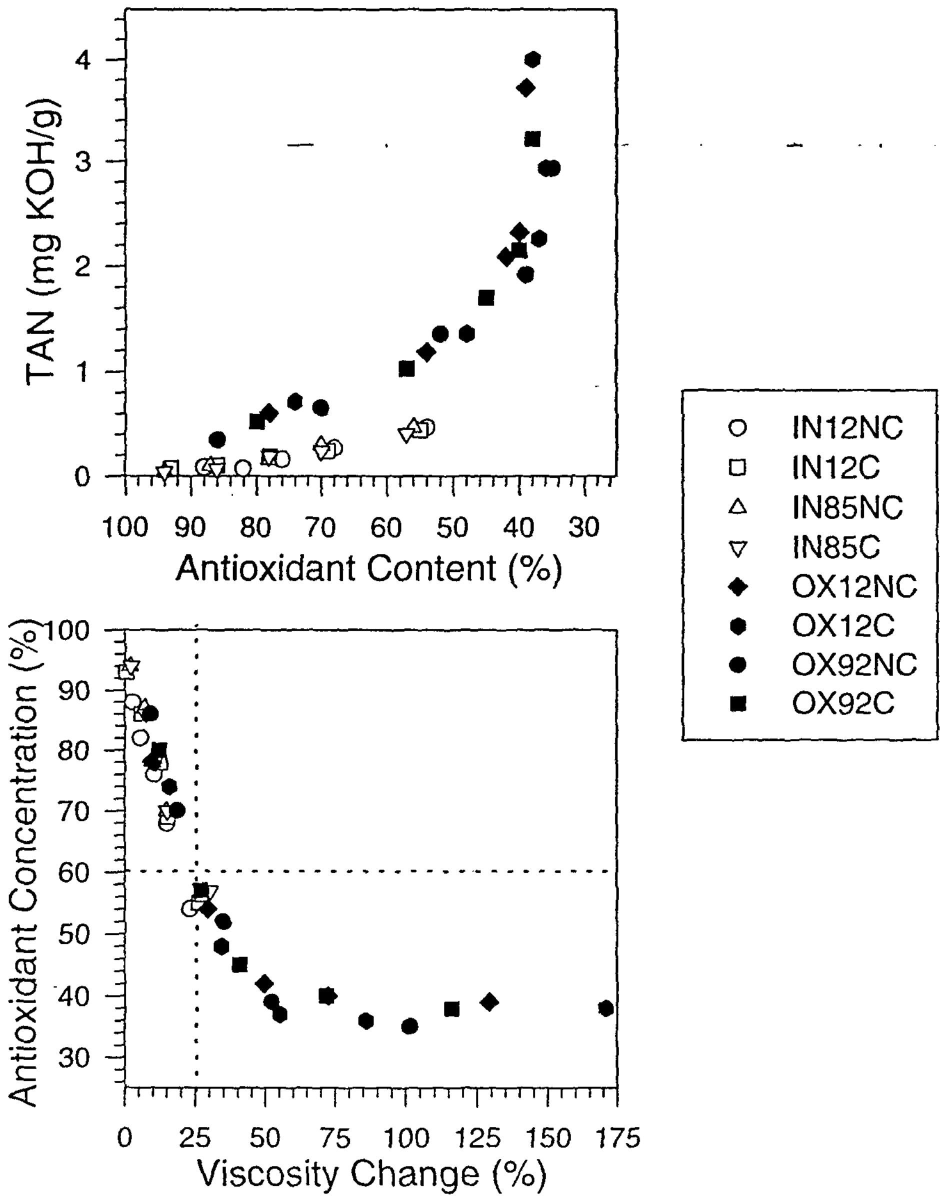

Figure 3. Total acid number results versus antioxidant content (a) and antioxidant content versus viscosity changes (b). Dotted lines indicate onset of chemical degradation in the oil samples.

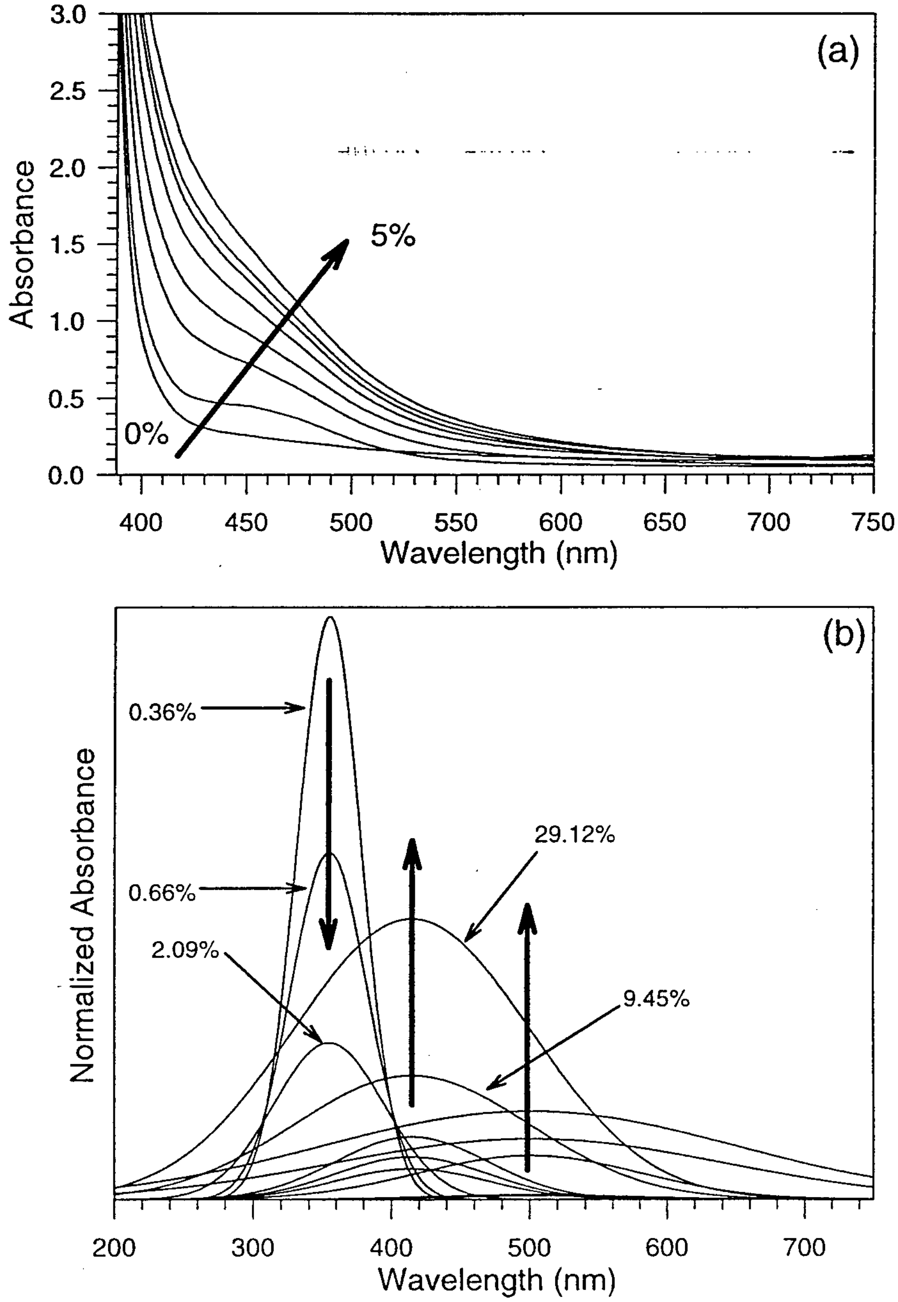

Figure 4. Changes in the absorbance spectra for the OX12NC, 13 hour sample diluted in as-received oil as a function of concentration (a), and changes in intensities for 355, 415, and 500 nm peaks with changes in concentration (b). The optical changes in oil samples are shown to be the result of changes in the three absorption peaks.

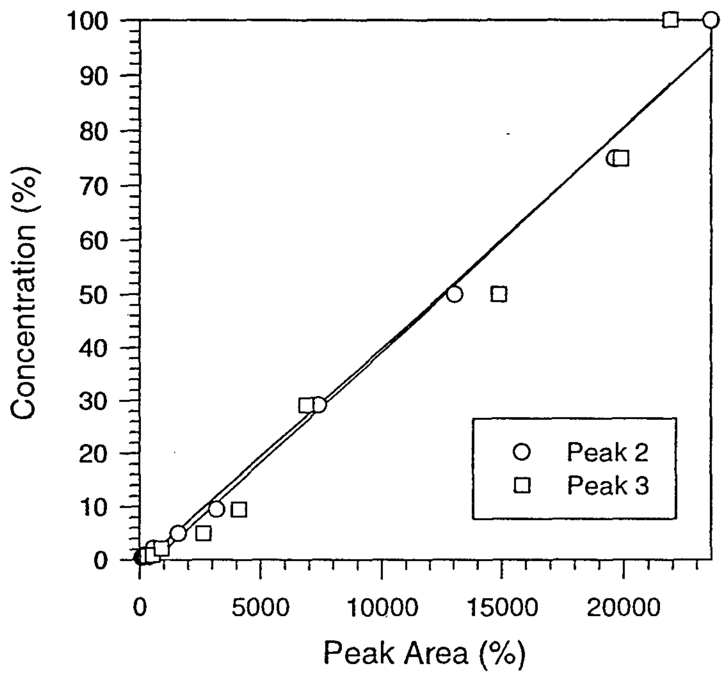

Figure 5. Absorbance values for peaks 2 and 3 for the OX12NC, 13 hour test sample diluted in as-received oil to concentrations listed in Table 5-2. Linear regression coefficients and slopes for peaks 2 and 3 are r^2=0.99, m=4.07 and r^2=0.98, m=4.16 respectively. Results show that absorption behavior of peaks 2 and 3 follow the Beer-Lambert law for concentration of high MW degradation products.

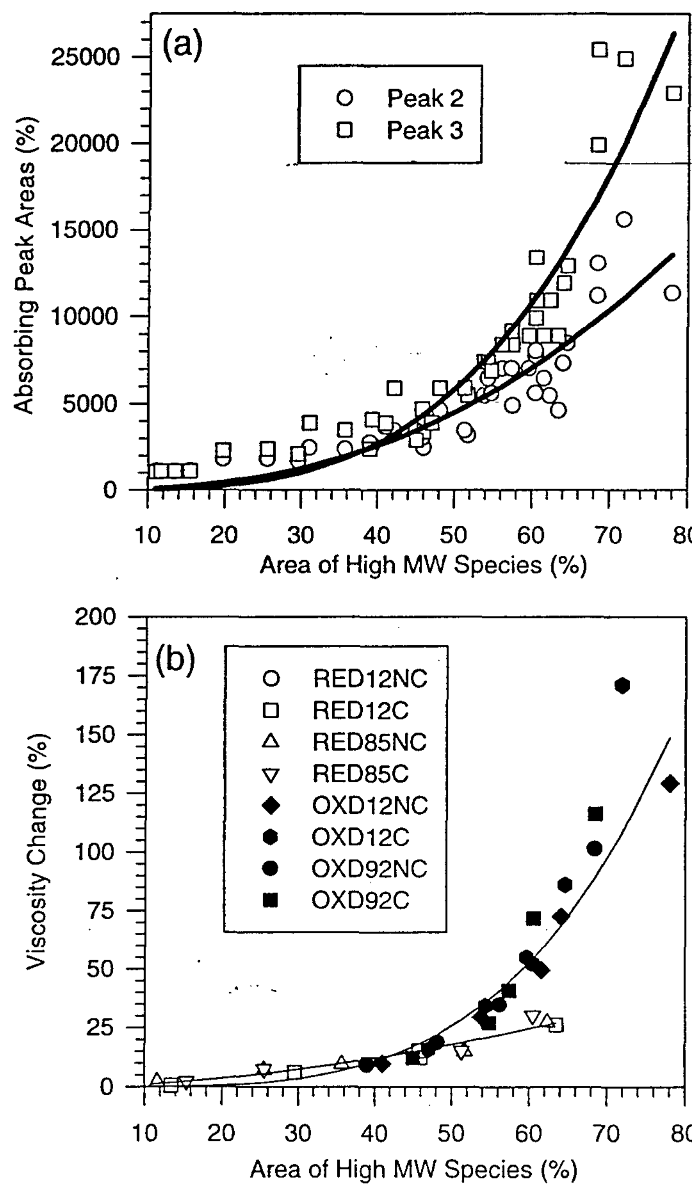

Figure 6. Changes in absorbance (a) for peak 2 ($y = 0.86 \cdot x^{1.34}$) area and peak 3 ($y = 0.14 \cdot x^{1.68}$) area with correlation coefficients of r^2=0.93 and 0.95 respectively , and changes in viscosity (b) versus changes in area of the high molecular weight species, with coefficients of r^2=0.82 and 0.93 for the oxidative and inert environments respectively. Results show that absorption peaks 2 and 3 represent different behavior for the high MW degradation products.

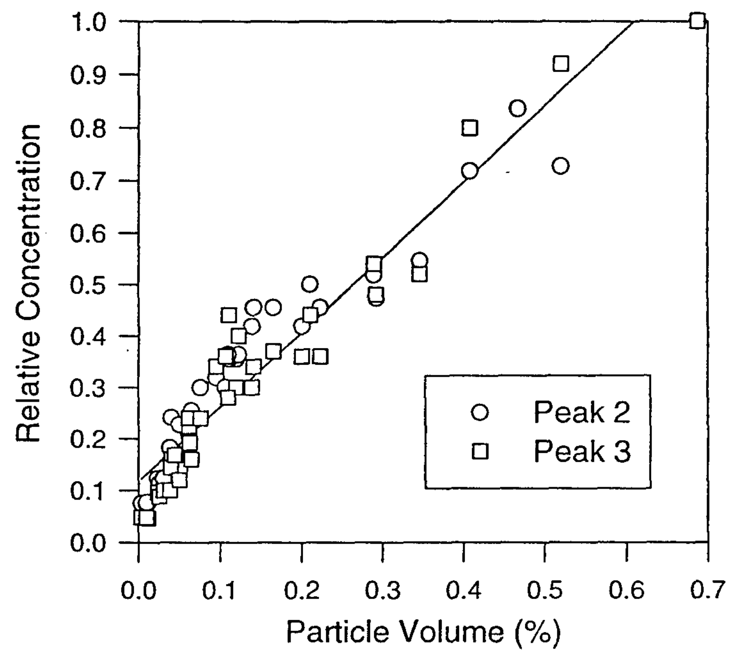

Figure 7. Relative concentration of high molecular weight species versus particle volume for absorbance peak 2 where r^2=0.93 and m=1.34, and for peak 3 where r^2=0.92 and m=1.55. The linear relationships show that the high MW degradation products act as particulate species.

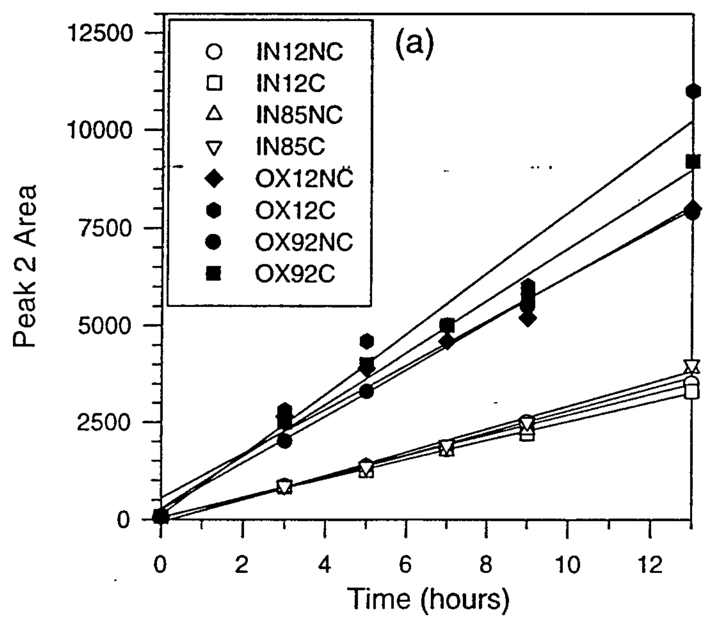

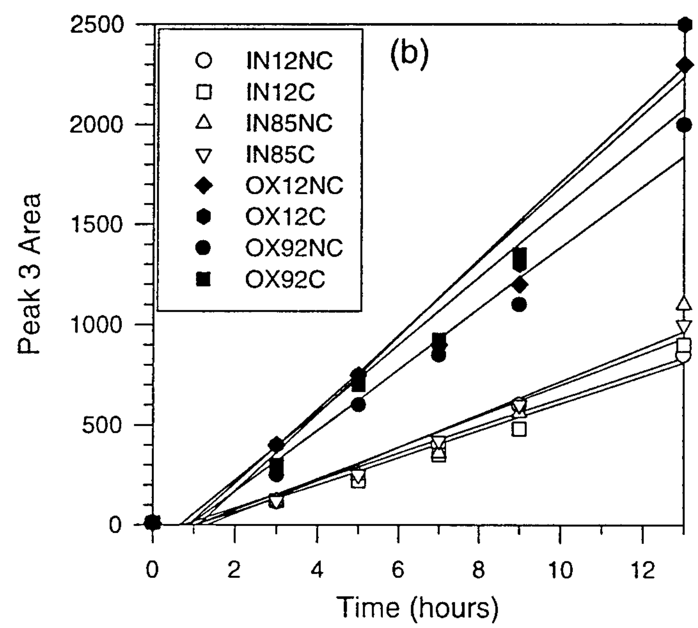

Figure 8. Changes in absorbance peaks 2 (a) and 3 (b) as a function of test time with linear regression for each test series. The linear relationships between peak areas and test time show that the absorption beahvior is characteristic of the high order kinetic reaction to form high MW degradation products.

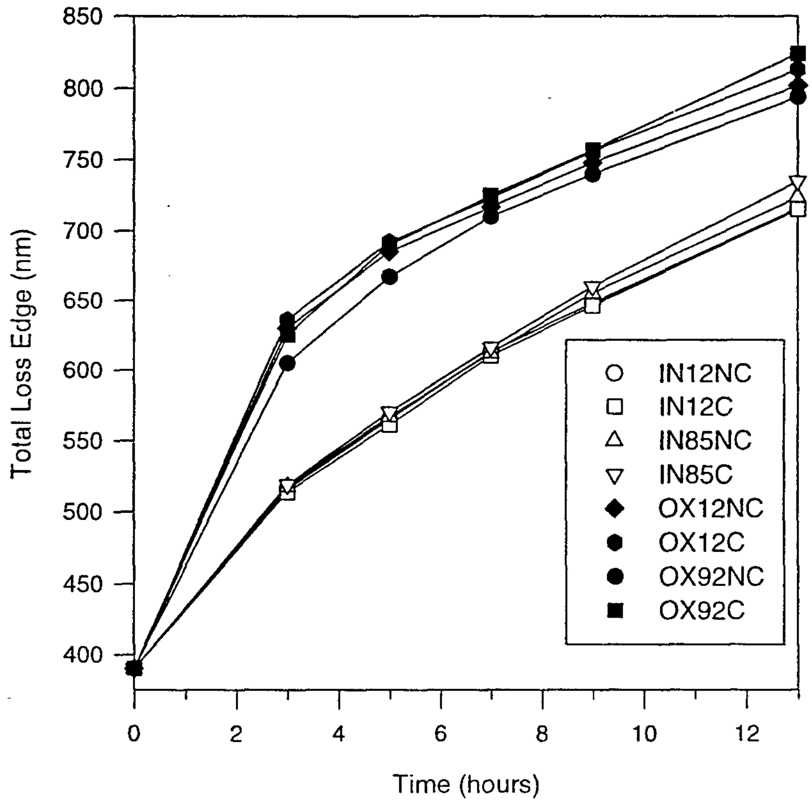

Figure 9. Total loss edge versus test time for degraded oil samples. The non-linear relationships show that changes in total loss edge values are not characteristic of the high order kinetic reaction which accounts for the formation of high molecular weight degradation products.

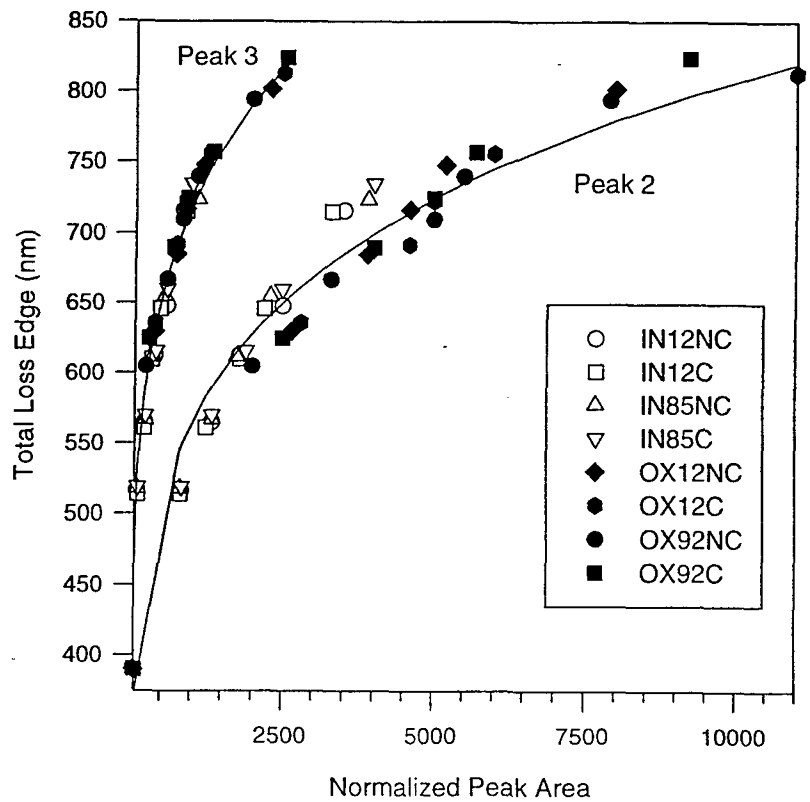

Figure 10. Total loss edge versus absorbing peaks 2 and 3 areas. Fitted curves reflect ($y = 190.59 \cdot x^{0.16}$) for peak 2 and ($y = 273.68 \cdot x^{0.14}$) for peak 3 with correlation coefficients of r^2=0.98 and 0.99 respectively. The non-linear relationships show that changes in total loss edge are not indicative of the optical behavior of the oil samples.

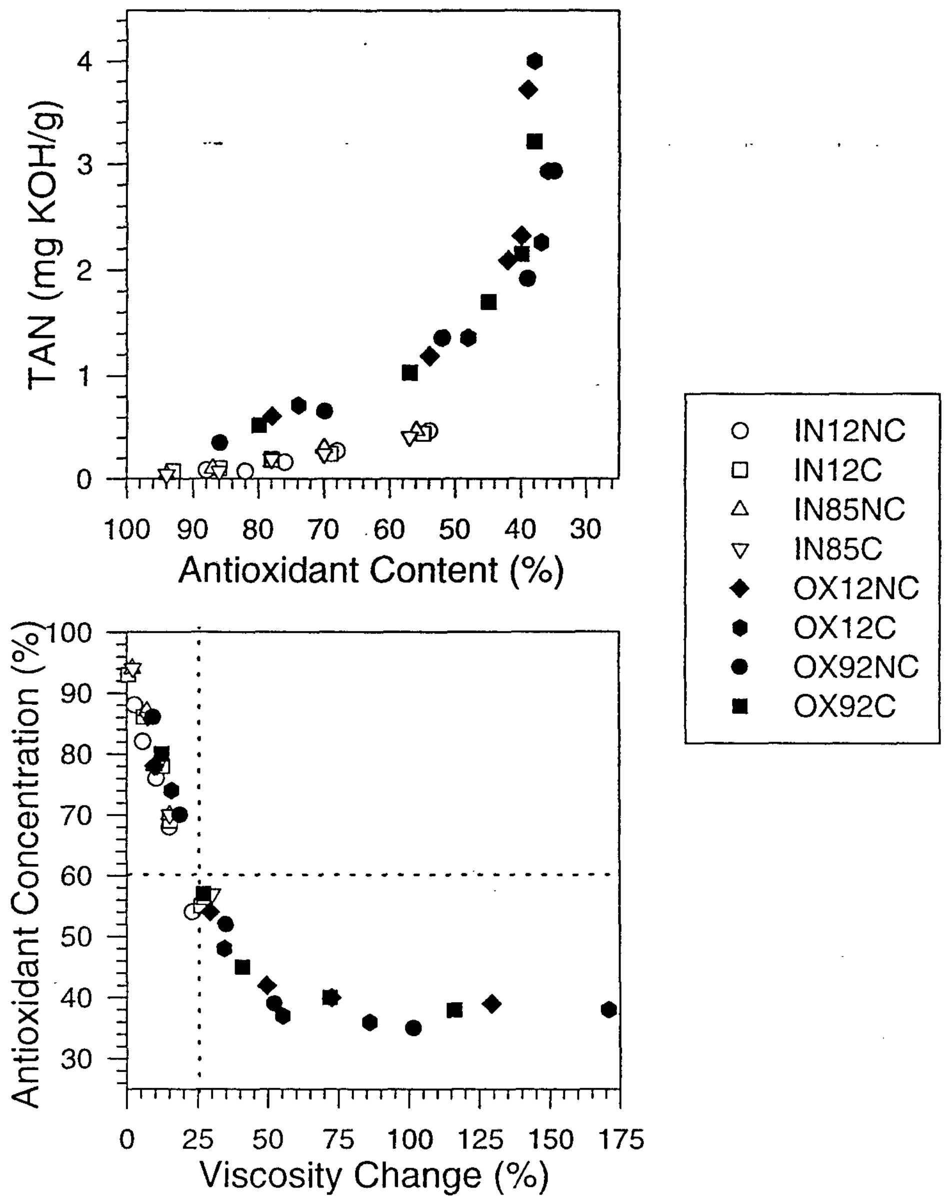

Figure 3. Total acid number results versus antioxidant content (a) and antioxidant content versus viscosity changes (b). Dotted lines indicate onset of chemical degradation in the oil samples.

APPENDIX 7, Robin A. Russell, "Determination of Metallo-Organic and Particulate Wear Metals in Lubricating Oils Associated with Hybrid Ceramic Bearings by Inductively Coupled Plasma Spectrometry," Abstract of Ph.D. Dissertation presented to the Graduate School, University of Florida, August 1997. Dissertation copy available upon request. J.D. Winefordner, advisor.

Abstract of Dissertation Presented to the Graduate School
of the University of Florida in Partial Fulfillment of the
Requirements for the Degree of Doctor of Philosophy

DETERMINATION OF METALLO-ORGANIC AND PARTICULATE WEAR
METALS IN LUBRICATING OILS ASSOCIATED
WITH HYBRID CERAMIC BEARINGS BY
INDUCTIVELY COUPLED PLASMA MASS SPECTROMETRY

By

Robin Ann Russell

August 1997

Chairman: James D. Winefordner
Major Department: Chemistry

It is possible to increase both the performance and operating environment of jet engines by using hybrid ceramic bearings. Our laboratory is concerned with investigating lubricating fluids for wear metals associated with silicon nitride ball bearings and steel raceways. Silicon nitride is characterized by low weight, low thermal expansion, high strength, and corrosion resistance. These attributes result in longer engine lifetimes than when metallic ball bearings are used. Before the routine use of ceramic ball bearings can be realized, the wear mechanisms of the materials should be thoroughly understood. One important variable in determining wear degradation is the concentration of metal present in the lubricating oils used with the bearings. A complete method for analyzing used lubricating oils for wear metal content must accurately determine all metal forms present.

Oil samples pose problems for routine analysis due to complex organic matrices. Nebulizing these types of samples into an Inductively Coupled Plasma - Mass Spectrometer introduces many problems including clogging of the sample cone with carbon and increasing interferences. In addition, other techniques such as Atomic Absorption Spectrometry and Atomic Emission Spectrometry are particle size dependent. They are unable to analyze particles greater than 10 μm in size.

This dissertation describes a method of analyzing lubricating oils for both metallo-organic and particulate species by ICP-MS. Microwave digestion of the oil samples eliminates the need for elaborate sample introduction schemes as well as the use of a modified carrier gas.

Al, Cr, Fe, Mg, Mo, Ni, Ti, and Y have been determined in both aqueous and organic media. Metallo-organic solutions of these metals were successfully digested, nebulized into the ICP, and the singly charged ions measured by mass spectrometry. Metal particulates in oil matrices have also been quantitatively determined by the above method. Linear analytical curves were obtained for these elements from the detection limits (~ 1 ppb) to greater than 1 ppm.

Used lubricating oil samples were also analyzed by microwave digestion ICP-MS. Oil samples were collected from a Rolling Contact Fatigue tester. Two bearing systems were evaluated: M50 steel balls on an M50 steel rod, and Si_3N_4 balls on an M50 steel rod. Improved operating conditions were obtained when the Si_3N_4 balls were used, which corresponds to longer engine lifetimes.

APPENDIX 8, S.A. Baker, B.W. Smith, and J.D. Winefordner, "Laser Ablation Coupled Mass Spectrometry with a Compact Laser Source," *Spectroscopic Perspectives*, 51[2], 1997.

Signed
Telephone

By S. A. Baker, B. W. Smith, and J. D. Winefordner*
Department of Chemistry,
University of Florida,
Gainesville, Florida 32611

Laser Ablation Inductively Coupled Plasma Mass Spectrometry with a Compact Laser Source

INTRODUCTION

Laser ablation (LA) as a sampling technique for inductively coupled plasma mass spectrometry (ICP-MS) was first reported by Gray in 1985.[1] Since that time, the technique has gained wide acceptance for the analysis of solids, because virtually any material can be sampled with the use of a focused, high-powered laser. Several excellent reviews have recently been written on the principles of LA-ICP-MS describing numerous applications of the technique.[2-5] Important advantages associated with laser sampling include the lack of sample preparation and dissolution steps, which can be time consuming and also can lead to contamination of the sample. In addition, LA-ICP-MS offers sub-ppm (paste per million) detection limits for most elements in a wide variety of matrices.

Despite the advantages associated with laser ablation, there are still a number of problems associated with the technique. Laser–material interactions are not completely understood.[3] An undefined amount of material will be ablated by each laser shot with a composition that may or may not stoichiometrically represent the bulk solid.[3] The end result is that matrix-matched standards are often required for calibration; however, alternative approaches have been studied.[6-9]

In spite of the difficulties associated with laser ablation, it is a useful sample introduction technique. For example, survey analysis of an unknown sample can be performed rapidly for both % level and ppb level elemental constituents. Unfortunately for most ICP-MS, the cost of laser ablation systems can be prohibitive. The most commonly used type of laser for LA-ICP-MS is the Nd:YAG operating at its fundamental wavelength (1064 nm)[4,10,11] or one of its harmonics (532 nm,[12] 355 nm,[12,13] and 266 nm[8,11-13]). Although it has been proposed that UV lasers may be more advantageous for LA-ICP-MS, the use of doubling crystals increases the complexity and expense of the system.[11,12]

The purpose of this paper is to report on the use of a compact and inexpensive Nd:YAG for LA-ICP-MS analysis of solids. These lasers, which were developed primarily for the opthalmic market, offer a simple, low-cost solid sampling option for

Received 3 March 1997; accepted 16 June 1997.
* Author to whom correspondence should be sent.

ICP-MS users. The device, which measures approximately four inches in length, is permanently aligned and thus requires no manual adjustments.[14] Recently, their use in a portable laser-induced breakdown spectrometer was reported.[15] In this paper, the capability of these compact lasers for LA-ICP-MS analysis of NIST aluminum and glass samples is demonstrated.

EXPERIMENTAL

The laser used in this study was a Nd:YAG (Kigre, Inc., Hilton Head, SC, MK-367) operating at 1064 nm. This laser provides nominal pulse energies of 20 mJ, pulse widths of ~4 ns, and a beam diameter of around 3 mm. It can be powered from either a 12-V dc power source or a transformer for 110/120-V operation and has an operational lifetime in excess of 300,000 shots.[14] It can either be operated in a manual firing mode or repetitively fired at a maximum repetition rate of 1 Hz. In our work, the laser was operated at 1 Hz, which required the use of a water-cooled mount (Kigre MK235236). The laser was focused onto the surface of the sample with a biconvex lens (FL = 6 cm). Samples were held in a glass ablation chamber, which was translated at ~50 μm/s on a modified syringe pump, to provide a partially fresh surface for each laser shot in order to achieve more representative sampling. The total cost of the laser system and sample stage was under $7000. Ablated material was transported to the ICP through a 1.5-m length of plastic tubing. For comparison studies, a Finningan MAT System 266 laser ablation accessory was used. This system provides a 266-nm Nd:YAG laser beam with a pulse energy of 1 mJ and a pulse width of 10 ns.

A Finnigan MAT SOLA ICP-MS was used in this study. Typical operating conditions for the experiment are listed in Table I. The system is operated in a "wet plasma" configuration, in which a solution blank is continuously introduced during the analyses.[8,16] While this approach does increase the level of some interferences, most notably oxides, we have found that this arrangement gives greater sensitivity and more stable signals in comparison to a dry plasma. The improvement in sensitivity is a factor of 10 or more, and precision is improved, on average, by a factor of 2.

TABLE I. ICP-MS operating conditions.

Radio-frequency power	1200 W
Coolant gas flow rate	15 L/min
Auxiliary gas flow rate	0.9 L/min
Nebulizer gas flow rate	0.65 L/min
Ablation chamber flow rate	0.35 L/min
Solution uptake rate	1.0 L/min
Scan conditions	
Faraday scans	
Scan range per isotope	1 amu
Number of passes	32
Number of channels per amu	8
Dwell time	64 ms
Multiplier scans	
Scan range per isotope	1 amu
Number of passes	128
Number of channels per amu	16
Dwell time	4 ms

IC
Av
Sp

The samples used in this study were NIST 601-604 aluminum standard reference materials, in which titanium is present at levels of 120 to 1000 ppm. In the analysis of these samples, ^{48}Ti was measured as well as ^{57}Fe for internal standardization. To demonstrate the utility of this laser for nonconducting samples, we also analyzed NIST glass samples (611, 612, and 617). In the glasses, ^{88}Sr and ^{43}Ca were measured, where Sr is present at levels from 41.5 ppm to 515.5 ppm and Ca is a major constituent of the glass matrix. All samples were used as received, with no surface modification or other preparation.

RESULTS AND DISCUSSION

Scanning electron microscopy was used to examine the laser-ablated NIST aluminum samples, as shown in Fig. 1. Figure 1a (top) shows the surface of the sample after 50 laser shots. It can be seen that the largest amount of ablation occurs in a region approximately 150 μm in diameter, but that the melting of the sample extends well beyond this area, as evidenced by the wavelike structures on the sample surface. Figure 1b (middle) is representative of typical analysis conditions, i.e., the sample was translated at 50 μm/s while the laser was fired at 1 Hz. The ablation track in this case is around 500 μm wide and very shallow. Once again, the wavelike structure can be clearly seen and is indicative of the fact that much of the material is removed by vaporization of the surface via the plasma that forms on the surface. For comparison, an ablation track formed by ablation with a 266-nm Nd:YAG is shown in Fig. 1c (bottom). It is evident from these figures that the ablation process is much more explosive with the UV laser than with the IR laser. This observation is most likely due to the fact that the laser interacts with the sample surface throughout the laser pulse for UV lasers, and the role of the surface plasma in ablation is minimal. Several researchers have compared the use of IR and UV lasers for ablation.[11,12,17] Only a limited comparison can be made in this work, however, since the pulse energy, pulse width, beam quality, and numerous other factors play a role in the ablation process.

A temporal profile of the Ti signal from NIST 604 is shown in Fig. 2. This figure indicates that, under the experimental conditions, even the low repetition rate of 1 Hz produced a "steady-state" signal. The profile contains a large number of spikes, which can be attributed to larger particles being vaporized in the ICP.

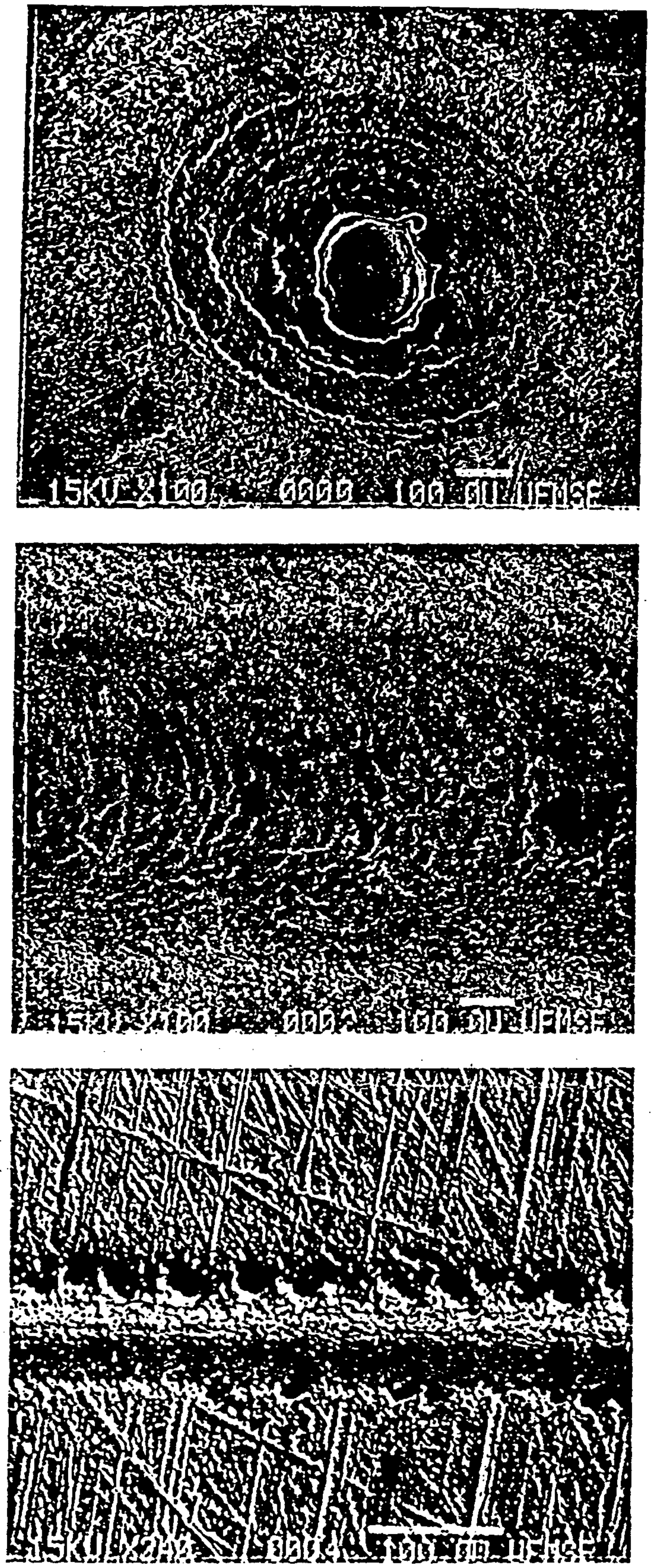

A linear calibration plot (R = 0.99) for Ti in the aluminum samples is shown in Fig. 3. It was necessary with these samples to measure ^{57}Fe in addition to ^{48}Ti, in order to account for differences in the mass ablated between samples and within a series of analyses on one sample. Although it is not exactly an internal standard, since its concentration varied between the samples, we accounted for these differences by normalizing the signal and thus mimicked the use of an internal standard. It is usually preferable to use a minor isotope of a major matrix constituent as the internal standard, but this was not possible because Al is monoisotopic and produced signal levels that saturated the detector. The precision of the normalized measurements (n = 5) ranged from 10 to 13%, compared to 17 to 24% without normalization. These values could be improved by using a shorter dwell time and a larger number of passes, but a minimum dwell time of 64 ms is required when using the Faraday detector. This means that a relatively long period of time is spent at each mass. The detection limit (3σ) for Ti in the aluminum samples is 0.3 ppm.

To assess the use of the laser for nonconducting samples, we analyzed NIST glasses. Figure 4 shows a linear calibration plot (R = 0.9999) for Sr in these glasses. Once again, an additional isotope (^{43}Ca) was measured to account for differences in the mass ablated. Differences in the mass ablated were as great as a factor of 4 between the glasses, due to the fact that the laser is absorbed differently by each glass. With the UV laser, differences in the ablated mass between samples was less than a factor of 2. The precision of the measurements (n = 5) ranged from 2 to 10%. The improved precision of

←

FIG. 1 Scanning electron microscope images of the aluminum surface after, from top to bottom, (a) 50 shots from the compact IR laser, (b) while translating the sample, and (c) with a UV laser while translating the sample. Magnifications of b and c are 100× and 240×, respectively (bar represents 100 μm).

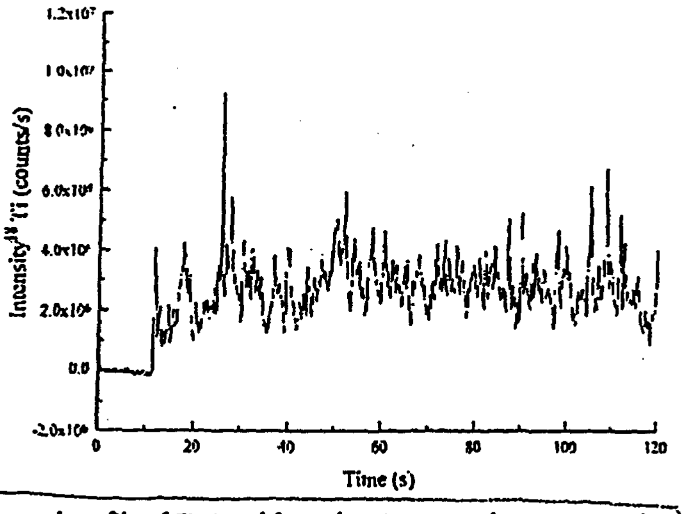

FIG. 2. *Temporal profile of Ti signal from the NIST 604 aluminum sample.*

1δ

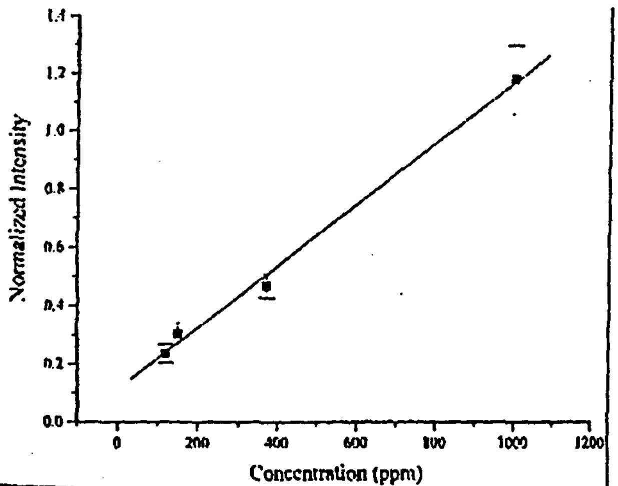

FIG. 3. *Calibration plot for Ti in NIST aluminum standard reference materials.*

2δ

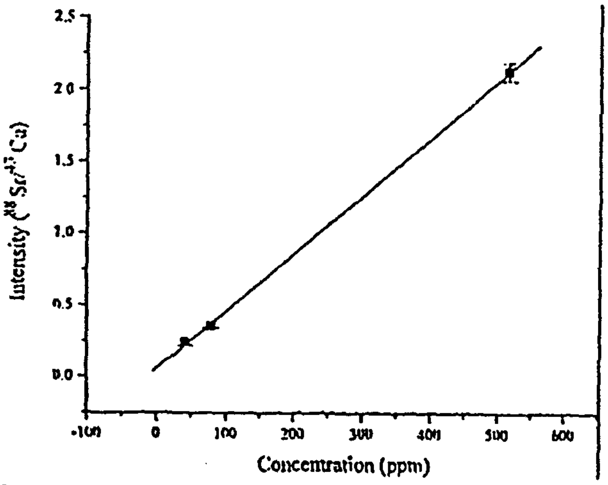

FIG. 4. *Calibration plot for Sr in NIST glass standard reference materials.*

3δ

these measurements is at least partially due to the shorter dwell times, which can be used with the multiplier detector. The detection limit (3σ) for Sr in the NIST glasses is 0.1 ppm. For comparison, the detection limit with UV laser ablation is 0.05 ppm. The improvement can be attributed to the larger mass of material that is ablated with the UV laser, due to increased absorption by the glass. Due to differences in laser ablation systems and ICP-MS instrumentation, direct comparisons with other researchers are difficult. Hager and co-workers reported a detection limit of 0.006 ppm for Sr in a glass matrix, but their work was performed with an IR laser with much higher energy (hundreds of mJ's) and a higher repetition rate (10 Hz).[4] This approach would result in much larger quantities being introduced to the ICP-MS and therefore, at least partially, explains the much lower detection limit. In addition, it is not clear whether single-ion monitoring was used (as opposed to multielement scanning) in determining the detection limit, as this can result in significant improvements in detection limits.

The results obtained with our compact laser system indicate that it can be successfully coupled with an ICP-MS to achieve sub-ppm detection limits for analytes in both conducting and nonconducting matrices. The system can be easily set up and provides a potentially useful and relatively inexpensive option for ICP-MS users.

ACKNOWLEDGMENTS

This work was supported by an Air Force Office of Scientific Research-University Research Initiative grant (F49620-93-1-0349). We would also like to acknowledge the Major Analytical Instrumentation Center at UF for use of the scanning electron microscope.

1. A. L. Gray, Analyst 110, 551 (1985).
2. S. A. Darke and J. F. Tyson, Microchem. J. 50, 310 (1994).
3. R. E. Russo, Appl. Spectrosc. 49, 14A (1995).

4. E. R. Denoyer, K. J. Freeden, and J. W. Hager, Anal. Chem. 63, 445A (1991).
5. S. A. Darke and J. F. Tyson, J. Anal. At. Spectrom. 8, 145 (1993).
6. J. W. Hager, Anal. Chem. 61, 1243 (1989).
7. F. E. Lichte, Anal. Chem. 67, 2749 (1995).
8. E. F. Cromwell and P. Arrowsmith, Anal. Chem. 67, 131 (1995).
9. S. M. Chenery and J. M. Cook, J. Anal. At. Spectrom. 8, 299 (1993).
10. P. Arrowsmith, Anal. Chem. 59, 1437 (1987).
11. T. E. Jeffries, N. J. G. Pearce, W. T. Perkins, and A. Raith, Anal. Comm. 33, 35 (1996).
12. C. Geertsen, A. Briand, F. Chartier, J.-L. Lacour, P. Mauchien, and S. Sjöström, J. Anal. At. Spectrom. 9, 17 (1994).
13. J.-M. [illegible] Spectrochim. Acta, Part B 51, 333 (1996).
14. Literature from Kigre, Inc. 100 Marshland Road Hilton Head Island, South Carolina.
15. K. Y. Yamamoto, D. A. Cremers, M. J. Ferris, and L. E. Foster, Appl. Spectrosc. 50, 222 (1996).
16. S. Chenery and J. M. Cook, J. Anal. At. Spectrom. 8, 299 (1993).
17. W. Sdorra, J. Brust, and K. Niemax, Mikrochim. Acta 108, 1 (1992).

APPENDIX 9, S.A. Baker, M.J. Dellavecchia, B.W. Smith, and J.D. Winefordner, "Analysis of silicon nitride bearings with laser ablation inductively coupled plasma mass spectroscopy," to be published in *Analytica Chimica Acta*, 1997.

18383

ELSEVIER

Analytica Chimica Acta 18383 (1997) 1–6

ANALYTICA CHIMICA ACTA

Analysis of silicon nitride bearings with laser ablation inductively coupled plasma mass spectrometry

Scott A. Baker, Matthew J. Dellavecchia, Benjamin W. Smith, James D. Winefordner*

Department of Chemistry, University of Florida, Gainesville, FL 32611, USA

Received 7 April 1997; received in revised form 16 June 1997; accepted 2 July 1997

Abstract

Laser ablation inductively coupled plasma mass spectrometry (LA-ICP-MS) was used for the analysis of silicon nitride ceramic bearings. Since calibration standards are not readily available for silicon nitride as well as many other ceramic materials, several calibration strategies have been assessed. Solution standards and a National Institute of Standards and Technology (NIST SRM) glass were demonstrated to be useful for the determination of trace and minor constituents in the bearings. Results for minor bearing constituents were verified with electron probe microanalysis (EPMA). Profilometry and weight loss measurements indicated that approximately 2 ng of silicon nitride was removed by each laser shot and that the efficiency of the LA-ICP-MS system was approximately 1 ion detected per 500 000 atoms removed for the Mg sintering aid present in these bearings.

Keywords: Inductively coupled plasma-mass spectrometry; Laser ablation; Ceramics; Silicon nitride; Calibration

1. Introduction

There is considerable interest in using silicon nitride (Si_3N_4) bearings for a wide variety of applications. Such an interest results from the unique chemical and physical properties which these ceramics possess. In comparison to conventional steel bearings, silicon nitride bearings offer high speed and acceleration capability because of their low density, extended temperature capability, longer lifetimes and lower wear rates, excellent corrosion resistance, and the ability to operate under conditions of marginal lubrication [1]. This combination of qualities has led to the investigation of silicon nitride bearings for use in high speed, high temperature applications, such as in the aerospace industry.

The physical and mechanical properties of ceramic materials are influenced by trace element impurities [2–4]. Therefore, comprehensive trace element characterization, in terms of both the bulk composition and spatial distribution of elements, is required for ceramic materials if they are to be used in demanding environments. Digestion procedures have been used for ceramics with analysis of the resulting solution by several techniques, including ICP-AES/MS [5,6] and flame AAS [5]. These procedures are difficult and time consuming, however, and can result in contamination of the sample. In addition, they only provide

*Corresponding author. Fax: 001 352 392 4651; e-mail: jdwin@chem.ufl.edu.

PII S0003-2670(97)00449-2

information on the bulk sample and tell nothing of the distribution of elemental constituents.

Direct sampling methods are preferred for the analysis of compact ceramics. Laser ablation is an effective method for direct sampling and its use in numerous applications has been reviewed [6,7]. The laser sampling technique has several advantages, including little to no sample preparation, ability to analyze both conducting and non-conducting samples, atmospheric operation, minimal sample contamination, high throughput, and the ability to obtain moderate spatial information on the distribution of elements. When combined with an ICP-MS, the technique provides excellent detection limits (sub-ppm) for most elements.

The major obstacle to the widespread applicability of laser ablation techniques is the significance of matrix effects, which arise from the complex nature of laser–material interactions [8,9]. As a result, matrix matched standards are often required for reliable quantitative measurements. In the case of ceramics, suitable standards are often not available, resulting in the need for alternative methods of calibration. Several techniques have been reported to overcome the limitation imposed by matrix-matching, including the use of fused beads or pelletized mixtures of diluent and analyte [10], and calibration based on solutions [11–13].

This paper reports on the development of methodology for reliable quantitative elemental analysis of silicon nitride ceramic bearings with the LA-ICP-MS technique. The work is based on the use of both solution-based calibration and calibration based on a National Institute of Standards and Technology (NIST) glass. The results obtained from the two methods are compared to one another, and with results obtained by electron probe microanalysis (EPMA). In addition, we characterized the ablation craters using both profilometry and scanning electron microscopy (SEM).

2. Experimental

2.1. Samples and reagents

Silicon nitride bearings (NBD-100 Cerbec, East Granby, CT) were mounted in epoxy and cut with a diamond blade wafering saw to obtain a flat surface. They were then polished to a 1 μm finish. These sample preparation steps were required for the EPMA analysis only. Laser ablation analyses could be performed directly on the intact bearing.

For the calibration studies, a 10 ppm multielement standard (High Purity Standards Charleston, SC) was diluted with deionized water and Optima-grade HNO_3 (Fisher Scientific, St. Louis, MO) was added to bring all solutions to 3% HNO_3. Concentrations of the solutions ranged from 1 to 50 ppb. In the glass-based calibration work, a National Institute of Standards and Technology glass was used (NIST 611). The concentration of most analytes in the glass is around 500 ppm.

2.2. Apparatus

The inductively coupled plasma mass spectrometer (ICP-MS) used in this work was a Finnigan MAT SOLA. Typical operating parameters are given in Table 1. In these studies, a combined flow of nebulized solution and carrier gas from the ablation chamber was introduced to the ICP at all times. In this way, identical plasma conditions are maintained whether an

Table 1
Typical ICP-MS operating conditions

Rf power	1200 W
Coolant gas flow rate	15 l/min
Auxiliary gas flow rate	0.9 l/min
Nebulizer gas flow rate	0.6 l/min
Ablation chamber flow rate	0.4 l/min
Solution uptake rate	1.0 ml/min
Scan conditions	
Faraday scans (major elements)	
Scan range per isotope	1 amu
Number of passes	32
Number of channels per amu	16
Dwell time	64 ms
Multiplier scans (minor and trace elements)	
Scan range per isotope (peak jumping)	0.25 amu
Number of passes	128
Number of channels per amu	16
Dwell time	4 ms

ablation aerosol or calibration solution is being analyzed. The ICP-MS lens settings and rf power were optimized using the ^{107}Ag signal from a 10 ppb solution.

The laser ablation system used in this work was the Finnigan MAT System 266. The ablation module consisted of a Nd : YAG laser operating at 266 nm, with associated optics and a CCD camera for remote viewing of the sample. It also included an x-y-z translation stage for adjustment of the laser focus and selection of the ablation site. The system was modified for this work by using a separate computer to control the translation stage. This allowed for translation of the sample while the laser was repetitively fired. The laser was operated at 5 Hz with a pulse energy of 1 mJ and pulse duration of 10 ns. Laser power density at the sample surface was around 5×10^{8} W/cm^2. The sample was translated at approximately 15 μm/s to provide a partially fresh surface for each ablation shot, resulting in larger ablation yields and more representative sampling. The typical analysis consisted of 300 to 400 laser pulses (60–80 s).

Ablation craters were characterized using an Alpha-Step 500 profilometer (Tencor Instruments, Santa Clara, CA) and a JEOL 35CF scanning electron microscope (SEM). For the SEM's, the silicon nitride samples were attached to mounts with carbon paint and coated with AuPd to provide a conductive surface. EPMA of the silicon nitride bearings was used for comparison with LA-ICP-MS results. For these analyses, a carbon coating was used since this resulted in lower background levels. The work was performed on a JEOL Superprobe 733.

2.3. Procedure

The solution calibration procedure involved measuring the intensity of a single isotope for each element and determining relative sensitivity factors (RSF's). The RSF is defined in Eq. (1), where E represents the element of interest and IS represents the internal standard.

$$\mathrm{RSF(E,IS)}=\frac{\mathrm{Sensitivity(E)}}{\mathrm{Sensitivity(IS)}}=\frac{\mathrm{Intensity(E)}}{\mathrm{Concentration(E)}}\times\frac{\mathrm{Concentration(IS)}}{\mathrm{Intensity(IS)}}. \qquad (1)$$

If (a) the condition of identical plasma conditions is met whether analyzing an ablated solid or a calibration solution and (b) the ablation aerosol is truly representative of the bulk ceramic, then RSF's obtained from solutions and the ceramic will be equal, i.e.

$$\mathrm{RSF(E/IS)}_{\mathrm{solution}}=\mathrm{RSF(E/IS)}_{\mathrm{ceramic}}. \qquad (2)$$

Provided that the concentration of the internal standard is known in the ceramic, the RSF's can be used to calculate the concentration of analytes from the expression

$$\mathrm{Concentration(E)}_{\mathrm{ceramic}}=\frac{\mathrm{Intensity(E)}_{\mathrm{ceramic}}}{\mathrm{Intensity(IS)}_{\mathrm{ceramic}}}\times\frac{\mathrm{Concentration(IS)}_{\mathrm{ceramic}}}{\mathrm{RSF}_{\mathrm{solution}}}. \qquad (3)$$

Obviously, the major requirement is that the concentration of an element in the ceramic is to be known and it serves as the internal standard. This can either be measured by some complementary technique, such as EPMA, or determined from the stoichiometry of the sample. In our case, the sample stoichiometry (60% silicon) was initially used to determine the concentration of a major constituent, the sintering aid magnesium, which was then used as the internal standard in all subsequent measurements. It would have been preferred to use a minor isotope of silicon (^{29}Si or ^{30}Si) as the internal standard directly; however, large interferences occurred at these masses and resulted in saturation of the electron multiplier detector. Magnesium was chosen as an alternative, since it was present at significant levels (1000 s of ppm) and possessed an isotopic pattern which allowed for its measurement using both the Faraday (^{24}Mg – 79% abundance) and multiplier (^{25}Mg – 10% abundance) detectors.

In the comparison of glass- and solution-based calibration, ^{59}Co was chosen as the internal standard since it was certified in the NIST glass and magnesium was not. The calibration procedure was similar, i.e., RSF's obtained from the glass matrix were used to calculate the concentrations of analytes in the silicon nitride bearing.

3. Results and discussion

3.1. Qualitative results and evaluation of methodology

A complete mass scan of the silicon nitride bearings (NBD 100) used in this study resulted in the identification of 24 elements. Although no attempt was made to quantify all of these elements, their estimated concentrations ranged from the hundreds of ppb level to thousands of ppm. For comparison, a newer grade of bearing material (NBD 200) was analyzed and contained much lower levels of impurities, with only the sintering aid (Mg) having a high concentration (>100 ppm). Only ten elements were present at high levels, enough to be detected with our LA-ICP-MS system. For this reason, the NBD 100 bearings were chosen for all subsequent work since they provided a more analyte-rich sample.

FOR LA-ICP-MS to be used for bulk analysis of the ceramic bearings, it was essential that the small surface layer sampled (~5 μm) on the exterior of the bearing be representative of the bulk material (Fig. 1). This was tested by analyzing the interior and exterior surfaces of a cut bearing. The measured concentrations of all analytes were identical within the measurement uncertainty, indicating that the relatively small volume sampled by laser ablation of the surface provided information on the bulk specimen.

As mentioned in Section 2, an isotope of magnesium was chosen as the internal standard for most of the quantitative measurements. A requirement for the use of internal standardization for obtaining accurate results is that the analyte and internal standard be distributed similarly over the area sampled, and that they exhibit similar behavior in transport to and excitation in the ICP. This was tested, albeit on a limited basis, by measuring the temporal response of the ^{25}Mg and ^{63}Cu signal over a period of 90 s, while the laser was repetitively fired (Fig. 2). The two signals correlated very well with one another and justified the use of ^{25}Mg as the internal standard for quantitative measurements.

(a)

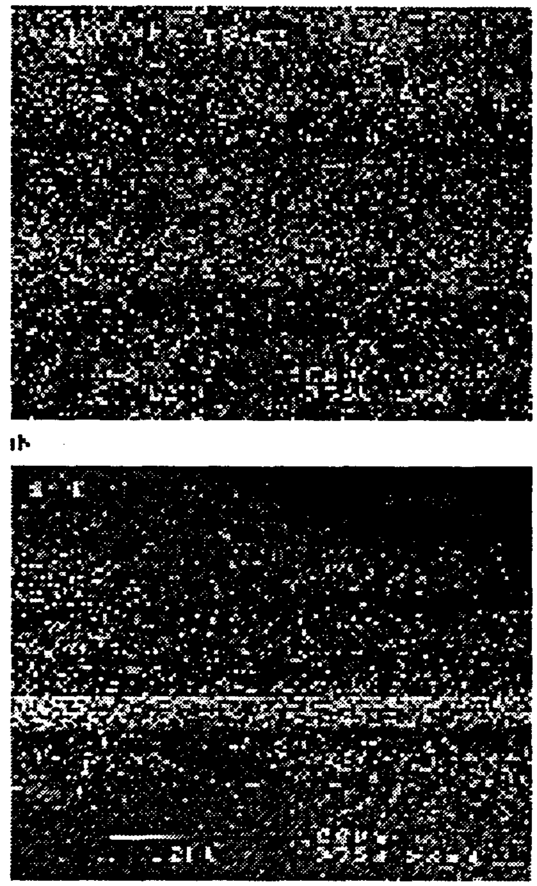

(b)

Fig. 1. SEM's of a laser ablation track in silicon nitride. Fig. 1(a) is a top view of the track and (b) was taken with the sample tilted at 50°. The depth of the track was estimated by profilometry to be approximately 5 μm.

3.2. Results from solution- and glass-based calibrations

Results for the analysis of a silicon nitride bearing using RSF's obtained from standard solutions are given in Table 2. For comparison, results obtained

Table 2
Results from LA-ICP-MS obtained with solution-based calibration and EPMA analyses

	Mg (ppm)	Co (ppm)	Al (ppm)	Ni (ppm)	Cu (ppm)	Sr (ppm)	Mo (ppm)	Ba (ppm)	La (ppm)	Nb (ppm)	Y (ppm)
LA-ICP-MS	7180	1420	2230	79	28	8.0	12	16	6.9	38	18
EPMA	7300	1300	2400								

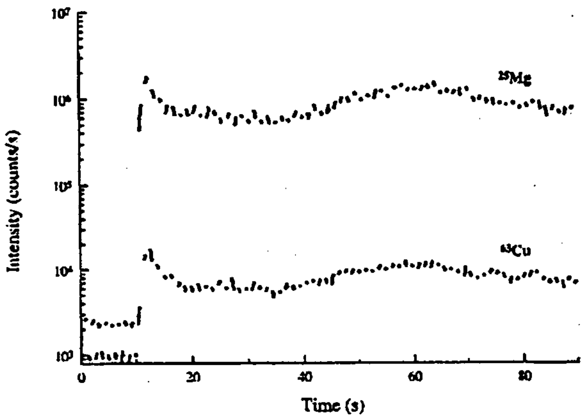

Fig. 2. Temporal profiles of ^{25}Mg and ^{63}Cu signals from silicon nitride bearing during continuous ablation.

with EPMA are provided for the three most concentrated elements (Mg, Co, Al) present in the silicon nitride. Because of the inferior sensitivity of EPMA, these were the only elements detectable in the sample by this method. The agreement between the techniques was excellent, suggesting that the use of solutions for calibration is effective for the analysis of ceramic materials. The precision of the techniques were similar, with % rsd's (n=10 for LA and n=5 EPMA) ranging from 2 to 15%.

In addition to solution-based calibration for silicon nitride ceramics, we investigated the use of NIST 611 glass as a calibration standard. In this work, a second bearing was analyzed. Similar to the procedure used for solutions, RSF's obtained from the glass sample were used to determine the concentration of analytes in the ceramic sample. A smaller number of elements was used in this work because of the limited number of certified elements in the glass. In several cases, the non-certified values provided by NIST were used (Co, Cu, and Zn). The results are presented in Table 3 and demonstrate that similar results were obtained for both solution- and glass-based calibrations.

The last row of this table represents an extension of the use of glasses for calibration. In this case, the absolute analyte sensitivites (intensity/concentration) from laser ablated glass were used with a correction factor to account for differences in the ablated mass between the glass and ceramic sample. The value of the correction factor was determined by measuring the ^{28}Si from both samples and taking into account the differences in nominal silicon concentration of the samples. Not surprisingly, the measured analyte concentrations agreed with those obtained by the other methods.

It would be beneficial to measure an isotope of silicon along with the analytes to directly compensate for variations in ablated mass; however, this was not feasible in the present system. The use of solutions produced high background levels (mainly oxides) and precluded the measurement of ^{29}Si and ^{30}Si with the multiplier detector. This could be remedied, at least in part, by incorporating a desolvation apparatus to decrease the solvent loading; however, this was not attempted in the present study. Alternatively, independent measurements of ablated mass, such as the use of acoustic waves generated by the ablation process [14], or measurement of the scattering signal produced by the mobilized ablation product [15,16] could prove useful for the analysis of ceramic materials with glass-based calibration.

3.3. Measurement of mass removed and system efficiency

Profilometry and weight loss measurements were performed on the silicon nitride samples to determine the amount of material removed by the ablation process and to determine the efficiency of the LA-ICP-MS system. As previously addressed, sample translation during ablation provides more representative sampling of the surface; however, it also results in a larger mass removal rate and subsequently higher

Table 3
Results from solution- and glass-based calibrations for silicon nitride

	Mn (ppm)	Co (ppm)	Ni (ppm)	Cu (ppm)	Zn (ppm)	Sr (ppm)
Results from solution RSF's	103	1540	58.5	9.01	9.23	6.84
Results from glass RSF's	123	1380	65.5	9.61	13.4	8.78
Results from glass sensitivities	119	1440	63.1	9.26	12.9	8.45

sensitivities. Profilometry measurements indicated that the volume ablation rate was nearly double in pL/s the case of sample translation compared to single spot sampling (3 pl/s compared to 1.6 pl/s). These correspond to mass ablation rates of 9 and 5 ng/s, respectively. This is due to the fact that a partially pristine surface is being ablated by each laser shot with translation of the sample. The removed masses agreed with those obtained by weighing the sample before and after approximately 50 000 laser shots. The observed ablation rates were used to determine a system efficiency for the sintering aid Mg (Mg ions detected/Mg atoms removed) of approximately 1 in 500 000. The efficiency of detection for all analytes is a function of the ablation process, transport process, ionization in the ICP, and mass spectrometer response.

4. Conclusions

The use of both solution- and glass-based calibrations has been demonstrated for the analysis of silicon nitride bearings. The results obtained from solutions were verified with a complementary technique, EPMA. Use of glasses for calibration provided similar results to those obtained from solutions and may prove useful in the future for a wide variety of ceramic materials. A large number of standard glass materials are presently available, making them very attractive as potential calibration materials for ceramics.

Acknowledgements

We thank Dr. James Adair for providing the silicon nitride bearings used in this work, Dr. Paul Holloway for use of the profilometer, and the Major Analytical Instrumentation Center (MAIC) at UF for the EPMA analyses. The work was supported by an Air Force Office of Scientific Research-University Research Initiative grant (F49620-93-1-0349).

References

[1] J.F. Chudecki, Ceram. Bull., 69 (1990) 1113.
[2] J.A.C. Broekaert, G. Tölg, Mikrochim. Acta, II (1990) 173.
[3] J.A.C. Broekaert, T. Graule, H. Jenett, G. Tölg and P. Tschöpel, Fresesnius' Z. Anal. Chem., 332 (1989) 825.
[4] L.K.L. Falk and E.U. Engström, J. Am. Ceram. Soc., 74 (1991) 2286.
[5] E.H. Homeier, S.A. Bradley and K.R. Karasek, J. Mat. Sci., 27 (1992) 1231.
[6] J.S. Crighton, J. Carroll, B. Fairman, J. Haines and M. Hinds, J. Anal. At. Spectrom., 11 (1996) 461R.
[7] S.A. Darke and J.F. Tyson, J. Anal. At. Spectrom., 8 (1993) 145.
[8] C.R. Phipps, R.W. Dreyfus, in: A. Vertes, R. Gijbels, F. Adams (Eds.), Laser Ionization Mass Spectrometry, Chap. 4, Wiley, New York, 1993.
[9] R.E. Russo, Appl. Spectrosc., 49 (1995) 14A.
[10] W.T. Perkins, R. Fuge and N.J.G. Pearce, J. Anal. At. Spectrom., 6 (1991) 445.
[11] E.F. Cromwell and P. Arrowsmith, Anal. Chem., 67 (1995) 131.
[12] S. Chenery and J.M. Cook, J. Anal. At. Spectrom., 8 (1993) 299.
[13] M. Thompson, S. Chenery and L. Brett, J. Anal. At. Spectrom., 4 (1989) 11.
[14] G. Chen and E.S. Yeung, Anal. Chem., 60 (1988) 2258.
[15] T. Tanaka, K. Yamamoto, T. Nomizu and H. Kawaguchi, Anal. Sci., 11 (1995) 967.
[16] S.A. Baker, B.W. Smith, J.D. Winefordner, unpublished data.
and

APPENDIX 10, Scott A. Baker, "Analysis of Glass, Ceramic, and Soil Samples Using Laser Ablation Inductively Coupled Mass Spectrometry," Abstract of Ph.D. Dissertation presented to the Graduate School, University of Florida, to be presented to the graduate school, May 1998. Dissertation copy available upon request. J.D. Winefordner, advisor.

Abstract of Dissertation Presented to the Graduate School
of the University of Florida in Partial Fulfillment of the
Requirements for the Degree of Doctor of Philosophy

ANALYSIS OF GLASS, CERAMIC, AND SOIL SAMPLES
USING LASER ABLATION INDUCTIVELY COUPLED MASS SPECTROMETRY

By

Scott A. Baker

May 1998

Chairman: James D. Winefordner
Major Department: Chemistry

Laser ablation (LA) as a direct solid sampling method for inductively coupled plasma mass spectrometry (ICP-MS) has been used for the analysis of glass, ceramic, and soil samples. The strength of this technique is that it can be applied to essentially any solid material and eliminates the need for difficult and time consuming dissolution procedures. The major limitation of LA-ICP-MS is the presence of matrix effects, making quantitation difficult in the absence of standards of identical composition.

This work was largely concerned with the development of methodology for obtaining accurate quantitative results from a variety of solid materials, including glasses, ceramics, and soils without the need for matrix-matched standards. The use of solution-based calibration for the analysis of a National Institute of Standards and Technology (NIST) glass resulted in excellent agreement (typically +/- 10%) with the certified values. Detection limits were in the sub-ppm range for all elements studied. The solution

calibration technique was also applied to silicon nitride ceramic bearings and the accuracy of the results were confirmed with X-ray microanalysis. In addition, standard glass materials were useful in the analysis of ceramics provided that differences in ablated mass were properly accounted for. To this end, the use of light scattering for measuring the amount of ablated material was evaluated. Light scattering was effective for mass normalization provided that the particle sizes of the ablation products were sufficiently similar.

The use of solution-based calibration for soil samples resulted in poorer agreement than in the case of glasses and ceramics; however, results were still within a factor of two of the certified concentration. Studies were performed to understand the reason for the poorer agreement found with soil samples. It was concluded that agreement with certified values was assured for these materials only through strict matrix matching or by using standard additions.

A compact, inexpensive laser was also evaluated for LA-ICP-MS measurements. It was used for the analysis of glass and aluminum samples and provided low to sub-ppm detection limits for the analytes studied.

APPENDIX 11, S.A. Baker, B.W. Smith, and J.D. Winefordner, "An Investigation of Light Scattering for Normalization of Signals in Laser Ablation Inductively Coupled Mass Spectrometry," submitted for publication.

In Press

To: Applied Spectroscopy

An Investigation of Light Scattering for Normalization of Signals in Laser Ablation Inductively Coupled Plasma Mass Spectrometry

S. A. BAKER, B. W. SMITH, and J. D. WINEFORDNER*

Department of Chemistry

University of Florida

Gainesville, FL 32611

*Author to whom correspondence should be sent.

ABSTRACT

Light scattering is evaluated for normalizing signals in laser ablation inductively coupled plasma mass spectrometry. The scattering signal produced from the transported ablation aerosol is measured with a laboratory-constructed cell. The technique is used to account for variations in the ablated mass within a matrix as well as between matrices. Matrices which are studied include brass, glass, soil, and Macor® ceramic. It is demonstrated that the technique is useful for normalizing analyte signals within a matrix; however, it is not as effective as the use of an internal standard in terms of the precision obtained. The utility of the technique to normalize between matrices is studied for glass, Macor®, and soil. The results indicate that light scattering is useful provided that the particle sizes generated are sufficiently similar.

Index Headings: laser ablation; ICP-MS; light scattering; normalization; glass; soil; ceramic; brass.

INTRODUCTION

Laser Ablation (LA) as a direct solid sampling technique for inductively coupled plasma mass spectrometry (ICP-MS) is becoming increasingly more important in atomic spectroscopy. Essentially any solid material can be vaporized with a focused, high-powered laser and thus sample preparation is minimal. The application of the technique has been demonstrated for a wide variety of matrices, including metals,[1,2] geological materials,[3-7] biological materials,[8-10] ceramics,[11,12] and polymers.[13] In addition to the versatility offered by laser sampling, the LA-ICP-MS technique offers sub ppm detection limits for most elements.

The technique does have limitations due to the complex nature of laser-material interactions, which results in an unknown quantity of ablated material with a composition which may or may not be representative of the bulk material.[14] Therefore, normalization techniques are needed to account for variations in the ablated mass and careful consideration of matrix effects is required if quantitative results are sought. Several authors have stressed the necessity of matrix matched standards for reliable results;[6,7,13] however, this is not possible in many cases. To deal with the problem, alternative calibration strategies have been assessed. These include the use of fused glass beads or pelleted mixtures of analyte and diluent,[15] as well as calibration based on solutions.[1,5]

To account for variations in ablated mass and improve the precision and accuracy of laser ablation measurements, the signal from a matrix element is commonly used as an internal standard.[1, 5, 6, 8, 13] This works well in terms of precision, provided the spatial distribution of the internal standard and the analyte are similar and the elements behave similarly in terms of ablation, transport, and ionization in the ICP. To improve the accuracy of LA-ICP-MS measurements, it is also required that the concentration of the internal standard be known. In many cases, this information is not readily available or can vary significantly, such as with many geological materials and multi-layered ceramics. In such instances, there is a need for independent measurement of the mass ablated.

Several techniques which independently measure differences in the mass ablated have been presented.[16-19] Pang, *et al.* demonstrated that the acoustic wave generated by the ablation process could be used to normalize analyte signals in LA-ICP-MS.[17] Their work resulted in modest improvements of the precision compared to the non-normalized signals from steel and aluminum alloy samples. Other work has involved measurements on the mobilized ablation products. Richner, *et al.* measured the light loss caused by scattering from ablated material as it passed through a cylindrical glass tube.[18] They reported that normalization of analyte signals from cast iron samples based on this technique was comparable to the use of an internal standard. Similarly, Tanaka, *et al.* used the light scattering signal produced from the transported aerosol to normalize analyte signals.[19] In their work with zirconium alloys, they also reported an improvement in precision which was comparable to internal standardization.

In the present work, we investigate the use of light scattering for normalization with several matrices, including brass, glass, soil, and Macor® (Corning Glass Works, Corning, NY) ceramic. It is demonstrated that a simple light scattering system can be used for mass correction for a variety of materials. This results in improved precision of LA-ICP-MS measurements; however, this method of normalization is not as good as the use of an internal standard. The major strength of the present technique is that it does not require any knowledge of the sample homogeneity or concentrations of elements, and is potentially useful for the accurate analysis of inhomogeneous sample as well as those for which standards are not readily available. This latter aspect was studied by examining the effectiveness of the light scattering system for normalization between different types of samples.

EXPERIMENTAL

The laser ablation system used in this work was a Finnigan MAT System 266. This accessory consists of a Spectron (UK) SL 401 Nd:YAG laser operating at 266 nm with associated optics and a CCD camera for remote viewing of the sample. It also includes an x-y-z translation stage for adjusting the focus of the laser beam and selecting the area of sample for analysis. The LA-ICP-MS system was modified by using a separate computer for control of the laser and allowed for translation of the sample while the laser was repetitively fired. Translation of the sample at ~ 15 μm/s provided a partially fresh surface for each laser shot, leading to more representative sampling of the bulk material as well as higher ablation rates. The laser was operated at 5 Hz, with pulse energies of ~ 0.2 mJ to 1 mJ and pulse widths around 10 ns in duration. The ablation cell used in this work was a smaller version of the one provided with the instrument and had a total volume of ~ 50 cm^3. Ablation products were transported to the ICP-MS through 1.5 m of 3/16" i.d. plastic tubing.

Typical operating and mass scanning conditions for the ICP-MS (Finnigan MAT SOLA, UK) are listed in Table I. A "wet plasma" was used in this work, meaning that a combined flow of nebulized solution blank and laser ablation products were combined at the base of the ICP torch.[1,5] We have found that this results in increased sensitivity by a factor of ten or more and precision is improved, on average, by a factor of two compared to dry plasma operation. Although a lower flow rate from the ablation chamber produced a more disperse collection of particles and subsequently lower scattering intensities, it was representative of typical conditions used in this laboratory for the quantitative analysis of materials by LA-ICP-MS.

The scattering cell, which is illustrated in Figure 1, was placed in-line with the transport tubing. It was placed approximately 0.5 m from the ablation chamber. The body of the scattering cell was a 4-way Swagelok®(Crawford Fitting Co., Solon, OH) connector with a 1.5 mm hole drilled in the top for measurement of the particle scattering at 90°. Smaller angle viewing would result in higher scattering intensities, but the present arrangement was chosen for its simplicity. Windows of the scattering cell were mounted at Brewster's angle on 3 cm extension arms made of stainless steel tubing. The arrangement produced less stray-light scatter from the windows and interior of the cell. A 3 mW polarized HeNe laser (Aerotech, Inc., Pittsburgh, PA) operating at 632.8 nm was used as the scattering source in these measurements. To improve the quality of the output beam, the laser was spatially filtered before the scatter cell with an adjustable iris.

An end-on photomultiplier tube (R647, Hamamatsu Photonics K.K., Japan) was used to collect the scatter produced as the ablation aerosol passed through the cell. The entire scatter assembly was enclosed in a light-tight box. An altenative arrangement, which would eliminate the need for darkness, would be the use of an interference filter which would transmit only a very narrow region of light centered at the HeNe wavelength. Signals from the PMT were amplified by a current to voltage amplifier (Keithley Instruments, Inc., Cleveland, OH) with a gain of 10^6 V/A and a rise time of 100 ms. The amplifier output was fed to a computer interface module (Stanford Research Systems, Inc., Palo Alto, CA) which was triggered at 100 Hz. Normalization measurements were made by integrating the scatter signal over a given number of shots, as well as averaging the "steady-state" level produced during continuous ablation of translated samples for a total of 200 shots (40 s).

NIST standard reference materials of glass (611, 612, 614, and 617) and brass (c1101, 1102, c1109, c1110) were used in assessing the utility of the scattering system for normalization of analyte signals within a particular matrix. In the glass samples, the ^{88}Sr isotope was measured with the ICP-MS as well a minor isotope of a major matrix constituent (^{43}Ca) in order to compare the results from scatter normalization with those obtained by internal standardization. The concentration of Sr in the glasses ranged from 41.72 ppm to 515.5 ppm. For the brass samples, the ^{68}Zn isotope was measured. Concentrations of Zn in these standards ranged from 15.2 % to 30.3 %. In the inter-matrix studies, NIST 611 glass, NIST 2704 soil, and a Macor® ceramic disc were used. The soil samples were pressed into pellets, without the addition of a binder at a pressure of 5000 psi, for laser ablation analyses. In these studies, the ^{28}Si isotope was measured since silicon is the major matrix element in each of the matrices.

The nature of the particulates produced from laser ablation of glass, soil, and Macor® was studied by collecting ablated material on 0.3 μm membrane filters (Millipore Corp., Bedford, MA). Because of the significant pressure drop created with the in-line filters, it was necessary to use a vacuum pump on the back side of the filter to eliminate flow restrictions. Flow conditions, identical to those used in the normalization experiments, were achieved by adjusting the pump valve and measuring the Ar flow rate with a rotameter. After collection, filters were glued onto mounts with conductive carbon paint and coated with AuPd for examination with a scanning electron microscope (JEOL 35CF, Japan).

RESULTS AND DISCUSSION

Scatter Signal Normalization and Comparison with Internal Standardization

Initial experiments with the scattering system were performed to determine if the scattering signals correlated with signals from the ICP-MS. Figure 2 illustrates typical (a) scatter and (b) mass spectrometric signals obtained from 50 laser shots on NIST 611 glass. It should be mentioned that the actual transit time for the scattering cell is ~1 s and ~3 s for the ICP-MS. The large number of spikes present in the scatter signal was assumed to be due to larger particles passing through the scatter cell based on visual observation. To evaluate the efficiency of the system in detecting changes in the mass removed, ablation was performed with different laser energies and focus positions. The total difference in the mass ablated over these conditions ranged over approximately one order of magnitude. A plot of the average scatter and ^{28}Si mass signals (Figure 3) demonstrated that the two signals were highly correlated (R = 0.98). In this example, differences in the mass ablated were generated by changing the laser sampling parameters (i. e. focus and pulse energy); however, these differences occured naturally over the series of glass standards under identical sampling conditions. This was probably due to differences in the surface characteristics of the glasses, since they were all completely opaque at 266 nm. Similar behavior has been reported by Mermet and co-worker in the laser ablation of glasses with a 266 nm Nd:YAG.[20]

In the absence of normalization, differences in the mass ablated between the samples would not allow small changes in analyte concentration to be detected. This is illustrated by a series of calibration curves for Sr in NIST glasses (Figure 4), where in (a), the non-normalized analyte signals are plotted; in (b), the scatter normalized signals are used; and in (c), the analyte signals are corrected by an internal standard (^{43}Ca). Without the use of normalization by scattering or internal standardization, a linear regression R value of 0.77 was obtained. R values obtained with the normalization techniques were both greater than 0.999. The precision of the scatter normalized measurements for 5 replicates and 200 laser pulses/replicate (5-12 % rsd) was not as good as those obtained with an internal standard (3-6 % rsd); however, the use of the former is not limited to homogeneous samples or those in which a suitable internal standard is available. This includes samples where the major matrix constituents do not have a minor isotope, resulting in ion intensities which would saturate the multiplier detector, or the isotope is interfered with from a sample consituent or some background species. The precision of the non-normalized signals ranged from 5-19 % rsd.

Precision of the scatter normalized measurements was slightly worse than that reported by Tanaka, *et al.*[19], although a direct comparison cannot be made because in the present work, a low energy UV laser was used for ablation; while in their work, a 150 mJ Nd:YAG operating at 1064 nm was used to ablate zironium alloys. This should result in significantly larger quantities being ablated, although the mass of material removed was not reported.

Although the main focus of the present work was to evaluate the effectiveness of scatter normalization with nonconducting matrices, NIST brass samples were also analyzed. Figure 5 demonstrates the use of scatter normalization for the calibration of Zn in these standards. The calibration plot exhibits a higher degree of correlation when the ^{66}Zn was corrected by the measured scatter signal ($R = 0.999$) as shown in (b) than when the analyte signal alone was plotted (a) ($R = 0.94$). Precision of the measurements was 6-11 % rsd (n=5, 200 pulses/measurement) for the normalized signals and 8-20 % rsd for the non-normalized values. Not only did the use of light scattering improve the precision of the measurements within a given sample, but it accounted for the different masses ablated between samples as evidenced by the improved fit of the regression line.

Comparison of Scatter Normalization for Glass, Soil, and Macor® Ceramic.

A comparison of glass, soil, and Macor® was made to assess the utility of the scattering system for corrections of mass ablated between these matrices. This was initiated, in part, by the desire to use glass standards for the calibration of ceramic materials. Results from this laboratory[21] suggest that NIST glasses may be suitable for the accurate analysis of some ceramics provided that differences in the ablated mass of the materials are accounted for. In the present work, a glass (NIST 611), soil pellet (NIST 2709), and Macor® disc were ablated to investigate the relationship between mass removed and scattering signal.

Correlation plots, similar to Figure 3, are shown in Figure 6 for the three different matrices. In this figure, the MS signals are normalized by the amount of silicon present in the samples to allow for a direct comparison of the matrices. Changes in the mass ablated were achieved by varying the energy of the laser. Slightly higher laser energies were used for the Macor® sample, since a smaller quantity of material was ablated for a given energy compared to the glass and soil samples. The laser energy ranged from 0.2 mJ to 1 mJ. Correlation between the scatter and MS signals was good for the glass ($R = 0.94$) and Macor® ($R = 0.96$) samples, but slightly worse for the soils ($R = 0.88$). Most importantly, the plot indicates that the scattering signal effectively accounted for differences in the mass ablated between the glass and ceramic samples as evidenced by the proximity of the data points for these materials. The similar scatter-MS signal relationship of glass and Macor® is more clearly illustrated in Figure 7, where a single regression line can be drawn through the set of data points with an $R = 0.97$. The scatter-MS signal relationship was significantly different for the soils. In this case, a larger scattering signal was produced per unit of matrix removed, which resulted in the soil data points lying closer to the scatter axis.

The nature of the particulate matter produced from ablation of these materials helped explain the experimental results. Scanning electron micrographs (SEM's) of the collected particles are shown in Figure 8. The pictures clearly demonstrate that the particles produced from (a) glass and (b) Macor® were both smaller and more similar than those from the (c) soil samples. The similarity in particle sizes for these matrices allowed for effective mass correction based on the scattering signal. The larger particle sizes produced from the soil sample resulted in a significantly different Scatter-MS signal relationship. This difference was not surprising; however, the larger soil particles, to a first approximation, should have produced a smaller scatter signal per unit mass compared to the other matrices. The opposite behavior that was observed in this study was most likely due to the fact that the larger particles the scatter cell "saw" were not efficiently transported to the ICP and would therefore not contribute to the MS signal. This is a limitation of the present system and could be alleviated by placing the scattering cell closer the ICP torch, resulting in a more representative view of the material introduced to the ICP-MS.

Figures 9 (a-c) are higher magnification images of particles collected for glass, ceramic, and soil, respectively. Most of the particles produced from glass and Macor® were nearly perfect spheres. These were formed by cooling of liquid material and suggested that the bulk of the ablated material was melted and then explosively removed from the sample.[22] Angular particles were also produced as a result of the mechanical and thermal shock of ablation, as well as a small amount of amorphous material which was most likely condensate from the gas phase. Such particle classifications have been described by other researchers as well.[22,23] The ablation product from soil was dominated by larger particles which resulted from mechanical and thermal shock, although each class of particle was seen. The greater presence of large particles was reasonable since these pressed pellets did not possess the mechanical rigidity of the glass and Macor® samples.

Weight loss measurements were performed for the glass and Macor® samples to verify that the mass ablated agreed with the experimental results. The samples were weighed before and after 40,000 laser shots at a laser pulse energy of 1 mJ. The average mass ablated for glass and Macor® was 16 ng/shot and 6.1 ng/shot, respectively. This agreed reasonably well with the scattering signals produced for ablation at this laser energy, and demonstrated that the scattering system was capable of measuring relatively small quantities of ablated material passing through the scatter cell.

Scattering sensitivity could be improved with a smaller observation angle and/or a shorter wavelength laser; however, the present system was sufficiently sensitive and easily set-up.

A simple measurement was made to assess whether matrix effects were significant between the glass, Macor®, and soil samples. Aluminum, which is a % level constituent in each sample, was measured in addition to silicon for each matrix. The RSF's (Al/Si) (defined in equation 1) obtained for the glass and Macor® were identical (RSF = 2.30), while soil produced a significantly different value (RSF = 3.40).

(1) $$RSF(Al/Si) = \frac{Intensity(Al)}{Concentration(Al)} \bullet \frac{Concentration(Si)}{Intensity(Si)}$$

This illustrated that matrix effects may not be significant between the glass and Macor® ceramic, suggesting the possibility of ceramic analysis using glasses for calibration.

CONCLUSION

The use of scattering for LA-ICP-MS signal normalization has been demonstrated for a variety of matrices. For measurements between matrices, it is important that the particle sizes generated by ablation be similar, as was demonstrated for glass, Macor®. and soil samples. The use of this technique is not as effective as the use of an internal standard in terms of the precision obtained; however, it requires no *a priori* knowledge of the sample heterogeneity or elemental composition. It provides a normalization alternative when a suitable internal standard is not available and may be useful for accurate analysis of ceramic materials based on glass standard reference materials.

ACKNOWLEDGMENTS

This work was supported by an Air Force Office of Scientific Research - University Research Initiative (AFOSR-URI) grant (F49620-93-1-0349). We would also like to acknowledge the Major Analytical Instrumentation Center (MAIC) at the University of Florida for use of the scanning electron microscope and Igor B. Gornushkin for his assistance with the light scattering system.

REFERENCES

1. M. Thompson, S. Chenery, and L. Brett, J. Anal. At. Spectrom. **4**, 11 (1989).
2. V. V. Kogan, M. W. Hinds, and G. I. Ramendik, Spectrochim. Acta. **49B**, 333 (1994).
3. A. M. Ghazi, T. E. McCandless, D. A. Vanko, and J. Ruiz, J. Anal. At. Spectrom. **11**, 667 (1996).
4. F. E. Lichte, Anal. Chem. **67**, 2479 (1995).
5. S. Chenery and J. M. Cook, J. Anal. At. Spectrom. **8**, 299 (1993).
6. J. G. Williams and K. E. Jarvis, **8**, 25 (1993).
7. B. J. Fryer, S. E. Jackson, and H. P. Longerich, Can. Mineral. **33**, 303 (1995).
8. P. M. Outridge and R. D. Evans, J. Anal. At. Spectrom. **10**, 595 (1995).
9. S. Wang, R. Brown, and D. J. Gray, Appl. Spectrosc. **48**, 1321 (1994).
10. R. D. Evans, P. M. Outridge, and P. Richner, J. Anal. At. Spectrom. **9**, 985 (1994).
11. J. S. Becker, U. Breuer, J. Westheide, A. I. Saprykin, H. Holzbrecher, H. Nickel, and H.- J. Dietze, Fres. J. Anal. Chem. **355**, 626 (1996).
12. I. D. Abell, D. Gregson, and S. Shuttleworth, in *The Physics and Chemistry of Carbides; Nitrides and Borides*, R. Freer, Ed. (Kluwer Academic Publishers, The Netherlands, 1990), pp. 121-130.
13. J. Marshall, J. Franks, I. Abell, and C. Tye, J. Anal. At. Spectrom. **6**, 145 (1991).
14. R. E. Russo, Appl. Spectrosc. **49**, 14A (1995).
15. W. T. Perkins, R. Fuge, and N. J. G. Pearce, J. Anal. At. Spectrom. **6**, 445 (1991).
16. G. Chen and E. S. Yeung, Anal. Chem. **60**, 2258 (1988).
17. H. Pang, D. R. Wiederin, R. S. Houk, and E. S. Yeung, Anal. Chem. **63**, 390 (1991).

18. P. Richner, M. W. Borer, K. R. Brushwyler, and G. M. Hieftje, Appl. Spectrosc. **44**, 1290 (1990).

19. T. Tanaka, K. Yamamoto, T. Nomizu, and H. Kawaguchi, Anal. Sci. **11**, 967 (1995).

20. M. Ducreux-Zappa and J. -M. Mermet, Spectrochim. Acta. **51B**, 333 (1996).

21. unpublished data.

22. M. Thompson, S. Chenery, and L. Brett, J. Anal. At. Spectrom. **5**, 49 (1990).

23. Y. Huang, Y. Shibata, and M. Morita, Anal. Chem. **65**, 2999 (1993).

FIGURE CAPTIONS

Fig. 1 Schematic of the light scattering set-up ((a) top view and (b) side view).

Fig. 2 Plots of (a) scatter and (b) mass spectrometric signals obtained from 50 laser shots on glass surface.

Fig. 3 Correlation plot of mass spectrometric and scatter signals from NIST glass.

Fig. 4 Calibration plots for Sr in NIST glass samples (a) without normalization, (b) with scatter normalization, and (c) with internal standardization.

Fig. 5 Calibration plots for Zn in NIST brass sample (a) without normalization and (b) with scatter normalization.

Fig. 6 Correlation plots of mass spectrometric and scatter signals from glass, macor, and soil samples.

Fig. 7 Correlation plot of mass spectrometric and scatter signals for glass (■) and macor (●) samples.

Fig. 8 Scanning electron micrographs of particles collected for (a) glass, (b) macor, and (c) soil. (Bar represents 10 μm.)

Fig. 9 Higher magnification images of (a) glass, (b) macor, and (c) soil particles. Note difference in the scale for soil (Bar represents 1 μm in (a) and (b); 10 μm in (c).)

Table I. ICP-MS Operating Conditions

Rf Power	1200 W
Coolant gas flow rate	15 L/min
Auxiliary gas flow rate	0.9 L/min
Nebulizer gas flow rate	0.6 L/min
Ablation chamber flow rate	0.4 L/min
Solution uptake rate	1.0 mL/min
Scan Conditions	
Faraday Scans (Major elements)	
Scan range per isotope	1 amu
Number of passes	32
Number of channels per amu	8
Dwell time	64 ms
Multiplier Scans (Sr & Ca in glass)	
Scan range per isotope	1 amu
Number of passes	256
Number of channels per amu	8
Dwell time	4 ms

Fig. 1

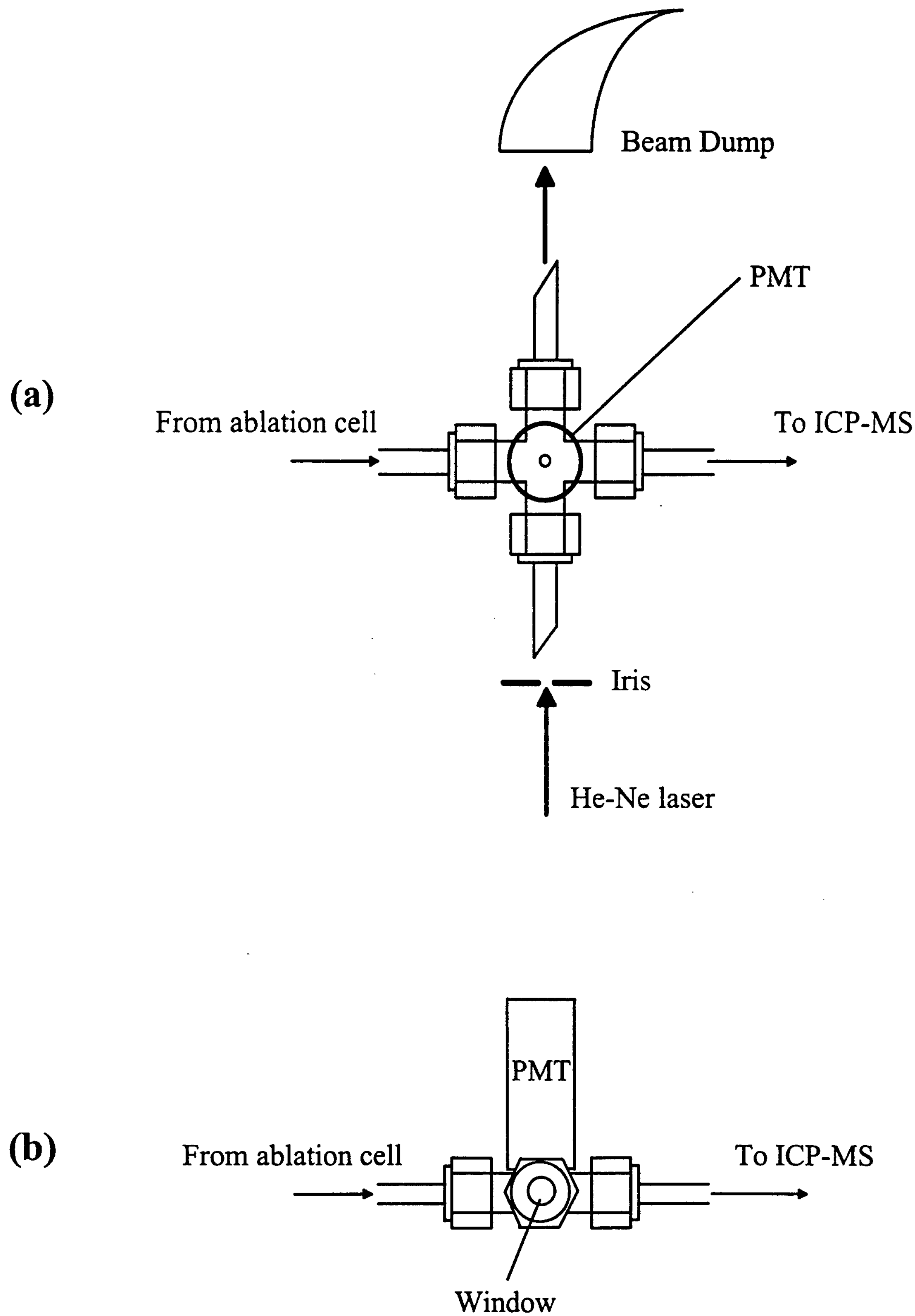

(a)
Beam Dump
PMT
From ablation cell
To ICP-MS
Iris
He-Ne laser
(b)
PMT
From ablation cell
To ICP-MS
Window

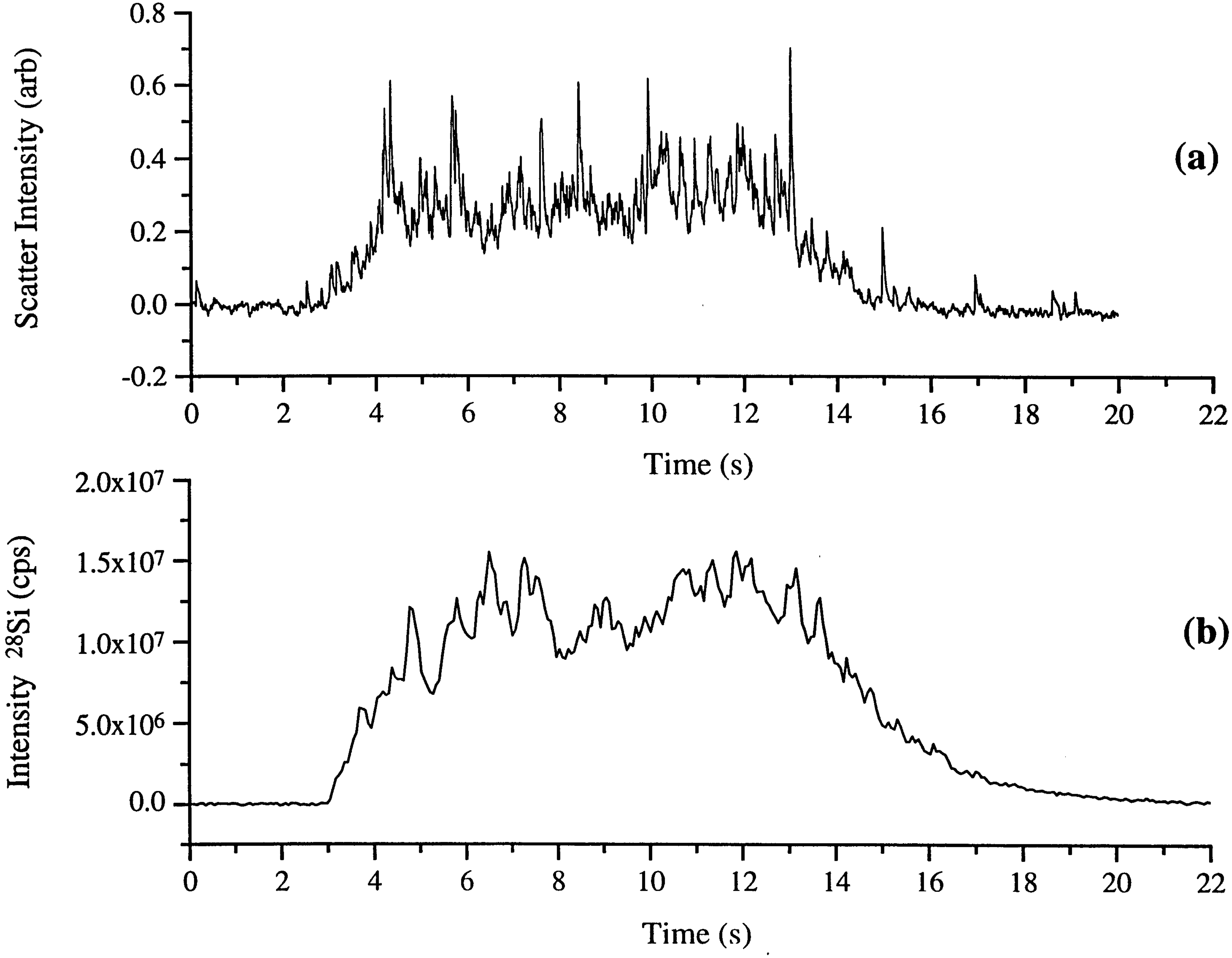
(a)
Scatter Intensity (arb)
0.8
0.6
0.4
0.2
0.0
-0.2
0 2 4 6 8 10 12 14 16 18 20 22
Time (s)
(b)
Intensity ^{28}Si (cps)
2.0x10^{7}
1.5x10^{7}
1.0x10^{7}
5.0x10^{6}
0.0
0 2 4 6 8 10 12 14 16 18 20 22
Time (s)

Fig 2

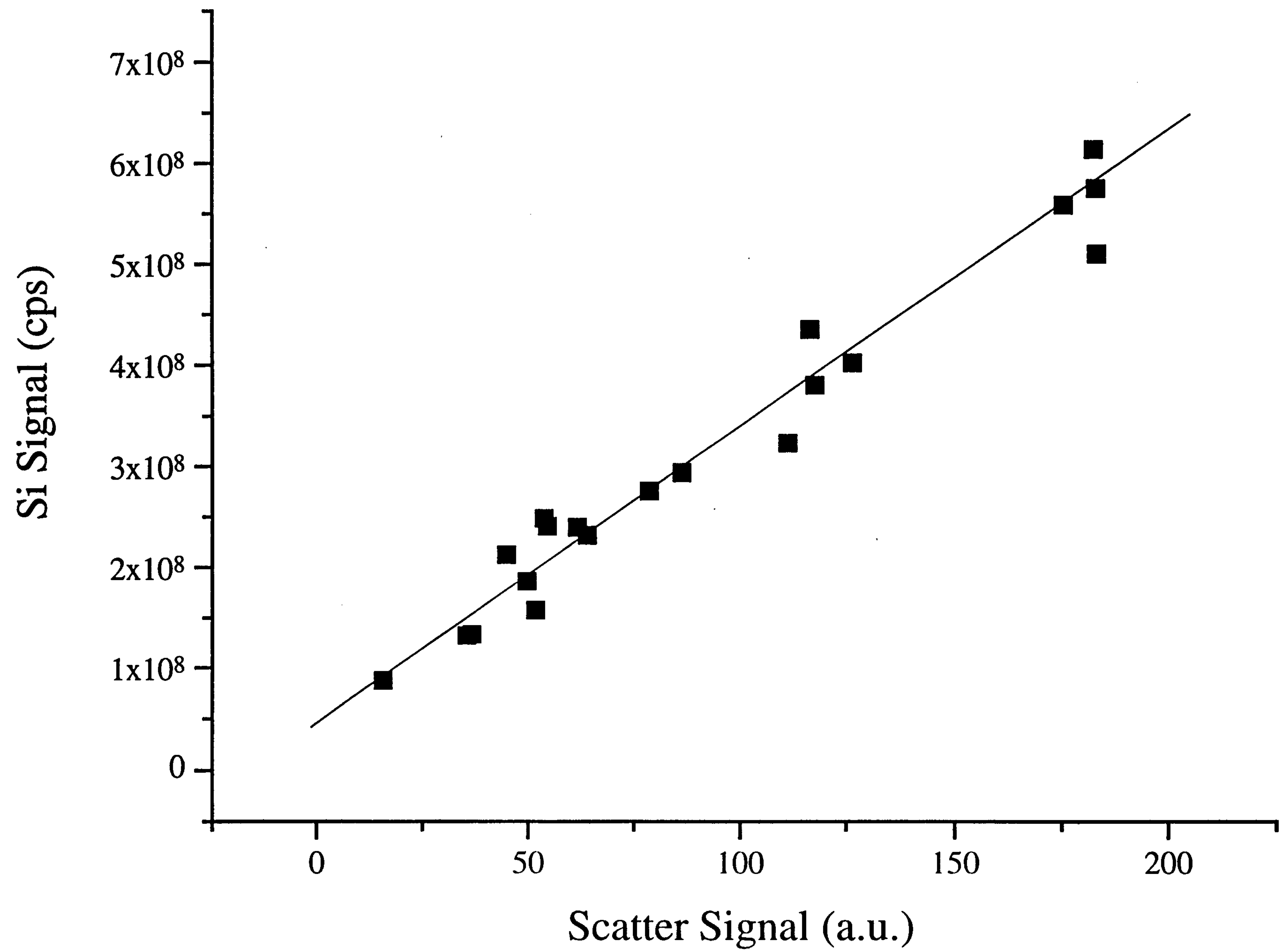
7x10⁸
6x10⁸
5x10⁸
4x10⁸
3x10⁸
2x10⁸
1x10⁸
0
Si Signal (cps)
0
50
100
150
200
Scatter Signal (a.u.)

Fig. 3

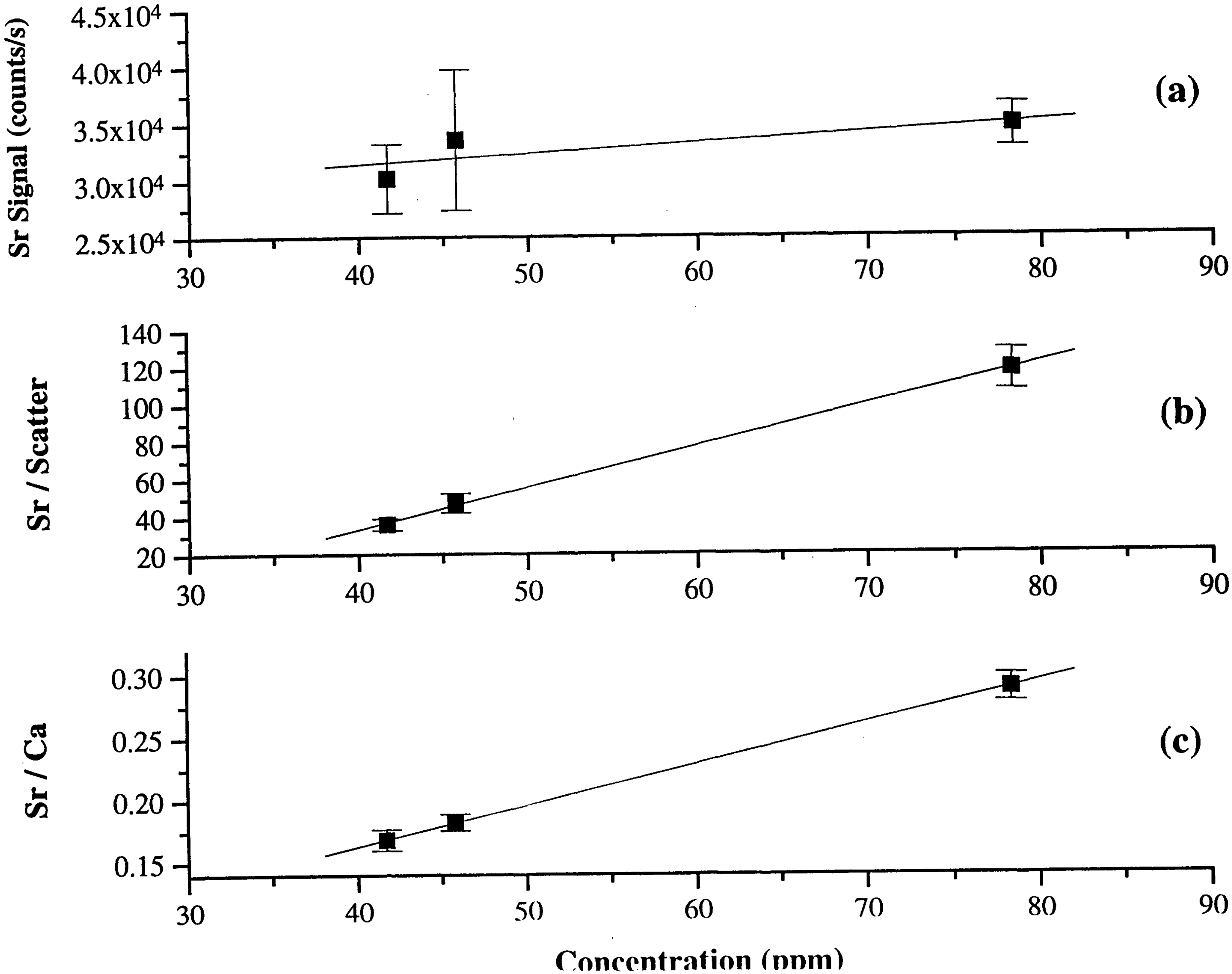
Sr Signal (counts/s)
4.5x10^4
4.0x10^4
3.5x10^4
3.0x10^4
2.5x10^4
(a)
Sr / Scatter
140
120
100
80
60
40
20
(b)
Sr / Ca
0.30
0.25
0.20
0.15
(c)
30
40
50
60
70
80
90
Concentration (ppm)

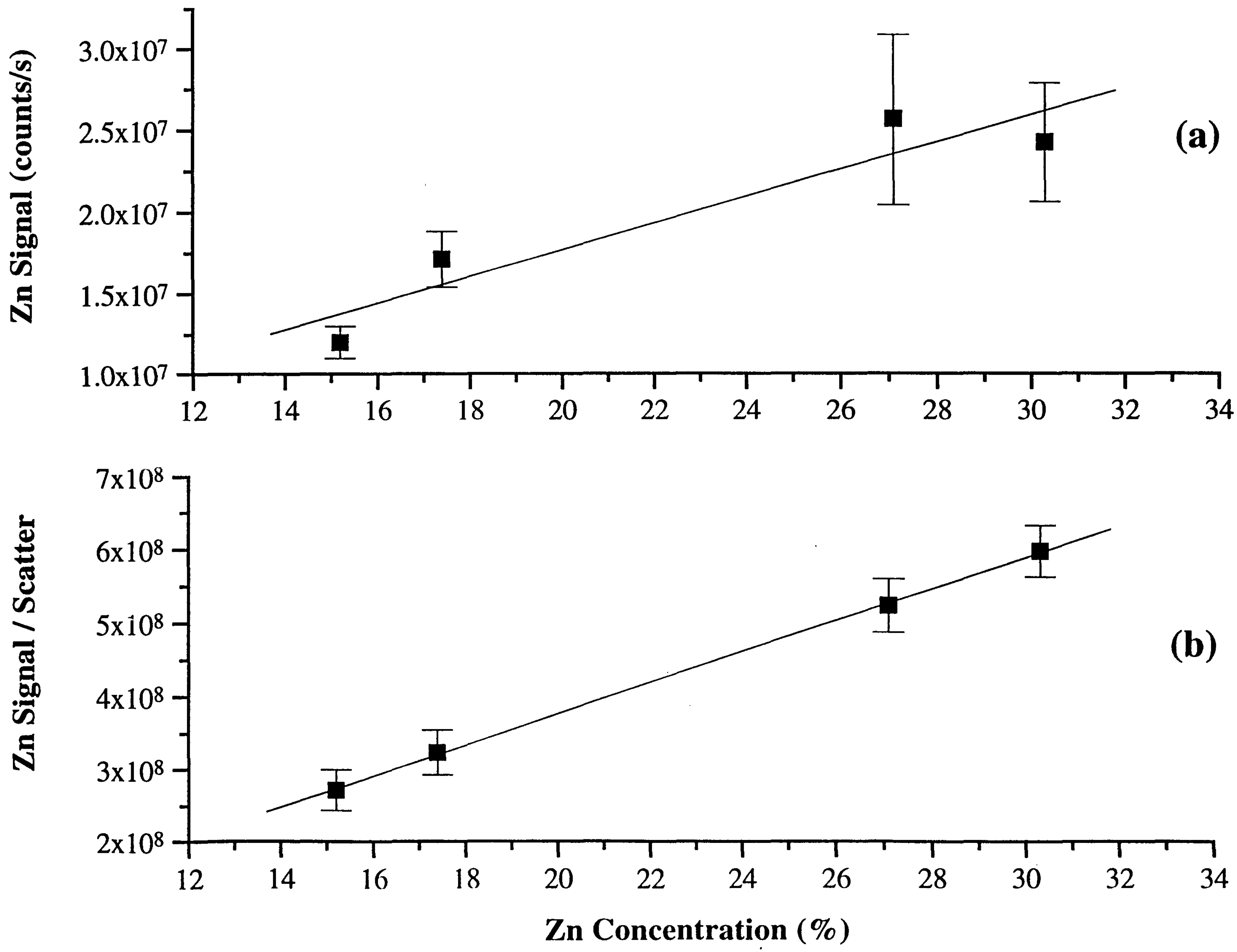
Zn Signal (counts/s)
3.0x10^7
2.5x10^7
2.0x10^7
1.5x10^7
1.0x10^7
(a)
Zn Signal / Scatter
7x10^8
6x10^8
5x10^8
4x10^8
3x10^8
2x10^8
(b)
12
14
16
18
20
22
24
26
28
30
32
34
Zn Concentration (%)

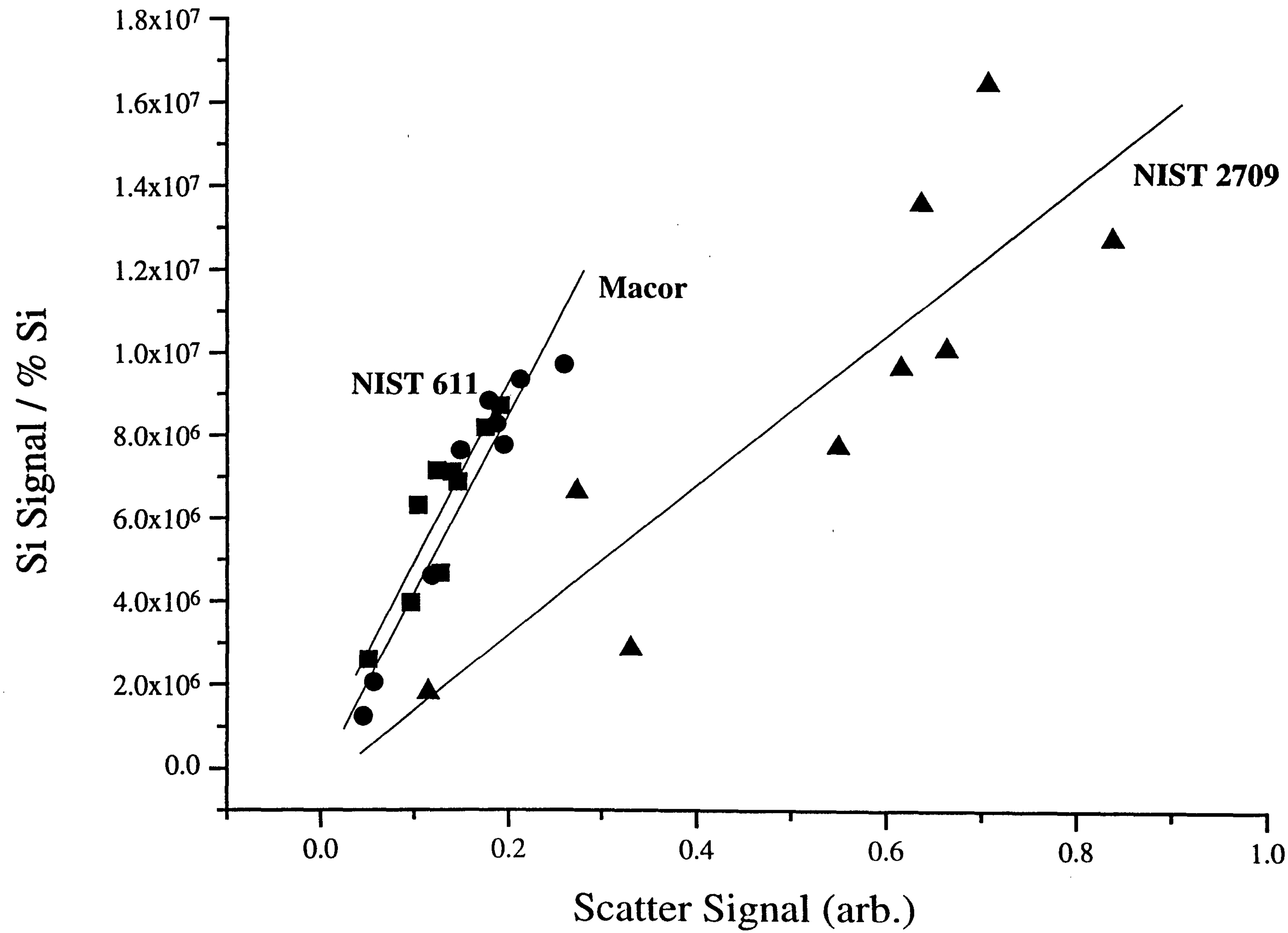
NIST 2709
Macor
NIST 611
Si Signal / % Si
1.8x10^7
1.6x10^7
1.4x10^7
1.2x10^7
1.0x10^7
8.0x10^6
6.0x10^6
4.0x10^6
2.0x10^6
0.0
0.0
0.2
0.4
0.6
0.8
1.0
Scatter Signal (arb.)

Fig. 6

Fig.7

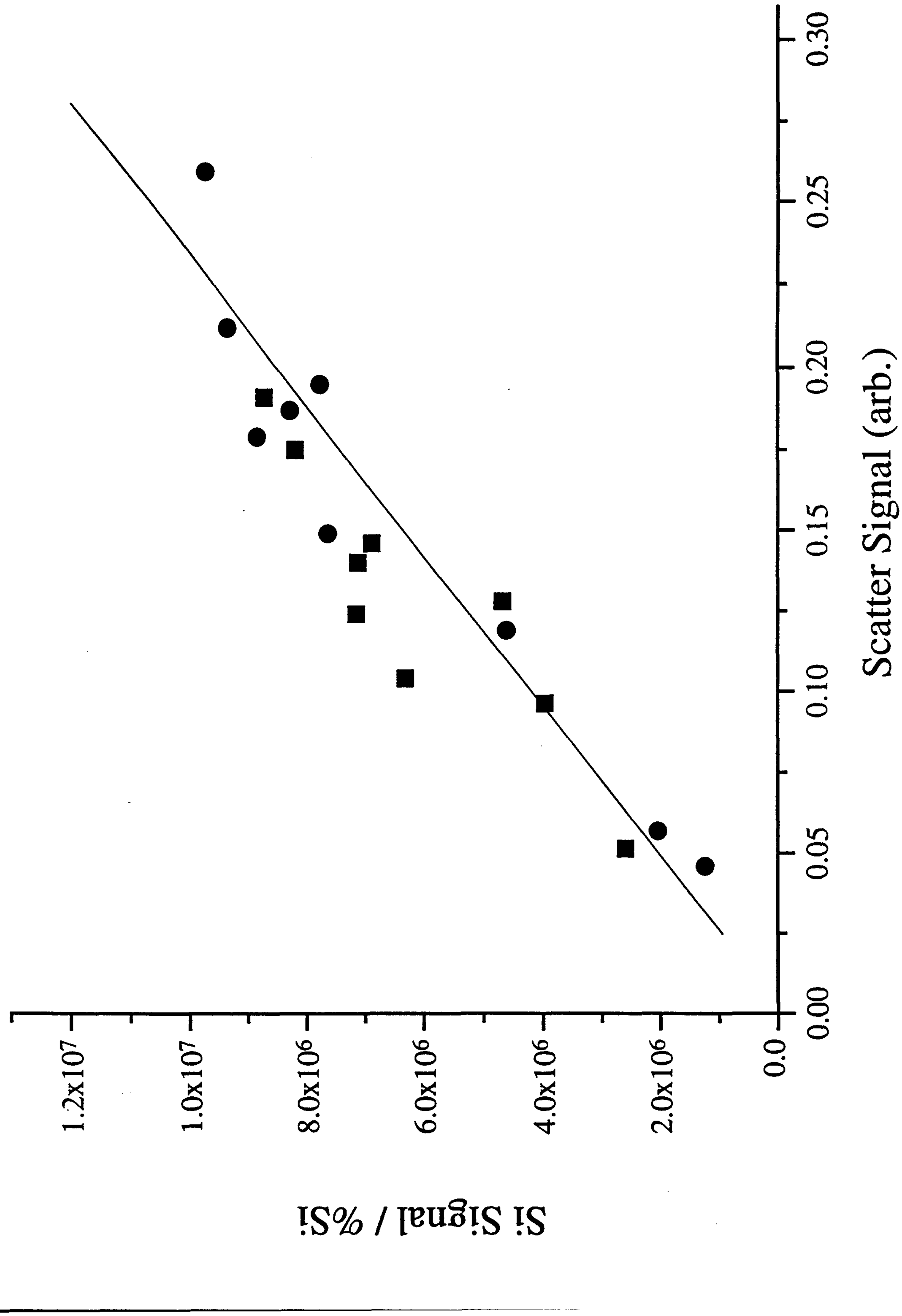

Si Signal / %Si
0.0
2.0x10^6
4.0x10^6
6.0x10^6
8.0x10^6
1.0x10^7
1.2x10^7
Scatter Signal (arb.)
0.00
0.05
0.10
0.15
0.20
0.25
0.30

Fig. 8

(a)

(b)

(c)

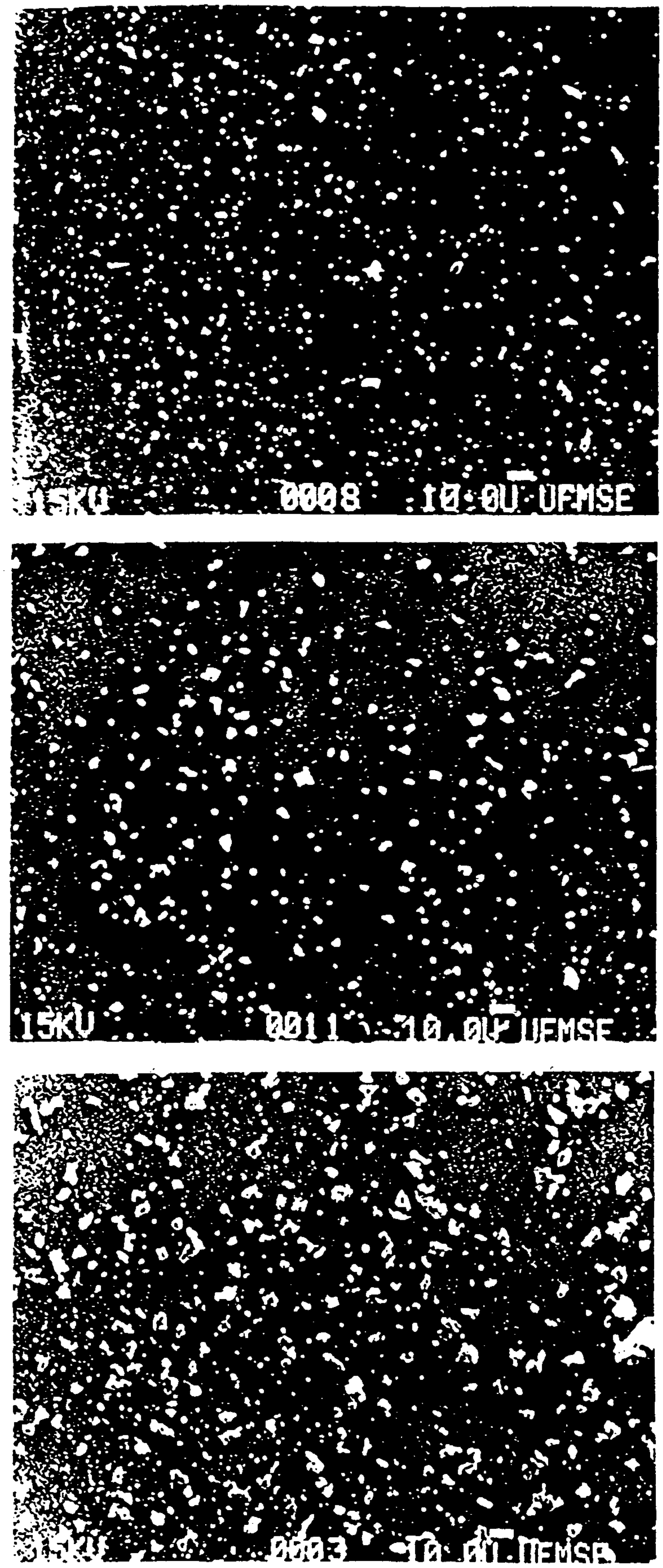

15KU 0008 10.0U UFMSE
15KU 0011 10.0U UFMSE
15KU 0003 10.0U UFMSE

Fig. 9

(a)

(c)

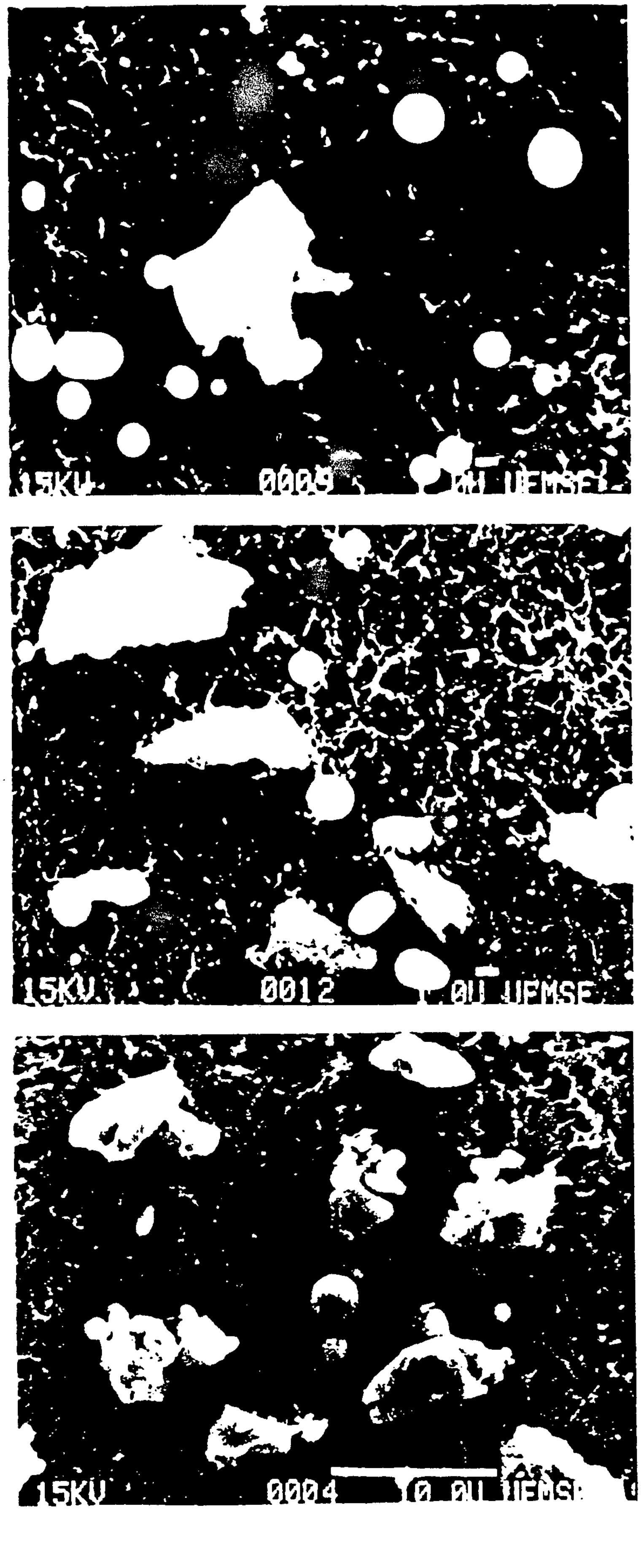

Task 2

APPENDIX 12, L-Y Chao And D.K. Shetty, "Wear and Fatigue Damage in Ball-on-Rod Rolling Assessed with Steel/Steel, Steel/Si_3N_4 and Si_3N_4/Si_3N_4 Contacts," to be submitted for publication.

APPENDIX 13, L-Y Chao And D.K. Shetty, "Wear and Fatigue Damage in Ball-on-Rod Rolling Assessed with Steel/Steel, Steel/Si_3N_4 and Si_3N_4/Si_3N_4 Contacts," ABSTRACT OF M.S. Thesis to be presented to the graduate scholl at the Univerisyt of Utah, 1998. Thesis copy available upon request. D.K. Shetty, advisor.

APPENDIX 14, S. Akunuri, "Wear Characteristics of Silicon Nitride-M50 Steel Hybrid Bearing System," Abstract of M.S. Thesis presented to the Graduate School, University of Florida, July 1995. Thesis copy available upon request. J.H. Adair, thesis advisor.

APPENDIX 15, F. Mohammadi, J.H. Adair, E.D. Whitney, and J.K. West, "An Infrared Spectroscopy Analysis of MgO-Doped Silicon Nitride," *Cer. Trans.*, 69, 53-58 (1995). Non-thesis M.S.

APPENDIX 16, D.J. Mitchell, J.J. Mecholsky, Jr., and J.H. Adair, "Rolling contact fatigue and wear analysis of M50-M50 all-steel and Si_3N_4-M50 hybrid bearing rolling element systems using lubricants contaminated with Arizona test dust or single crystal α-Al_2O_3 particulate.

APPENDIX 17, D. J. Mitchell, R. Sabia, E.D. Whitney, and J. H. Adair, "Characterizing the Performance of Advanced Rolling Element Materials," *Cer. Engr. & Sci. Proc.*, 18[4], 85-92, (1997).

APPENDIX 18, R. Sabia, Herb A.J. Chin, and J.H. Adair, "Friction and Wear Properties of Silicon Nitride/M-50 Steel Sliding Couples in Degraded Ester-Based Lubricant," submitted for publication.

APPENDIX 19, R. Sabia, D.J. Mitchell, and J.H. Adair, "Effects of Oil Degradation on the Friction and Wear Properties of Silicon Nitride/M-50 Steel Sliding Couples," *Cer. Engr. & Sci. Proc.*, 18[3], 361-368, (1997).

APPENDIX 20, S. Atluri, and D. W. Dareing, "Traction Behavior and Physical Properties of Powder Graphite Lubricants Compacted to Hertzian Pressure Levels," submitted for publication.

APPENDIX 21, P. Cento and D. W. Dareing, "Evaluation of Ceramic Materials in Hybrid Ball Bearings," submitted for publication.

APPENDIX 12, L-Y Chao And D.K. Shetty, "Wear and Fatigue Damage in Ball-on-Rod Rolling Assessed with Steel/Steel, Steel/Si_3N_4 and Si_3N_4/Si_3N_4 Contacts," to be submitted for publication.

Wear and Fatigue Damage in Ball-on-Rod Rolling Assessed with Steel/Steel, Steel/Si_3N_4 and Si_3N_4/Si_3N_4 Contacts

Luen-Yuan Chao and Dinesh K. Shetty
Department of Materials Science and Engineering
University of Utah
Salt Lake City, UT 84112

Abstract

The wear rates, life cycles and fatigue damage in rolling-contact fatigue tests of two bearing-grade silicon nitride materials and two bearing steels (M-50 and AISI-52100) were examined in oil-lubricated conditions. Tests were performed using a three-ball-on-rod rolling contact fatigue tester. Specific materials combinations for the balls and rods were AISI-52100 steel versus M-50 steel, AISI-52100 steel versus silicon nitride (I) and silicon nitride (II) versus silicon nitride (I), respectively. The wear volume loss was assessed using the profilometer and weight measurement techniques. Morphologies of the worn surfaces were characterized using scanning electron microscopy. In the case of AISI-52100 steel in rolling contact with M-50 steel, fatigue lives were controlled exclusively by spallings of the rods. At a contact stress of 5.4 GPa, linearized Weibull plots of the fatigue lives indicated a Weibull slope of 2.27 and L_{10} (the estimated life cycles at the failure probability of 0.1) of 3.9 million stress cycles. In the case of AISI-52100 steel in rolling contact with silicon nitride (I), two types of surface finish were employed for the silicon nitride (average roughness $R_a = 0.18$ μm and 0.08 μm). When the silicon nitride with higher surface roughness was used, fatigue lives were controlled by the wear on the steel balls and the rods showed negligible wear and a polished surface. The volume loss of the balls was found to be linearly proportional to the number of stress cycles. When the silicon nitride with the lower surface roughness was used, fatigue lives were determined either by ball failures or suspensions of the tests at one hundred hours. Both the silicon nitride rods and the steel balls suffered negligible wear in this condition. In the case of silicon nitride (II) in rolling contact with silicon nitride (I), wear behaviors were examined at three different contact stress levels (4.5, 5.5 and 6.5 GPa). Wear losses of the rods and the balls were measured as a function of the stress cycles by suspending tests at different durations. For all the

function of the stress cycles by suspending tests at different durations. For all the conditions, the initial wear rates were high, then steady-state wear rates accompanied by constant surface morphologies on the contact surfaces followed.

I. INTRODUCTION

With the increasing need for energy conservation and adoption of new design features of bearing components in aerospace, nuclear and automotive industries, rolling bearings are now required to service at higher temperatures and higher speeds in order to be more efficient. To satisfy the requirements of these applications, the rolling elements must have sufficient dimensional stability, and oxidation and corrosion resistance to maintain close tolerance and stable operation over long periods in service. Traditional bearing steels, limited by their high temperature hardness, are not qualified for such applications. As a result, over the past three decades research has focused on investigating the feasibility of using structural ceramics as bearing elements[1-7].

Of various structural ceramics evaluated to date, silicon nitride (Si_3N_4) appears to be the most promising material because of its excellent tribological (friction and wear) properties and ability to be processed to near defect-free condition[8,9]. From reaction-bonded and pressureless sintered silicon nitrides to hot-pressed silicon nitride in the 1980s, the rolling contact fatigue and wear resistance of silicon nitride had been continuously improved and eventually became better than those of the bearing steels through controlled processing and microstructure tailoring. To date, the state-of-the-art bearing-grade silicon nitride materials, fabricated by direct hot-isostatic-pressing (HIPing) or pre-sintering and post-HIPing techniques, have even superior rolling contact fatigue and wear resistance than the hot-pressed silicon nitride. With controlled surface finish, current bearing-grade silicon nitride materials provide low coefficients of friction under marginal lubricating conditions. Bearing-grade silicon nitride materials are now employed in hybrid bearings in the form of rolling elements[9] and are being designed in the form of all-ceramic bearings for gas-turbine engines[10].

Successfully employing silicon nitride in advanced bearing applications requires complete understanding of the fatigue and wear properties of silicon nitride. Investigations of such properties of silicon nitride have been conducted in both sliding- and rolling-contact conditions. Most experiments focus on investigating the effects of controlled variables (the mating materials, load, temperature, etc.) on the wear behavior and fatigue lives of silicon nitride.

In sliding contact, Fischer and Tomizawa[11,12] investigated the friction and wear of Si_3N_4 sliding on itself in various dry and humid environments. In dry atmospheres, wear occurred by micro-fractures. In humid environments, wear occurred predominantly by tribochemical reaction associated with the formation of a soft, amorphous, surface layer of SiO_2, the friction coefficient was influenced by the sliding speed, load and temperature. Jahanmir and Fischer[13] investigated the sliding friction and wear of silicon nitride under hydrocarbon lubricants (hexadecane and hexadecane with stearic acid), the friction coefficients and wear rates in those conditions were much lower than in humid air and water environments, which suggested tribochemical reaction was strongly affected by the existence of hydrocarbon at the interface. Sutor[14] studied the wear behaviors of silicon nitride sliding against itself and against M-50 steel at different temperatures and loading conditions, oxidation was found to be an important factor for the wear of both M-50 and Si_3N_4. At high temperatures, the Si_3N_4/M-50 Steel contact had lower friction and wear rate than the Si_3N_4/Si_3N_4 contact due to a lubricating effect of the metal oxides. The damage and surface morphologies of Si_3N_4 in sliding contact at different environments were discussed by Kimura et al.[15]. Recently, the effects of load and temperature on the wear and friction coefficient of Si_3N_4 were systematically studied by Dong and Jahanmir[16], and a transition diagram was suggested.

In rolling contact studies, most investigations, in the early days, mainly focused on evaluating the rolling contact fatigue lives of different grade silicon nitride materials and demonstrating the feasibility of using silicon nitride as a bearing material[5-7]. Systematic studies on the wear behaviors of silicon nitride were limited. Kim et al.[17] investigated the wear behavior of Si_3N_4 in dry rolling contact using a rotating ring-on-ring tester. They observed that the wear rate and wear coefficient increased with increasing load and the wear volume increased proportionally to the number of revolutions. Akazawa and Kato[18] investigated the wear particles of Si_3N_4 in dry rolling - 1% sliding contact using a similar apparatus. Their results indicated that the wear particles of Si_3N_4 were rich in oxygen and silicon, and suggested them to be SiO_2, the size of the wear particles depended on the roughness of the contact surfaces. Lucek[19] used a three-ball-on-rod rolling contact fatigue tester to evaluate the fatigue lives and wear loss of various materials. The HIPed silicon nitride showed the longest fatigue life and least amount of wear as compared to M-50, sialon and hot-pressed silicon nitride. Factors that affecting the rolling contact fatigue life of silicon nitride were discussed by Nishihara et al.[20], fatigue lives were mainly controlled by spallations in a similar pattern of bearing steels. Spallation of silicon nitride could initiate from microstructural defects such as, pores, metallic inclusions and agglomerates, surface cracks generated during grinding could also produce surface failures during rolling contact.

According to the above literature review, it is clear that information on the wear behavior including wear rate and wear mechanism of Si_3N_4 in rolling contact is limited. Systematic studies on this subject are essential for generalized and reliable applications of silicon nitride employed rolling bearings. The present paper discusses the results of a recent effort to study the fatigue lives, wear and surface morphologies of two silicon nitrides and two bearing steels when they are in rolling contacts. Experiments were conducted using a three-ball-on-rod rolling contact fatigue tester. Specific contacts include: (1) bearing steel (AISI-52100) versus bearing steel (M-50), (2) bearing steel (AISI-52100) versus a pre-sintered and post-HIPed Si_3N_4 and (3) a direct HIPed Si_3N_4 versus a pre-sintered and post-HIPed Si_3N_4.

II. EXPERIMENTS

(1). Test Materials

Rolling contact fatigue tests were conducted using four different materials, two bearing steels and two silicon nitride materials. The two bearing steels are M-50 tool steel and AISI-52100 high-carbon chromium steel. Table 1 lists several selected material properties of the four materials. The M-50 steel was obtained in the form of rods, 9.52 mm in diameter and 76.2 mm in length. Surface of these rods was prepared by a three-step grinding procedure and finished with 600 grit diamond wheel. The average roughness (R_a) of the finished surface was measured to be 0.18 μm. The AISI-52100 bearing steel was obtained in the form of balls with their surfaces both finished and deliberately roughened. The average roughness of the finished balls and roughened balls are 0.013 μm and 0.089 μm, respectively.

The two silicon nitride materials investigated in this study are the state-of-the-art bearing grade materials, one is a pressureless sintered and post-HIPed silicon nitride with Y_2O_3 and Al_2O_3 as the sintering additives§, this material is designated as material I in this

§ Grade TSN-03NH, Toshiba Corp., Japan.

paper; the other is a direct-HIPed silicon nitride with MgO as the sintering additive¶, this material is designated as material II in this paper. Figures 1(A) and 1(B) show the microstructures of the two ceramics, elongated β-Si3N4 grains can be seen in both materials. The average grain sizes are submicron in both although the sintered and post-HIPed silicon nitride has a slightly higher aspect ratio than the direct-HIPed silicon nitride. Material I was obtained in the form of rods with 76.2 mm (3-in) in length and 9.7 mm in diameter with a rough ground surface. Material II was obtained in the form of balls with a polished surface.

(2). Rolling Contact Fatigue Test

Experiments were performed on a three-ball-on-rod rolling-contact fatigue (RCF) tester. Figure 2 shows schematically the geometry and rolling condition of the test, the design features and testing procedures of this tester have been described by Glover[21]. The cylindrical specimen, 76.2 mm (3-in) in length and 9.5 mm (0.375-in) in diameter, is held vertically by a precision collet. Three balls, 12.7 mm (0.5-in) in diameter, are equally spaced by a bronze retainer (which is not shown in the figure) and are radially loaded against the cylindrical specimen through the thrust loading of the two tapered bearing cups. The thrust load on the bearing cups is applied by mechanically forcing the upper cup towards the lower cup against three pre-calibrated coil springs associated with the assembly.

The collet and the specimen are rotated by an electric motor mounted in line with the specimen below the tester bench. The three balls are, in turn, driven by the rod and rotate around the rod at a lower speed. A synthetic lubricant with standard specifications, Mil-L-23699, was used in the tests§. Lubricant was supplied by drip feeding onto the top of the rod. Dripping rate was controlled at about 10 drops per minute. A vibration detector coupled with a shutdown device was used to monitored the vibration of the assembly. When a preset vibration level was exceeded, the motor was automatically stopped.

The three-ball-on-rod RCF tester was designed to efficiently generate rolling-contact fatigue data and compare the fatigue performance of various materials. For example, Lucek[19] have used this tester to evaluate the rolling contact fatigue lives and wear behaviors of different materials including M-50 steel, sialon, hot-pressed and direct HIPed Si_3N_4. An important feature of this tester is that since the applied load is pre-calibrated according to the original dimensions of the rod and balls, for materials which suffer from

¶ Grade NBD200, Cerbec Inc., CT, USA.
§ Exxon 2380 Turbo Oil.

wear during test, the contact stress decreases as the wear volume increases[19]. This feature may affect the kinetics of the wear behaviors of the rolling elements.

(3). AISI-52100 Steel (Ball) versus M-50 Steel (Rod)

The first set of tests was conducted using M-50 steel as the rod material and AISI-52100 steel with roughened surface as the balls. The fatigue life data obtained in this series of tests provided the performance of the state-of-the-art bearing steel as a reference. The fatigue life and wear behavior of silicon nitride materials were, thereafter, compared to those of the bearing steels. The initial Hertzian contact stress was selected to be 5.4 GPa.

(4). AISI-52100 Steel (Ball) versus Si_3N_4, I (Rod)

The second set of tests was conducted using the silicon nitride material I as the rod and AISI-52100 steel as the balls. For the silicon nitride, two types of surface finish were employed. In the first type, the surface was ground according to the same procedure as employed for M-50 steel, this resulted in a surface roughness (R_a) of 0.18 μm. In the second type, the surface was further lapped to an average roughness of 0.08 μm. For the balls, both the finished and roughened balls were used in rolling contact with the two types of silicon nitride. The initial Hertzian contact stress was calibrated to be 5.5 GPa.

(5). Si_3N_4, II (Ball) versus Si_3N_4, I (Rod)

The third set of tests was conducted using the silicon nitride material I as the rod and silicon nitride material II as the balls. The combination of the rolling element and the material was based on the availability of the material in the required geometries. For the rod, the silicon nitride material I with the as-ground surface was used. The silicon nitride balls, on the other hand, was obtained in the finished state with an average surface roughness of 0.005 μm. Rolling contact fatigue tests were conducted at three different stress levels, 4.5, 5.5 and 6.5 GPa. Studies focused on the wear and fatigue damage of the two materials, wear volume loss and surface morphology was monitored as a function of stress cycles by suspending tests at different durations.

(6). Cleaning Procedure for the Tested Rods and Balls

To remove the remaining grease on the rolling elements after test, the following procedure was employed. The elements were first ultrasonically cleaned in hexane for ten minutes, the ultrasonically cleaned elements were then rinsed in fresh hexane for five minutes, the balls and rods were finally rinsed in acetone for one minute and dried. Scanning electron microscopic examinations indicated that this procedure was satisfactory.

(7). Assessment of the Wear Volume Loss

The wear volume loss of the rods was assessed using two techniques. In the first technique, the surface profile of the wear track on the rod was measured with a profilometer perpendicular to the rolling direction. Wear volume was calculated by multiplying the enclosed area of the valley with the diameter of the rod. Three profiles were measured on each track at approximately 120^o apart, the average cross-sectional area was used. In the second technique, the weights of the rods or the balls were measured before and after the test to obtain the weight loss of each element, the wear volume loss was calculated from the weight loss using the densities of the materials. Comparison of the results obtained from the two methods will be presented in a later section.

III. RESULTS AND ANALYSIS

(1). Rolling-Contact Fatigue Lives of M-50 Steel (Rod) in Rolling Contact with AISI-52100 Steel (Balls)

Figure 3 shows the linearized Weibull plots of the fatigue lives of M-50 steel in rolling contact with roughened AISI-52100 balls. In this series of tests, fatigue lives were exclusively determined by spalling of the rods, weight measurements and surface profiles of the wear tracks indicated that wear volume losses on the rods and balls were both very small. Figure 4 shows the scanning electron micrographs of two typical spalls of M-50 steel. In the two micrographs, the rolling direction is indicated by the arrows. A two-parameter Weibull distribution function was used to fit these data, which resulted in a Weibull slope of 2.27 and L_{10} (the estimated stress cycles at the failure probability of 0.1) of 3.9 million stress cycles.

(2). Fatigue Lives and Wear of Si_3N_4, I (Rod) in Rolling Contact with AISI-52100 Steel (Balls)

In the condition of Si_3N_4 in rolling contact with steel balls, results are discussed in two categories. In the first category, the silicon nitride rods used had a as-ground surface (i.e. $R_a = 0.18\ \mu m$). Totally sixteen tests were conducted, eight tests were performed using the steel balls with the polished surface ($R_a = 0.013\ \mu m$) and the other eight tests were performed using the roughened steel balls ($R_a = 0.089\ \mu m$). All sixteen tests were stopped by the automatic shutdown device due to excessive vibration. Fig. 3 shows the linearized Weibull plots of these data in comparison with the data obtained from M-50 steel. Since the lifetime durations of those tests using the polished balls and of those tests using the roughened balls were very similar, these data were mixed and statistically ranked together.

Results of the weight measurements indicated that the weight loss of the balls was significant in every test and the weight loss of the silicon nitride rod was, however, too small to be measured. Therefore, the excessive vibration was probably due to the excessive uneven wear on the steel balls. This was further confirmed by the surface profiles on the wear track obtained from profilometer measurements and observations of the worn surfaces under the scanning electron microscopy. The surface profile measured in the direction perpendicular to the wear track on the rod showed no indication of wear, but profiles on the balls indicated that the balls were significantly flattened out on their rolling orbits. Figures 5(a) and 5(b) show the scanning electron micrographs of the original surface of a roughened steel ball and the worn surface after rolling contact with silicon nitride for 23.2 hours (the longest one, corresponds to ~ 11.97 million stress cycles). It is evident that the original surface feature caused by the roughening procedure has been completely removed by the rolling motion and the worn surface reveals significant plastic deformation.

In the second category, the silicon nitride rod used had a lapped surface (i.e. R_a = 0.08 μm). Six tests were performed, three tests with the roughened steel balls and three tests with the polished steel balls. For the three tests with the roughened balls, the durations (28 ~ 66 hours) are all longer than those of the tests in the first category, all three tests were stopped due to spallings occurred on one of the three balls. For the three tests with the polished balls, two of them were suspended at 100 hours, and one test was stopped due to spalling occurred on one of the balls. For comparison, the six data are also plotted in Fig. 3 along with the 16 data in the first category. Weight measurements, surface profiles and scanning electron microscopic examinations all indicated that both the steel balls and silicon nitride rod suffered from very minor and negligible wear from these tests. Figure 5(c) shows the worn surface of a roughened steel ball after rolling contact with the lapped silicon nitride for 28.1 hours (~ 14.5 million stress cycles), the surface feature shown in Fig. 5(c) is close to the feature of the original surface, i.e. Fig. 5(a), but smoother (more like it has been further polished). However, the surface morphology of Fig. 5(c) is very different from the morphology shown in Fig. 5(b) which has been in rolling contact with the as-ground silicon nitride for comparable number of stress cycles and suffered significant wear.

For all tests in the above two categories, the weight loss of each steel ball was converted to the volume loss using the density of the ball (see Table 1). Within each test, the average volume loss the three balls was calculated and plotted in Figure 6 as a function of the stress cycles. It is clear that the difference in the wear behaviors of the steel balls of the two categories is significant. When the steel balls are in rolling contact with a silicon nitride having higher surface roughness, the balls wear rapidly and the volume loss is almost proportional to the number of stress cycles. On the other hand, when the steel balls are in rolling contact with a silicon nitride having low surface roughness, the steel balls suffer from negligible wear. In the meantime, it is interesting to note that disregarding the surface roughness of the silicon nitride, the wear behavior of the polished and roughened steel balls appeared to be the same. This is probably due to the fact that silicon nitride has much higher hardness than that of AISI-52100 steel and, therefore, the surface roughness of the steel balls has very small influence on the wear behavior of such combination.

(3). Wear and Fatigue Damage of Si_3N_4, I (Rod) in Rolling Contact with Si_3N_4, II (Balls)

Fatigue-life distributions of the two bearing-grade silicon nitride materials when they were in rolling contact against each other under the designed contact stresses were not assessable within a practical time frame. This is probably because that fatigue lives of silicon nitride are typically determined by spallings which initiated from microstructural defects, and the two silicon nitride materials being investigated, fabricated with controlled and improved processing techniques, have achieved almost defect-free condition. Therefore, experiments were designed to focus on studying the wear and surface morphologies after rolling contact fatigue as a function of stress cycles.

It is the objective to conduct fatigue tests at three different stress levels (4.5, 5.5 and 6.5 GPa). To date, rolling contact fatigue tests have been conducted under two contact stresses, 5.5 and 6.5 GPa. In both conditions, wears on the rods and balls were evident from both weight measurements and surface profiles of the wear tracks. A typical surface profile of the wear track on a silicon nitride rod is shown in Figure 7. Similar pattern of the profile has been reported by Lucek[19]. The volume loss of the rod calculated from surface profiles are compared to the volume loss calculated from the weight measurements in Figure 8. It can be seen that the agreement between the two sets of data is very good, which indicates that the volume loss estimated from either of the two methods is reliable. It was, however, due to the following two reasons that the weight measurement technique was selected to be used for further analysis: (1) it was found that the shape of the profile, the maximum depth and the cross-sectional area slightly varies at different locations within each track, which implied that the wear was not exact uniform along the entire track and (2) the volume loss of the ball is not easy to calculate form the surface profile.

Figure 9 shows the wear volume loss of the silicon nitride rod as a function of stress cycles at two different contact stresses (5.5 and 6.5 GPa). At each condition (i.e.

stress cycles), two tests were performed and only the average volume loss is plotted in this figure. The data obtained at the contact stress of 6.5 GPa indicated that the wear rate of the rod was initially high and then reached a steady state where the wear rate was small. At 5.5 GPa, the data are not complete yet. However, it can be seen that the wear volume loss is less than that at 6.5 GPa.

Figure 10 shows the wear volume loss of the silicon nitride balls as a function of stress cycles measured from those same tests as indicated in Fig. 9. Since there were three balls per each test, totally six balls were involved at each condition. The average volume loss and the standard deviation at each condition are plotted. At 6.5 GPa, the wear behavior of the balls reveals the same trend as of the rod, the wear rate was initially high and then a steady-state wear followed.

The surface morphologies of the rod and the balls after rolling contact were examined using the scanning electron microscopy. Figures 11(a) and (b) show the surface morphology change of the silicon nitride rod, the surface morphology shown in Fig. 11(a) is the original as-ground surface, the grinding grooves with their widths in the range about 1 ~ 2 μm can be seen. Fig. 11(b) shows the worn surface after rolling contact with the silicon nitride balls at 5.5 GPa for 100 hours, the grinding grooves were all disappeared but left a polished surface. The worn surface also has somewhat similar features of a etched surface where the β-Si_3N_4 grains can be roughly seen and certain amount of the grain boundary phase has been removed. The worn surface in Fig. 11(b) also suggestes that plastic deformation have occurred during rolling contact.

Figures 12(a) and (b) show the surface morphology change of the silicon nitride balls that have been in rollin contact with the rod at the same contact stress for the same amount of time (i.e. 5.5 GPa for 100 hours, however, note that the stress cycles on each ball is 1/3 of the stress cycles on the rod). Fig. 12(a) is the original as-polished surface and Fig. 12(b) is the worn surface. Note that the worn surface reveals similar features of the rod material, i.e. plastic deformation, grain boundary phase being removed and the β-Si_3N_4 grains.

IV. DISCUSSION

The present paper summarizes the results obtained from three different combinations of materials in rolling contact assessed using a three-ball-on-rod rolling contact fatigue tester, steel/steel, steel/Si_3N_4 and Si_3N_4/Si_3N_4. The rolling contact fatigue lives of the state-of-the-art bearing steel, M-50, when in rolling contact with an old generation bearing steel (AISI-52100), were exclusively determined by spallings. The fatigue lives can be described by a two-parameter Weibull distribution.

When the silicon nitride (material I) was in rolling contact with the bearing steel, AISI-52100, two different results were obtained based on the surface roughness of the silicon nitride. When the silicon nitride with the higher surface roughness was used, fatigue lives were determined exclusively by the wear on the steel balls and the silicon nitride showed negligible wear and a polished surface. The volume loss of the steel balls was found to be linearly proportional to the number of stress cycles. When the silicon nitride with the lower surface roughness was used, tests were terminated either by ball failures or suspensions of the tests at one hundred hours without failure of either component. Both the silicon nitride rods and the steel balls suffered negligible wear in this series. These results probably suggested that surface roughness of the silicon nitride played an important role in building the elasto-hydrodynamic film during rolling contact. The elasto-hydrodynamic film is generally believed to be an important factor for the wear of the rolling elements.

In the case of silicon nitride in rolling contact with silicon nitride, wear volume loss has been established as a function of stress cycles at 6.5 GPa for both elements. Experiments are continuing to complete the data at 5.5 and 4.5 GPa. The kinetics of the wear behavior, for both elements, from a fast wear rate regime to a steady-state wear regime is probably controlled by two factors: (1) the nature of the specific rolling contact fatigue tests used in this study, in other words, the contact stress decreased when the materials suffered from wear, and (2) change of the morphologies of the contact surfaces from the as-machined surfaces to plastically deformed and very fine-scaled polished surfaces, which led to a continuous change of the structure of the elasto-hydrodynamic film between the two faces.

V. CONCLUSIONS

The wear rate, life cycles and fatigue damage in rolling-contact fatigue tests of two bearing-grade silicon nitrides and two bearing steels were examined in oil-lubricated conditions. Results are concluded as follows

(1). In the steel/steel contact, the fatigue lives are exclusively determined by spalling and wear volume losses on both rolling elements are very small.

(2). In the steel/Si_3N_4 contact, fatigue performance is very sensitive to the surface roughness of the silicon nitride. Higher surface roughness of the silicon nitride leads to high wear rate on the steel, low surface roughness of the silicon nitride leads to very low wear rate on the steel. In both cases, silicon nitride shows negligible wear and a polished surface.

(3). In the Si_3N_4/Si_3N_4 contact, both the rod and the ball show an initial high wear rate regime followed by a steady-state regime with low wear rates. In the steady state regime, the morphologies of the contact surfaces remain almost constant.

ACKNOWLEDGEMENT

This research is initiated by University of Florida and sponsored by AFOSR/URI. University of Utah participated in this project as a subcontractor to University of Florida. Financial support from the two places is greatly acknowledged.

REFERENCES

1. E. V. Zaretsky and W. J. Anderson, " Rolling-Contact Fatigue Studies with Four Tools Steels and a Crystallized Glass Ceramic," Transactions of the ASME, *Journal of Basic Engineering*, December, 603-12 (1961).
2. K. M. Taylor, L. B. Sibley, and J. C. Lawrence, " Development of a Ceramic Rolling Contact Bearing for High Temperature Use," *Wear*, **6**, pp 226-40 (1963).
3. D. Scott and J. Blackwell, " Hot Pressed Silicon Nitride as a Rolling Bearing Material - A Preliminary Assessment," *Wear*, **24**, pp 61-67 (1973).
4. R. J. Parker and E. V. Zaretsky, " Fatigue Life of High-Speed Ball Bearings with Silicon Nitride Balls," Transactions of ASME, *Journal of Lubrication Technology*, **97** [7] 350-57 (1975).
5. H. R. Baumgartner, " Ceramic Bearings for Turbine Applications"; pp 423-43 in Proc. of the Fifth Army Materials Technology Conference, 1978.
6. B. Bhushan and L. B. Sibley, " Silicon Nitride Rolling Bearings for Extreme Operating Conditions," *ASLE Transactions*, **25** [4] 417-28 (1982).
7. R. N. Katz and J. G. Hannoosh, " Ceramics for High Performance Rolling Element Bearings: A Review and Assessment," *Int. J. High Technology Ceramics*, **1**, pp 69-79 (1985).
8. J. F. Chudecki, " Ceramic Bearings - Applications and Performance Advantages in Industrial Applications," SAE Technical Paper Series, paper No. 891904 (1989).
9. Material Innovations, " Silicon Nitride for High-Performance Bearings," *Ceramic Bulletin*, **69** [7] 1113-15 (1990).
10. G. Hamburg, P. Cowley, and R. Valori, " Operation of an All-Ceramic Mainshaft Roller Bearing in a J-402 Gas-Turbine Engine," *Lubrication Engineering*, **37** [7] 407-415 (1981).
11. T. E. Fischer and H. Tomizawa, " Interaction of Tribochemistry and Microfracture in the Friction and Wear of Silicon Nitride," *Wear*, **105**, pp 29-45 (1985).
12. H. Tomizawa and T. E. Fischer, " Friction and Wear of Silicon Nitride at 150 ^oC to 800 ^oC," *ASLE Transactions*, **29** [4] 481-88 (1986).
13. S. Jahanmir and T. E. Fischer, " Friction and Wear of Silicon Nitride Lubricated by Humid Air, Water, Hexadecane and Hexadecane + 0.5 Percent Stearic Acid," *STLE Transactions*, **31** [1] 32-43 (1987).
14. P. Sutor, " Tribology of Silicon Nitride and Silicon Nitride-Steel Sliding Pairs," *Ceramic Engineering and Science Proc.*, July-Dec. Vol. **5**, pp 460-69 (1984).
15. Y. Kimura, K. Okada, and Y. Enomoto, " Sliding Damage of Silicon Nitride in Plane Contact"; pp. 361-368 in Wear of Materials, Vol. **1**, edited by K. C. Ludema (1989).
16. X. Dong nad S. Jahanmir, " Wear Transition Diagram for Silicon Nitride," *Wear*, **165**, pp 169-80 (1993).
17. S.S. Kim, K. Kato, K. Hokkirigawa and H. Abe, " Wear Mechanism of Ceramic Materials in Dry Rolling Friction," *Journal of Tribology*, **108** [10] 522-526 (1986).
18. M. Akazawa and K. Kato, " Wear Properties of Si_3N_4 in Rolling-Sliding Contact," *Wear*, **124**, pp 123-132 (1988).
19. J. W. Lucek, " Rolling Wear of Silicon Nitride Bearing Materials," Presented at the Gas Turbine and Aerospace Congress and Exposition, June 1990. ASME Paper No. 90-GT-165.
20. Y. Nishihara, H. Nakashima, N. Tsushima, and S. Ito, " Factors That Affect Rolling Contact Fatigue Life of Ceramics and Rolling Contact Fatigue Life of Ceramic Balls and Rollers," Presented at the Gas Turbine and Aeroengine Congress and Exposition, June 1990. ASME Paper No. 90-GT-377.

21. D. Glover, " A Ball-Rod Rolling ContactFatigue Tester," *Rolling Contact Fatigue Testing of Bearing Steels, ASTM STP 771*, J. J. C. Hoo, ed., American Society for Testing and Materials, pp 107-24 (1982).

Table 1. Selected Properties of the Two Silicon Nitrides and Bearing Steels.

Material	Density (g/cm^3)	Young's Modulus (GPa)	Poisson's Ratio	Fracture Toughness ($MPa\sqrt{m}$)
Si_3N_4, I (Grade: TSN-03NH)	3.23	308	0.29	5.15±0.06#
Si_3N_4, II (Grade: NBD-200)	3.16	320	0.26	4.1*
M-50	7.80	207	0.29	-
AISI-52100	7.80	207	0.29	-

Measured by the authors using the chevron-notched short-bar technique.

* Reported by the manufacturer.

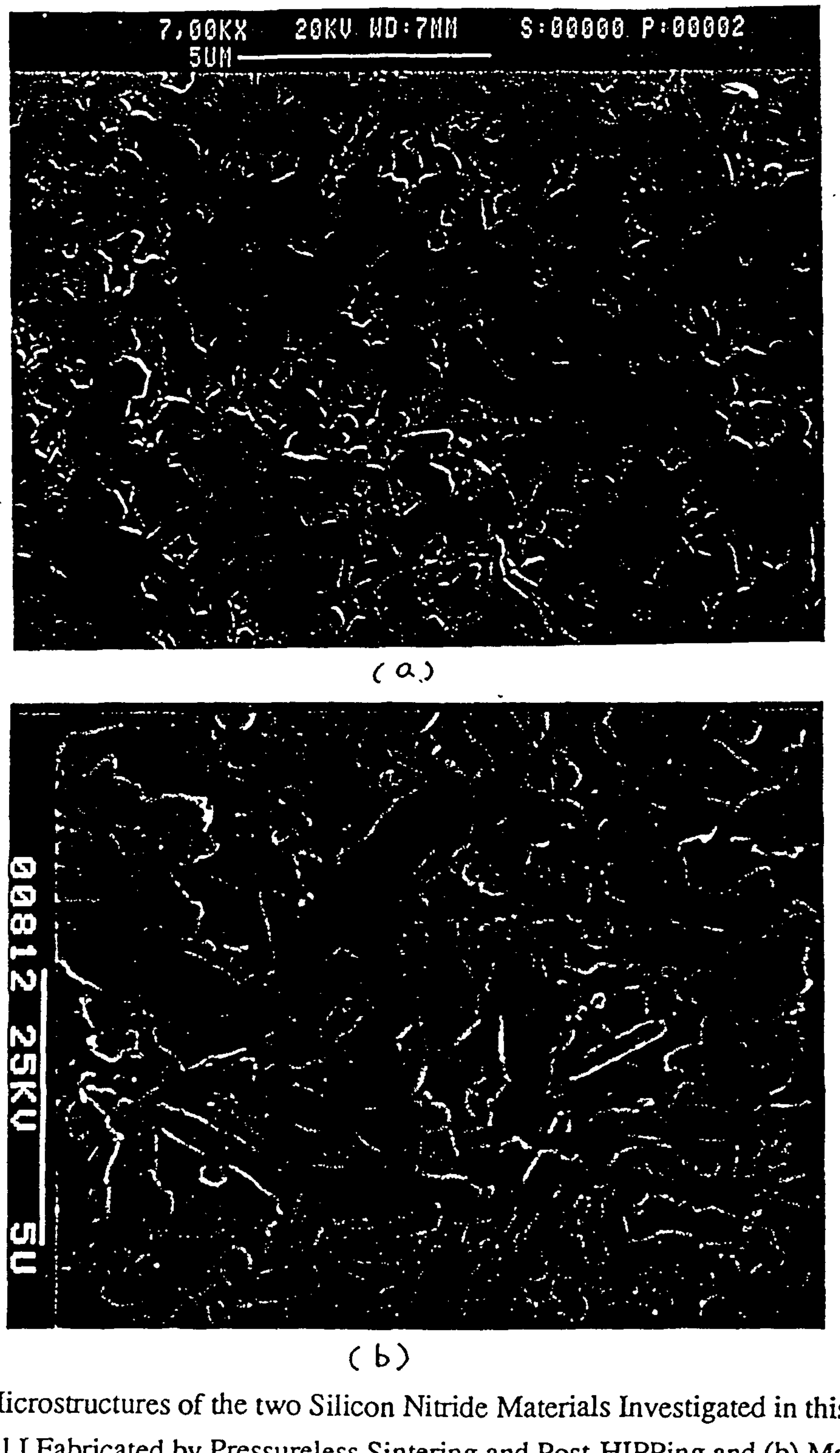

Figure 1. Microstructures of the two Silicon Nitride Materials Investigated in this Study. (a). Material I Fabricated by Pressureless Sintering and Post-HIPPing and (b) Material II Fabricated by Direct HIPPing.

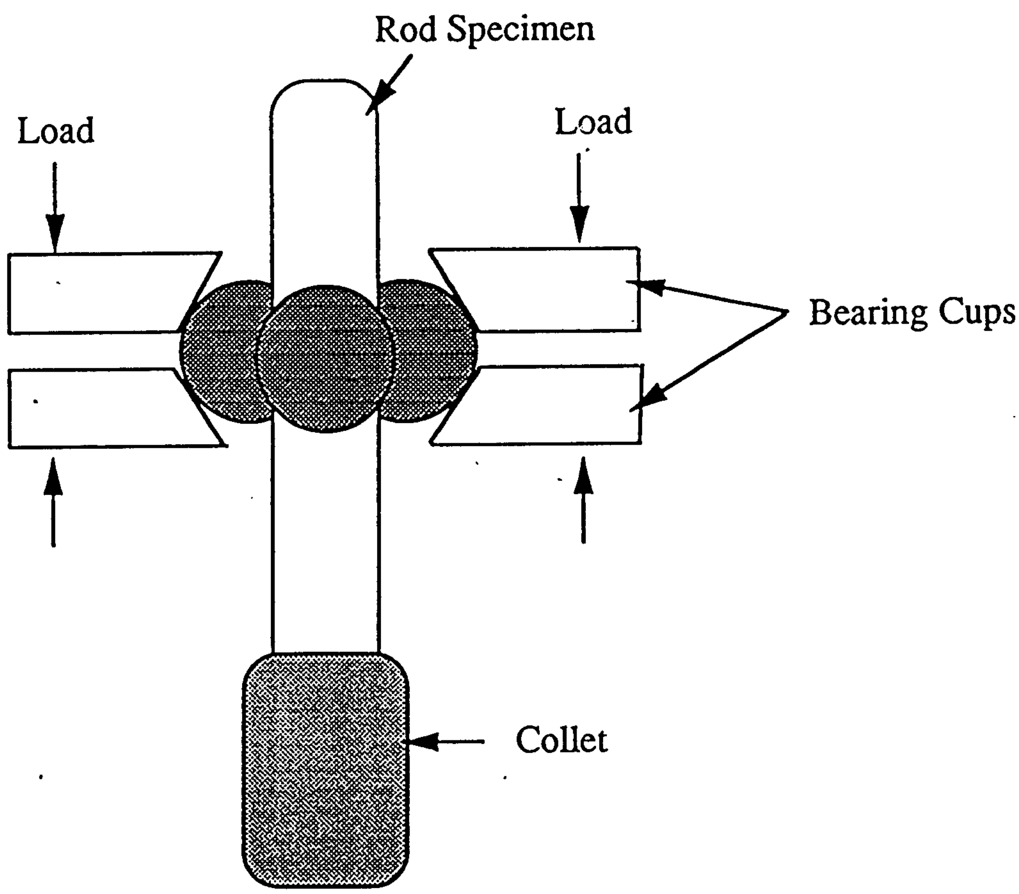

Figure 2. Three-Ball-on-Rod Rolling Contact Fatigue Tester Used in This Study

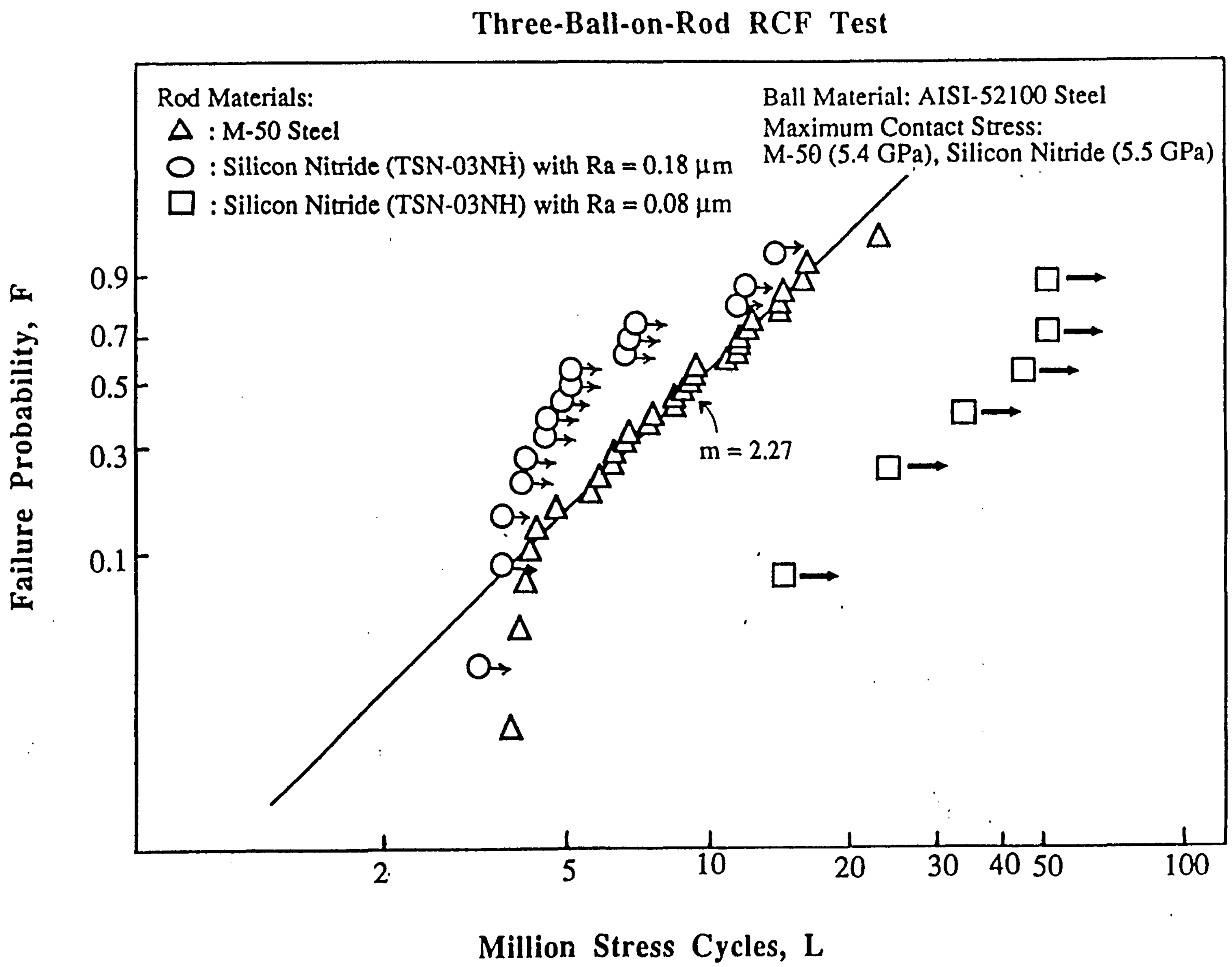

Figure 3. Linearized Weibull Plots of the Rolling Contact Fatigue Data.

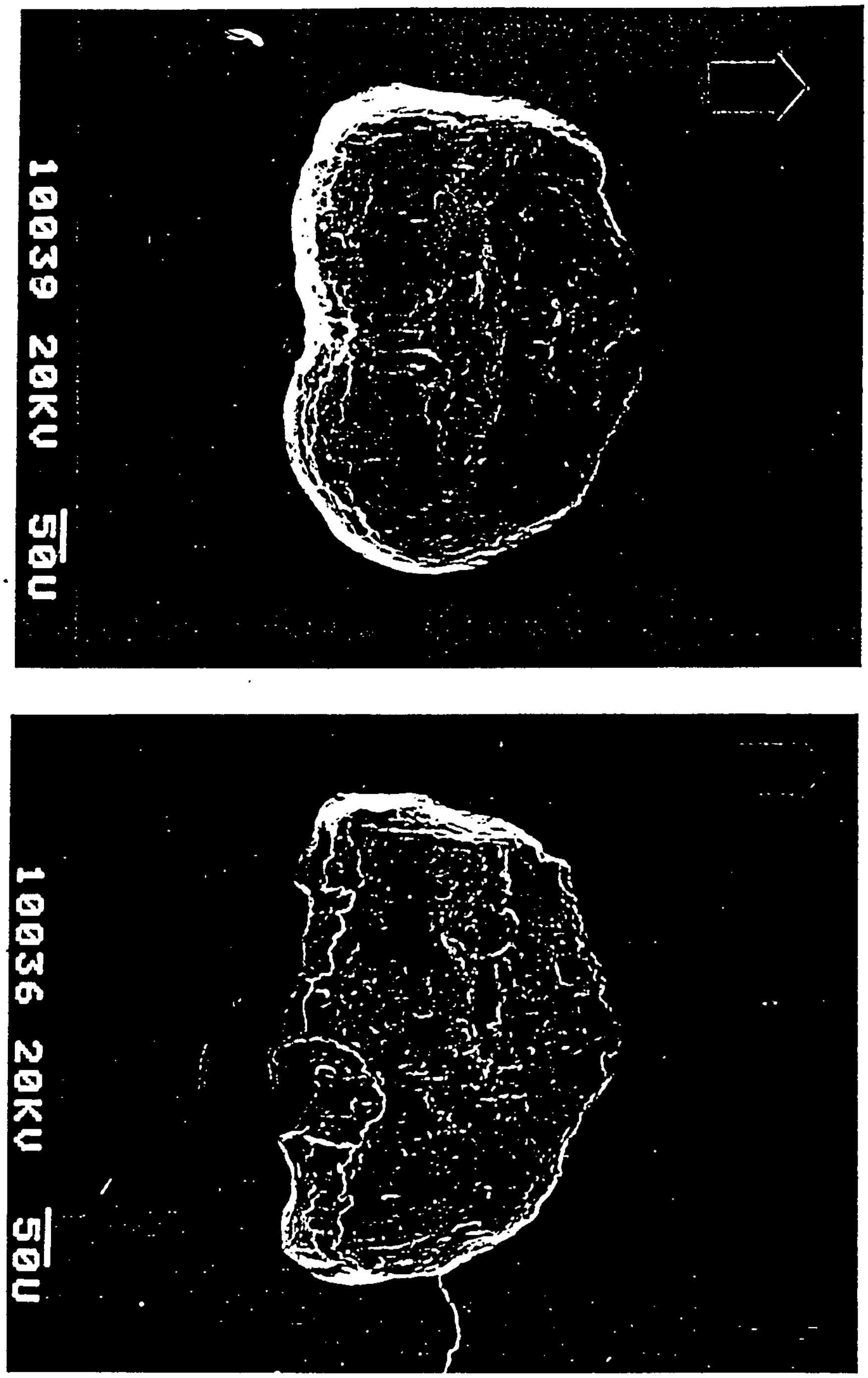

Figure 4. Typical Spallings of M-50 Steel When in Rolling Contact with AISI-52100 Steel. (Arrows Indicate the Rolling Direction)

(a)

(b)

Figure 5. Scanning Electron Micrographs of the Surface of a AISI-52100 Steel Ball, (a) the Original Surface and (b) the Worn Surface after Rolling Contact with Silicon Nitride Rod with As-Ground Surface.

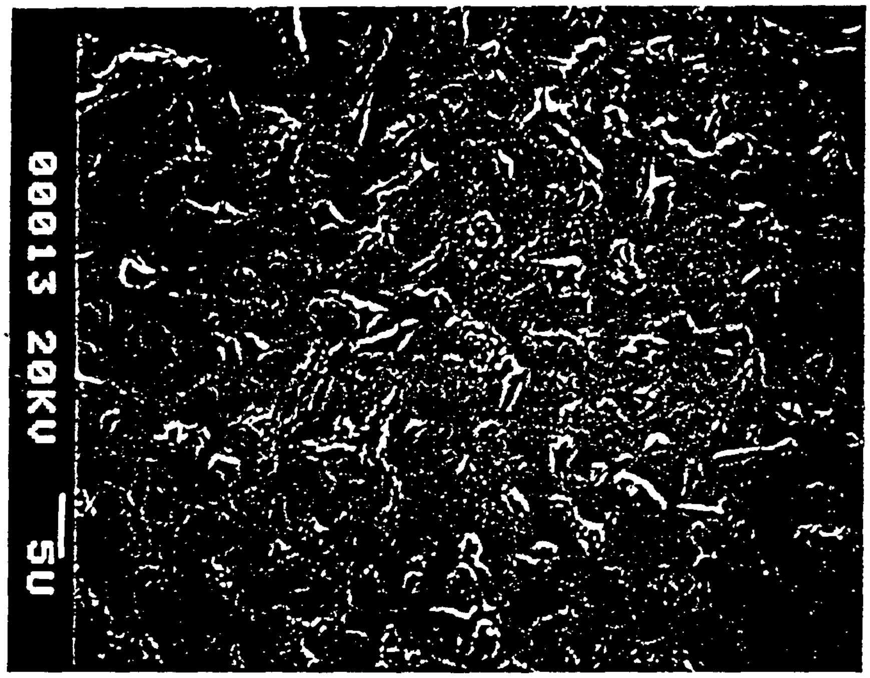

(C)

Figure 5 (c). Scanning Electron Micrograph of the Worn Surface of a Roughened AISI-52100 Steel Ball after Rolling Contact with Silicon Nitride Rod with As-Lapped Surface.

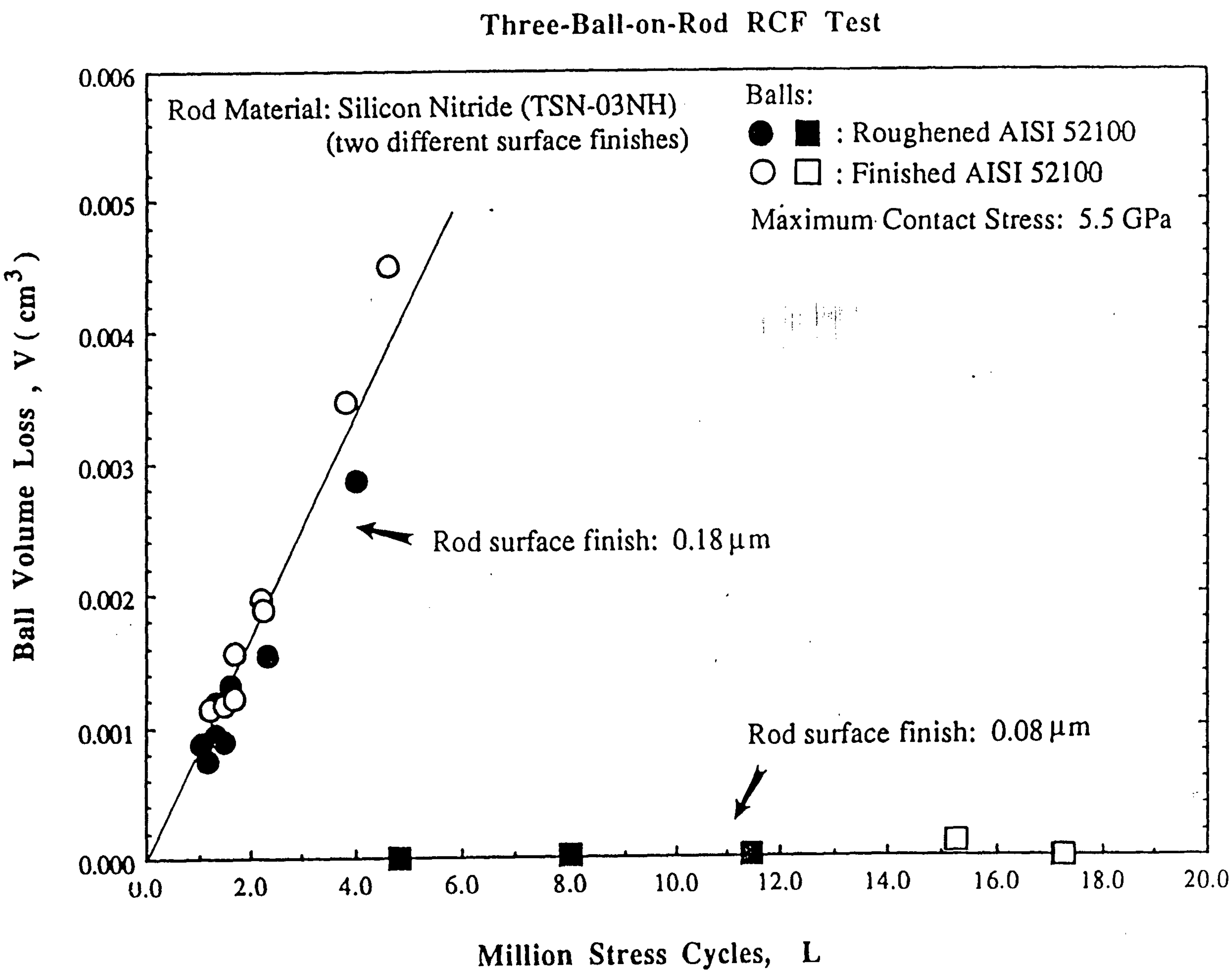

Figure 6. Comparison of the Volume Loss as a Function of Stress Cycles of AISI-52100 Steel Balls in Rolling Contact with Silicon Nitride Rods Having Different Surface Finish.

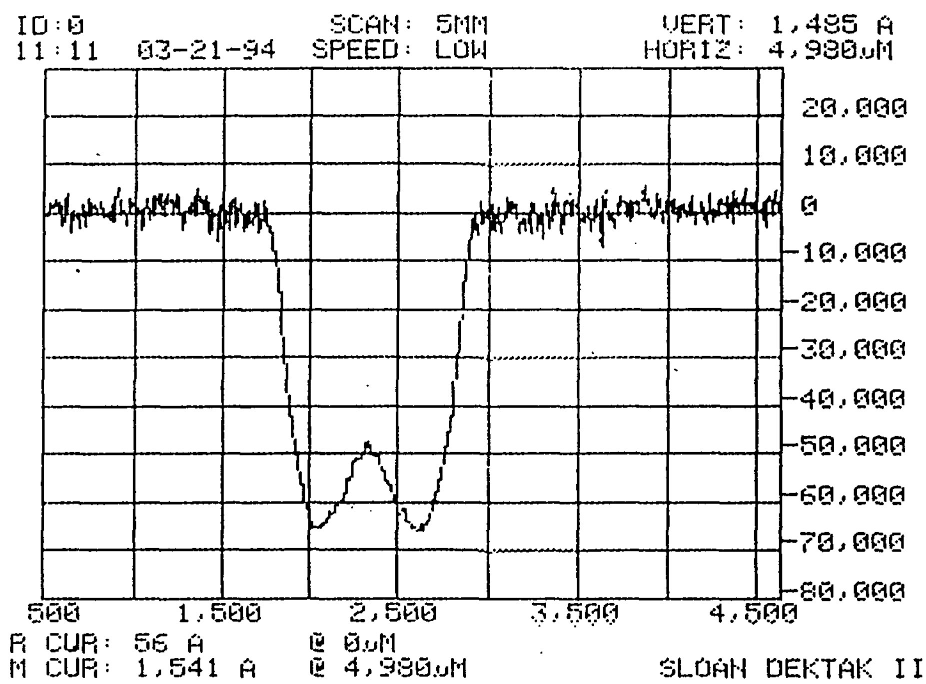

Figure 7. Typical Surface Profile of a Wear Track on a Silicon Nitride (Material I) Rod. (after Rolling Contact with Si_3N_4 (Material II) Balls at 5.5 GPa for 100 Hours)

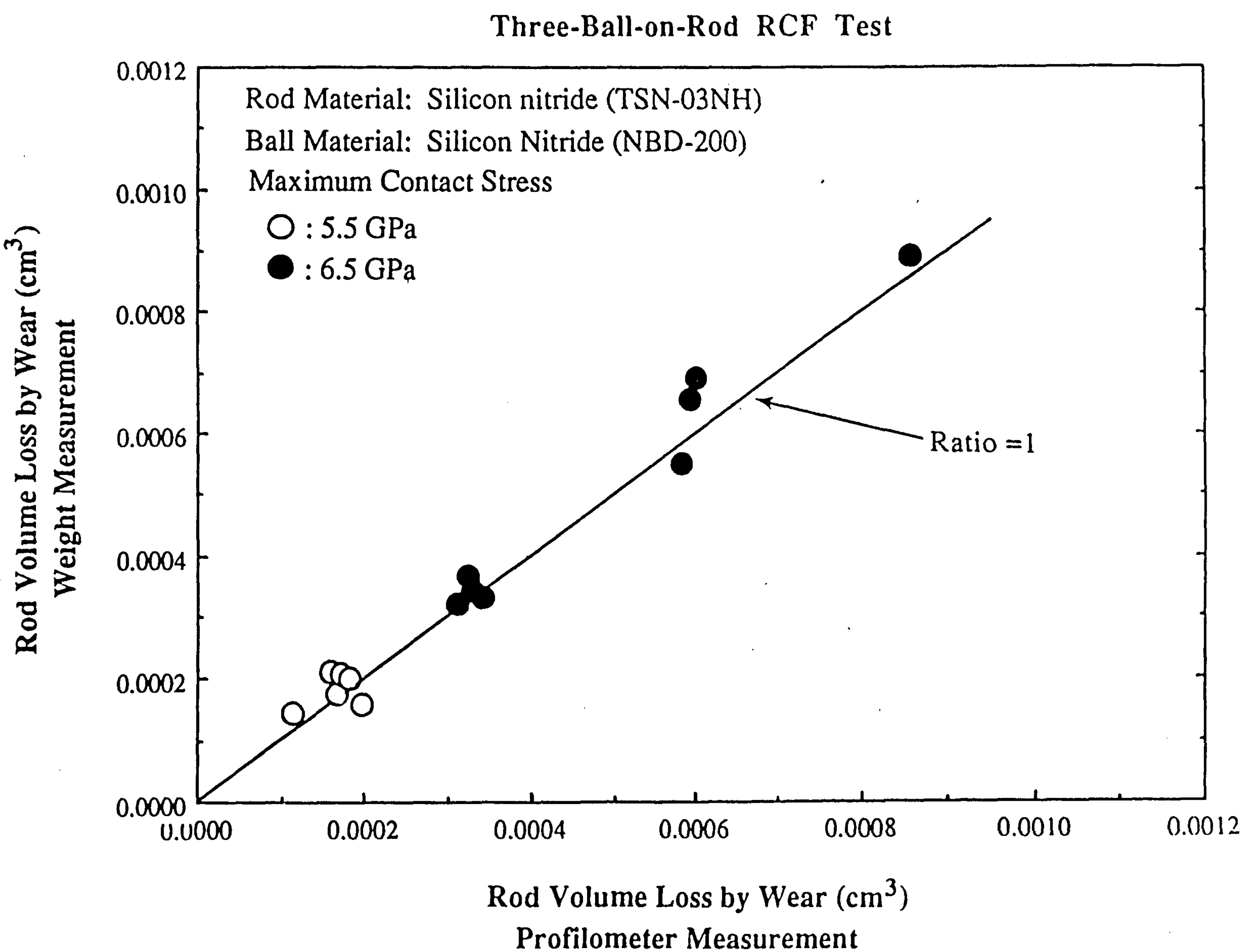

Figure 8. Comparison of the Volume Loss Data Calculated from the Weight Measurement and the Surface Profile Techniques.

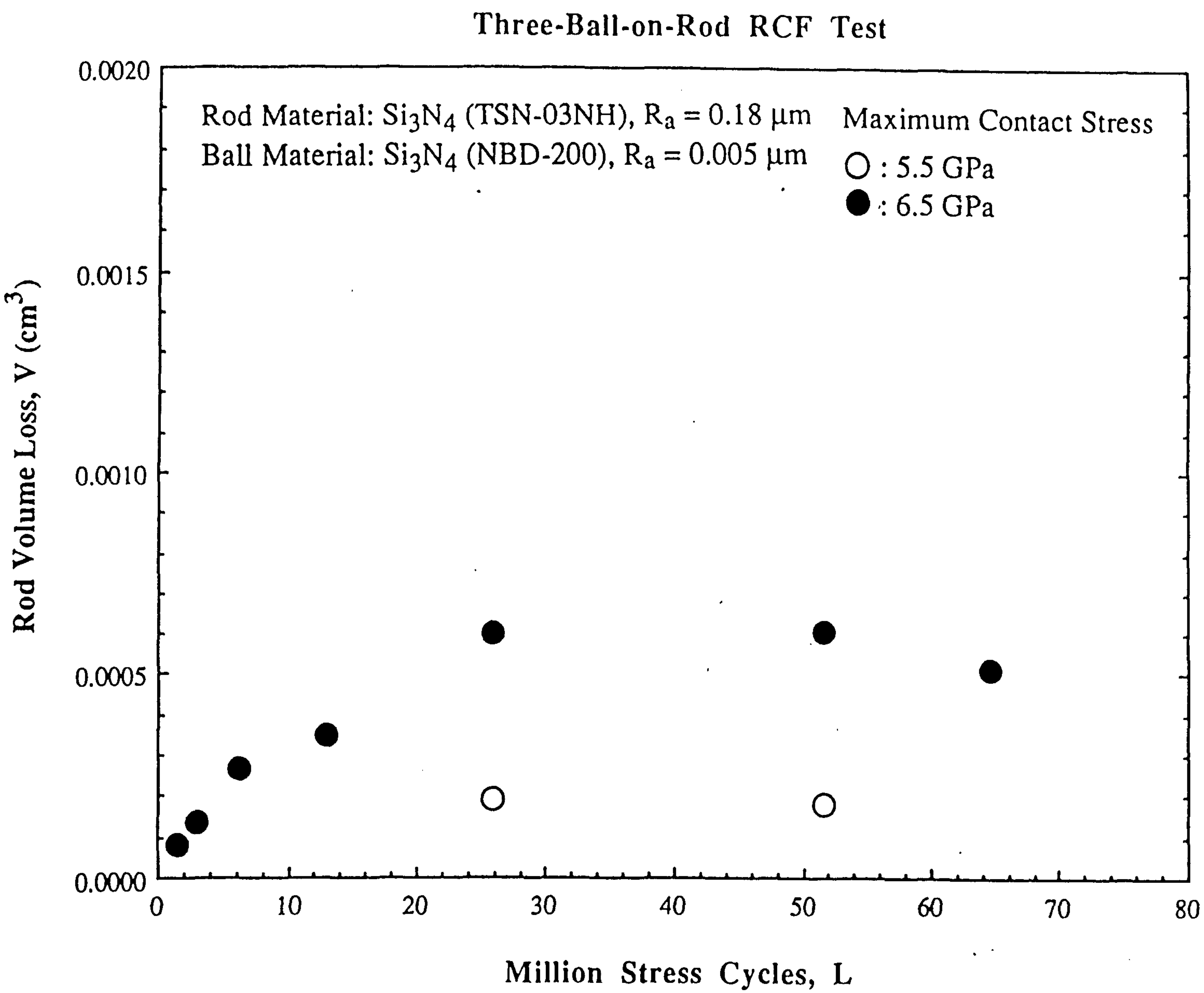

Figure 9. Silicon Nitride (Material I) Rod Volume Loss As a Function of Stress Cycles When in Rolling Contact with Silicon Nitride (Material II) Balls.

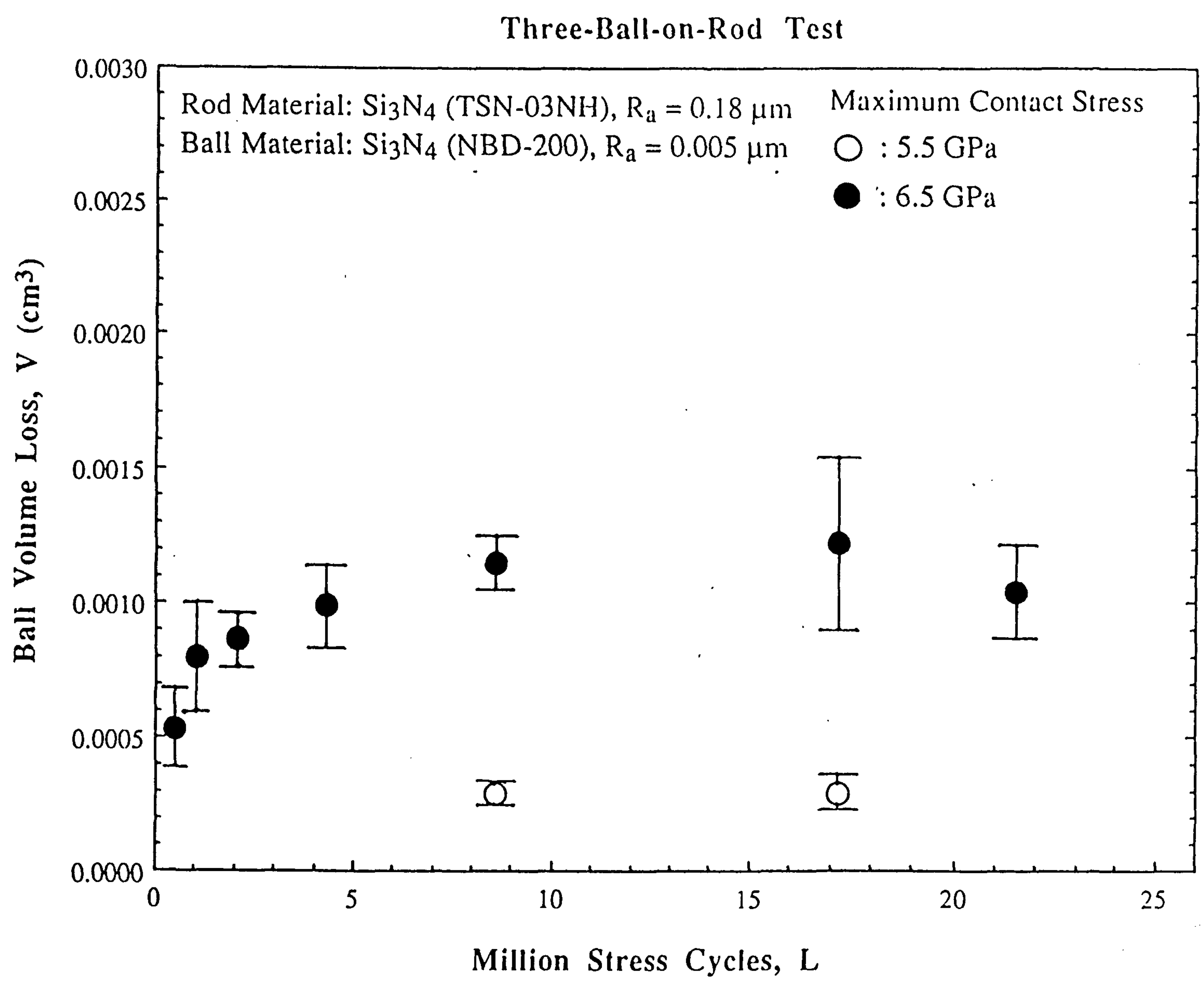

Figure 10. Silicon Nitride (Material II) Ball Volume Loss As a Function of Stress Cycles When in Rolling Contact with Silicon Nitride (Material I) Rod.

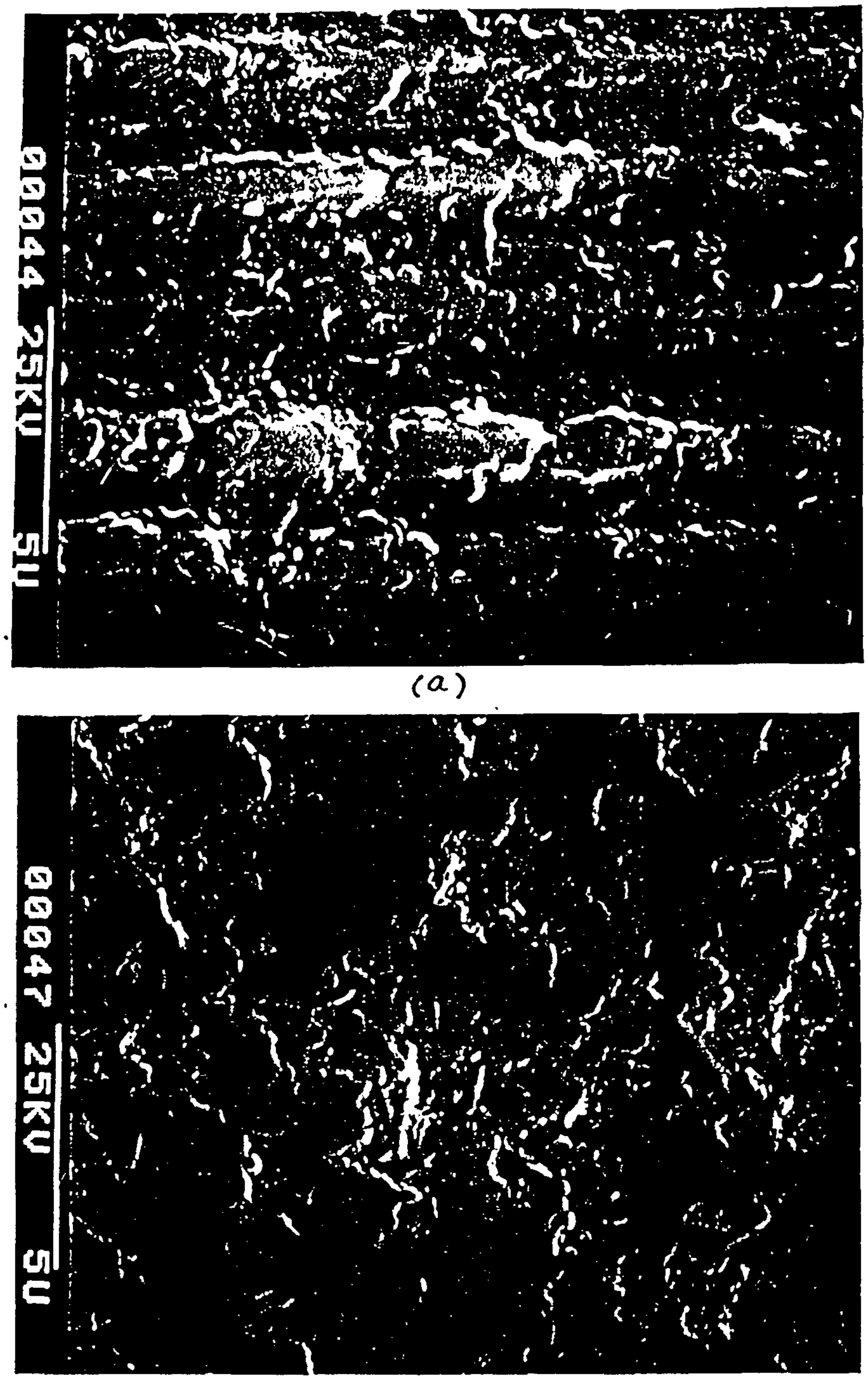

(a)

(b)

Figure 11. Surface Morphologies of the Silicon Nitride (Material I) Rod, (a) the Original As-Ground Surface and (b) the Worn Surface After Rolling Contact with Silicon Nitride (Material II) Balls at 5.5 GPa for 100 Hours (~ 52 Million Stress Cycles).

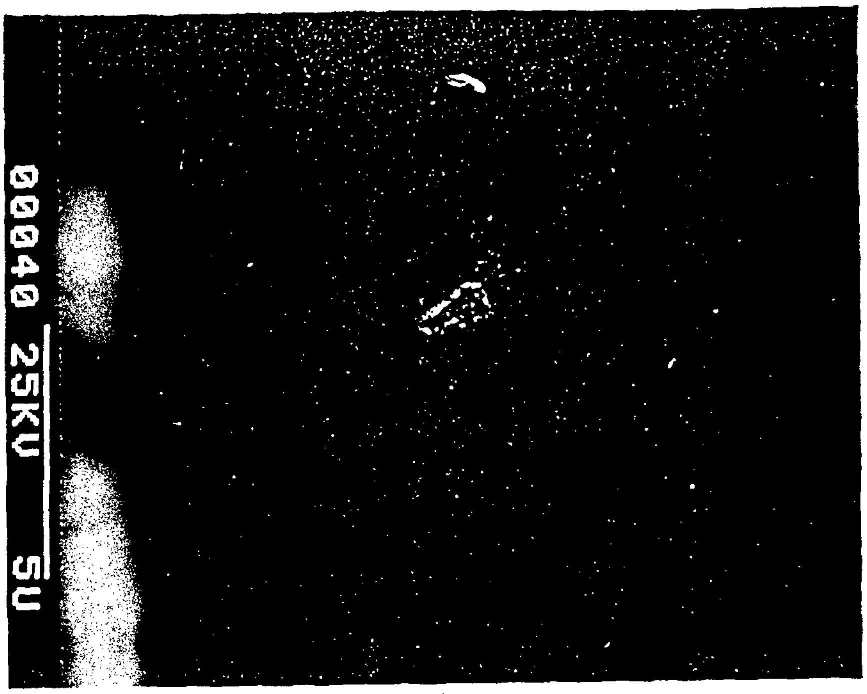

(a).

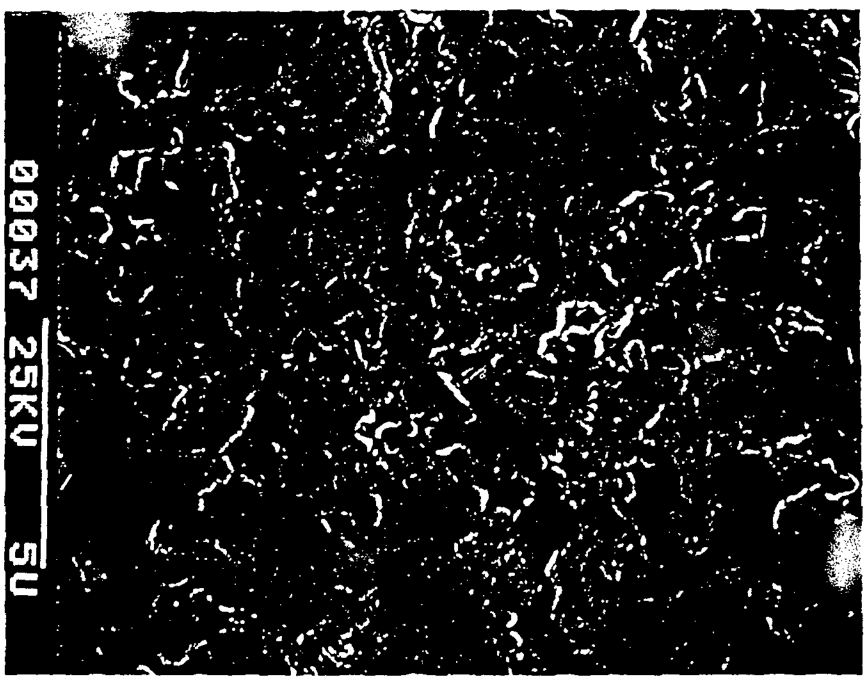

(b)

Figure 12. Surface Morphologies of the Silicon Nitride (Material II) Ball, (a) the Original As-Polished Surface and (b) the Worn Surface After Rolling Contact with Silicon Nitride (Material I) Rod at 5.5 GPa for 100 Hours (~ 17.3 Million Stress Cycles).

APPENDIX 13, L-Y Chao And D.K. Shetty, "Wear and Fatigue Damage in Ball-on-Rod Rolling Assessed with Steel/Steel, Steel/Si_3N_4 and Si_3N_4/Si_3N_4 Contacts," ABSTRACT OF M.S. Thesis to be presented to the graduate scholl at the Univerisyt of Utah, 1998. Thesis copy available upon request. D.K. Shetty, advisor.

Wear and Fatigue Damage in Ball-on-Rod Rolling Assessed with Steel/Steel, Steel/Si_3N_4 and Si_3N_4/Si_3N_4 Contacts

Luen-Yuan Chao and Dinesh K. Shetty
Department of Materials Science and Engineering
University of Utah
Salt Lake City, UT 84112

Abstract

The wear rates and surface damage in rolling-contact fatigue tests of two bearing-grade silicon nitride materials and two bearing steels (M-50 and AISI-52100) were examined in oil-lubricated conditions. Tests were performed using a three-ball-on-rod rolling contact fatigue tester. Specific materials combinations for the balls and rods were AISI-52100 steel versus M-50 steel, AISI-52100 steel versus silicon nitride (I) and silicon nitride (II) versus silicon nitride (I), respectively. The wear volume loss was assessed using the profilometer and weight measurement techniques. Morphologies of the worn surfaces were characterized using scanning electron microscopy. In the case of AISI-52100 steel in rolling contact with M-50 steel, fatigue lives were controlled exclusively by spallings of the rods. At contact stress of 5.4 GPa, linearized Weibull plots of the fatigue lives indicated a Weibull slope of 2.27 and L_{10} of 3.9 million stress cycles. In the case of AISI-52100 steel in rolling contact with silicon nitride (I), two types of surface finish were employed for the silicon nitride (average roughness R_a = 0.18 μm and 0.08 μm). When the silicon nitride with higher surface roughness was used, fatigue lives were controlled by the wear on the steel balls and the rods showed negligible wear loss and a polished surface. The volume loss of the balls was found to be proportional to the number of stress cycles. When the silicon nitride with the lower surface roughness was used, fatigue lives were determined either by ball failures or suspensions of the tests at one hundred hours. Both the silicon nitride rods and the steel balls suffered negligible wear in this condition. In the case of silicon nitride (II) in rolling contact with silicon nitride (I), wear behaviors were examined at three different contact stress levels (4.5, 5.5 and 6.5 GPa). Wear loss of the rods and the balls was measured as a function of the stress cycles by suspending tests at different durations. For all the conditions, the initial wear rates were high, then steady-state wear rates accompanied by constant surface morphologies on the contact surfaces appeared.

OUTLINE

I. Introduction

II. Experiments

(1). Test Materials

(2). Rolling Contact Fatigue Tests

(i). M-50 Steel Rod in Rolling Contact with AISI-52100 Balls

(ii). Si_3N_4 (I) Rod in Rolling Contact with AISI-52100 Balls

(iii). Si_3N_4 (I) Rod in Rolling Contact with Si_3N_4 (II) Balls

III. Results and Analysis

(1). Rolling Contact Fatigue Lives of M-50 Steel.

(2). Effect of Surface Finish of Si_3N_4 on the Rolling Wear of AISI-52100 Steel.

(3). Wear Behaviors of Silicon Nitride (I) in Rolling Contact with Silicon Nitride (II).

IV. Discussions

V. Conclusions

Three-Ball-on-Rod RCF Test

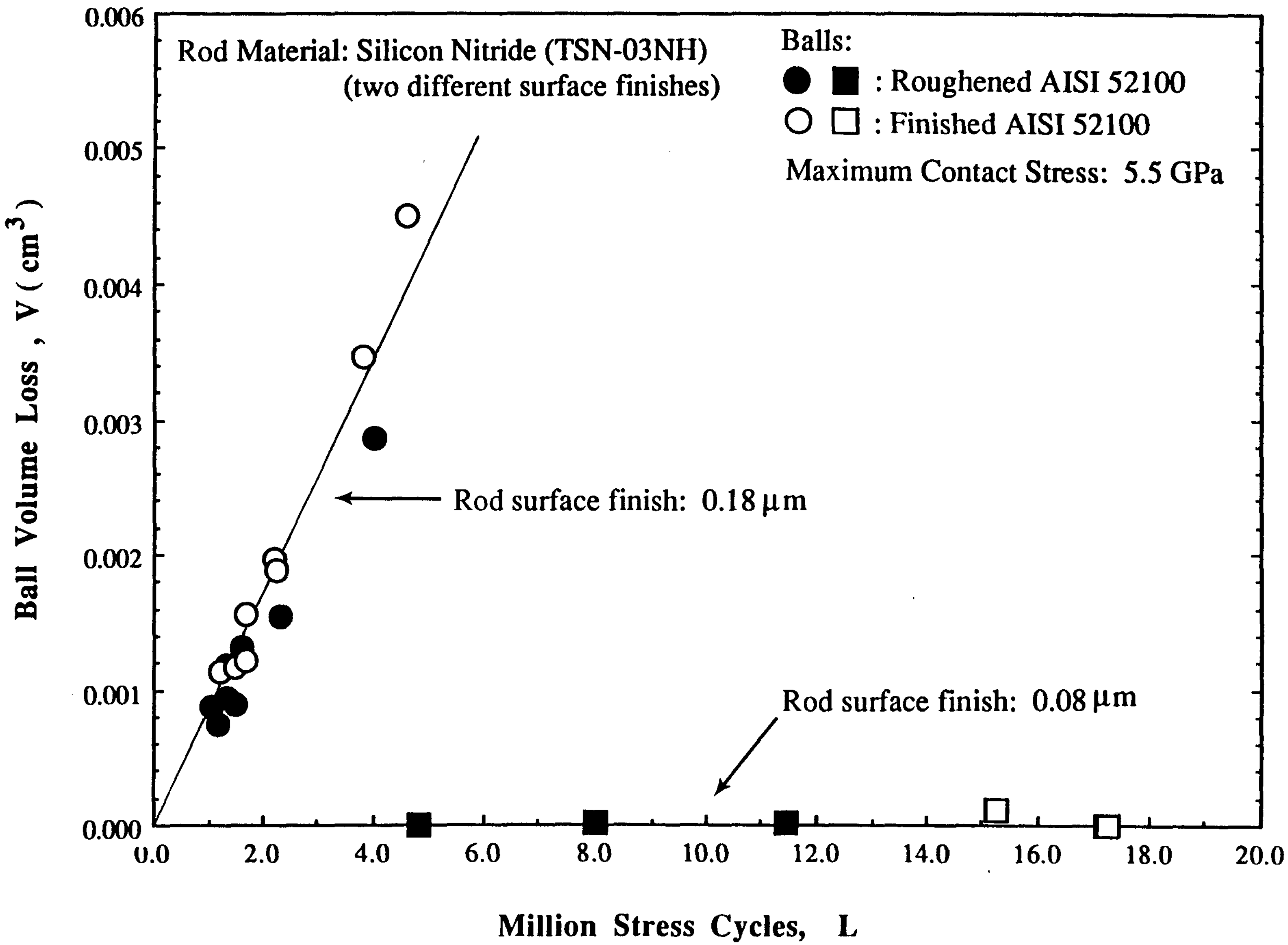

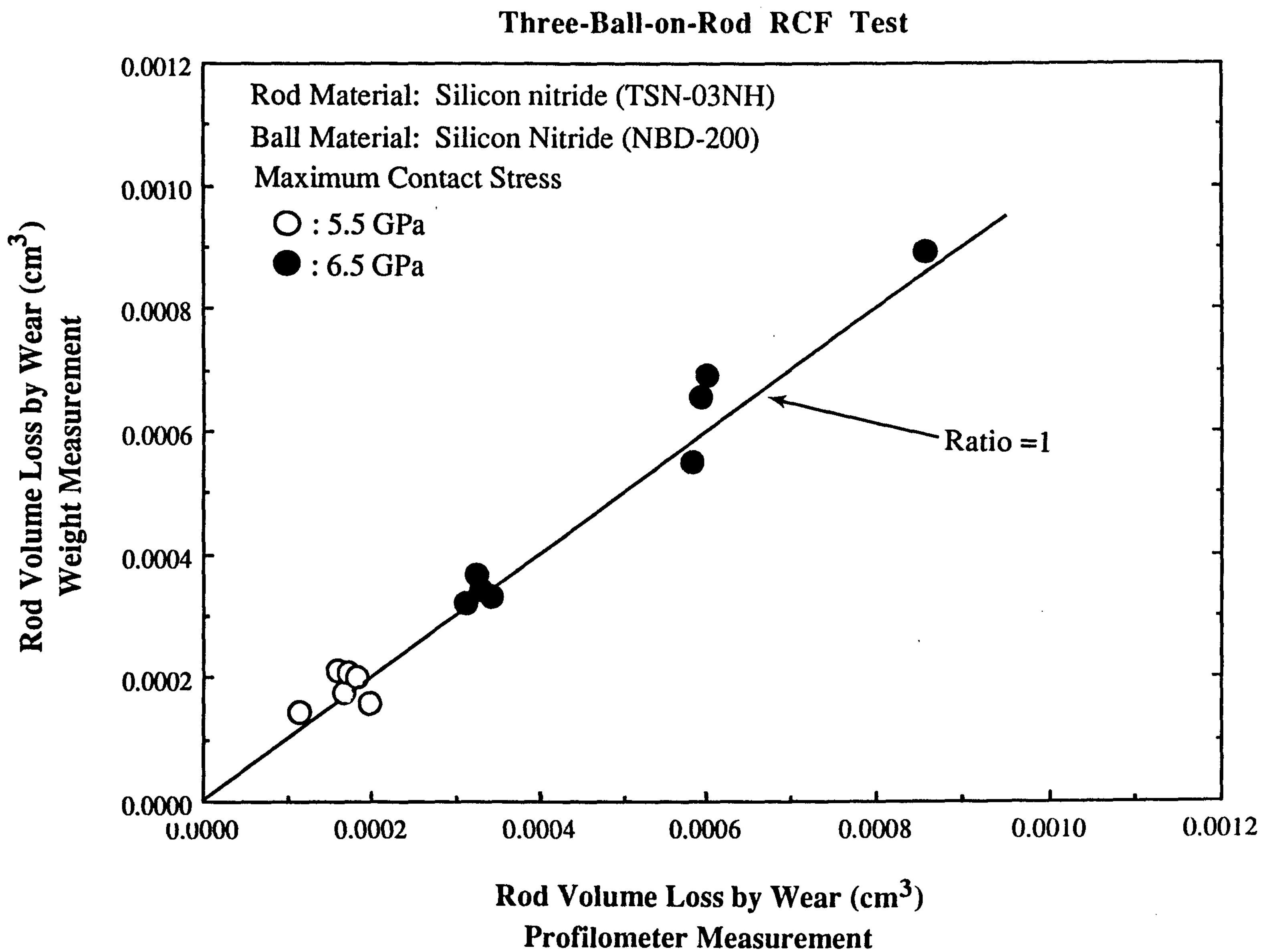

Three-Ball-on-Rod RCF Test
Rod Material: Silicon nitride (TSN-03NH)
Ball Material: Silicon Nitride (NBD-200)
Maximum Contact Stress
: 5.5 GPa
: 6.5 GPa
Ratio =1
0.0000
0.0002
0.0004
0.0006
0.0008
0.0010
0.0012
Rod Volume Loss by Wear (cm3)
Weight Measurement
Rod Volume Loss by Wear (cm3)
Profilometer Measurement

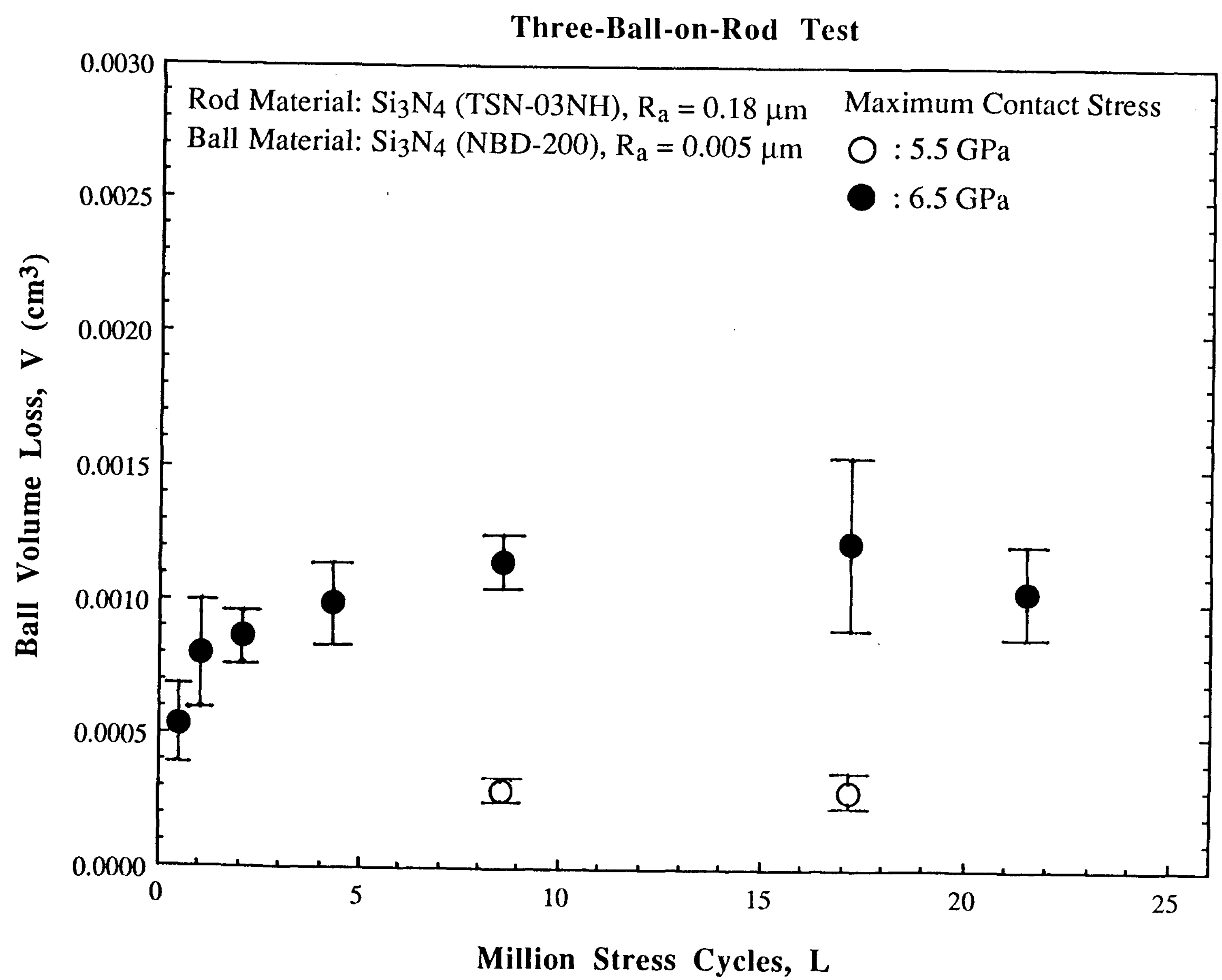

Three-Ball-on-Rod Test
Rod Material: Si3N4 (TSN-03NH), Ra = 0.18 μm
Ball Material: Si3N4 (NBD-200), Ra = 0.005 μm
Maximum Contact Stress
: 5.5 GPa
: 6.5 GPa
0.0030
0.0025
0.0020
0.0015
0.0010
0.0005
0.0000
0
5
10
15
20
25
Ball Volume Loss, V (cm3)
Million Stress Cycles, L

APPENDIX 14, S. Akunuri, "Wear Characteristics of Silicon Nitride-M50 Steel Hybrid Bearing System," Abstract of M.S. Thesis presented to the Graduate School, University of Florida, July 1995. Thesis copy available upon request. J.H. Adair, thesis advisor.

Abstract of Thesis Presented to the Graduate School
of the University of Florida in Partial Fulfillment of the
Requirements for the degree of Master of Science

WEAR CHARACTERISTICS OF
SILICON NITRIDE-M50 STEEL HYBRID BEARING SYSTEM

By
Sreeram Akunuri

December 1995

Chairperson: James H. Adair
Major Department: Materials Science and Engineering

The overall objective of this thesis is to characterize the wear behavior of the silicon nitride-M50 steel hybrid bearing system as a function of several important parameters including the initial Hertzian contact stress, relative humidity, temperature, linear speed, lubrication, and surface treatment. The primary objective of this research is to isolate the effect of each parameter listed above. The wear characteristics of this hybrid system are strongly dependent on combinations of the above parameters.

The lubricated tests were performed using Exxon Turbo Oil 2380 and, as expected, there is a significant improvement in the friction and wear properties. The friction coefficient increases at first and then reduces with increase in initial Hertzian contact pressure. EDS analysis indicates considerable amount of oxide formation on both pin and disk, which affects the friction and wear behavior. The compaction of the oxides into a glaze at higher Hertzian contact pressures, which acts as a solid lubricant, could be the reason for the low wear

rates at higher Hertzian contact pressures. Significant amount of material transfer from pin to disk and vice versa is seen in EDS analysis.

Variation in linear speed in the range of 6.5 cm/s to 14.5 cm/s did not significantly change the friction coefficient values. The effect of relative humidity on the friction coefficient was more profound in the unlubricated tests than in the lubricated tests. The wear rates decreased with percent relative humidity. The silicon presence on the wear track on the M50 steel disk indicates that the silicon nitride also undergoes wear, but to a lesser extent. The presence of iron on the pin and silicon on the disk, in the form of oxides, indicates that there is significant amount of material transfer from the pin to the disk and vice versa. The results indicate that relative humidity plays an important role in material transfer.

DLC coated samples showed a drastic reduction in the friction coefficient under unlubricated conditions. The friction coefficient increased as %RH increased at room temperature tests, indicating that atmospheric conditions play a role in the wear properties of DLC coated samples.

The friction coefficient increases as a function of temperature, in the range of 50 to 300°C. There is a reduction in the friction coefficient at 400°C and then increases for the 500°C test. The DLC coating degrades by oxidation at high temperatures and at 400°C the low friction coefficients could be attributed to oxide gases formed which act like a lubricant and reduce the friction coefficient at these temperatures. AFM results indicate the presence of pits on the M50 steel disk, which could be due to the reaction between the steel and the lubricant.

APPENDIX 15, F. Mohammadi, J.H. Adair, E.D. Whitney, and J.K. West, "An Infrared Spectroscopy Analysis of MgO-Doped Silicon Nitride," *Cer. Trans.*, 69, 53-58 (1995). Non-thesis M.S.

APPENDIX 16, D.J. Mitchell, J.J. Mecholsky, Jr., and J.H. Adair, "Rolling contact fatigue and wear analysis of M50-M50 all-steel and Si_3N_4-M50 hybrid bearing rolling element systems using lubricants contaminated with Arizona test dust or single crystal α-Al_2O_3 particulate.

Rolling contact fatigue and wear analysis of M50-M50 all-steel and Si_3N_4-M50 hybrid bearing rolling element systems using lubricants contaminated with Arizona test dust or glycothermally synthesized α-Al_2O_3 particulate

David J. Mitchell, John J. Mecholsky, Jr, James H. Adair
Department of Materials Science and Engineering
University of Florida, Gainesville, FL 32611, USA

Abstract

Ball-on-rod rolling contact fatigue experiments were performed using the M50-M50 all-steel bearing system and the Si_3N_4-M50 hybrid bearing system. Experiments were performed using a jet turbine engine lubricant in as-received condition or with particulate contaminants added. The added particulate contaminants were Arizona test dust or glycothermally synthesized α–Al_2O_3. Wear performance of the all-steel and hybrid bearing systems were compared with and without particulate contaminants in the lubricant. Wear surfaces were analyzed using optical microscopy, scanning electron microscopy, surface profilometry, and atomic force microscopy. Wear mechanisms, specific wear rates, roughness of wear track surfaces, and failure mechanisms were determined for all systems. The primary wear mechanism produced in rolling contact fatigue experiments is shown to be contact stress fatigue, with secondary mechanisms of indenting, cutting and plowing occurring as particulate debris passes through the elastohydrodynamic lubricant layer in the bearing-race gap.

1. Introduction

Improvements in rolling bearing design, material compositions, and lubricants have advanced bearing performance dramatically in the past 20 years. Advances in ceramic rolling element compositions, metal microstructure control, and lubricant additives have increased bearing performance and lifetimes [1]. The use of Si_3N_4 rolling elements in a thrust bearing has been predicted to produce a 2.5x gain in bearing lifetime in an aircraft gas turbine engine [2]. Pratt & Whitney has had success inserting advanced hybrid bearings using Si_3N_4 rolling elements in the US Space Shuttle liquid oxygen fuel turbopumps and in the engines of the next generation of US fighter aircraft. The improved wear resistance and lifetime of hybrid bearings using Si_3N_4 rolling elements offer advantages in fuel economy and repair costs. Si_3N_4 rolling elements have a low thermal expansion coefficient, high strength and hardness, high thermal and chemical stability, and low density, providing less centrifugal force on the raceway at high rotational speeds. Ceramic rolling elements are also non-magnetic and, unlike all-steel bearings, will not weld when exposed to extreme rotational speed, friction, heat, or loss of lubricant during operation. The major disadvantage of Si_3N_4 rolling elements is their increased cost over all-steel bearings. Reducing the cost of production and non-destructive evaluation (NDE) of hot isostatically pressed (HIP) Si_3N_4 rolling elements is necessary for the introduction of high quality hybrid bearings into major applications.

While these performance improvements benefit bearing system operations, they bring new challenges to researchers evaluating and comparing different rolling element material candidates. Current bearing and lubrication systems are potentially capable of infinite fatigue life, given proper elastohydrodynamic lubrication (EHL) and performance within a fatigue limit stress. Different life analysis techniques are being explored to better represent the conditions actually experienced by bearings in service and to take into account the fatigue limit stress [3-5]. Researchers are seeking consistent methods to accelerate RCF tests in a manner representative of the bearing's true environment. Initially, Hertzian contact stresses were raised to over 6 GPa (870 ksi). When ceramic-metal hybrid bearing test specimens experience high contact stresses, there is an initial widening of the wear track on the softer metal surface, causing an increased contact area, and a resultant decrease in Hertzian contact stress. The reduction in stress occurs even if the load is held constant, because the area supporting the load is larger. This is not representative of actual jet engine bearing conditions. Actual bearing stresses in jet engines do not normally exceed 2-3 GPa (290-435 ksi), while many fatigue test rigs operate around 5.5 GPa (800 ksi). At stresses near 6 GPa (870 ksi) one particular Si_3N_4 rolling element composition performed poorly compared to another, whereas in service both performed equally well [6]. For some ceramic compositions this high Hertzian stress affects the mode of wear, but this is not always the case [7]. Thus it is important to balance accelerated testing conditions with component materials to produce representative bearing life and performance results. The accelerated testing conditions explored in this research were high Hertzian contact stress, lubricant contaminated with Arizona Test Dust (ATD) particulate, and lubricant contaminated with glycothermally synthesized α–Al_2O_3 particulate. The particulate contaminants were added to the lubricant to evaluate their capability of reducing test time and the wear mechanisms they induce.

Contamination of the lubricant by particulate debris is one of the most common failure initiators in operating bearing systems [8-10]. A common wear scenario in actual jet engine bearing systems occurs when hard particles remain after grinding and finishing operations during the machining and assembly of the engine components. These particles are difficult to remove and some inevitably remain as the lubricant is added to the engine for the first time. Pre-denting the rolling elements has been explored by other research teams [11]. Pre-denting the samples, while representing the effect of particles in the system, makes it difficult to evaluate how the material responds to contaminant particles over time. Advances in surface finish techniques are negated, and the response of the surface finish to the other components in the system is impossible to discern if samples are roughened before testing. The lubricant does thermally degrade during use, but actual jet engines burn oil during operation. Fresh lubricant is added after running, which replenishes additives. Adding oil does not remove contaminants from the system, however, which means that particulate contaminated lubricants are the most representative accelerated wear testing systems [12]. Particulate contaminated lubricants enable accelerated wear testing without increasing the Hertzian contact stress to a level which may change the wear and failure mechanisms relative to the stress environments experienced in operation. Bearing materials, lubricant type and particulate contaminant composition, size distribution, hardness, and morphology are interrelated factors which determine the combination of wear mechanisms which will result.

2. Experimental Method

2.1. Rolling contact fatigue experiments

This study was performed using a rolling contact fatigue (RCF) test apparatus (NTN-Bower) with a three-ball-on-rod configuration [13]. Bearing systems simulated were the M50-M50 all-steel system and the Si_3N_4 ball-M50 race hybrid bearing system. The balls are thrust-loaded against the rod by two cups held in place with three equally spaced springs. The springs help maintain a constant load during the test, provided the wear track does not become wider than the initial Hertzian contact region. The rod samples used for all experiments were 9.5 mm (3/8 in) diameter rods made of M50 VIM VAR steel (R_c=61.4). The ball samples were 12.7 mm (1/2 in) diameter grade 5 balls made from M50 VIM VAR steel (R_c=61.4) or Toshiba TSN-03NH Si_3N_4 (H_v~1500). In order to represent jet engine conditions, a MIL-L-23699 jet engine lubricant was used. The rod sample was driven at 3600 rpm producing 2.389 stress cycles per revolution. All particulate contaminated lubricant tests were run using a concentration of 1 gram of powder to 4 liters of oil (0.006 volume percent particulate). The RCF experiments were run under the accelerated testing conditions listed in Table 1.

2.2. Particulate contaminants

Researchers have been using ATD to accelerate bearing tests for many years. The 'fine' grade of ATD used for these tests consists of particles >70 µm in diameter with a broad particle size distribution and random particle morphologies. The average chemical composition of the ATD was provided by the vendor (Powder Technology Incorporated) and is shown in Figure 1. ATD is composed primarily of SiO_2 and Al_2O_3, with the remainder being various other oxides. The Al_2O_3 particles used in this study were glycothermally synthesized to produce a chemically pure and phase pure α–Al_2O_3 powder with a mean particle size of 1-3 µm, a narrow particle size distribution, and a highly controlled platelet morphology [14]. Particle size distributions of the two powders are shown in Figure 2. The ATD size distribution was specified by the vendor and was determined using a Multisizer IIE (Coulter) particle size analyzer. The Al_2O_3 distribution was determined using an electro-zone (Elzone®) particle size analyzer. The Al_2O_3 contaminated lubricant should provide a more consistent test environment at lower stresses because of its smaller, more uniform particle size and narrow size distribution. It also simulates a common wear scenario in actual jet engine bearing systems of hard particulate contaminants in the lubrication system. The particle size and morphological differences between the ATD and Al_2O_3 powders are apparent in the scanning electron photomicrographs shown in Figure 3(a) (JEOL 6400 SEM) and (b) (JEOL 35CF SEM), respectively.

2.3. Wear analysis

Optical microscopy (Nikon OPTIPHOT metallurgical optical microscope with polarizing lenses) was used to determine wear mechanisms on M50 rod wear track surfaces. Scanning electron microscopy (Joel 35CF SEM) was used to investigate M50 and Si_3N_4 ball wear track surfaces to determine wear mechanisms. Wear tracks on M50 rod samples were analyzed using profilometry (Sloan Dektak surface profilometer with a Dektak FLM controller and a 10 cm chart recorder) to calculate the volume specific wear rate. Three surface profiles were taken at 120 degree intervals around the diameter of the wear track on the M50 test rod, and their average area was integrated around the circumference of the rod to determine the volume of wear material removed. The roughness (R_a) of the M50 rod wear track surfaces was determined using atomic force microscopy (Topometrix TMX 2000 scanning probe microscope). Atomic force microscopy is a powerful analytical tool for probing the surface of materials, providing a topographical image of the material surface as well as roughness values. The topographical image provides a three-dimensional atomic picture of the wear surface, thoroughly exposing wear characteristics and embedded debris. Optical microscopy and SEM were used to characterize the primary failure mechanism on M50 and Si_3N_4 sample wear surfaces, which was spallation. The primary wear mechanism produced in RCF experiments is contact stress fatigue, with secondary wear mechanisms of indenting, cutting and plowing resulting from particulate contaminants in the lubrication system [15-16].

3. Results and Discussion

3.1. Wear mechanisms - optical microscopy

The wear surfaces produced on M50 rods using M50 balls and as-received oils under low and high stress conditions are shown in Figures 4(a) and (b). In both cases the wear mechanism is contact stress fatigue, resulting in an overrolling appearance on the wear surface, where the original machining marks are flattened. The few indentations present were most likely generated from wear material which was removed from the bearing element surfaces and deposited into the lubricant. Longer test times resulted in more plastic flow of wear material towards the outside of the wear track under all experimental conditions. The wear surfaces produced on M50 rods using Si_3N_4 balls and as-received oils under low and high stress conditions are shown in Figures 5(a) and (b). The low stress case shown in Figure 5(a) resulted in typical over-rolling wear behavior with minor indentation damage. Figure 5(b) shows the high stress hybrid bearing case, which produced tortuosity on the M50 rod wear surface which may be due to extensive subsurface grain boundary damage. We have not attempted to determine the exact nature of this wear mechanism because jet engines operate at much lower stresses and thus do not exhibit this type of wear. This type of wear surface was only generated in the Si_3N_4 test operating at 6.29 GPa (912 ksi) Hertzian contact stress. The secondary wear mechanism of indenting was observed more extensively when particulate contaminants were introduced to the lubricant. The optical photomicrographs in Figures 6 and 7 confirm that lubricants contaminated with glycothermally synthesized α-Al_2O_3 particles produce a more finely indented structure on the wear surface than those with conventional ATD powders in both all-steel and hybrid bearing systems. The finer the indentations, the more consistent the testing should be, particularly when ceramic elements are involved due to their dependence of fracture toughness on critical flaw size.

3.2. Wear mechanisms - scanning electron microscopy

Figures 8(a) and (b) show the wear surface of an M50 ball which was run with an M50 rod under a lubricant contaminated with ATD particulate. Figures 9(a) and (b) show the wear surface of a Si_3N_4 ball which was run with an M50 rod under an ATD particulate contaminated lubricant. Comparison of the topographical differences between Figures 8 and 9 indicates that more wear occurred on the M50 ball surface than on the Si_3N_4 ball surface. Larger spall defects, such as the one at the bottom right of Figure 8(a), occurred more frequently on M50 ball surfaces than on the Si_3N_4 surfaces. Wear mechanisms such as indenting, cutting, and plowing are exposed on the M50 ball wear surface in Figures 8(a) and (b). The cutting and plowing damage is evident in the alignment of the scars on the wear surface, which follow the direction of rolling. Large, sharp indentors may cause subsurface lateral cracks which develop into the microspalls. Figures 9(a) and (b) show that very little wear occurred on the Si_3N_4 surface. A few microspalls were observed, indicating the presence of large, sharp indentors causing subsurface lateral cracking. The spallation on the Si_3N_4 surface was much less severe than that observed on the M50 surface. The cutting and plowing damage is not present on the Si_3N_4 wear surfaces due to the higher hardness of the Si_3N_4 relative to the ATD particulate. This limited wear by the ATD particles on the Si_3N_4 balls did not appreciably decrease the test times of Si_3N_4-M50 hybrid experiments, compared with runs using as-received lubricants.

Figure 10 shows the wear surface of an M50 ball run with an M50 rod, under a lubricant contaminated with glycothermally synthesized α-Al_2O_3 particles. Figure 11 shows the wear surface of a Si_3N_4 ball run with an M50 rod, also under α-Al_2O_3 particulate contaminated lubricant. Figures 10(b) and 11(b) show larger flaws found on each of the wear surfaces. It is apparent from the wear topography differences between Figures 10 and 11 that the M50 ball surface was worn more by the Al_2O_3 particles than the Si_3N_4 surface. Figures 10(a) and (b) expose the wear mechanism of indenting in its most obvious state. The large hexagonal α-Al_2O_3 platelets caused perfect hexagonal indentations in the softer M50 wear surface, as well as non-symmetrical indentations from three-body wear with smaller particles on end. The larger indentations may cause subsurface damage which can eventually result in spallation of material from the surface. The lack of cutting and plowing damage on the M50 surface by the Al_2O_3 particles shown in Figures 10(a) and (b) compared to the ATD run shown in Figures 8(a) and (b) is due to the smaller particle size and distribution of the Al_2O_3 particulate. The extremely large particles in the ATD powders may get wedged in front of the rolling element and be unable to move between the ball and race. This may result in the particle cutting or plowing through the rod (or race) material as it is ground into smaller particles. The larger particle size of the ATD powder is the reason more damage is generated in the all-steel system by the ATD particles than by the Al_2O_3 particles. Using an Al_2O_3 particulate with a larger particle size should induce more wear in the all-steel system. Comparison of Figures 11(a) and (b) with Figures 9(a) and (b) indicates that more damage is inflicted on the Si_3N_4 surface by the Al_2O_3 particles, than by the softer ATD particles. ATD particles are comminuted by the Si_3N_4 surface, while the Al_2O_3 particles cause noticeable flaws. This results in dramatic reductions in test times of hybrid bearing experiments using Al_2O_3 particulate contaminants.

3.3. *Specific wear rate*

Specific wear rate is the volume of material removed divided by the number of stress cycles experienced during the test. Figure 12 is a plot of specific wear rate on M50 rod wear tracks versus the number of stress cycles experienced during each experiment, e.g. lifetime of tests. Under all experimental conditions the specific wear rate of the M50 rod decreased with increasing test lifetime. This indicates that more wear of the M50 rod occurs in the first 100 million stress cycles of testing than in the remainder of the test. The Al_2O_3 experiments (open diamonds) resulted in higher wear rates and lower lifetimes than the other accelerated testing conditions. The fact that ATD contaminated lubricants did not reduce test times in either the all-steel or hybrid system is apparent from the insignificant wear rates (solid diamonds and squares). The tests using ATD contaminated lubricants did not fail until more than 200 million stress cycles, and did not reduce test times over the as-received experiments.

3.4. *Roughness of wear tracks*

The roughness of wear track surfaces is another method of evaluating the extent of wear. Figure 13 is a comparison of the R_a roughness values of M50 rod wear track surfaces produced under the eight experimental conditions described in Table 1. On the horizontal axis, the number 0 is the average value of an as-received rod. The numbers 1 through 8 refer to the experimental condition numbers listed in the first column of Table 1. Experimental condition numbers 1 through 4 are roughness values of all-steel bearing system runs, and the values of numbers 4 through 8 are of hybrid bearing tests. The roughness values indicate that more wear occurs on the M50 rod wear surface when tested with Si_3N_4 balls than the all-steel system. This data is exaggerated by the fact that the hybrid system was tested at a higher stress level than the all-steel system. These experiments were performed under constant load conditions rather than under constant stress to enable rotating experiments through multiple test heads, improving statistical accuracy. The same applied load results in a higher Hertzian contact stress in the hybrid system than in the all-steel system because of the higher elastic modulus of the Si_3N_4 rolling elements.

The roughness values of experimental condition numbers 3 and 4 in Figure 13 show that the ATD particles, with their large particle size, produced more wear in the all-steel system than the Al_2O_3 particles, even though ATD is softer. The lower stress produced in the all-steel experiments results in an increase in the EHL layer thickness over the hybrid system. If the EHL layer is thicker than the particulate contaminants, then three body wear is less prevalent. The ATD particles did not have the same effect on the hybrid system. Comparison of the roughness values of experimental condition numbers 7 and 8 in Figure 13 confirms that the Al_2O_3 particles result in more wear in the Si_3N_4-M50 hybrid bearing system than ATD particles. The optical photomicrographs in Figures 7(a) and (b) indicate that larger indentations are produced on the M50 rod wear surface by ATD contaminated lubricants than by Al_2O_3 contaminated lubricants. However, the wear surface produced under the Al_2O_3 contaminated lubricant is rougher on an atomic scale, indicating a more efficient accelerated wear mechanism, resulting in more defects of smaller average size.

Figure 14(a) shows an AFM image of an M50 rod wear track tested with Si_3N_4 balls and a lubricant contaminated with ATD particulate. The original finishing marks remain present after almost 600 hours of testing. Figure 14(b) shows an AFM plot of a wear track tested with Si_3N_4 balls and a lubricant contaminated with Al_2O_3 particles. The two white vertical protrusions are Al_2O_3 particles embedded in the M50 rod. The original finishing marks have been removed by abrasive wear in 40 hours, indicating more wear is induced in the hybrid bearing RCF system by Al_2O_3 particulate than by ATD, due to the greater hardness of Al_2O_3 particles.

3.5. Failure mechanisms

The primary failure mechanism in RCF experiments involving M50 steel and Si_3N_4 samples is advanced spallation resulting from subsurface damage due to local inelastic deformations or an improper sintering process [15]. The lateral cracking will begin below the surface and propagate toward the material surface, ultimately dislodging a conical shape of material, known as a spall, from the sample surface. Most RCF tests result in spallation of the rod sample, simulating a raceway failure. This is consistent with actual bearing scenarios, where the raceway is the most common initial component failure. Occasionally tests will result in spallation of the ball sample. Figures 15 and 16 show optical photomicrographs of spalls on M50 rod wear tracks. Figures 15(a-c) are examples of the spalls produced from all-steel experiments, and Figures 16(a-d) show examples of spalls from hybrid bearing experiments. The most common failure initiator in these RCF experiments was spallation of the M50 rod, regardless of the other experimental conditions. The direction that the ball was rolling over the rod is indicated by an arrow in each photomicrograph.

Figures 15 and 16 show that spalls produced from the different experimental conditions were all of similar shape and size, indicating that spallation resulting from subsurface damage is the primary failure mechanism in both the all-steel and hybrid bearing systems under all conditions tested. Experiments using all-steel samples under ATD contaminated lubricants were stopped before spalls large enough to shut down the tests occurred due to excessive test times. Microspalls were evident, however, on the wear surface. The scanning electron micrographs in Figures 17(a) and (b) show a spall on a Si_3N_4 ball. This failure is suspected to be a result of an improper sintering process, where a large subsurface stress from a void, defect or impurity was present, which caused this large amount of material to be removed through spallation. This was the only spall detected on a Si_3N_4 ball during this study.

4. Conclusions

Figure 18 is a schematic representation of the wear process which occurs in the Si_3N_4-M50 hybrid bearing system when particulate contaminants are present in the lubrication system. It is adapted from the schematic developed by Chen et al. under contact loading conditions [15]. The primary wear mechanism produced in RCF experiments is contact stress fatigue when using as-received oils. Secondary wear mechanisms are involved when particulate contaminants are present in the lubricant system. Three body wear from smaller particles can result in cutting or plowing damage. Indentations from larger particles passing through the bearing-race gap may result in lateral subsurface cracks and grain boundary damage which can lead to spallation, and ultimately to rolling element failure. Extremely large particles may become wedged in front of the rolling element causing additional cutting and plowing damage as grinding of the large particle occurs. The general trend of decreasing specific wear rate with increasing lifetime was observed for all experimental conditions, indicating that more wear of the M50 rod occurs in the first 100 million stress cycles of testing than in the remainder. The Al_2O_3 contaminated lubricant tests of hybrid bearing elements resulted in higher wear rates on the M50 rods and lower lifetimes than the tests with ATD contaminated oils. The ATD contaminated lubricants did not significantly reduce test times in either bearing system compared to experiments using as-received lubricants.

It appears from the roughness values of M50 rod wear tracks that more wear occurs on the M50 rod wear surface when tested with Si_3N_4 balls than in the all-steel system. This data is exaggerated, however, by the fact that the hybrid system was tested at a higher stress level than the all-steel system in these experiments. Wear resistance in the Si_3N_4-M50 hybrid bearing system can be reduced by incorporating a race material with a hardness value closer to that of Si_3N_4. This will result in less wear of the race material by the Si_3N_4 rolling elements. Comparison of the roughness values and AFM images of M50 rod wear track surfaces confirms that the Al_2O_3 particles result in more wear in the Si_3N_4-M50 hybrid bearing systems than softer ATD particles. While the Al_2O_3 contaminated lubricant results in finer macroscopic indentations, the wear surface is rougher on an atomic scale, indicating a more efficient acceleration mode, resulting in more defects of smaller average size. Performing RCF experiments with a lubricant contaminated with highly defined α-Al_2O_3 particles is an effective method of reducing test times to evaluate the wear performance of advanced rolling element materials. The primary failure mechanism in RCF experiments involving M50 steel and Si_3N_4 rolling elements is spallation resulting from subsurface material damage due to local inelastic deformations or an improper sintering process.

Hertzian contact stresses in RCF tests must be maintained at a level where the mode of wear is representative of that experienced in the actual bearing environment. Hard-particulate contamination of the lubricant is a common wear scenario in actual bearing environments. Particulate contaminants with a controlled morphology, smaller particle size, and size distribution generate smaller, more uniform surface defects. Smaller surface defects should lead to more consistent RCF tests and less variability in lifetime results, particularly when ceramic elements are involved due to their dependence of fracture toughness on critical flaw size. This will allow the researcher to compare lifetime data between two candidate rolling element materials with more confidence and potentially fewer runs.

Acknowledgments

The authors gratefully acknowledge the Air Force Office of Scientific Research Grant Number F49620-93-1-0349DEF for primary support of this project, with additional support by Pratt & Whitney and MRC bearings. We thank Dr. Charles Beatty and Mr. Tom Joseph, of the UF Materials Science and Engineering Department, for performing the AFM analysis.

References

[1] Bhushan, B., Sibley, L. B., "Silicon Nitride Rolling Bearings for Extreme Operating Conditions," *ASLE Trans.*, **25** [4] 417-428 (1982).

[2] Miner, J. R., Dell, J., Galbato, A. T., Ragen, M. A., "F-117-PW-100 Hybrid Ball Bearing Ceramic Technology Insertion, "*Trans. ASME - Jour. of Eng. for Gas Turb. and Power*, **118**, pp 434-442 (1996).

[3] Harris, T. A., McCool, J. I., "On the Accuracy of Rolling Bearing Fatigue Life Prediction," *ASME Jour. of Trib.*, **118**, pp 297-310 (1996).

[4] Harris, T. A., 1966, *Rolling Bearing Analysis*, John Wiley, 1966, (3rd Ed. published by Wiley in 1991).

[5] Zaretsky, E. V., Poplawski, J. V., Peters, S. M., "Technical Note - Comparison of Life Theories for Rolling Element Bearings," *STLE Trib. Trans.*, **39** [2] 501-503 (1996).

[6] Mechanical Technology Incorporated, "Bearing Industry Technology Modernization Report - Final Report," MTI Report No. 91TR20, January (1992).

[7] Dill, J. F., "Hybrid Bearing Technology for Advanced Turbomachinery: Rolling Contact Fatigue Testing," *Trans. ASME - Jour. of Eng. for Gas Turb. and Power*, **118**, pp 173-178 (1996).

[8] Sayles, R. S., Macpherson, P. B., "Influence of Wear Debris on Rolling Contact Fatigue," *Rolling Contact Fatigue Testing of Bearing Steels, ASTM STP 771*, J. J. C. Hoo, Ed., ASTM (1982).

[9] Chiu, Y. P., Paerson, P. K., Dezzani, M., Daverio, H., "Fatigue Life and Performance Testing of Hybrid Ceramic Ball Bearings," *Lubr. Eng.*, **52** [3] 198-204 (1996).

[10] Williams, J. A., Hyncica, A.M., "Mechanisms of Abrasive Wear in Lubricated Contacts," *Wear*, **152**, pp 57-74 (1992).

[11] Nixon, H. P., Zantopulos, H., "Fatigue Life Comparisons of Tapered Roller Bearings with Debris-Damaged Raceways," *Lubr. Eng.*, **51** [9] 732-736 (1995).

[12] Mitchell, D. J., Sabia, R., Whitney, E. D., Adair, J. H., "Characterizing the Performance of Advanced Rolling Element Materials," Proceedings of the Annual ACERS Engineering Ceramics Division's Cocoa Beach Ceramic Composites Convention (1997).

[13] Glover, D., "A Ball-Rod Rolling Contact Fatigue Tester," *Rolling Contact Fatigue Testing of Bearing Steels, ASTM STP 771*, J. J. C. Hoo, Ed., American Society for Testing and Materials (1982).

[14] Cho, S. B., Venigalla, S., Adair, J. H., "Morphological Forms of α-Alumina Particles Synthesized in 1,4-Butanediol Solution," *Jour. Am. Ceram. Soc.*, **79** [1] 88-96 (1996).

[15] Chen, Z., Cuneo, J. C., Mecholsky, J. J., Jr, Hu, S., "Damage Processes in Si_3N_4 Bearing Material Under Contact Loading," *Wear*, **198,** pp 197-207 (1996).

[16] Chao, L., Shetty, D. K., Adair, J. H., Mecholsky, J. J., Jr, "Development of Silicon Nitride for Rolling-Contact Bearing Applications: A Review," J. Mater. Educ., **17**, pp 245-303 (1995).

Table 1 Experimental Conditions

Number	Ball	Rod	Lubricant Type	Lubricant Condition	Hertzian Stress
1	M50	M50	MIL-L-23699	As-Received	5.19 GPa (753 ksi)
2	M50	M50	MIL-L-23699	As-Received	5.47 GPa (793 ksi)
3	M50	M50	MIL-L-23699	Arizona Test Dust	5.19 GPa (793 ksi)
4	M50	M50	MIL-L-23699	Fine Al_2O_3	5.19 GPa (753 ksi)
5	Si_3N_4	M50	MIL-L-23699	As-Received	5.97 GPa (866 ksi)
6	Si_3N_4	M50	MIL-L-23699	As-Received	6.29 GPa (912 ksi)
7	Si_3N_4	M50	MIL-L-23699	Arizona Test Dust	5.97 GPa (866 ksi)
8	Si_3N_4	M50	MIL-L-23699	Fine Al_2O_3	5.97 GPa (866 ksi)

Component	% of Total Mass
SiO_2	68 - 76
Al_2O_3	10 - 15
Fe_2O_3	2 - 5
Na_2O	2 - 4
CaO	2 - 5
MgO	1 - 2
TiO_2	0.5 - 1
K_2O	2 - 5

Fig. 1. Average chemical composition of Arizona test dust (ATD) particulate.

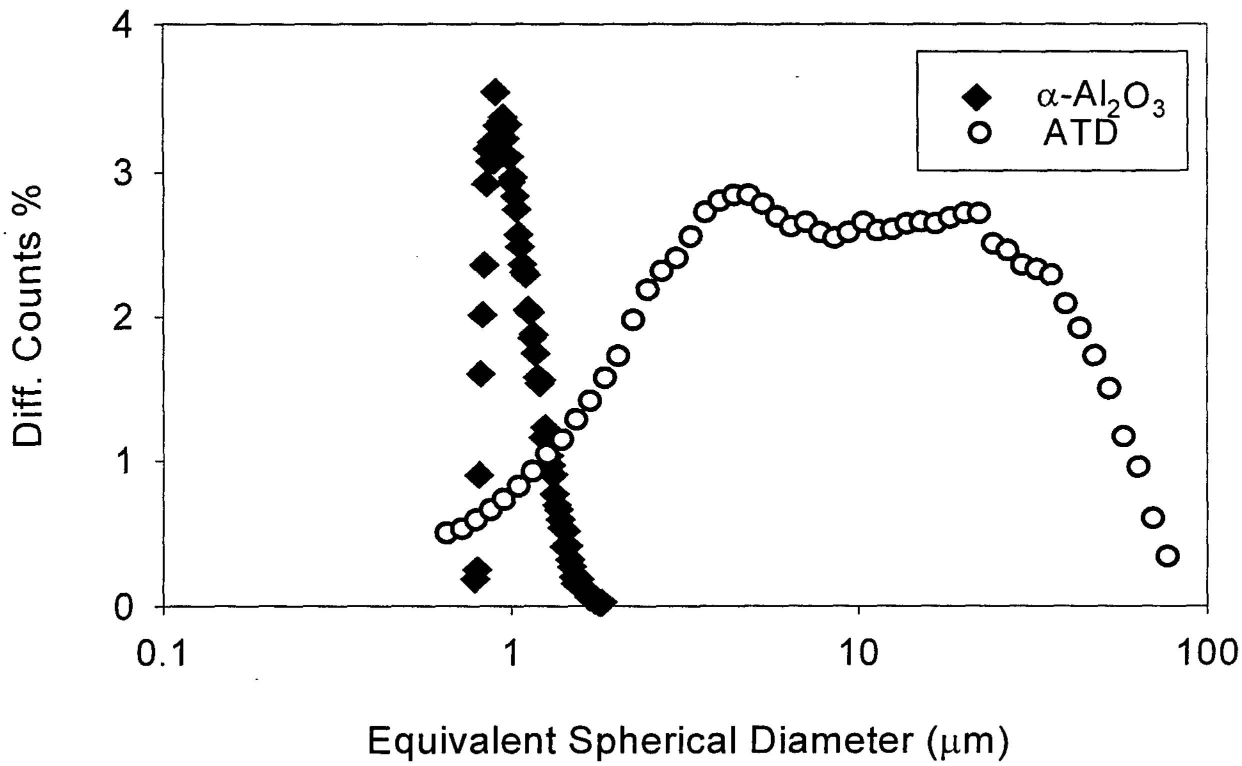

Fig. 2. Particle size distributions for ATD and α-Al_2O_3 powders.

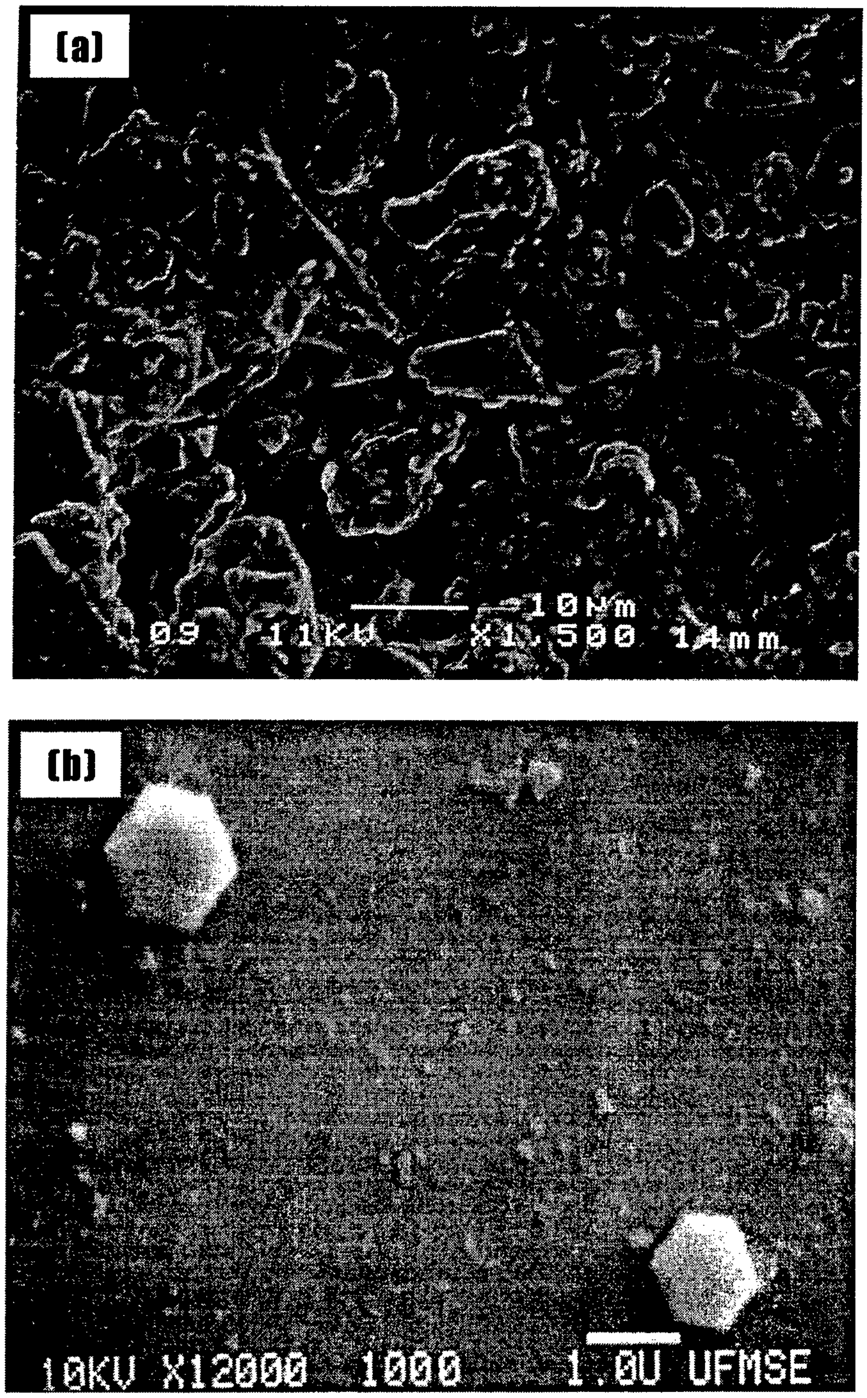

Fig. 3. SEM photomicrographs of particulate contaminants, (a) ATD, (b) α-Al_2O_3.

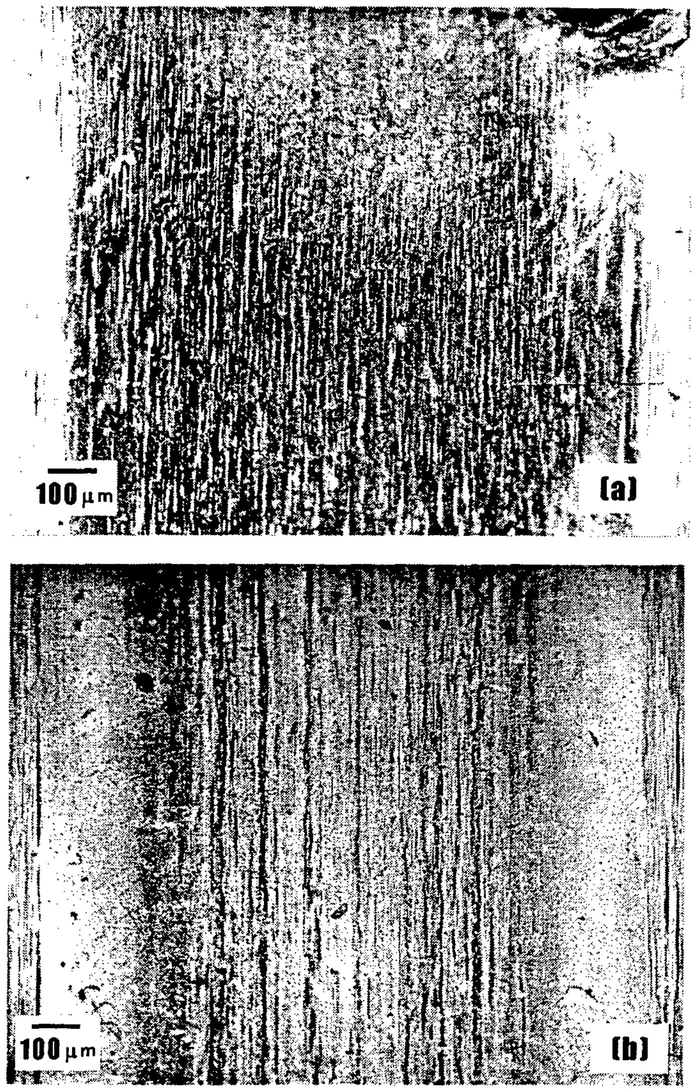

Fig. 4. Optical photomicrographs of wear tracks on M50 rods run with M50 balls and as-received oil, (a) 5.19 GPa, 690 h, (b) 5.47 GPa, 351 h.

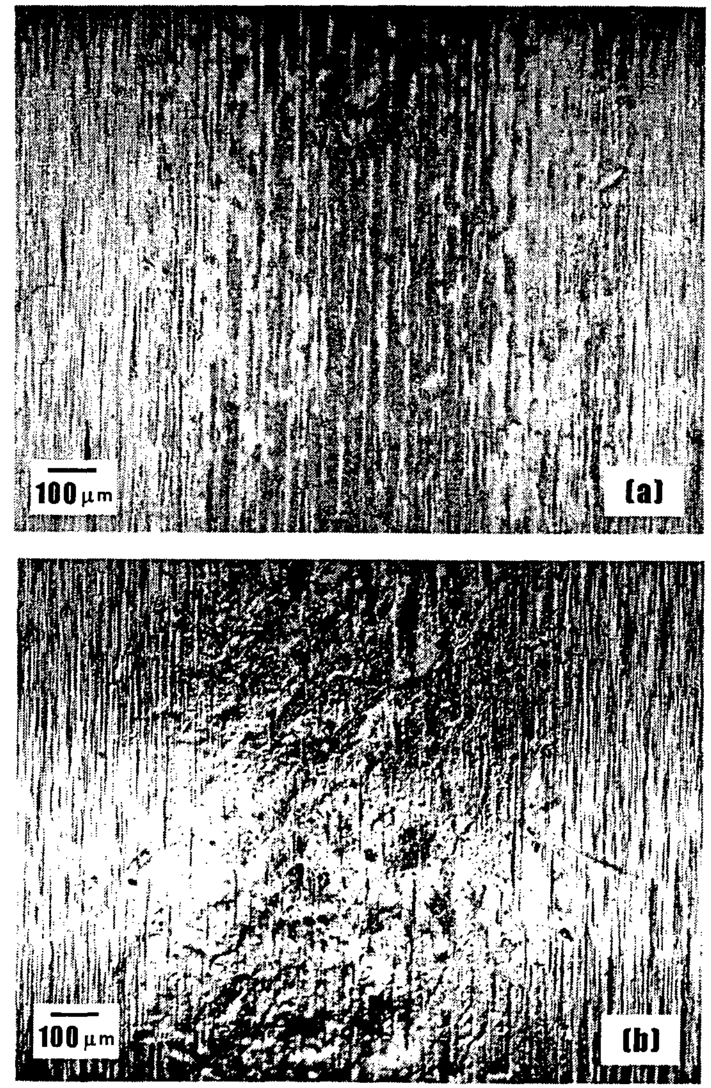

Fig. 5. Optical photomicrographs of wear tracks on M50 rods run with Si_3N_4 balls and as-received oil, (a) 5.97 GPa, 315 h, (b) 6.29 GPa, 68 h.

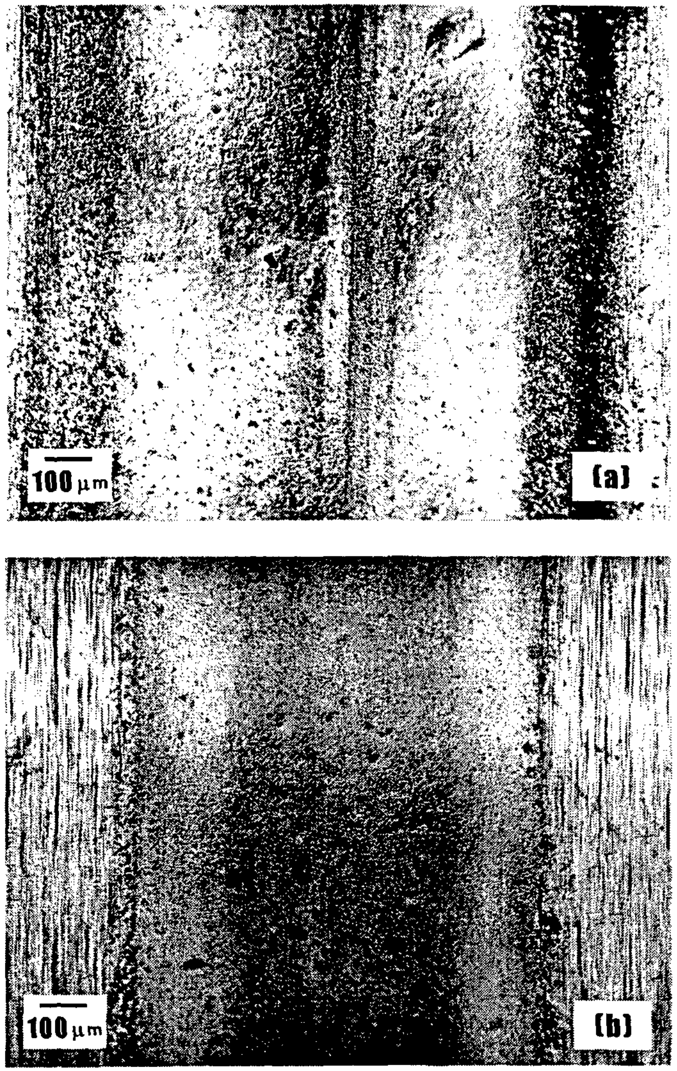

Fig. 6. Optical photomicrographs of wear tracks on M50 rods run with M50 balls, (a) ATD in oil, 5.19 GPa, 440 h, (b) Al_2O_3 in oil, 5.19 GPa, 603 h.

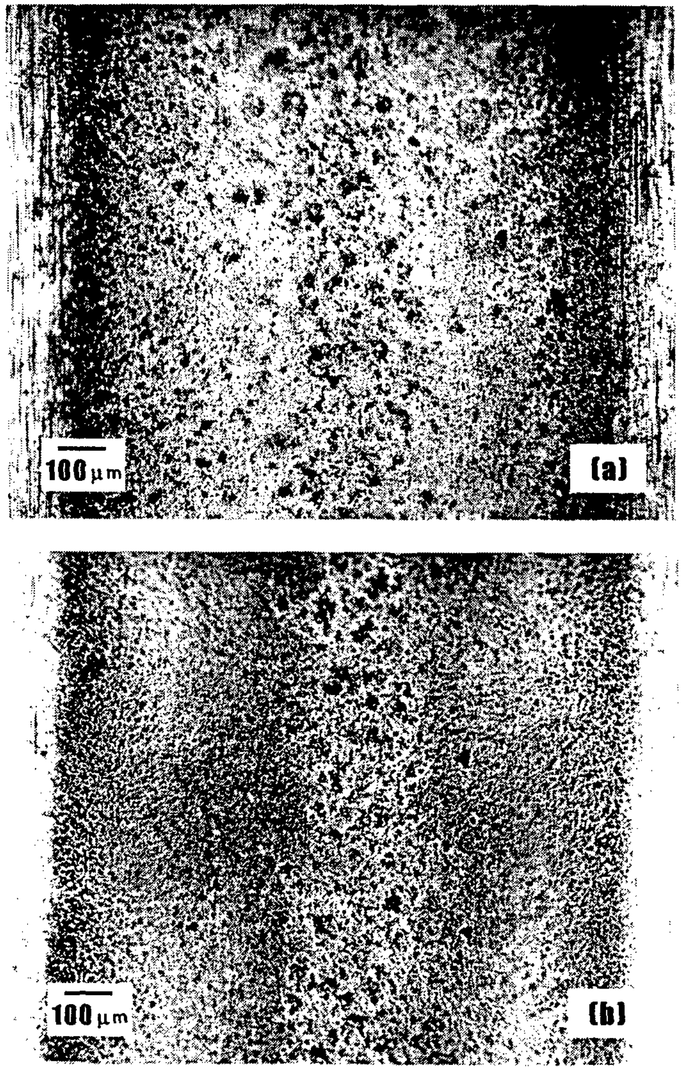

Fig. 7. Optical photomicrographs of wear tracks on M50 rods run with Si_3N_4 balls, (a) ATD in oil, 5.97 GPa, 578 h, (b) Al_2O_3 in oil, 5.97 GPa, 114 h.

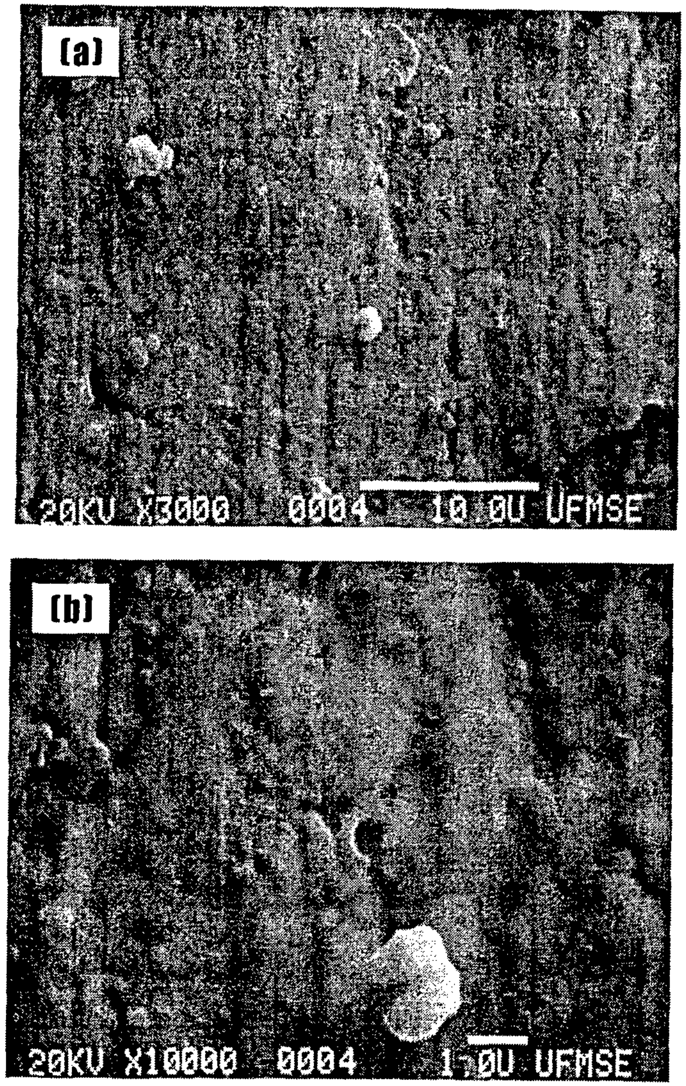

Fig. 8. Scanning electron micrographs of a wear track on an M50 ball run with an M50 rod, ATD in oil, 5.19 GPa, 440 h, (a) 3,000x, (b) 10,000x.

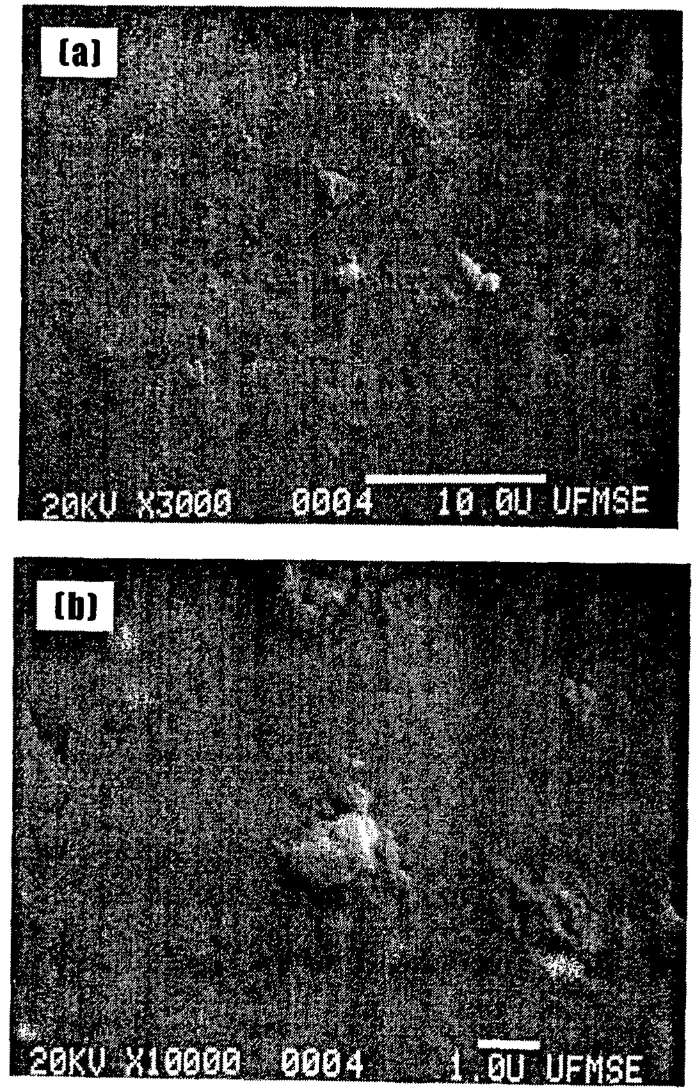

Fig. 9. Scanning electron micrographs of a wear track on a Si_3N_4 ball run with an M50 rod, ATD in oil, 5.97 GPa, 578 h, (a) 3,000x, (b) 10,000x.

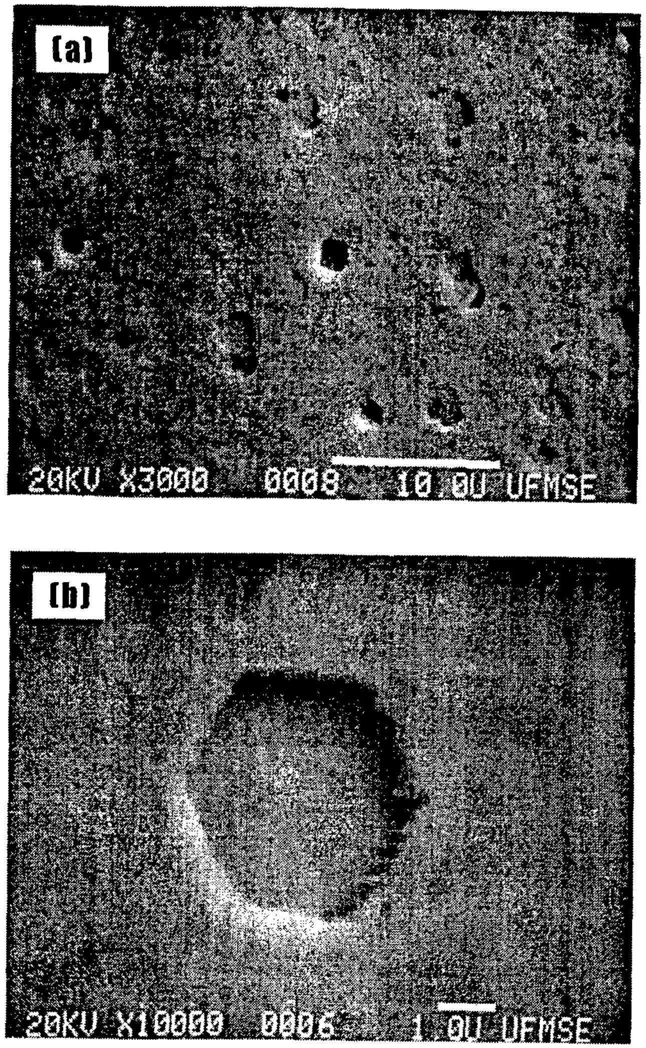

Fig. 10. Scanning electron micrographs of a wear track on an M50 ball run with an M50 rod, Al_2O_3 in oil, 5.19 GPa, 603 h, (a) 3,000x, (b) 10,000x.

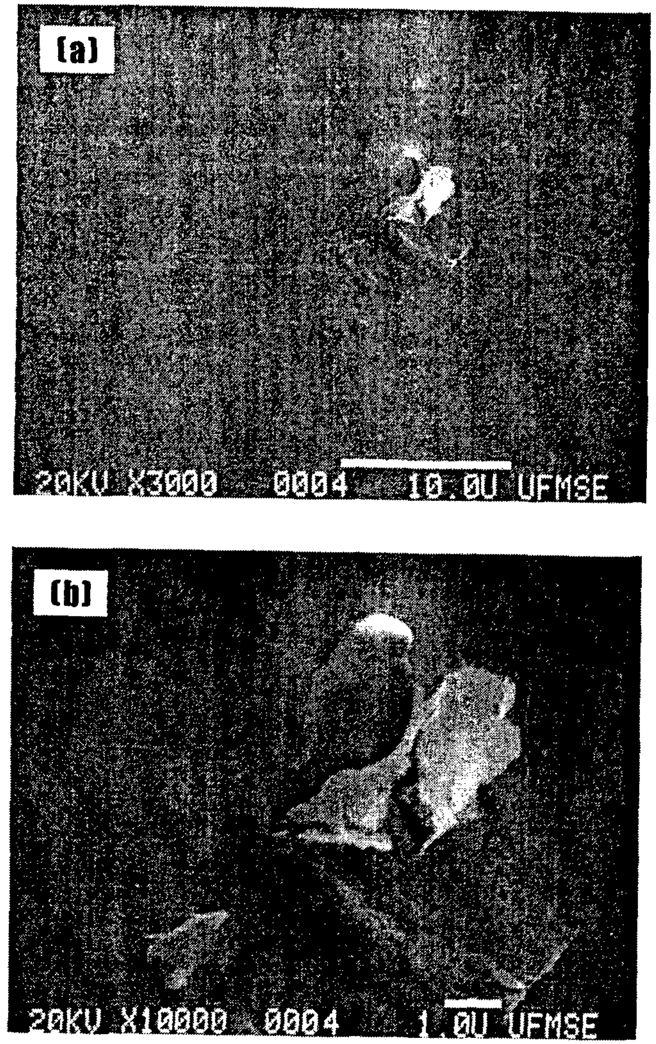

Fig. 11. Scanning electron micrographs of a wear track on a Si_3N_4 ball run with an M50 rod, Al_2O_3 in oil, 5.97 GPa, 114 h, (a) 3,000x, (b) 10,000x.

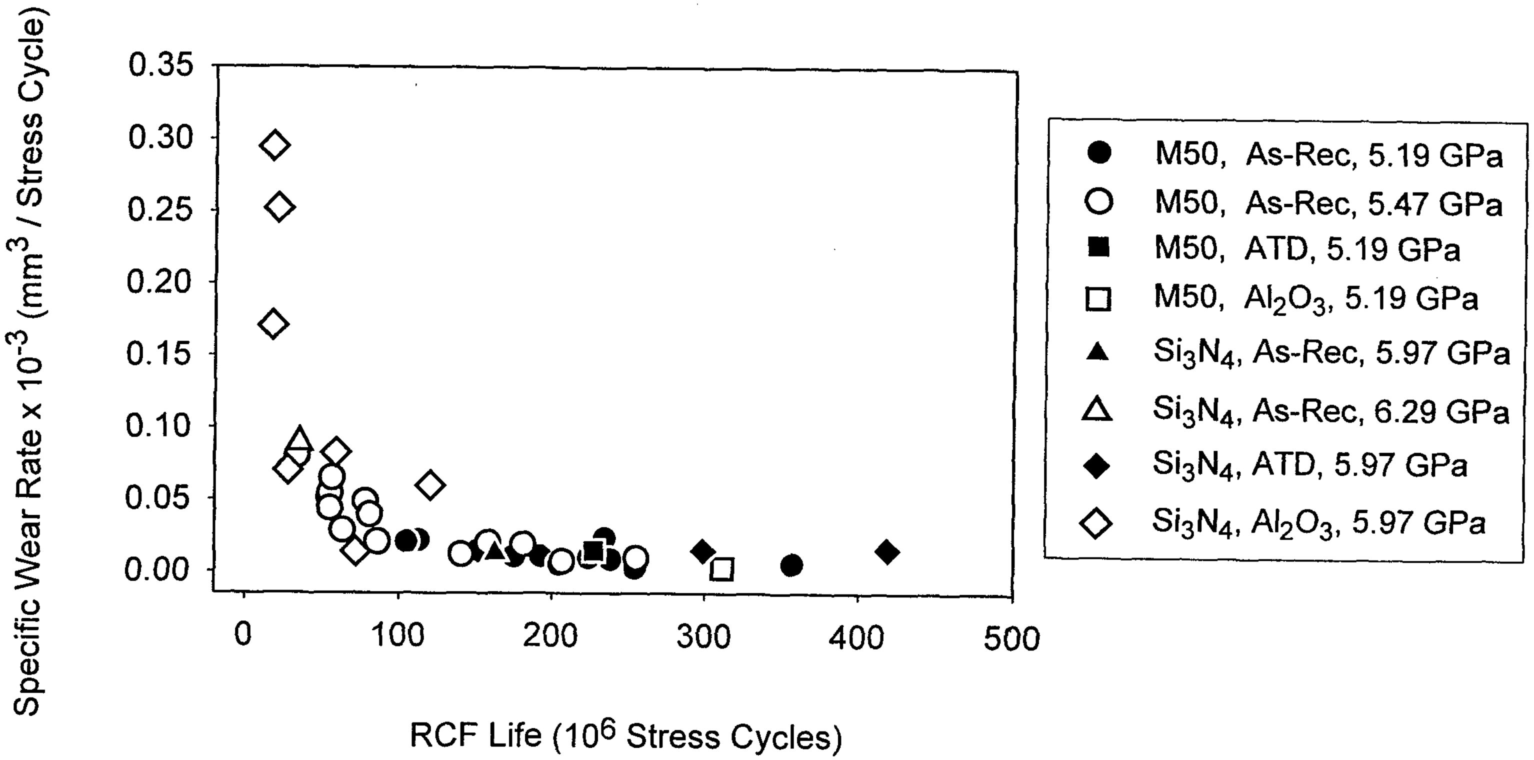

Fig. 12. Specific wear rate of wear tracks on M50 rods.

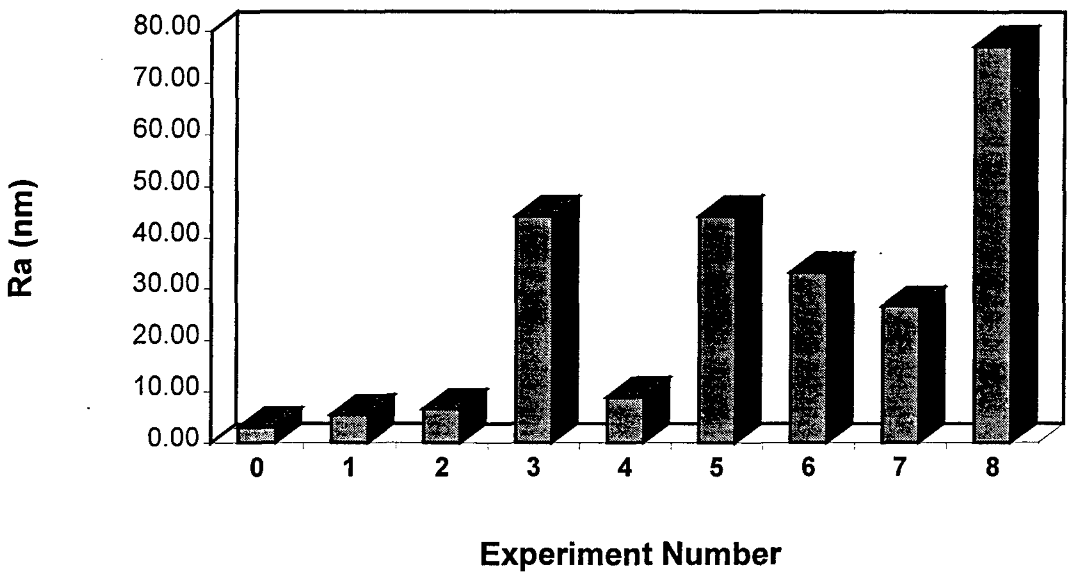

Fig. 13. Roughness values for M50 rod wear tracks. On the horizontal axis, the number 0 represents the as-received M50 rod R_a value, and numbers 1 through 8 refer to the experimental condition numbers in the first column of Table 1.

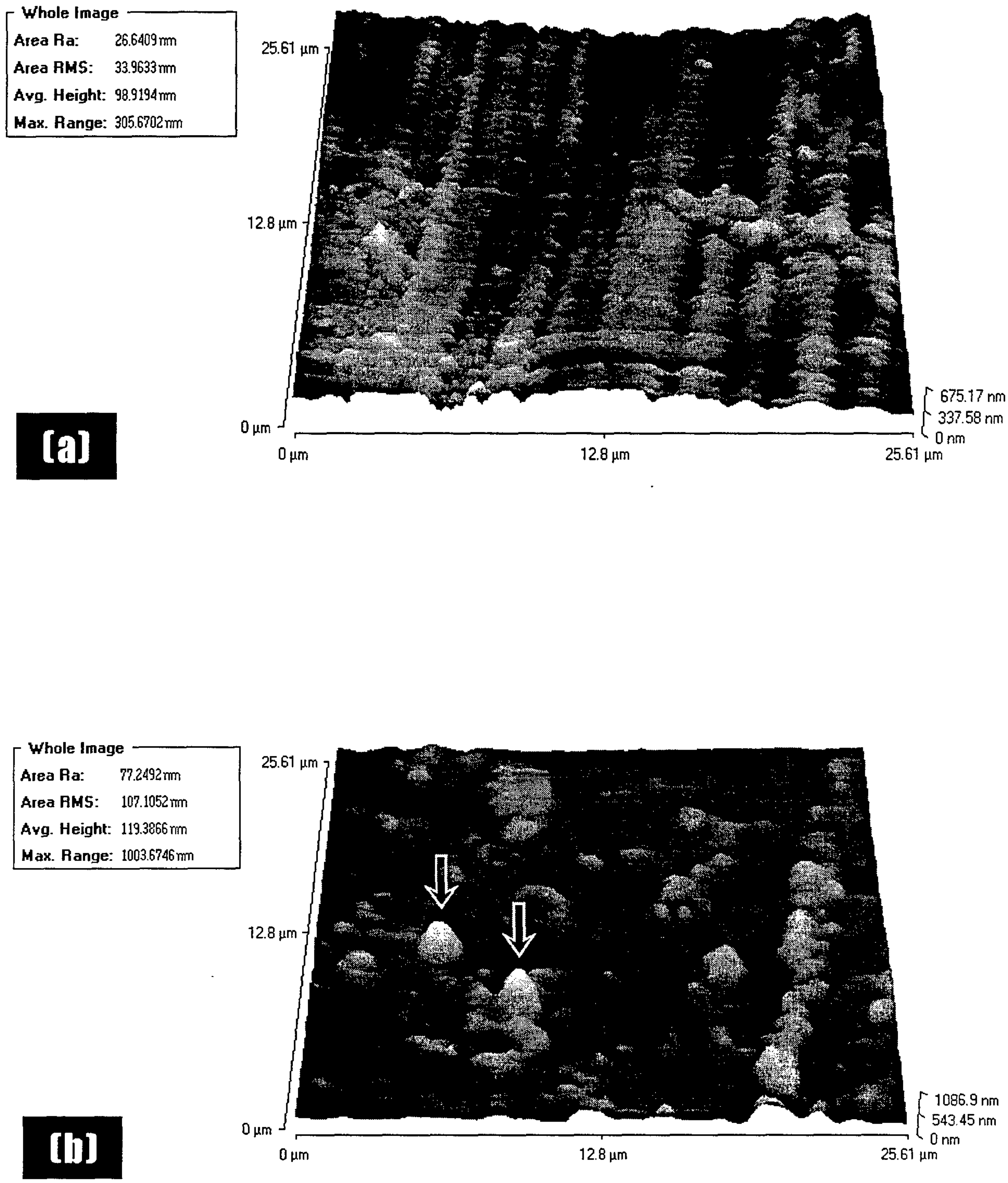

Fig. 14. Atomic force micrographs of wear track surfaces on M50 rods run with Si_3N_4 balls, 5.97 GPa, (a) ATD in oil, 578 h, (b) Al_2O_3 in oil, 40 h. Arrows indicate embedded Al_2O_3 particles.

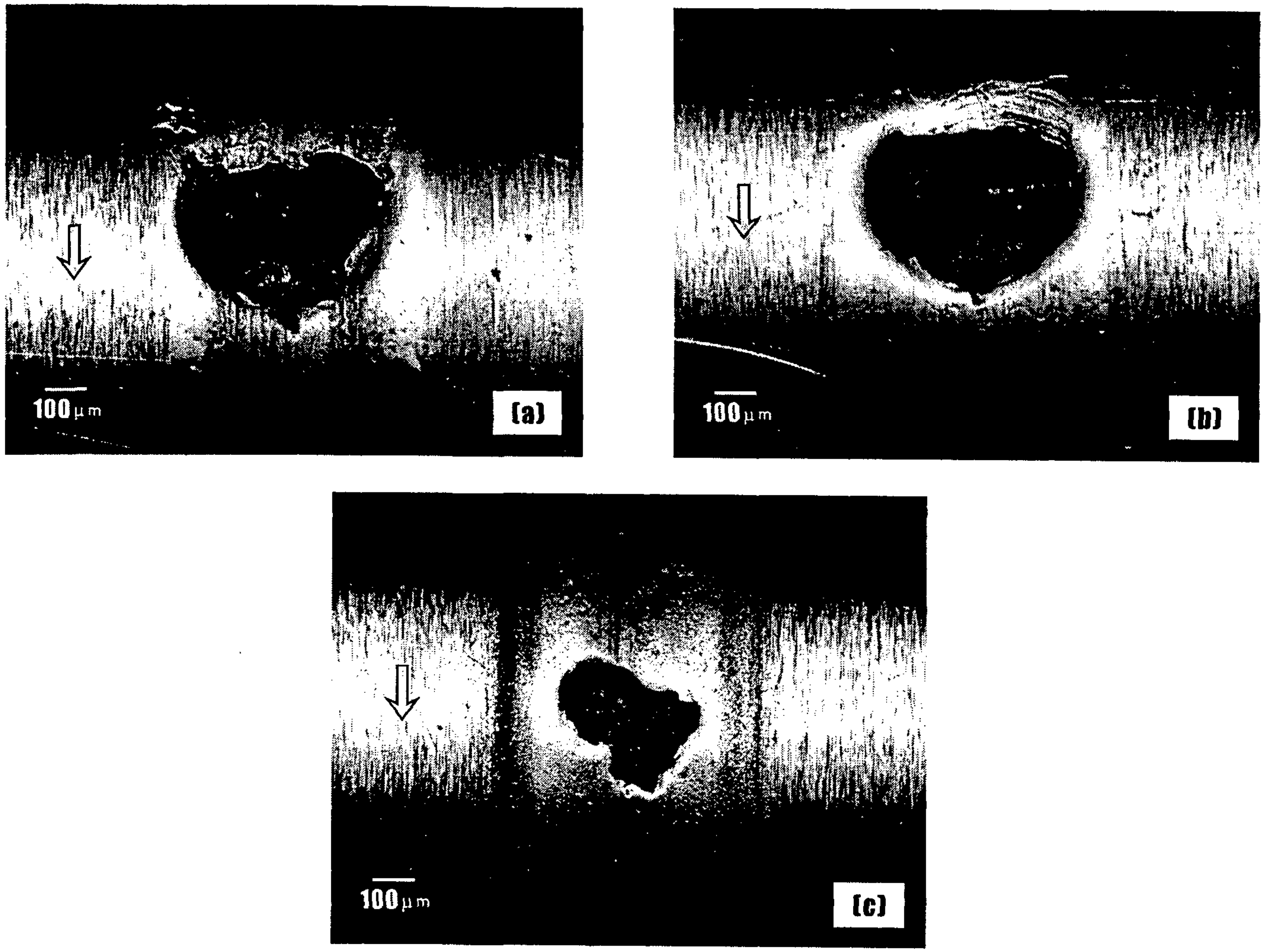

Fig. 15. Optical photomicrographs of spalls on M50 rods run with M50 balls, (a) 5.19 GPa, as-rec. oil, 372 h, (b) 5.47 GPa, as-rec. oil, 167 h, (c) 5.19 GPa, ATD in oil, 440 h. Arrows indicate direction of rolling.

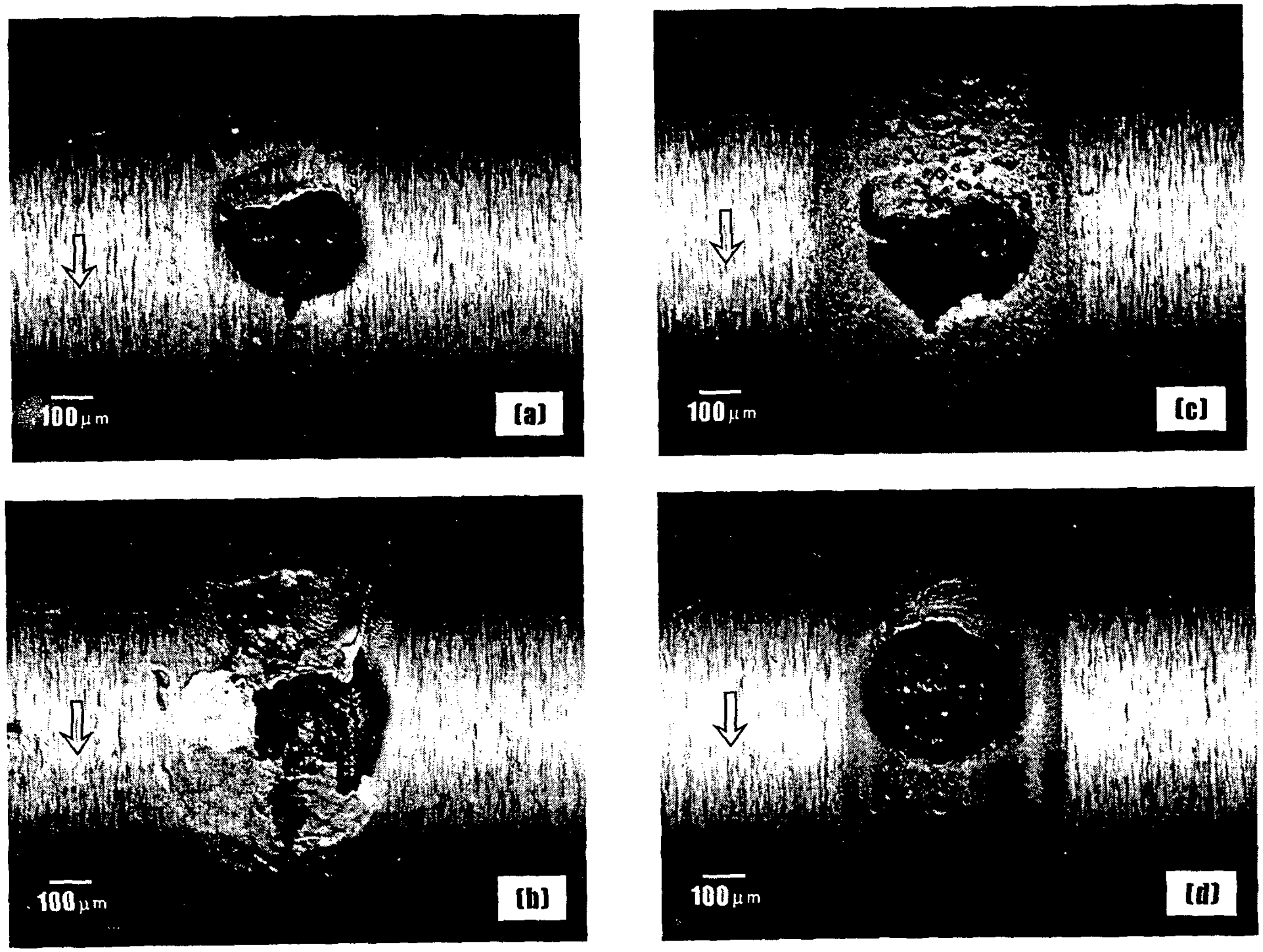

Fig. 16. Optical photomicrographs of spalls on M50 rods run with Si_3N_4 balls and, (a) 5.97 GPa, as-rec. oil, 315 h, (b) 6.29 GPa, as-rec. oil, 68 h, (c) 5.97 GPa, ATD in oil, 578 h, (d) 5.97 GPa, Al_2O_3 in oil, 54 h. Arrows indicate direction of rolling.

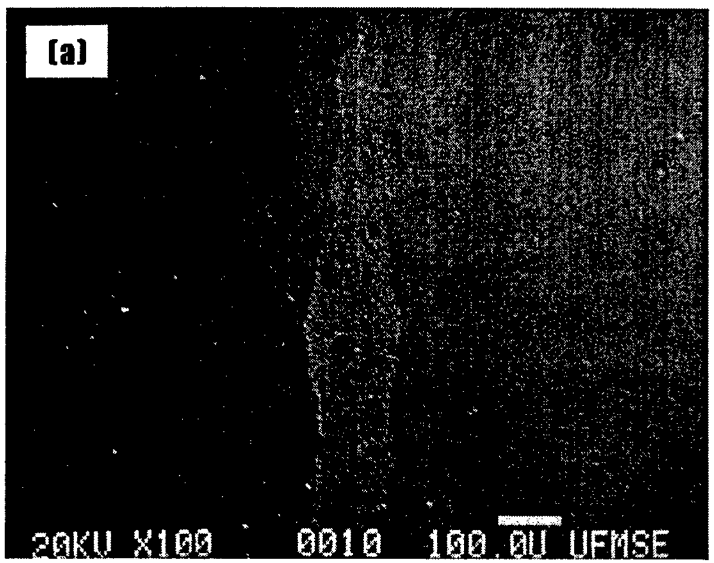

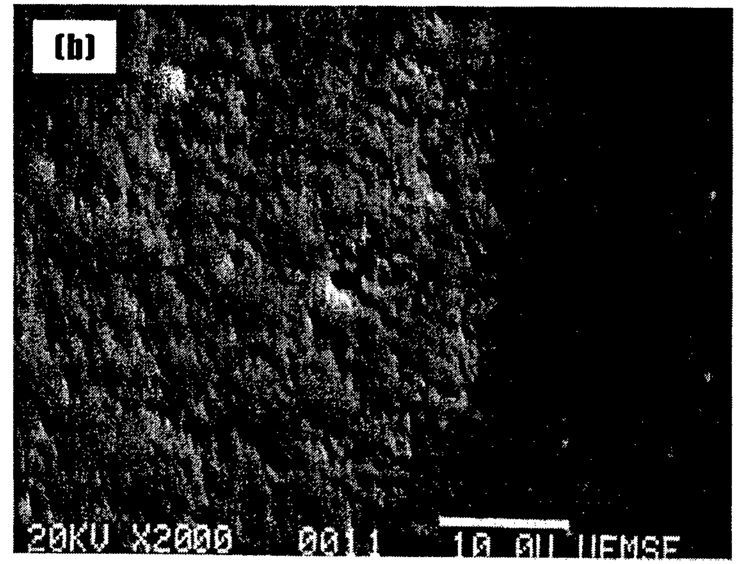

Fig. 17. Scanning electron micrographs of a spall on a Si_3N_4 ball which was run with an M50 rod, Al_2O_3 in oil, 5.97 GPa, 114 h, (a) 100x, (b) 2,000x.

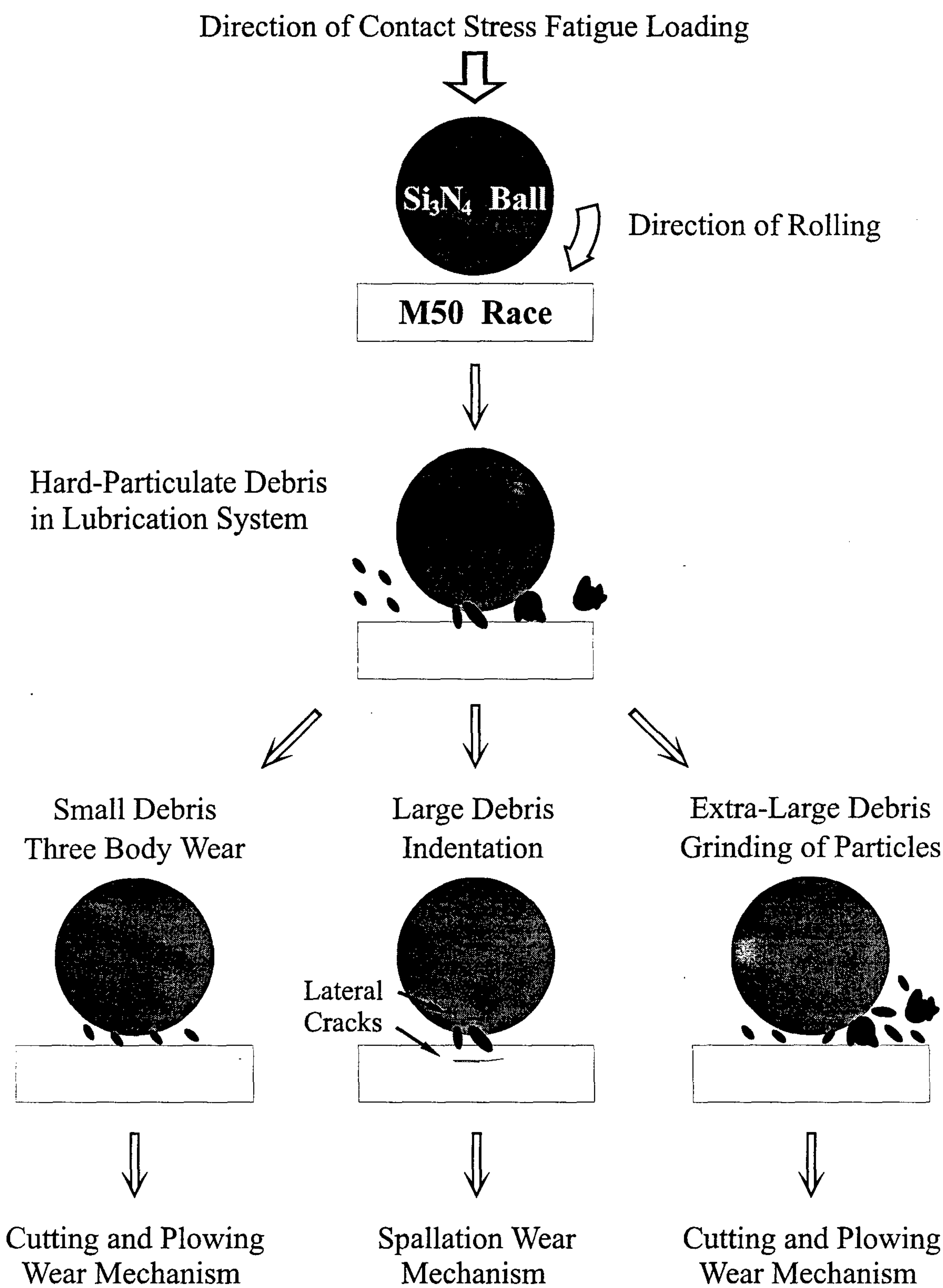

Fig. 18. Schematic diagram of the mechanisms occurring in the wear process of the Si_3N_4-M50 hybrid ball bearing system when particulate contaminants are present in the lubrication system.

APPENDIX 17, D. J. Mitchell, R. Sabia, E.D. Whitney, and J. H. Adair, "Characterizing the Performance of Advanced Rolling Element Materials," *Cer. Engr. & Sci. Proc.*, 18[4], 85-92, (1997).

CHARACTERIZING THE PERFORMANCE OF ADVANCED ROLLING ELEMENT MATERIALS

D.J. Mitchell, R. Sabia, E.D. Whitney, J.H. Adair
Department of Materials Science and Engineering
University of Florida, Gainesville, FL 32611

ABSTRACT

Various methods for the acceleration of Rolling Contact Fatigue (RCF) tests of M50 steel and hybrid M50-Si_3N_4 bearing systems were explored. The acceleration methods investigated were high Hertzian contact stress, roughening or pre-denting the rolling element surface, lubricant contaminated with Arizona Test Dust, lubricant contaminated with fine Al_2O_3 particles, and thermally degraded lubricant. The advantages and disadvantages of each method were analyzed and compared. Weibull analysis was performed on all-steel and hybrid systems in order to observe how each behaves under the various acceleration conditions. The results of the Weibull analyses will be reported in a subsequent paper. Structural changes were analyzed using conventional techniques such as scanning electron microscopy, optical microscopy and surface profilometry, as well as novel techniques such as atomic force microscopy.

INTRODUCTION

Improvements in rolling bearing design, material compositions and lubricants have advanced bearing performance dramatically in the past 20 years. Advances in ceramic rolling element compositions, metal microstructure control and lubricant additives have increased performance and lifetimes (1). The use of Si_3N_4 rolling elements in a thrust bearing has been predicted to produce a 2.5x gain in B_{10} lifetime in an aircraft gas turbine engine (2). While these performance increases enhance bearing system operations, they bring new challenges to researchers evaluating and comparing different rolling element material candidates. Today's current bearing and lubrication systems are potentially capable of infinite fatigue life, given proper lubrication and performance maintained within a fatigue limit stress. Different life analysis techniques are being explored to better represent the conditions actually experienced by bearings in service and to take into account the fatigue limit stress (3-5). Rolling element research is not a standard science. There are many test configurations which combine various types of samples to determine the fatigue life of bearing components, and as many methods to analyze the resulting data.

Researchers are seeking consistent methods to accelerate RCF tests in a manner representative of the bearing's true environment. Initially, Hertzian contact stresses were raised to over 6 GPa (870 ksi). When ceramic-metal hybrid bearing test specimens experience high contact stresses, there is an initial widening of the wear track on the softer metal surface, causing an increased contact area, and a resultant decrease in Hertzian contact stress. The reduction in stress occurs even if the load is held constant, because the area supporting the load is larger. This is not representative of actual jet engine bearing conditions. Actual bearing stresses experienced in jet engines do not normally exceed 2-3 GPa (290-435 ksi), and many fatigue test rigs operate around 5.5 GPa (800 ksi). At stresses near 6 GPa (870 ksi) one particular Si_3N_4 rolling element composition performed poorly compared to another, whereas in service both performed equally well (6). For some ceramic compositions this high Hertzian stress does not affect the mode of wear, but for others it does (7). This highlighted the importance of balancing test acceleration techniques with component materials to produce representative life and performance results. The acceleration methods explored in this research were high Hertzian contact stress, lubricant contaminated with Arizona Test Dust (ATD), which is the ASTM standard for contaminating lubricants in bearing tests, lubricant contaminated with a glycothermally synthesized α–Al_2O_3 powder, and thermally degraded lubricant.

Contamination of the lubricant by particulates is one of the most common failure initiators in operating bearing systems (8-10). Pre-denting the rolling elements has been explored by other research teams (11). Pre-denting the samples, while representing the effect of particles in the system, makes it difficult to evaluate how the material responds to contaminant particles over time. Advances made in surface finish techniques are negated, and the response of the surface finish to the other components in the system is impossible to discern if samples are roughened before testing. The lubricant does thermally degrade during use, but actual jet engines burn oil during operation. Fresh lubricant is added after running, which replenishes depleted additives. Adding oil does not remove contaminants from the system, however, leaving particulate contaminated lubricants as the most representative acceleration technique.

EXPERIMENTAL METHOD

This study was performed using a NTN-Bower Rolling Contact Fatigue (RCF) test apparatus with a three-ball-on-rod configuration (12). The balls are thrust-loaded against the rod by two cups held in place with three equally spaced springs. The springs help maintain a constant load during the test, provided the wear track does not become wider than the initial Hertzian contact region. The materials used were 9.5 mm (3/8 in) diameter rods made of M50 VIM VAR steel (Rc=61.4) and 12.7 mm (1/2 in) diameter grade 5 balls made from M50 VIM VAR steel (Rc=61.4) or Toshiba TSN-03NH Si_3N_4 (Hv~1500). In order to represent actual conditions, a MIL-L-23699 jet engine lubricant was used. The rod sample was driven at 3600 rpm producing 2.389 stress cycles per revolution. All particulate tests were run using a concentration of 1 gram of powder to 4 liters of oil. The RCF experiments were run under the acceleration conditions listed in Table I.

Table I. Experimental Conditions

Number	Ball	Rod	Lubricant Type	Lubricant Condition	Hertzian Stress
1	M50	M50	MIL-L-23699	As-Received	5.19 GPa (753 ksi)
2	M50	M50	MIL-L-23699	As-Received	5.47 GPa (793 ksi)
3	M50	M50	MIL-L-23699	Thermally Degraded	5.47 GPa (793 ksi)
4	M50	M50	MIL-L-23699	Arizona Test Dust	5.19 GPa (753 ksi)
5	Si_3N_4	M50	MIL-L-23699	As-Received	5.97 GPa (866 ksi)
6	Si_3N_4	M50	MIL-L-23699	As-Received	6.29 GPa (912 ksi)
7	Si_3N_4	M50	MIL-L-23699	Arizona Test Dust	5.97 GPa (866 ksi)
8	Si_3N_4	M50	MIL-L-23699	Fine Al_2O_3	5.97 GPa (866 ksi)

Particulate Contaminants

Researchers have been using ATD to accelerate bearing tests for many years. The 'fine' grade of ATD used for these tests consists of particles >70 μm in diameter with a broad particle size distribution and random particle morphologies. ATD is composed of approximately 60-70% SiO_2, 10-15% Al_2O_3, and the remainder of various other oxides. The Al_2O_3 particles used in this study were glycothermally synthesized to produce a chemically and phase pure α–Al_2O_3 powder with a mean particle size of 2-4 μm, a narrow particle size distribution and a highly controlled platelet morphology (13). Particle size distributions of the two powders are shown in Figure 1. The ATD distribution came from the vender, Powder Technology Incorporated, and was determined using a Coulter Multisizer IIE. The Al_2O_3 distribution was determined using an Elzone® electro-zone particle size analyzer. The Al_2O_3 contaminated lubricant should provide a more consistent test environment at lower stresses because of its smaller, more uniform particle size, and simulate a common wear scenario in actual jet engine bearing systems. The morphological differences between the ATD and Al_2O_3 powders are apparent in the scanning electron photomicrographs shown in Figure 2.

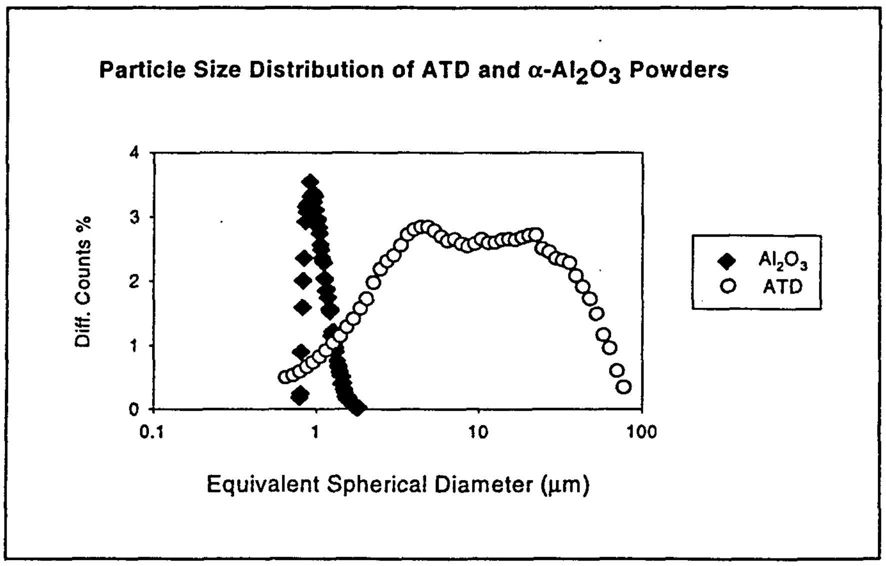

Fig. 1: Particle size distribution comparison of ATD and α-Al_2O_3 powders.

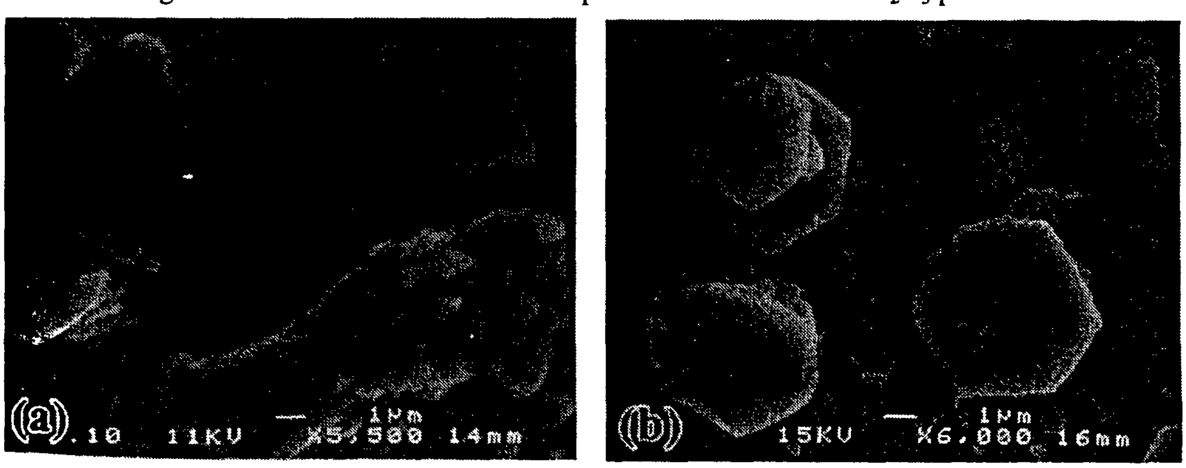

Fig. 2: Scanning electron micrographs of particulate contaminants, (a) ATD, (b) α-Al_2O_3.

RESULTS AND DISCUSSION

Optical microscopy was used to characterize ball and rod sample surfaces to observe wear mechanisms relative to test conditions. Optical microscopy was used extensively due to its low cost, reliable results and efficient characterization rate. Wear tracks on M50 rod samples were analyzed using profilometry to calculate the volume specific wear rate. The roughness (R_a) of the wear track surfaces was determined using atomic force microscopy (AFM). The AFM also provides a three-dimensional atomic picture of the wear surface, thoroughly exposing wear characteristics and embedded debris.

Optical Microscopy

The following photomicrographs were taken on a Nikon OPTIPHOT metallurgical optical microscope with a Microflex AFX-IIA photomicrographic attachment. Polarizing lenses were used to completely expose the wear surface features. Figures 3 through 6 are photo-micrographs of wear tracks on M50 rods run with an as-received lubricant, a lubricant contaminated with ATD, a lubricant contaminated with Al_2O_3, and a thermally degraded lubricant, respectively. The operating stress and number of hours the test ran is reported in each figure caption. The wear surfaces produced using as-received oils under low and high stress conditions are shown in Figure 3. The low stress case, shown in Figure 3a, resulted in typical over-rolling wear behavior, where the original machining marks are flattened. Figure 3b shows the high stress case, which produced a tortuosity on the wear surface which may be due to subsurface grain boundary damage. We have not attempted to determine the exact nature of this wear mechanism because jet engines operate at much lower stresses and thus do not exhibit this type of wear. This type of wear surface was only generated in the test run at 6.29 GPa (912 ksi). The wear mechanism changes to indenting when particulate debris is introduced to the lubricant. The optical photomicrographs in Figures 4 and 5 illustrate that glycothermally synthesized α-Al_2O_3 powders produce a more finely indented structure on the wear surface than conventional ATD powders. The finer the indentations, the more consistent the testing should be, particularly when ceramic elements are involved due to their dependence of fracture toughness on critical flaw size. Figure 6 is a photomicrograph of a wear track produced by running with a thermally degraded lubricant. The mode of wear when using a thermally degraded lubricant is over-rolling, with more plastic flow of wear material towards the outside of the wear track than in the tests using as-received oils.

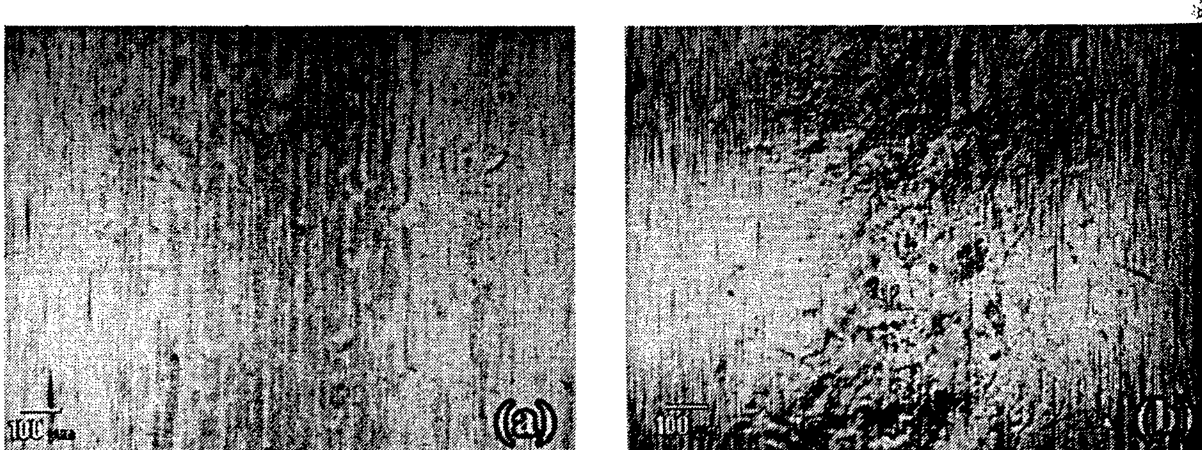

Fig. 3: Wear track on M50 rod run with Si_3N_4 balls, (a) 5.97 GPa, 315 h, (b) 6.29 GPa, 68 h.

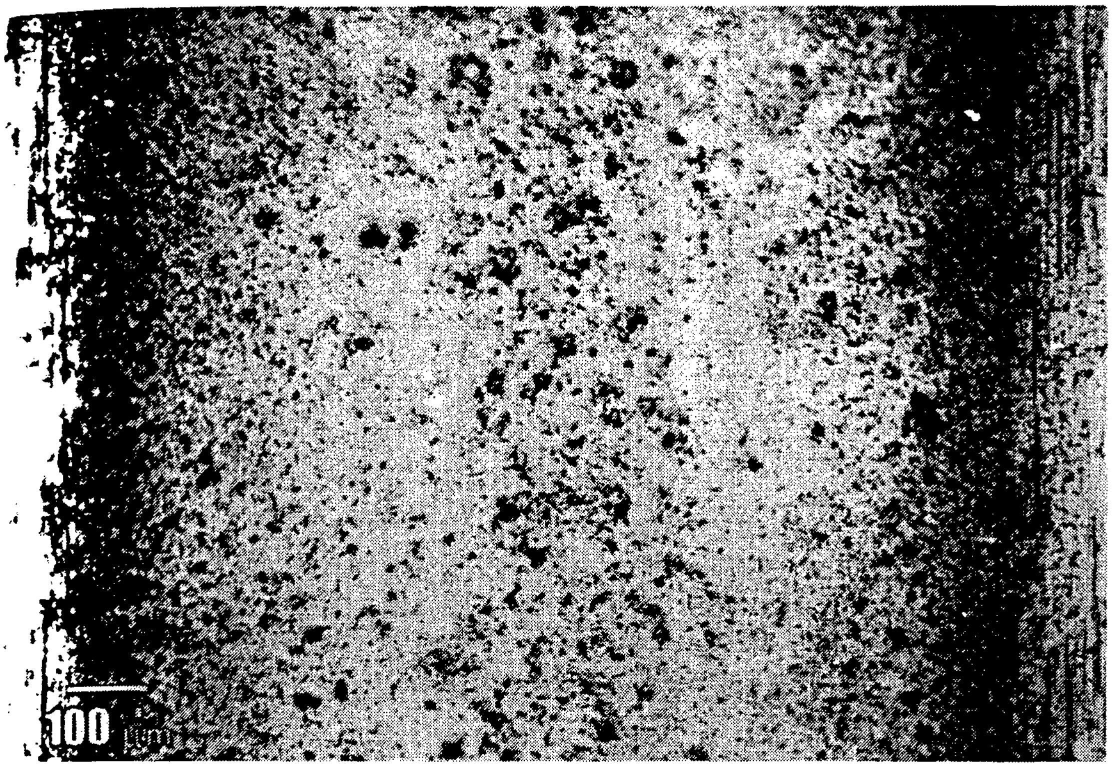

Fig. 4: Wear track on M50 rod run with Si_3N_4 balls, ATD in lubricant, 5.97 GPa, 578 h.

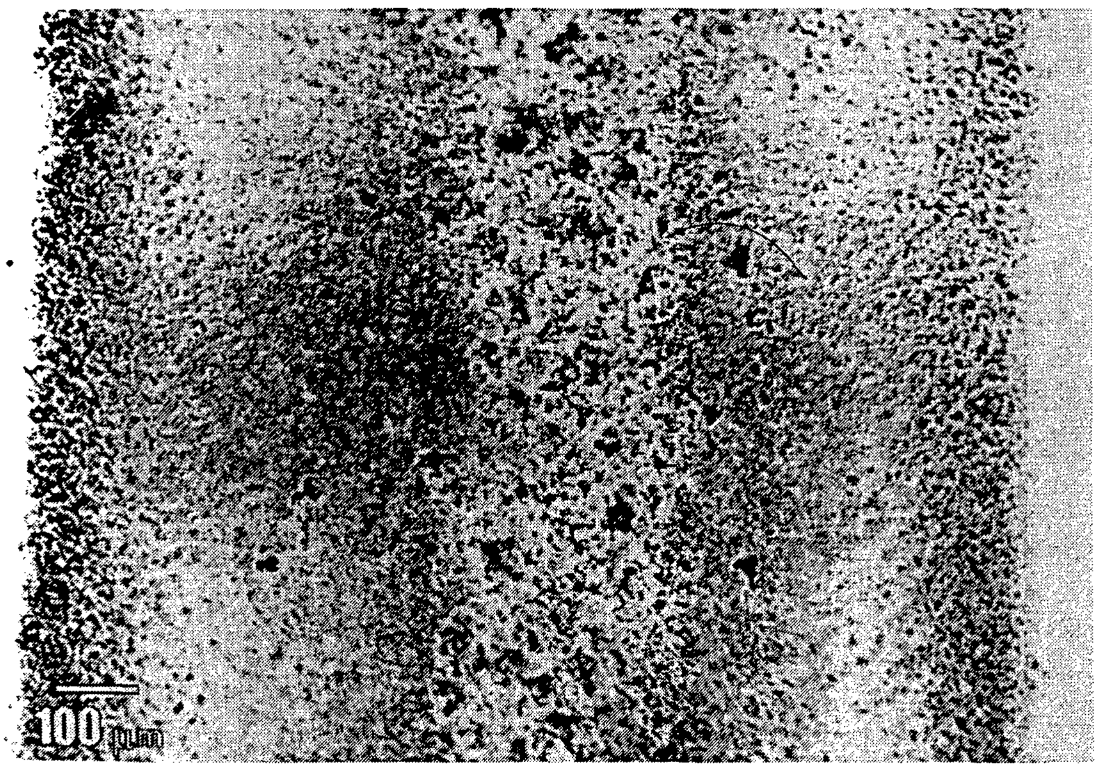

Fig. 5: Wear track on M50 rod run with Si_3N_4 balls, Al_2O_3 in lubricant, 5.97 GPa, 114 h.

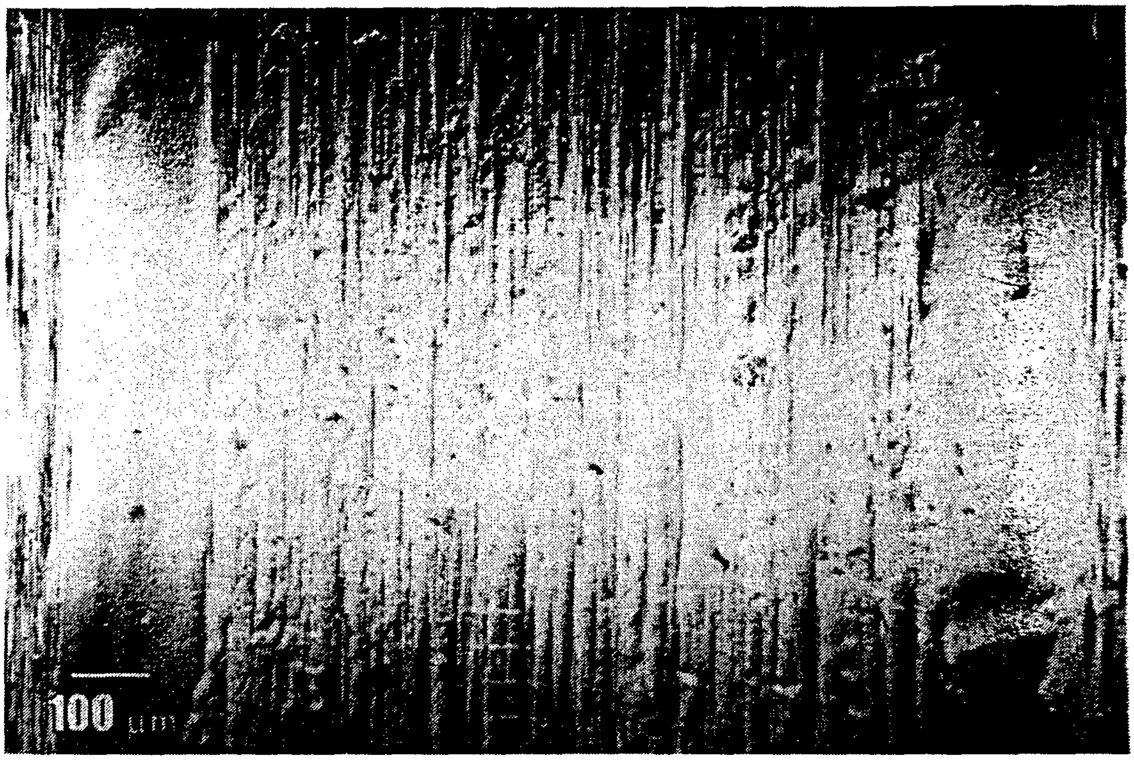

Fig. 6: Wear track on M50 rod run with M50 balls, thermally degraded lubricant, 5.47 GPa, 95 h

Profilometry

Profiles were obtained on a Sloan Dektak surface profilometer with a Dektak FLM controller and a 10 cm Sloan chart recorder. Three profiles were taken, at 120 degree intervals around the diameter of the wear track on the test rod, and their average area was integrated around the circumference of the rod to determine volume of wear material removed.

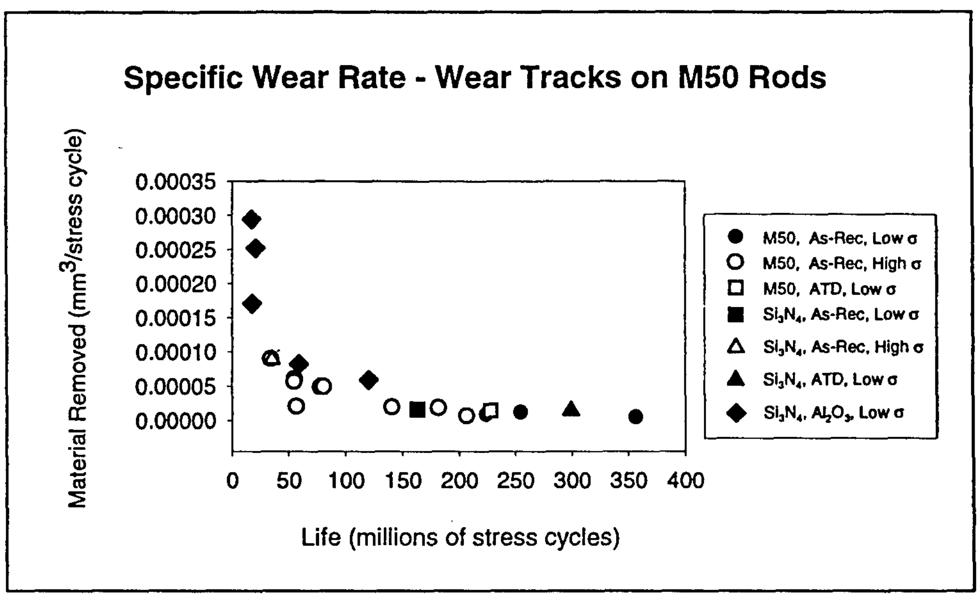

Fig. 7: Specific wear rate of wear tracks on M50 rods.

Figure 7 is a plot of rod wear material removed data versus the number of stress cycles experienced during the tests, which provides specific wear rate information. The general trend of specific wear rate decreasing as lifetime increases occurred for all test conditions. The Al_2O_3 tests, represented by the solid diamonds, resulted in higher wear rates and lower lifetimes than the other acceleration techniques.

Atomic Force Microscopy

Atomic force microscopy is a powerful analysis tool for probing the surface of materials, providing a topographical image of the atomic surface as well as roughness values. The AFM used was a Topometrix TMX 2000 scanning probe microscope placed on a Sloan vibration isolation table. Figure 8 is a comparison of the R_a roughness values of rod wear tracks produced under the eight acceleration conditions. On the horizontal axis, the number 0 is the average value of an as-received rod. The numbers 1 through 8 refer to the numbers of the acceleration conditions in Table I. Figure 9 is an AFM image of an M50 rod wear track run with Si_3N_4 balls and a lubricant contaminated with Al_2O_3 particles. The two vertical protrusions are Al_2O_3 particles embedded in the M50 rod.

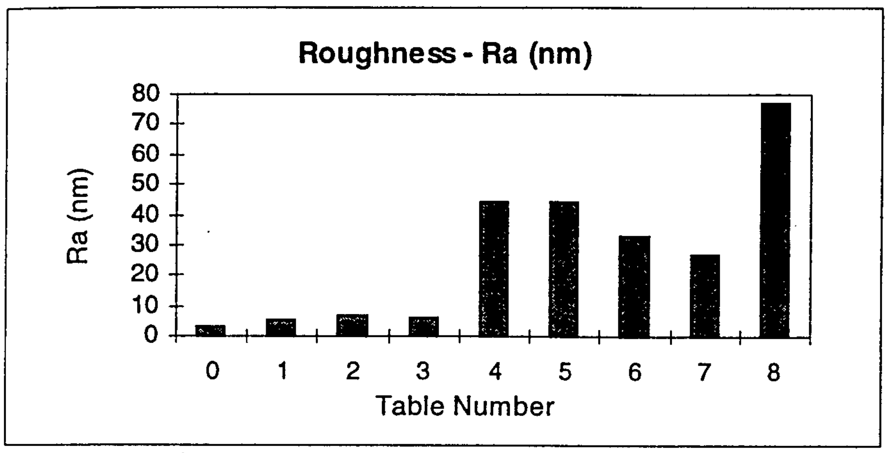

Fig. 8: Roughness values for M50 rod wear tracks. On the horizontal axis, the number 0 represents the as-received M50 rod R_a value, and numbers 1 through 8 refer to the test numbers in Table I.

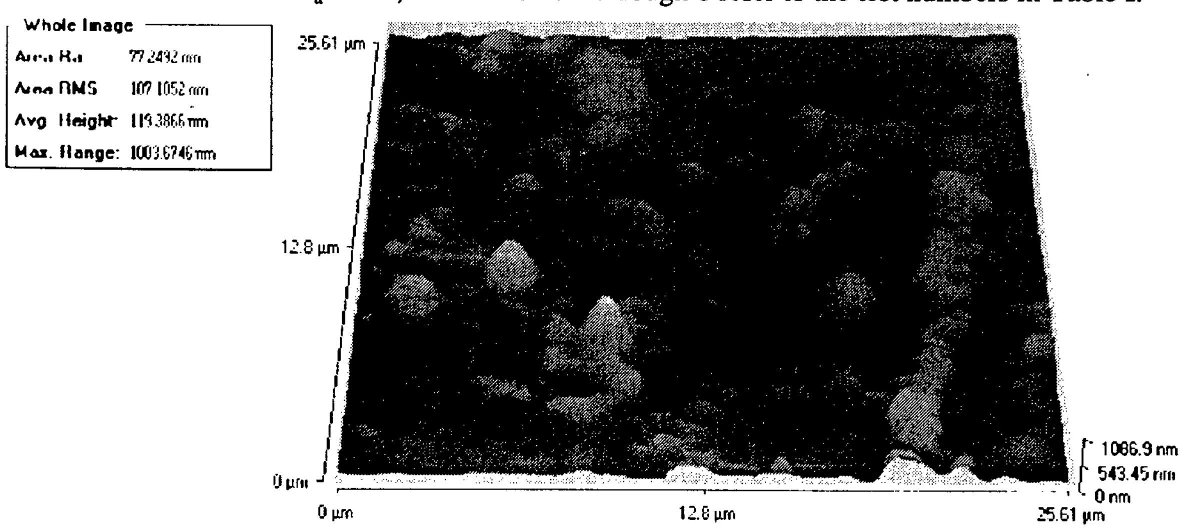

Fig. 9: Surface of wear track on M50 rod run with Si_3N_4 balls, Al_2O_3 in oil.

CONCLUSIONS

Hertzian contact stresses in RCF tests must be maintained at a level where the mode of wear is representative of that experienced in the actual bearing environment. Hard-particulate contamination of the lubricant is a common wear scenario in actual bearing environments. Particulate contaminants with a smaller particle size and size distribution generate smaller, more uniform surface defects. While the Al_2O_3 contaminated lubricant results in finer indentations, the wear surface is rougher on an atomic scale, indicating a more efficient acceleration mode, resulting in more defects of smaller average size. Smaller surface defects should lead to more consistent RCF tests and less variability in the lifetime results, particularly when ceramic elements are involved due to their dependence of fracture toughness on critical flaw size. This will allow the researcher to compare lifetime data between two candidate rolling element materials with more confidence and potentially fewer runs. Any improvement in these two areas increases efficiency and expedites data collection. More runs need to be performed under each acceleration condition to enable statistical comparison by Weibull analysis, which allows us to calculate and plot the variability of each lubricant degradation scenario. Additional results and wear analysis will be the subject of a subsequent paper. The next step in this research is to reduce the Hertzian contact stress to 3 GPa (435 ksi) while maintaining acceptable test times.

ACKNOWLEDGEMENTS

We thank the Air Force Office of Scientific Research, Pratt & Whitney and MRC bearings for funding and supporting this project. Thank you to Dr. Charles Beatty and Tom Joseph, UF Materials Science and Engineering Department, for performing the AFM analysis.

REFERENCES

(1) Bhushan, B., Sibley, L. B., "Silicon Nitride Rolling Bearings for Extreme Operating Conditions," *ASLE Trans.*, **25** [4] 417-428 (1982).

(2) Miner, J. R., Dell, J., Galbato, A. T., Ragen, M. A., "F-117-PW-100 Hybrid Ball Bearing Ceramic Technology Insertion," *Trans. ASME - Jour. of Eng. for Gas Turb. and Power*, **118**, pp 434-442 (1996).

(3) Harris, T. A., McCool, J. I., "On the Accuracy of Rolling Bearing Fatigue Life Prediction," *ASME Jour. of Trib.*, **118**, pp 297-310 (1996).

(4) Harris, T. A., 1966, *Rolling Bearing Analysis*, John Wiley, 1966, (3rd Ed. published by Wiley in 1991).

(5) Zaretsky, E. V., Poplawski, J. V., Peters, S. M., "Technical Note - Comparison of Life Theories for Rolling Element Bearings," *STLE Trib. Trans.*, **39** [2] 501-503 (1996).

(6) Mechanical Technology Incorporated, "Bearing Industry Technology Modernization Report - Final Report," MTI Report No. 91TR20, January (1992).

(7) Dill, J. F., "Hybrid Bearing Technology for Advanced Turbomachinery: Rolling Contact Fatigue Testing," *Trans. ASME - Jour. of Eng. for Gas Turb. and Power*, **118**, pp 173-178 (1996).

(8) Sayles, R. S., Macpherson, P. B., "Influence of Wear Debris on Rolling Contact Fatigue," *Rolling Contact Fatigue Testing of Bearing Steels, ASTM STP 771*, J. J. C. Hoo, Ed., ASTM (1982).

(9) Chiu, Y. P., Paerson, P. K., Dezzani, M., Daverio, H., "Fatigue Life and Performance Testing of Hybrid Ceramic Ball Bearings," *Lubr. Eng.*, **52** [3] 198-204 (1996).

(10) Williams, J. A., Hyncica, A.M., "Mechanisms of Abrasive Wear in Lubricated Contacts," *Wear*, **152**, pp 57-74 (1992).

(11) Nixon, H. P., Zantopulos, H., "Fatigue Life Comparisons of Tapered Roller Bearings with Debris-Damaged Raceways," *Lubr. Eng.*, **51** [9] 732-736 (1995).

(12) Glover, D., "A Ball-Rod Rolling Contact Fatigue Tester," *Rolling Contact Fatigue Testing of Bearing Steels, ASTM STP 771*, J. J. C. Hoo, Ed., American Society for Testing and Materials (1982).

(13) Cho, S. B., Venigalla, S., Adair, J. H., "Morphological Forms of α-Alumina Particles Synthesized in 1,4-Butanediol Solution," *Jour. Am. Ceram. Soc.*, **79** [1] 88-96 (1996).

APPENDIX 18, R. Sabia, Herb A.J. Chin, and J.H. Adair, "Friction and Wear Properties of Silicon Nitride/M-50 Steel Sliding Couples in Degraded Ester-Based Lubricant," submitted for publication.

FRICTION AND WEAR PROPERTIES OF SILICON NITRIDE/M-50 SLIDING SLIDING COUPLES IN A DEGRADED, ESTER-BASED LUBRICANT

Robert Sabia,*[1] David Mitchell,*[1] Herbert A.J. Chin,[2] and James H. Adair*[1]
[1]University of Florida
Materials Science and Engineering
Gainesville, FL 32611
[2]Pratt & Whitney Aircraft
West Palm Beach, Fl 33410

*Member, Society of Tribologists and Lubrications Engineers

ABSTRACT

The effect of ester-based oil degradation on the wear behavior of the silicon nitride/M50 steel system has been studied in order to understand the influence of oil degradation on hybrid bearing performance. Degraded oil samples were generated by heating a conventional gas turbine jet engine lubricant (MIL-L-23699C) to temperatures between 200-300°C for various times. Lubricant degradation was characterized using total acid number, antioxidant concentration, rheometry, surface tension, optical spectroscopy, and molecular weight via gel permeation chromatography. Coefficient of friction and rate of wear were measured for Si_3N_4*-M50 steel as a function of degree of lubricant degradation using a pin-on-disk test apparatus under a Hertzian contact stress of 1.6 GPa at 25±1°C. Results show significant physical and chemical changes which could not be attributed to any specific degradation product. Degradation is shown to increase the coefficient of friction but showed no correlations to wear measurements.*

KEY WORDS

Degradation, Friction, Lubrication, Wear.

INTRODUCTION

Current understanding of the effects of oil degradation on the wear behavior of the silicon nitride/M-50 system is limited. Synthetic ester-based lubricants are composed of complex additive packages blended with multiple base stocks. Formulations vary between both vendor and grade. Friction and wear studies performed are usually simplified by testing individual additives and base stocks, allowing easy determination of system interactions and behavior. These simplifications are limited in relation to real-life systems in use, with possible interactions between numerous oil constituents not observable. Further hindering understanding of these oil systems are degradation tests which are also simplified and do not allow for analysis of competing degradation mechanisms.

Bearing Design

All-metal ball bearings are designed to allow the ball elements to roll along the inside of the bearing raceway, generating subsurface shear stresses which if excessive, ultimately lead to spallation (1). Conventional design incorporates materials with high elastic moduli, such as metals and ceramics, and the use of liquid lubricants which reflect Newtonian behavior to generate a contact area which is consistent with elastohydrodynamic lubrication (EHL or EHD) (1-3). With ideal rolling contact and EHL behavior, the ball and outer raceway elastically deform under high pressures within the contact region, generating a larger contact area. Oil is drawn into the contact region under hydrodynamic lubrication. The high pressure increases the lubricant viscosity, creating a film which separates the ball and raceway, allowing the ball to roll with only a small degree of sliding (1). The higher the viscosity, the thicker the film and, therefore, the better protection against wear (assuming adequate flow) (4). However, non-ideal behavior does exist within rolling bearing systems (1). Large amounts of slip and spin result as centripetal forces and gyroscopic moments separate the contact angle between raceways, increasing torque and breaking down the EHL layer (1,2,5,6). Surfaces come into contact, generating high wear rates and increased temperatures. The combination of these non-ideal behaviors result in the generation of other modes of lubrication, namely those characteristic of dry lubrication and boundary lubrication, in which surface wear and tribochemical reactions occur to a much greater extent.

Wear of Bearing Components

The behavior of wear falls into two general categories, namely mechanical wear and tribochemical wear (7-8). Mechanical wear can include different mechanisms, including adhesion, abrasion, and fatigue. Tribochemical wear mechanisms include oxidation and corrosion, where contaminants and degradation products react with sliding surfaces to either promote or hinder the rate of material removal. The effectiveness of a given material in preventing the generation of wear is dependent on material properties and surface condition. High yield strength, fracture strength, hardness, toughness, corrosion resistance, and low thermal conductivity at both low and high operating temperatures help to minimize the generation of debris and organometallic products (8-9).

Behavior of Lubricants

Under proper EHL conditions, the lubricant offers further advantages by cooling the bearing and removing debris from the contact area. However, under non-idea behavior such as boundary lubrication conditions, the lubricant serves a second purpose by lowering the coefficient of friction and thus minimizing wear. The chemical properties of the lubricant dictate the effectiveness in reducing friction by either forming protective oxide films (typical of silicon nitride reacting with water and M-50 steel reacting with tricresylphosphate) or the formation of organic compounds typically catalyzed by metallic surfaces (10-11). Additive compounds containing phosphorous and sulfur have been shown to lower friction and the rate of wear, whereas chlorine containing compounds have been shown to have the opposite effect (10).

Oil Monitoring

Current oil monitoring techniques fall into three main categories. These categories include study of basic fluid parameters such as viscosity and total acid number, analytical techniques used to determine chemical changes in additive concentrations and base stock, and off-line techniques which have been developed to give quick information on oil condition.

Basic Fluid Parameters

As a first look at the extent of degradation in used oil samples, two basic techniques are used. For extent to which degradation has affected the physical condition of the oil, viscosity testing is employed. To determine the extent to which the oil has chemically degraded, total acid number (based on ASTM 664-89) is determined. Total acid number (TAN) is a technique in which a small amount of the oil sample is dissolved in solvents and titrated using 0.1N alcoholic KOH. As a result, the amount of KOH solution needed to titrate the oil sample to a specific pH represents the concentration of base neutralized acidic sites on the various oil constituents and degradation products.

Analytical Techniques

Due to the complexity of additive packages used in synthetic oils, analytical techniques must be utilized to monitor for additive levels, degradation products, and contaminants. Infrared spectroscopy is capable for such analysis due to equipment sensitivity and flexibility (12). Spectrometric techniques, such as atomic absorption, rotrode or rotating disc atomic emission spectroscopy, and inductively coupled plasma atomic emission spectroscopy are used for elemental analysis of wear metal concentrations (13-15). Differential scanning calorimetry is used to determine oxidation onset or autoignition temperature (15). Chromatographic methods, including gas chromatography and gel permeation chromatography, are used to discern additive concentrations as well as degradation patterns and products (15-16).

Off-line Techniques

Over the past decade, a number of techniques have been developed to determine the condition of degraded oil samples. Through the investigations of Kauffman et al., one particular technique has earned most notable recognition: the Remaining Useful Lubricant Life Evaluation Rig (RULLER) (17-19). A small sample of degraded oil is dissolved into a solvent and tested using a voltametric method to determine the antioxidant concentration is the oil sample. Taking into account that the lubricant begins to degrade before the antioxidant content is completely depleted, the percent of antioxidant remaining is related to the remaining useful life of the used oil, thus determining when an engine's oil must be changed.

Oil Degradation Mechanisms

The most common mechanisms for the degradation of these polyolester lubricants are thermal and thermal-oxidation degradation mechanisms (20). Both degradation processes consist of a free radical chain mechanism, in which free radicals are generated through either a carbon-carbon scission mechanism [scheme 1, below], a hydroperoxide radical mechanism [2 and 3], or through direct reaction with oxygen [4] (16,18,20-24). Free radical molecules (XH) then act to polymerize other lubricant constituents by starting reaction chains via abstraction of hydrogen atoms from parent hydrocarbons. Antioxidant species act to satisfy these free radicals (e.g., R· and RO_2·) by donating a hydrogen [5].

$$R\text{-}CH_2\text{-}CH_3 \rightarrow R\cdot + R\text{-}CH_2\text{-}CH_2\cdot \qquad [1]$$

$$R\cdot + O_2 \rightarrow RO_2\cdot \qquad [2]$$

$$RO_2\cdot + RH \rightarrow RO_2H + R\cdot \qquad [3]$$

$$RH + O_2 \rightarrow R\cdot + HO_2\cdot \qquad [4]$$

$$RO_2\cdot + XH \rightarrow RO_2H + X\cdot \qquad [5]$$

Primary ester byproducts include hydroxyl groups (-OH), carbonyl groups (-C=O), alkenes (-C=C-), and conjugated dienes (-C=C-C=O) (16-21). Antioxidant additives act to eliminate this free radical chain propagation mechanism by donating a proton to the free radicals, therefore rendering them inactive. The antioxidant molecule then becomes a free radical, but stabilizes itself usually by a resonance to accommodate the excess energy (22). In this method, antioxidants retard thermal and thermal-oxidation degradation mechanisms.

Typical ester degradation products include the formation of carboxylic acids, ketones, aldehydes, alcohol, water, and the formation of new ester species (16,21). Both alcohol and water can form when alkyl hydroperoxides thermally degrade and form alkoxy and hydroxy radicals [6], which then react with the parent hydrocarbon [7 and 8] (16). The formation of carboxylic acid, aldehyde, and ketone species involves the oxidative degradation of the base ester in the presence of a free radical [9] (21). Transesterification, which can result in the formation of either higher or lower molecular weight molecules, occurs by reaction with an alcohol and is typically catalyzed by a weak acid [10] (25). The formation of high molecular weight degradation products can occur by condensation reactions between oxidized ester products [11] and is accompanied by the generation of water (21).

$$RH + O_2 \rightarrow RO\cdot + \cdot OH \qquad [6]$$

$$RO\cdot + RH \rightarrow ROH + R\cdot \qquad [7]$$

$$\cdot OH + RH \rightarrow HOH + R\cdot \qquad [8]$$

$$R_1\text{-}\overset{\overset{O}{\|}}{C}\text{-}O\text{-}CH{<}^{R_2}_{R_3} \xrightarrow{RO_2\cdot,\,O_2} R_1\text{-}\overset{\overset{O}{\|}}{C}\text{-}O\text{-}\overset{\overset{R_2}{|}}{\underset{\underset{OOH}{|}}{C}}\text{-}R_3 \longrightarrow R_1\text{-}\overset{\overset{O}{\|}}{C}\text{-}H + HOO\text{-}\overset{\overset{O}{\|}}{C}\text{-}R_2 \longrightarrow R_1\text{-}\overset{\overset{O}{\|}}{C}\text{-}OH + HO\text{-}\overset{\overset{O}{\|}}{C}\text{-}R_2 \qquad [9]$$

$$R_1\text{-}\overset{\overset{O}{\|}}{C}\text{-}O\text{-}R_2 + R_3OH \xrightarrow{\text{Acid}} R_1\text{-}\overset{\overset{O}{\|}}{C}\text{-}O\text{-}R_3 + R_2OH \qquad [10]$$

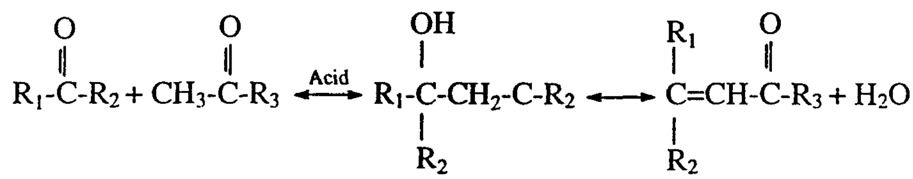

[11]

Objective

The objective of this investigation was to explore the effects of oil degradation on friction and wear of the silicon nitride/M-50 steel system using a conventional synthetic oil. Oil samples have been thermally degraded and characterized to determine oil condition before performing friction and wear tests.

MATERIALS AND METHODS

Samples of as-received synthetic ester-based turbine oil (meeting MIL-L-23699C) were tested at temperatures of approximately 220, 260, and 290±5°C (referred to as schedules 1 through 3 respectively) for test periods of 3, 5, 7, and 9 hours (designation example: Sch 1, 3 hrs). The test apparatus consisted of 500 ml of as-received oil placed in a 1000 ml Pyrex beaker on a manually controlled heating plate with a K-type thermocouple inserted into the oil. Humidity was not controlled during these tests. Each of the twelve test samples represents an independent oil degradation experiment.

Characterization of the degraded oil samples was performed using various analytical techniques to obtain insight into the physical and chemical changes generated in the oil samples. Viscosity measurements on the samples were performed using a variable speed cone and plate viscometer (Brookfield RVDV-III, Brookfield Engineering Laboratories, Inc., Stoughton, MA 02072). Temperature was held at 40±0.1°C using a constant temperature water bath. Shear stress and viscosity measurements were made at shear rates between 0.75 and 450 s^{-1}. Surface tension measurements were made for the oil samples using the maximum bubble pressure method (SensaDyne PC9000 Surface Tensiometer, Chem-Dyne Research Corporation, Mesa, AZ 85275). Concentration of the antioxidant additive for each sample was determined using the Remaining Useful Lubricant Life Evaluation Rig (University of Dayton Research Institute, Dayton, OH 45469) (17-19). Changes in acid levels generated during degradation were determined for each sample using a titration method which generated total acid number values (ASTM 664-89, using aqueous buffers and titrating to a pH of 11).

Optical absorption characteristics for the oil samples were determined using a variable wavelength spectrometer (Ultrospec III, Pharmacia LKB Biochrom LTD, Cambridge, England) with ±0.1% accuracy, covering the ultraviolet and visible regions of the electromagnetic spectrum between 200 and 900 nm. Total loss edge values were determined by extrapolating the tangent for each data curve to the intercept of the wavelength axis at 0 transmittance. Additional spectrometry analysis was performed using transmission FTIR (20SXB and Omnic™ software, Nicolet Instrument Corporation, Madison, WI 53711) with nitrogen purge, analyzing chemical changes in the oil samples through analysis of the characteristic vibrational peaks.

Gel-permeation chromatography (Waters™ Chromatography Division, Millipore Corporation, Milford, MA 01757) was performed using 50 to 300.000 molecular weight range columns (Phenogel, Phenomenex, Torrence, CA 90501), a UV/VIS detector at 216 nm, and tetrahydrofuran as the solvent carrier. The columns were calibrated using polystyrene molecular weight standards and toluene. In order to accurately compare results from each run, the area under each data curve was normalized.

Effects of oil degradation on the friction and wear behavior of the silicon nitride/M-50 steel system were measured by tribological experiments using the previously degraded oil samples. The test apparatus was a pin-on-disk machine (ISC-200PC Tribometer, Implant Sciences Corporation, Wakefield, MA 01880) designed to reflect boundary lubrication conditions for a liquid environment. Commercial yittria/alumina doped silicon nitride 3.2 mm diameter bearing grade (surface finish = 0.2 μm) bearing balls were used as pin materials. M-50 steel 41.3 mm diameter rolling elements were cut into 6.35 mm thick disks using a precision wire electrical discharge machine (HS-100, Raycon Corporation, Ann Arbor, MI 48104), ground and lapped to a 0.2 μm surface finish (Superfinishers, Inc., Macedonia, OH 44056), heat treated to attain high hardness (R_c>62), and used as disk materials. Parameters for all experiments included a 2000g (19.61N) load, 8.5 cm/s linear speed, 50% relative humidity atmosphere, and 25±1°C. The corresponding initial Hertzian contact stress was 1.6 GPa and the theoretically predicted initial contact diameter was 111.69 μm. Wear track radii on the disk materials were varied at 10.0, 12.5, and 15.0 mm, allowing for multiple tests on each disk sample.

Friction data determined by lateral displacement at constant load was recorded as a function of sliding distance for the duration of testing. Coefficient of friction values for each experiment were taken at sliding distances of 2500 meters, allowing for adequate run-in time. Analysis of wear tracks for both surfaces was performed using a scanning electron microscope (6400 Scanning Electron Microscope, Joel USA, Inc., Peabody, MA

01961). Wear data for disk materials is reported as wear track thickness/sliding distance (μm/1000m), and wear data for pin materials is reported in terms of the specific wear rate (weight loss/sliding distance).

RESULTS AND DISCUSSION

Results of the techniques used to characterize the oil samples are shown in Table 1. The results show the same general trends for each test method as a function of test time. As viscosity increased, total loss edge increased, total acid number increased and antioxidant content decreased, with surface tension remained relatively constant at 0.04 N/m. Antioxidant concentration fell below the 50% level for the most extreme test samples, suggesting a high degree of degradation. However, TAN results only showed moderate increases to 1.48 mg KOH/g.

Results for viscosity testing performed at 40±0.1°C showed all samples had Newtonian behavior without Bingham yield points. Viscosity values for each sample are given in Table 1, where a general trend of increasing viscosity as test time proceeds is observed for the three schedules. Viscosities for samples from schedule 1 fluctuated about the 23.2 cP value of the as-received oil sample, whereas results for schedules 2 and 3 yielded significant viscosity increases up to 50%. The observance of an initial negative change in viscosity of -2.3% for the schedule 1, 3 hour sample is not considered significant.

Transmittance measurements in the ultraviolet and visible regions performed on samples from the 290°C heating schedule 3 are shown in Figure 1. As with samples for all three heating schedules, results showed negligible transmission results in the ultraviolet region, with the majority of relative data existing above 375 nm. Inflections observed at approximately 525 and 675 nm are equipment specific anomalies, and therefore do not represent spectral characteristics of the samples. Characteristic to the data presented was a trend of decreasing transmission as a function of test time. Variations from the general behavior for these samples is attributed to modest fluctuations in the heating schedules. Also characteristic to these samples was an increase in the total loss edge as a function of test time, shown in Table 1.

Comparison of total loss edge data and viscosity results are shown in Figure 2, where viscosity is plotted in percent change and a master line generated by linear regression analysis. The regression coefficient (r^2) for the line $y = 546.50 + 5.44 \cdot x$ was found to be 0.96, and the slope was 5.4. This correlation suggests that the optical behavior of the oil samples and the viscosity changes are related, possibly by a common factor(s). However, the as-received oil sample was found to have a total loss edge value of 390 nm, which is not consistent with the results for the degraded oil samples.

Results from infrared analysis yielded peaks for the as-received sample as shown in Figure 3 and Table 2: Strong absorption peaks between 2850-3000 cm^{-1} and a weak peak at 1465 cm^{-1} reflect hydrocarbon stretch. A strong peak at 1743 cm^{-1} represents one or more carbonyl peaks for ester structures within the base oil. A variety of lower intensity peaks between 1000-1465 cm^{-1}, which include the C-C(=O)-O (lactone) and the O-C-C peaks, were not distinguishable (26). For the degraded oil samples, peak broadening as a function of test time was observed for the carbonyl peak. This is the result of the generation of new carbonyl peaks, however the structure(s) associated with the new species is not discernible. Transesterification, the formation of ketones, and the formation of carboxylic acids are possible sources for the new carbonyl species (26).

Results from GPC testing for schedule 3 (290±5°C) are shown in Figure 4. The as-received oil sample showed peaks at 215, 360, 565, 775, and 1125 molecular weights (MW). As a function of test time, samples from all three heating schedules yielded decreasing intensities for the 216 and 360 MW peaks, and increasing intensities for the 565, 775, and 1125 MW peaks. Samples for Schedules 2 and 3 showed the generation of a higher molecular weight species in the form of a broad peak between 1500-3000 MW. The decrease in intensity for the low molecular weight species can be attributed in part to evaporation. Increases in the intensity of the higher molecular weight species and the generation of the 1500-3000 MW peak suggests reaction between the species with decreasing intensities. Further information is gained from data for the 5 hour test sample from Schedule 3 (290±5°C), which shows in Figure 4 the generation of two low intensity peaks at approximately 31,500 and 101,000 MW. For the 7 hour sample, the 31,500 MW peak is not observed and the 101,000 MW peak is of lower intensity. For the 9 hour sample, neither peaks are present. These results suggest the generation of high molecular weight species which are no longer soluble in the oil. These insoluble species are commonly referred to as sludge. The base ester undergoes a reaction to form new ester, ketone, or carboxylic acid species which generate higher molecular weight ester species, which subsequently deposit as a carbonaceous residue.

In order to compare the effects of oil degradation on the friction and wear behavior of the silicon nitride/M-50 steel system in the current work, a method to quantify the extent of degradation for samples from each heat schedule was developed.

Since oil degradation is reflected by both physical and chemical changes, and since these changes are reflected in viscosity and total acid number measurements, a correlation between these experimental values and the oil condition for each sample must be made. Assuming that changes in viscosity are the result of the formation of high molecular weight degradation products which act as particulate species (e.g., carbonaceous particles), the Einstein equation for changes in viscosity as a function of particle volume for Newtonian fluids (27) may be used:

$$\eta^* = \eta o \cdot (1 + \frac{5}{2} \cdot \phi) \qquad (1)$$

The η^* refers to the experimental viscosity, η_o refers to the as-received viscosity, and ϕ refers to the percent particle volume of the system. From this relation, the molal concentration of particulate species may be determined assuming a set density for the particulate species (for this study the density was assumed to be 2.0 g/cc). From the TAN values, molal values which reflect the number of base neutralized acidic sites may also be calculated. A combination of the two molal values can be used to generate an overall molal concentration value for the oil samples:

$$MC = \frac{m_{TAN} + m_{\phi}}{m^*_{TAN} + m^*_{\phi}} \qquad (2)$$

MC refers to the molal concentration of the degraded oil, m_{TAN} refers to the molal value calculated from TAN values, m_{ϕ} refers to the molal value determined from the particle volume, m^*_{TAN} and m^*_{ϕ} refer to the molal values for the most degraded sample in the study (Sch 2, 9 hrs).

Results for coefficient of friction measurements are plotted versus the molal concentration as shown in Figure 5. Friction values range from 0.08 and 0.12. From the regression curve drawn for all data points, a general increase in friction is observed as the degree of degradation increases. Results for wear measurements (see Figure 6) showed values for the specific wear rate of the pin surface range between 14.2 and 47.4 pg/m. Rate of wear values for the disk surfaces range between 9.1 and 18.8 μm/1000m (see Figure 7). However, no correlations were found for the rate of wear versus the overall molal concentration of degradation products for the lubricant.

CONCLUSIONS

Characterization performed on the oil samples showed viscosity changes between -2.3% and 49.4% relative to the as-received oil. Results of molecular weight analysis of the samples for the most extreme testing conditions showed the formation of high molecular weight species, which subsequently were removed as test time proceeded, suggesting the formation of insoluble species (sludge). In correlation with infrared spectrometry results which showed peak broadening, the precise degradation mechanism for the system at hand could not be determined, as the formation of carboxylic acids, ketones, and esters (via transesterification) are all possible reaction products.

A linear relationship was found to exist between total loss edge values and changes in viscosity. This observation suggests that the changes in optical behavior of the oil are dependent on physical changes which result during degradation. This correlation also suggests that optical properties may be used to monitor oil degradation *in-situ*.

Results from friction and wear testing of the previously degraded oil samples under boundary lubrication conditions showed the coefficient of friction to increase with respect to oil condition. Results for wear measurements under boundary lubrication conditions showed the rate of wear for both the silicon nitride and M-50 surfaces to be independent of oil condition with no correlation of rate of wear to the characterization techniques used for this report.

ACKNOWLEDGMENTS

The Authors gratefully acknowledge the support of the Air Force Office of Scientific Research Grant Number F49620-93-12-0349DEF. Thanks are also given to Michael Zamorra, Dr. Jim Kunetz and Ahmad R. Hadba of the University of Florida Department of Materials Science and Engineering, and Guy La Torre of US Biomaterials, Inc. for their assistance with characterization. the authors would also like to thank Pratt & Whitney for laboratory and equipment use in the West Palm Beach location.

REFERENCES

(1) Jackson, A., "Elastrohydrodynamic Lubrication (EHL)," Lubrication Engineering, 47, pp. 833-835, (1991).

(2) Denape, J., Masri, T., and Petit, J-A., "Influence of Surface Roughness and Oil Aging on Various Ceramic-Steel Contacts Under Boundary Lubrication," Journal of Engineering Tribology, 209, pp. 173-182, (1995).

(3) Hamrock, B.J., "Elastrohydrodynamic Lubrication - Status of Understanding," in New Directions in Materials, Wear, and Surface Interactions, Tribology in the 80's, W. R. Loomis, ed., Noyes Publications, (1985) pp. 484-505.

(4) Lin, J.F., and Chen, Y.N., "Tribological Reaction Generated on Ceramic-Stellite Couples Under Dry Sliding Contact and Water- and Oil-Lubricated Conditions," Wear, 177, pp. 139-149, (1994).

(5) Gentle, C.R., "Bearings with Ceramic Balls - The Effect of Reduced Lubricant Supply on the Minimum Load," Prec. Instn. Mech. Engrs., 20, pp. 253-256, (1994).

(6) Sliney, H.E., and Dellacorte, C., "The Friction and Wear of Ceramic/Ceramic andCeramic/Metal Combinations in Sliding Contact," Lubrication Engineering, 50, 7, pp. 571-576, (1994).

(7) Akagaki, T. and Kato, K., "Effects of Hardness on the Wear Mode Diagram in Lubricated Sliding Friction of Carbon Steels," Wear, 141, pp. 1-15, (1990).

(8) Kato, K. "Tribology in Ceramics," Wear, 136, pp. 117-133, (1990).

(9) Lucek, J.W., and Hannoosh, J.G., "Field Experience in Ceramic Bearings," Cerbec, Inc., East Granby, CT, (1992).

(10) Gates, R.S., and Hsu, S.M., "Effect of Selected Chemical Compounds on the Lubrication of Silicon Nitride," Tribology Transactions, 34, pp. 417-425, (1991).

(11) Klaus, E.E., Duda, J.L., and Wu, W.T., "Lubricated Wear of Silicon Nitride," Lubrication Engineering, 47, 8, pp. 679-684, (1991).

(12) Coates, J.P., and Setti, L.C., "Infrared Spectroscopy as a Tool for Monitoring Oil Degradation," in Aspects of Lubricant Oxidation, ASTM STP 916, W.H. Stadtmiller and A.N. Smith, eds., American Society for Testing and Materials, Philadelphia, (1886) pp. 57-78.

(13) Hosang, G.W., "Experimental and Computed Performance Characteristics of High-Speed Silicon Nitride Hybrid Ball Bearings," Journal of Engineering for Gas Turbnes and Power, 113, pp. 635-643, (1991).

(14) Kauffman, R.E., Saba, C.S., Rhine, W.E., and Eisentraut, K.J., "Chemical Nature of Wear Debris," ASLE Transactions, 28, 3, pp. 400-406, (1985).

(15) Pachuta, D.G., Thich, J.A., Knipple, R.W., and Stephanic, D.A., "Experiences with an Analytical Montioring Program Designed for Commercial Flight Tests of Advanced Mil-23699 Turbine Fluids," in Turbine Oil Monitoring, ASTM STP 1021, W.C. Young and R.S. Robertson, eds., American Society for Testing and Materials, Philadelphia, (1989), pp. 54-76.

(16) Jones, W.R. Jr, "Thermal and Oxidative Stabilities of Liquid Lubricants," in New Directions in Lubrication, Materials, Wear, and Surface Interactions, Tribology in the 80's, Loomis, W.R. Jr, ed., Noyes Publications, (1985).

(17) Kauffman, R.E., "Development of a Remaining Useful Life of a Lubricant Evaluation Technique. Part III: Cyclic Voltammetric Methods," Lubrication Engineering, 51, 11, pp. 709-716, (1995).

(18) Kauffman, R.E., "On-Line and Off-Line Techniques for Monitoring the Thermal and Oxidative Degradations of Aircraft Turbine Engine Oils - Part I: Laboratory Evaluations," Lubrication Engineering, 51, 11, pp. 914-921, (1995).

(19) Kauffman, R.E., "Remaining Useful Life Measurements of Deisel Engine Oils, Automotive Engine Oils, Hydraulic Fluids, and Greases Using Cyclic Voltammetric Methods," Lubrication Engineering, 51, 3, pp. 223-229, (1995).

(20) Hsu, S.M., Ku, C.S., and Pei, P.T., "Oxidative Degradation Mechanisms of Lubricants," Aspects of Lubricant Oxidation, ASTM STP 916, W.H. Stadtmiller and A.N. Smith, eds., American Society for Testing and Materials, Philadelphia, (1986), pp. 27-48.

(21) Bakunin, V.N., and Parenago, O.P., "A Mechanism of Thermo-Oxidative Degradation of Polyol Ester Lubricants," Journal of Synthetic Lubrication, 9, 2, 127-143, 1992.

(22) Hunter, M., Klaus, E.E., and Duda, J.L., "A Kinetic Study of Antioxidant Mechanisms," Lubrication Engineeering, 49, 6, pp. 492-498, (1993).

(23) Jones, W.R., "The Furture for Liquid Lubricants and Additives, Thermal and Oxidative Stabilities of Liquid Lubricants," in New Directions in Lubrication, Materials, Wear, and Surface Interactions, Tribology in the 80's, Loomis, W.R., ed., Noyes Publications, (1985).

(24) Klaus, E.E., "Status of New Directions of Liquid Lubricants," in New Directions in Materials, Wear, and Surface Interactions, Tribology in the 80's, William R. Loomis, ed., Noyes Publications, (1985) pp. 354-375.

(25) Fieser, L.F. and Fieser, M., Organic Chemistry, D. C. Heath and Company, New York, (1950).

(26) Silverson, R.M., Bassler, G.C., and Morrill, T.C., Spectrometric Identification of Organic Compounds, John Wiley & Sons, (1991).

(27) Einstein, A., Investigations on the Theory of the Brownian Movement, Dover Publications, Inc., USA, (1956).

Table 1. Physical data determined for individual test samples. "Sch" refers to schedule number and "hrs" refers to hours tested, where Sch 1=220°C, Sch 2=260°C, and Sch=290°C (±5°C).

Sample ID	Viscosity (cP)	Total Loss Edge (nm)	TAN (mg KOH/g)	Antioxidant Content (%)	Surface Tension (N/m)
As-received	23.23	390	0.37	NA	0.036
Sch 1, 3 hrs	22.69	525	0.58	96	0.039
Sch 1, 5 hrs	24.11	570	0.75	91	0.039
Sch 1, 7 hrs	23.81	567	0.69	90	0.037
Sch 1, 9 hrs	24.36	616	1.19	80	0.039
Sch 2, 3 hrs	25.42	565	1.00	85	0.039
Sch 2, 5 hrs	26.78	620	1.19	--	0.039
Sch 2, 7 hrs	28.65	678	1.67	73	0.040
Sch 2, 9 hrs	30.03	712	1.87	54	0.040
Sch 3, 3 hrs	26.13	595	0.97	70	0.039
Sch 3, 5 hrs	28.00	675	0.91	58	0.038
Sch 3, 7 hrs	32.99	785	1.42	49	0.038
Sch 3, 9 hrs	34.69	810	1.48	48	0.039

Table 2. List of identifiable absorbance peaks in the infrared spectra.

Absorbance Peak	Attributed Vibration
1465 cm^{-1}	Hydrocarbon (C-H)
1743 cm^{-1}	Carbonyl (C=O)
2850-3000 cm^{-1}	Hydrocarbon (C-H)

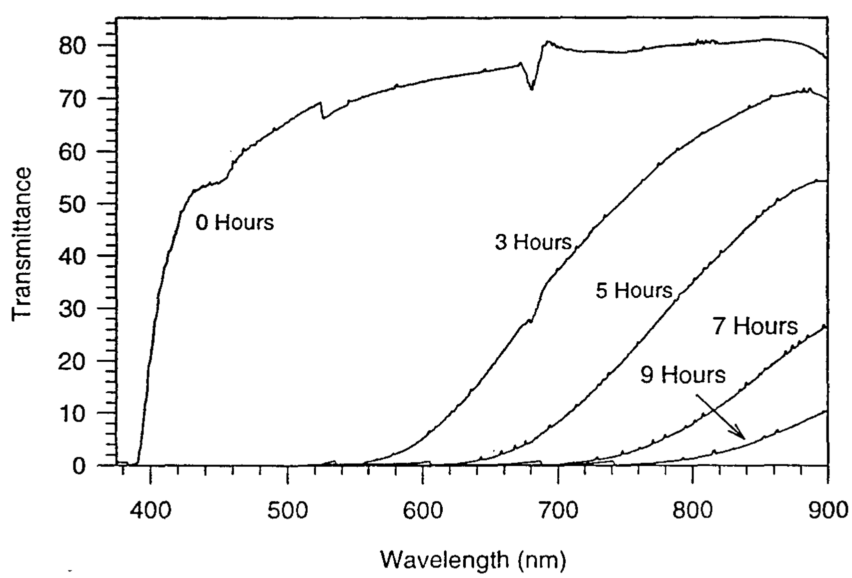

Figure 1. UV/VIS spectrometry data for samples run according to heating schedule 3. Results show a decrease in transmittance and a shift of the total loss edge to high wavelengths with decreasing oil condition.

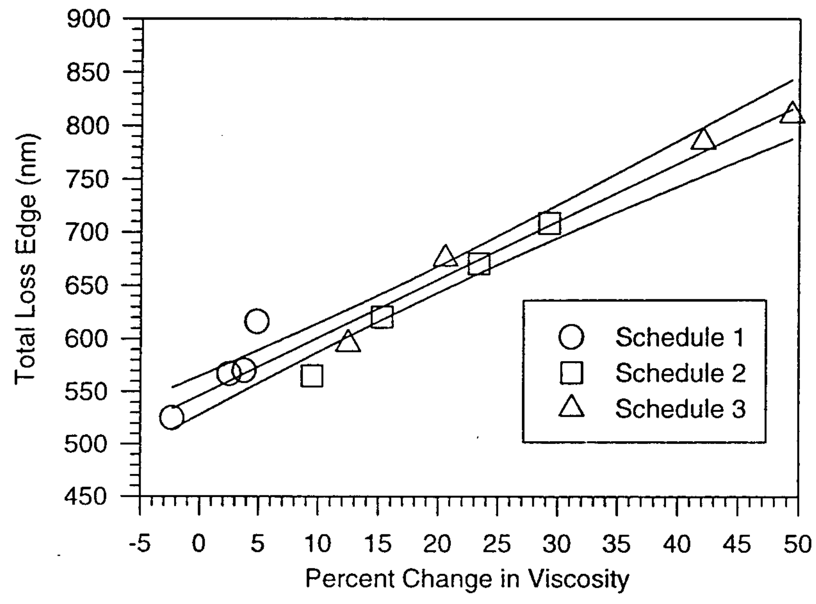

Figure 2. Total loss edge versus change in viscosity, fitted with the relationship $y = 546.50 + 5.44 \cdot x$ and 95% confidence intervals. The relationship between the optical properties and the change in viscosity with degradation of the oil is linear.

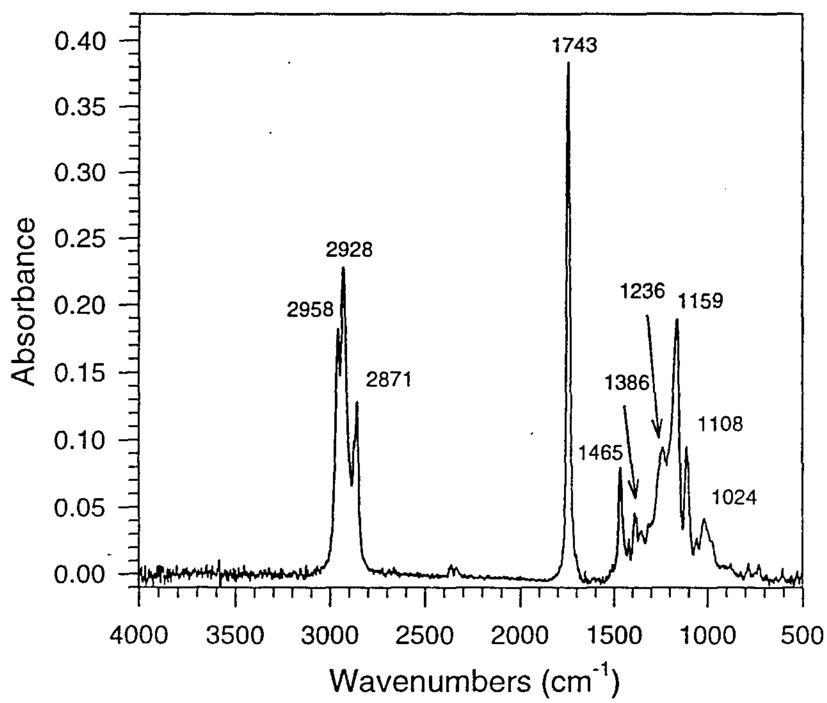

Figure 3. Infrared spectra for the as-received, syntheitc ester-based lubricant sample (MIL-L-23699C). Peaks located between 2850-3000 cm^{-1} and 1465 cm^{-1} represent hydrocarbon structures, and the 1743 cm^{-1} peak represents an ester carbonyl peak. Peaks between 1000-1400 cm^{-1} represent C-O stretch from esters.

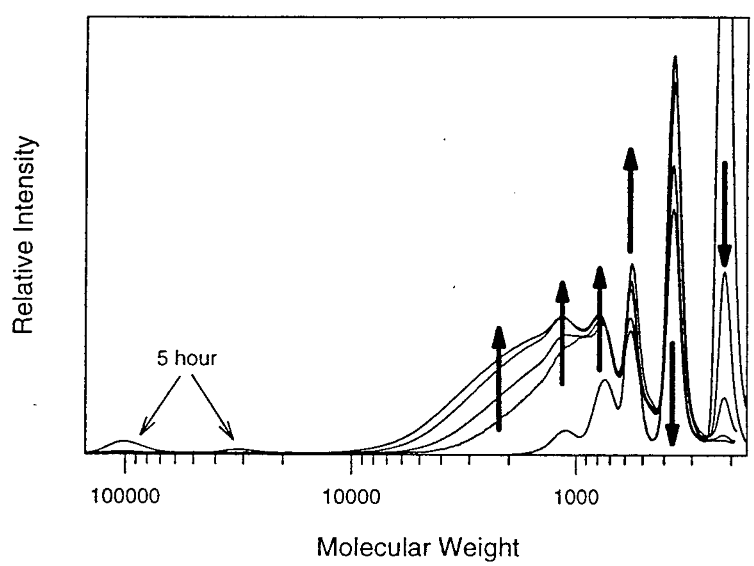

Figure 4. GPC data for Schedule 3 (290±5°C). Arrows indicate direction of changes with increasing test time. Lower MW species decrease in concentration as higher MW species and products increase in concentration with test time. The formation and subsequent removal of high MW degradation products at 101,000 and 31,500 MW suggest sludge formation.

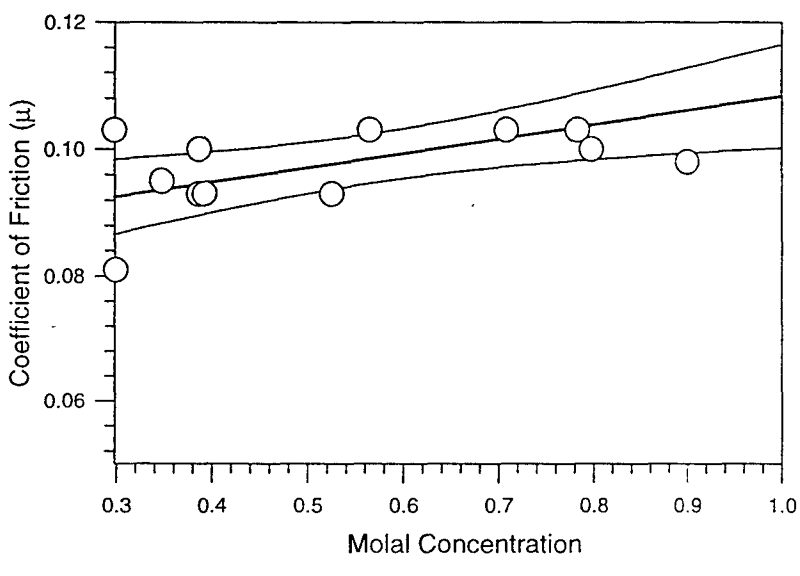

Figure 5. Coefficient of friction data for oil samples plotted versus molal concentration of the degradation product (Eq. (2)). showing a general increase in friction with increasing degradation of the lubricant. The outside lines represent 95% confidence intervals.

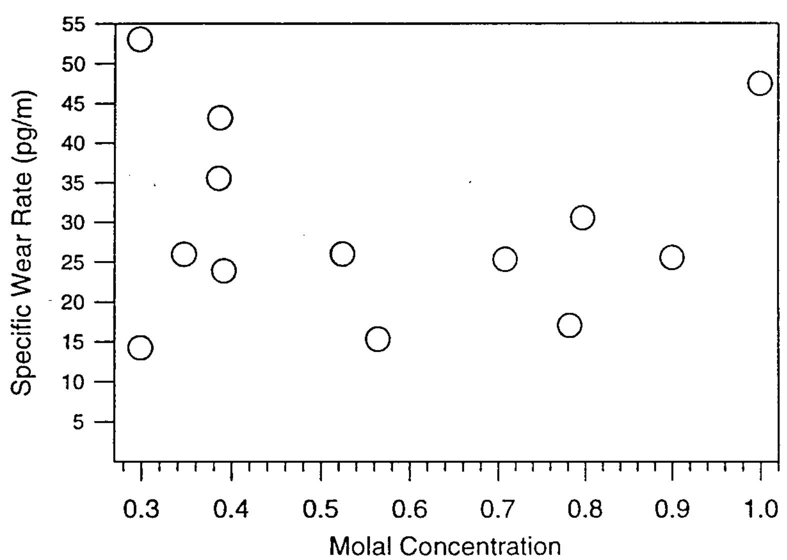

Figure 6. Rate of wear data for pin surfaces given in weight loss versus sliding distance (picograms/meters) plotted against molal concentration of the degradation product for oil the samples (Eq. (2)). No correlation was found beteen oil degradation rate and rate of wear of the pin.

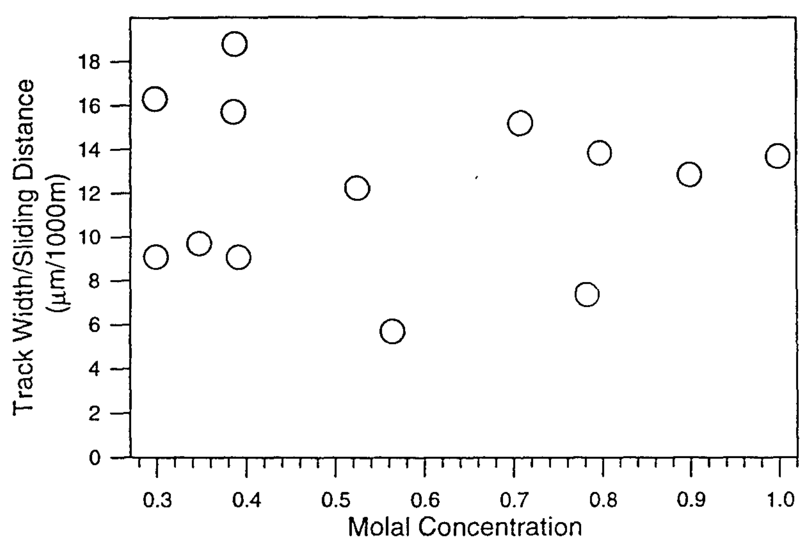

Figure 7. Rate of wear data for disk surfaces given in increasing track width versus sliding distance (microns/meters) plotted against molal concentration of the degradation product for oil the samples (Eq. (2)). No correlation is shown between oil degradation condition and rate of wear of the disk.

APPENDIX 19, R. Sabia, D.J. Mitchell, and J.H. Adair, "Effects of Oil Degradation on the Friction and Wear Properties of Silicon Nitride/M-50 Steel Sliding Couples," *Cer. Engr. & Sci. Proc.*, 18[3], 361-368, (1997).

EFFECTS OF OIL DEGRADATION ON THE FRICTION AND WEAR PROPERTIES OF SILICON NITRIDE/M-50 STEEL SLIDING COUPLES

Robert Sabia, David Mitchell, and James H. Adair
University of Florida
Materials Science and Engineering
Gainesville, FL 32611

ABSTRACT

The effect of oil degradation on the wear behavior of the silicon nitride/M50 steel system has been studied in order to understand the influences of oil degradation on bearing performance. Degraded oil samples were generated by heating a conventional gas turbine lubricant (MIL-L-23699) to temperatures between 200-300°C for various times. Sample characterization was performed using total acid number, antioxidant concentration, rheometry, surface tension, spectroscopy, and gel permeation chromatography. Coefficient of friction and rate of wear were measured on the oil samples using a pin-on-disk test apparatus under a Hertzian contact stress of 1.6 GPa at 25±1°C. Results show significant physical and chemical changes which could not be attributed to any specific degradation product. Degradation is shown to increase the coefficient of friction, with no correlations to wear measurements.

INTRODUCTION

Conventional bearing design incorporates materials with high elastic moduli, such as metals and ceramics, and the use of liquid lubricants which reflect Newtonian behavior to generate a contact area which are consistent with elastohydrodynamic lubrication (EHL) [Den95,Ham85,Jac91,Wak74]. Under proper EHL conditions, the lubricant offers advantages by cooling the bearing and removing debris from the contact area. Under non-ideal behavior when surface come into contact (i.e. boundary lubrication conditions) the lubricant serves a second purpose by lowering the coefficient of friction and thus minimizing wear. The chemical properties of the lubricant dictate the effectiveness in reducing friction by either forming protective oxide films (typical of silicon nitride reacting with water and M-50 steel reacting with tricresylphosphate) or the formation of organic compounds typically catalyzed by metallic surfaces [Gat91,Kla91].

Understanding the behavior and effects of oil degradation is critical for two reasons. First, each lubricant vendor and grade offer variable performance characteristics due to proprietary additive packages, thus the lubricant selected directly impacts the lifetime of a bearing. Second, liquid lubricants offer the means for *in-situ* sampling and monitoring of engine performance. As a result, the objective for this research is to develop an understanding of the effects of oil degradation on the friction and wear properties of the silicon nitride/M-50 steel system using a conventional lubricant.

MATERIALS AND METHODS

Samples of as-received Exxon turbine oil ETO 2380[1] (MIL-L-23699) were tested at temperatures of approximately 220, 260, and 290±5°C (referred to as schedules 1 through 3 respectively) for test periods of 3, 5, 7, and 9 hours (designation example: Sch 1, 3 hrs). The test apparatus consisted of 500 ml of as-received oil placed in a 1000 ml Pyrex beaker on a manually controlled heating plate with a K-type thermocouple inserted into the oil. Humidity was not controlled during these tests. Each of the twelve test samples represents an independent oil degradation experiment.

Characterization of the degraded oil samples was performed using various analytical techniques yielding insight into the physical and chemical changes generated in the oil samples. Viscosity measurements on the samples were performed using a variable speed cone and plate viscometer.[2] Temperature was held at 40±0.1°C using a constant temperature water bath. Shear stress and viscosity measurements were made at shear rates between 0.75 and 450 s^{-1}. Surface tension measurements were made for the oil samples using the maximum bubble pressure method.[3] Concentration of the antioxidant additive for each sample was determined using the remaining useful lubricant life evaluation rig[4] (RULLER) [Kau89,Kau95a,Kau95b]. Changes in acid levels generated during degradation were determined for each sample using a titration method which generated total acid number values (ASTM 664-89).

Optical absorption characteristics for the oil samples were determined using a variable wavelength spectrometer[5] with ±0.1% accuracy, covering the ultraviolet and visible regions of the electromagnetic spectrum between 200 and 900 nm. Total loss edge values were determined by extrapolating the tangent for each data curve to the intercept of the wavelength axis at 0 transmittance. Additional spectrometry analysis was performed using transmission FTIR[6] with nitrogen purge, analyzing chemical changes in the oil samples through analysis of the characteristic vibrational peaks.

Gel-permeation chromatography (GPC),[7] was performed in the 50 and 300,000 molecular weight range[8] using a UV/VIS detector at 216 nm and tetrahydrofuran as the solvent carrier. The columns were calibrated using polystyrene molecular weight standards and toluene. In order to accurately compare results from each run, the area under each data curve was normalized.

Effects of oil degradation on the friction and wear behavior of the silicon nitride/M-50 steel system were measured by tribological experiments using the previously degraded oil samples. The test apparatus was a pin-on-disk machine,[9] designed to reflect boundary lubrication conditions for a liquid environment. Commercial yttria/alumina doped silicon nitride 3.2 mm diameter bearing grade (surface finish = 0.2 μm) bearing balls were used as pin materials. M-50

---

[1] Exxon Company USA, A Division of of the Exxon Corporation, Houston, TX 77252.
[2] Brookfield RVDV-III, Brookfield Engineering Laboratories, Inc., Stoughton, MA 02072.
[3] SensaDyne PC9000 Surface Tensiometer, Chem-Dyne Research Corporation, Mesa, AZ 85275.
[4] University of Dayton Research Institute, Dayton, OH 45469.
[5] Ultrospec III, Pharmacia LKB Biochrom LTD, Cambridge, England.
[6] 20SXB and Omnic™ software, Nicolet Instrument Corporation, Madison, WI 53711.
[7] 600E System Controller, 610 Fluid Unit, 717 Auto Sampler, and 996 Photodiode Array Detector, Waters™ Chromatography Division, Millipore Corporation, Milford, MA 01757.
[8] Phenogel 4.6×300 mm columns, with 5 μm particles and 100, 500, 10^4 and 10^5 Å pore sizes, Phenomenex, Torrence, CA 90501.
[9] ISC-200PC Tribometer, Implant Sciences Corporation, Wakefield, MA 01880.

steel 41.3 mm diameter rolling elements supplied by MRC Bearings, Inc.[10] were cut into 6.35 mm thick disks using a precision wire electrical discharge machine,[11] ground and lapped to a 0.2 μm surface finish,[12] heat treated to attain high hardness (R_c>52), and used as disk materials. Parameters for all experiments included a 2000g (19.61N) load, 8.5 cm/s linear speed, 50% relative humidity atmosphere, and 25±1°C. The corresponding initial Hertzian contact stress was 1.6 GPa and the theoretically predicted initial contact diameter was 111.69 μm. Wear track radii on the disk materials were varied at 10.0, 12.5, and 15.0 mm, allowing for multiple tests on each disk sample.

Friction data determined by lateral displacement at constant load was recorded as a function of sliding distance for the duration of testing. Coefficient of friction values for each experiment were taken at sliding distances of 2500 meters, allowing for adequate run-in time. Analysis of wear tracks for both surfaces was performed using a scanning electron microscope.[13] Wear data for disk materials is reported as wear track thickness/sliding distance (μm/1000m), and wear data for pin materials is reported in terms of the specific wear rate (weight loss/sliding distance).

RESULTS AND DISCUSSION

Results of the techniques used to characterize the oil samples are shown in Table 1. The results show the same general trends for each test method as a function of test time. As viscosity increased, total loss edge increased, total acid number increased, antioxidant content decreased, and surface tension remained relatively constant at 0.04 N/m. Antioxidant concentration fell below the 50% level for the most extreme test samples, suggesting a high degree of degradation. However, TAN results only showed moderate increases to 1.48 mg KOH/g.

Table 1. Physical data determined for individual test samples. "Sch" refers to schedule number and "hrs" refers to hours tested, where Sch 1=220°C, Sch 2=260°C, and Sch=290°C (±5°C).

Sample ID	Viscosity (cP)	Total Loss Edge (nm)	TAN (mg KOH/g)	Antioxidant Content (%)	Surface Tension (N/m)
As-received	23.23	390	0.37	NA	0.036
Sch 1, 3 hrs	22.69	525	0.58	96	0.039
Sch 1, 5 hrs	24.11	570	0.75	91	0.039
Sch 1, 7 hrs	23.81	567	0.69	90	0.037
Sch 1, 9 hrs	24.36	616	1.19	80	0.039
Sch 2, 3 hrs	25.42	565	1.00	85	0.039
Sch 2, 5 hrs	26.78	620	1.19	--	0.039
Sch 2, 7 hrs	28.65	678	1.67	73	0.040
Sch 2, 9 hrs	30.03	712	1.87	54	0.040
Sch 3, 3 hrs	26.13	595	0.97	70	0.039
Sch 3, 5 hrs	28.00	675	0.91	58	0.038
Sch 3, 7 hrs	32.99	785	1.42	49	0.038
Sch 3, 9 hrs	34.69	810	1.48	48	0.039

[10] MCR Bearing Division of SKF Aerospace Bearings, USA, Inc., Jamestown, NY 14702.
[11] HS-100, Raycon Corporation, Ann Arbor, MI 48104.
[12] Superfinishers, Inc., Macedonia, OH 44056.
[13] 6400 Scanning Electron Microscope, Joel USA, Inc., Peabody, MA 01961.

Results for viscosity testing performed at 40±0.1°C showed all samples to exhibit Newtonian behavior without Bingham yield points. Viscosity values for each sample are given in Table 1, where a general trend of increasing viscosity as test time proceeds is observed for the three schedules. Viscosities for samples from schedule 1 fluctuated about the 23.2 cP value of the as-received oil sample, whereas results for schedules 2 and 3 yielded significant viscosity increases up to 50%. The observance of an initial negative change in viscosity of -2.3% for the schedule 1, 3 hour sample is not considered significant

Transmittance measurements in the ultraviolet and visible regions performed on samples from the 285°C heating schedule are shown in Figure 1. As with samples for all three heating schedules, results showed negligible transmission results in the ultraviolet region, with the majority of relative data existing above 375 nm. Inflections observed at approximately 525 and 675 nm are equipment specific anomalies, and therefore do not represent spectral characteristics of the samples. Characteristic to the data presented was a trend of decreasing transmission as a function of test time. Variations from the general behavior for these samples is attributed to modest fluctuations in the heating schedules. Also characteristic to these samples was an increase in the total loss edge as a function of test time, shown in Table 1.

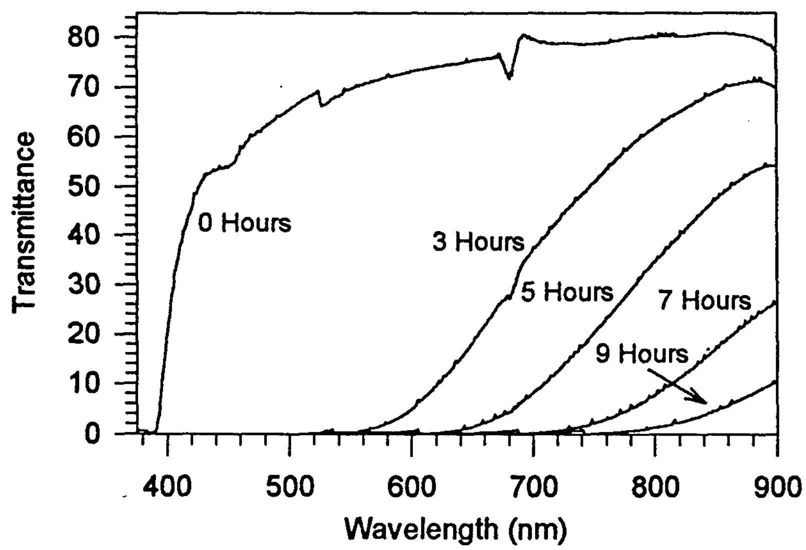

Figure 1. UV/VIS spectrometry data for samples run according to heating schedule 3.

Comparison of total loss edge data and viscosity results are shown in Figure 2, where viscosity is plotted in percent change and a master line generated by linear regression analysis. The regression coefficient (r^2) for the line $y = 546.50 + 5.44 \cdot x$ was found to be 0.96, and the slope was 5.44. This correlation suggests that the optical behavior of the oil samples and the viscosity changes are related, possibly by a common factor(s). However, the as-received oil sample was found to have a total loss edge value of 390 nm, which is not consistent with the results for the degraded oil samples.

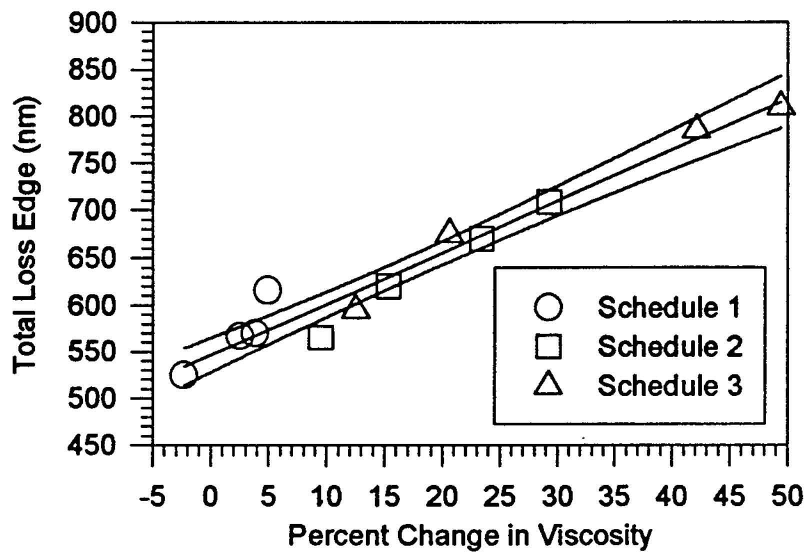

Figure 2. Total loss edge versus change in viscosity, fitted with the relationship $y = 546.50 + 5.44 \cdot x$ and 95% confidence intervals.

Results from infrared analysis yielded peaks for the as-received sample as follows (see Table II): Strong absorption peaks between 2850-3000 cm^{-1} and a weak peak at 1465 cm^{-1} reflect an alkane structure. A strong peak at 1743 cm^{-1} represents one or more carbonyl peaks for ester structures within the base oil. A variety of lower intensity peaks between 1000-1465 cm^{-1}, which include the C-C(=O)-O (lactone) and the O-C-C peaks, were not distinguishable.[Sil81] For the degraded oil samples, peak broadening as a function of test time was observed for the carbonyl peak. This is the result of the generation of new carbonyl peaks, however the structure(s) associated with the new species is not discernible. Transesterification, the formation of ketones, and the formation of carboxylic acids are possible sources for the new carbonyl species.[Sil91]

Table II. List of identifiable absorbance peaks in the infrared spectra.

Absorbance Peak	Attributed Vibration
1465 cm^{-1}	Alkane (C-H)
1743 cm^{-1}	Carbonyl (C=O)
2850-3000 cm^{-1}	Alkane (C-H)

Results from GPC testing for schedule 3 (290±5°C) are shown in Figures 3. The as-received oil sample showed peaks at 215, 360, 565, 775, and 1125 molecular weights (MW). As a function of test time, samples from all three heating schedules yielded decreasing intensities for the 216 and 360 MW peaks, and increasing intensities for the 565, 775, and 1125 MW peaks. Samples for Schedules 2 and 3 showed the generation of a higher molecular weight species in the form of a broad peak between 1500-3000 MW. The decrease in intensity for the low molecular weight species can be attributed in part to evaporation. Increases in the intensity of the higher molecular weight species and the generation of the 1500-3000 MW peak suggests reaction between the species with decreasing intensities. Further information is gained from data for the 5 hour test sample from Schedule 3 (290±5°C), which shows in Figure 3 the generation of two low intensity peaks at approximately 31,500 and 101,000 MW. For the 7 hour sample, the 31,500 MW peak is not observed and the 101,000 MW peak is of lower intensity. For the 9 hour sample, neither peaks are present. These results suggest the generation of high molecular weight species which are subsequently removed, a process referred to as coking. Comparing these results with infrared data, a general description of the coking process can be drawn. The base ester undergoes a reaction to form new ester, ketone, or carboxylic acid species which generate higher molecular weight ester species, which subsequently deposit as a carbonaceuos residue.

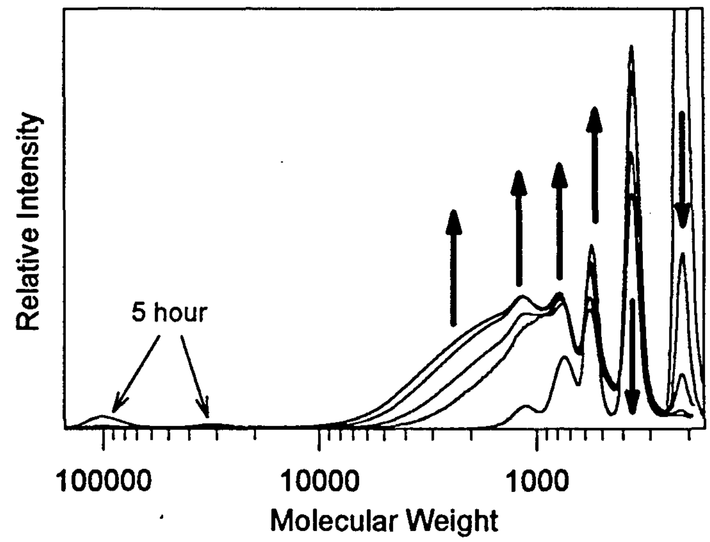

Figure 3. GPC data for Schedule 3 (290±5°C). Arrows indicate direction of changes with increasing test time.

In order to compare the effects of oil degradation on the friction and wear behavior of the silicon nitride/M-50 steel system in the current work, a method to quantify the extent of degradation for samples from each heat schedule was developed. Since oil degradation is reflected by both physical and chemical changes, and since these changes are reflected in viscosity and total acid number measurements, a correlation between these experimental values and the oil condition for each sample must be made. Assuming that changes in viscosity are the result of the formation of high molecular weight degradation products which act as particulate species (e.g., carbonaseuos particles), the Einstein equation for changes in viscosity as a function of particle volume for Newtonian fluids [Ein56] may be used:

$$\eta^* = \eta o \cdot (1 + \frac{5}{2} \cdot \phi) \tag{1}$$

The η^* refers to the experimental viscosity, η_o refers to the as-received viscosity, and ϕ refers to the percent particle volume of the system. From this relation, the molal concentration of particulate species may be determined assuming a set density for the particulate species (for this study the density was assumed to be 2.0 g/cc). From the TAN values, molal values which reflect the number of base neutralized acidic sites may alos be calculated. A combination of the two molal values can be used to generate an overall molal concentration value for the oil samples:

$$MC = \frac{m_{TAN} + m_\phi}{m^*_{TAN} + m^*_\phi} \tag{2}$$

MC refers to the molal concentration of the degraded oil, m_{TAN} refers to the molal value calculated from TAN values, m_ϕ refers to the molal value determined from the particle volume, m^*_{TAN} and m^*_ϕ refer to the molal values for the most degraded sample in the study (Sch 2, 9 hrs).

Results for coefficient of friction measurements are plotted versus the aforementioned molal concentration as shown in Figure 4. Friction values range from 0.08 and 0.12. From the regression curve drawn for all data points, a general increase in friction is observed as the degree of degradation increases. Results for wear showed values for the specific wear rate of the pin surface range between 14.2 and 47.4 pg/m. Rate of wear values for the disk surfaces range between 9.1 and 18.8 μm/1000m. No correlations were found for the rate of wear versus the overall molal concentration.

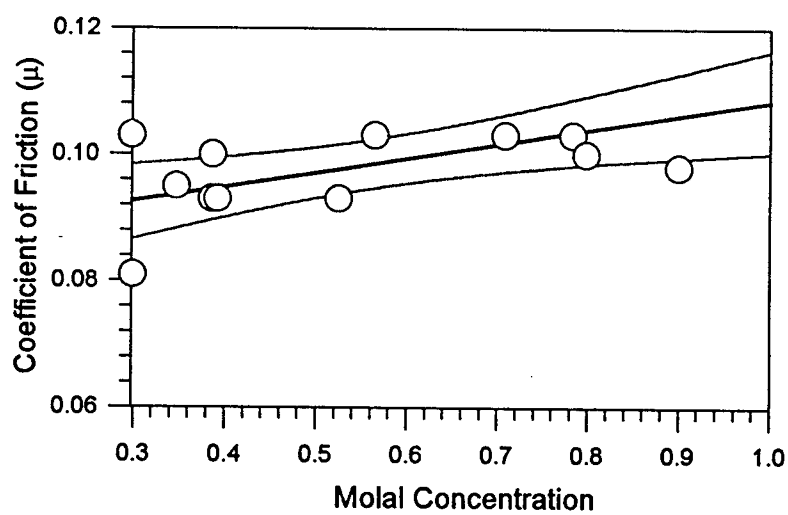

Figure 4. Coefficient of friction data for oil samples plotted versus molal concentration of the degradation product (Eq. (2)).

CONCLUSIONS

Characterization performed on the oil samples showed viscosity changes between -2.3% and 49.4% relative to the as-received oil. Results of molecular weight analysis of the samples for the most extreme testing conditions showed the formation of high molecular weight species, which subsequently removed as test time proceeded, suggesting coking behavior. In correlation with infrared spectrometry results which showed peak broadening effects, the degradation mechanism for the system at hand could not be determined, as the formation of carboxylic acids, ketones, and esters (via transesterification) are all possible reaction products.

A linear relationship was found to exist between total loss edge values and changes in viscosity. This observation suggests that the changes in optical behavior of the oil is dependent on physical changes which result during degradation. This correlation also suggests that optical properties may be used to monitor oil degradation *in-situ*.

Results from testing friction and wear testing of the previously degraded oil samples under boundary lubrication conditions showed the coefficient of friction to increase with respect to oil condition. Results for wear measurements under boundary lubrication conditions showed the rate of wear for both the silicon nitride and M-50 surfaces to be independent of oil condition with no correlation of rate of wear to the characterization techniques used for this report.

REFERENCES

Den95 Denape, J., Masri, T., and Petit, J.A., "Influence of Surface Roughness and Oil Aging on Various Ceramic-Steel Contacts Under Boundary Lubrication," Journal of Engineering Tribology, 209, 173, 182, 1995.

Ein56 Einstein, A., "Investigations on the Theory of the Brownian Movement, " Dover Publications, Inc., USA, 1956.

Gat91 Gates, R.S., and Hsu, S.M., "Effect of Selected Chemical Compounds on the Lubrication of Silicon Nitride," Tribology Transactions, 34, 417-425, 1991.

Ham85 Hamrock, B.J., "Elastrohydrodynamic Lubrication - Status of Understanding," New Directions in Materials, Wear, and Surface Interactions, Tribology in the 80's, Edited by W. R. Loomis, Noyes Publications, 484-505, 1985.

Jac91 Jackson, A., "Elastrohydrodynamic Lubrication (EHL)," Lubrication Engineering, 833-835, 1991.

Kau89 Kauffman, R.E., "Developement of a Remaining Useful Life of a Lubricant Evaluation Technique. Part III: Cyclic Voltammetric Methods," Lubrication Engineering, 45, 11, 709-716, 1995.

Kau95a Kauffman, R.E., "On-Line and Off-Line Techniques for Monitoring the Thermal and Oxidative Degradations of Aircraft Turbine Engine Oils - Part I: Laboratory Evaluations," Lubrication Engineering, 51, 11, 914-921, 1995.

Kau95b Kauffman, R.E., "Remaining Useful Life Measurements of Deisel Engine Oils, Automotive Engine Oils, Hydraulic Fluids, and Greases Using Cyclic Voltammetric Methods," Lubrication Engineering, 51, 3, 223-229, 1995.

Kla91 Klaus, E.E., Duda, J.L., and Wu, W.T., "Lubricated Wear of Silicon Nitride," Lubrication Engineering, 47, 8, 679-684, 1991.

Sil91 Silverson, R.M., Bassler, G.C., and Morrill, T.C., "Spectrometric Identification of Organic Compounds," John Wiley & Sons, 1991.

Wak74 Wakelin, R.J., "Tribology: The Friction, Lubrication, and Wear of Moving Parts," Annual Reveiw of Materials Science, Huggins, R.A., Bube, R.H., and Roberts, R.W., Eds., 4, 1974

APPENDIX 20, S. Atluri, and D. W. Dareing, "Traction Behavior and Physical Properties of Powder Graphite Lubricants Compacted to Hertzian Pressure Levels," submitted for publication.

Traction Behavior and Physical Properties of Powder Graphite Lubricants Compacted to Hertzian Pressure Levels

by

Sathish Atluri and Don W. Dareing*
The University of Southwestern Louisiana
Lafayette, LA

(Second Revision)

June 1996

Key Words: Powder Graphite, Traction Coefficients,

Rolling Contact Bearings

*Currently Professor and Head of the Mechanical and Aerospace Engineering and Engineering Science Department, University of Tennessee, Knoxville

Traction Behavior and Physical Properties of Powder Graphite Lubricants Compacted to Hertzian Pressure Levels

by

Sathish Atluri and Don W. Dareing

ABSTRACT

The paper gives a method for predicting traction coefficients of graphite powder lubricants. The analysis is based on the assumption that unconsolidated powder lubricants behave as elastic solids when compressed to Hertzian pressure levels in rolling contact regions. This assumption is supported by the classic work of P. W. Bridgman who studied the effects of extreme pressure on physical properties of several chemical substances, including graphite. The paper also gives bulk modulus data for graphite powder compressed up to 690 MPa (100,000 psi) and shows how this property can be used to predict the film thickness of graphite powder in Hertzian contact.

INTRODUCTION

The objective of this study was to analytically predict traction coefficients for dry graphite powder lubricants. The basic assumption here is that a thin film of highly compacted graphite powder can be analyzed as a solid film having elastic properties up to the point of yielding. This assumption is consistent with the experimental work of Bridgman (1) (2) (3). Graphite powder lubricants are assumed to be unconsolidated prior to entry to a Hertzian contact region. Once delivered into the contact region, the powder lubricants are compacted to Hertzian pressure levels and undergo physical changes.

The analytical prediction of traction coefficients for solid films typically require the following information:

- thickness of the solid film or coating

- shear strength of the solid film (lubricant)
- coefficient of friction between solid film and contact surface
- Modulus of elasticity/rigidity
- Poisson's ratio

The film thickness of a compacted graphite film is not initially known but can be predicted from calculations based on bulk modulus, which is a function of Hertzian pressure. A procedure for computing film thickness is given later in the paper. Film thickness also depends on delivery rate of the powder lubricant and speed of rotation of the disks as well as load. Bulk modulus for a premium graphite powder was determined as part of this study up to a compressive stress of 690 MPa (100,000 psi). This stress level is adequate to cover the example traction calculations given in the paper.

The shear strength of highly compacted graphite powder is also documented in Bridgman's (1) (2) (3) papers. The coefficient of friction of compacted graphite was established by Boyd and Robertson (6). The modulus of elasticity/rigidity was extracted from the bulk modulus. Poisson's ratio was approximated using data given in reference (7).

Both the modulus of elasticity (E) and modulus of rigidity (G) affect the flexibility matrix used to determine surface displacements in the Hertzian contact region. Lower value of E and G give lower values of surface shear stress and a reduction in traction coefficients for a given slip velocity ratio.

The sections below describe the experimental steps that were taken to determine bulk modulus and how all the above information was used to determine traction coefficients for graphite films. The study also gives a direct method for predicting film thickness of dry powder lubricants using bulk modulus data.

PHYSICAL PROPERTIES OF COMPACTED GRAPHITE POWDER LUBRICANTS

Shear Strength: Bridgman (1) (2) (3) studied the shearing phenomena of a number of chemical substances including carbon (graphite). His experimental arrangement is illustrated in Figure 1 and is explained by Bridgman as follows:

> *"Two cylindrical blocks, B ("pistons"), of hardened steel of the highest physical properties carry very short cylindrical bosses about 6.33 mm. in diameter, ground flat on the face. Between the two cylindrical blocks there is a rectangular block, C ("anvil"), of steel of the same quality, ground flat and parallel on the two surfaces facing the blocks. The material to be studied is placed at A in the form of a thin disk between each piston and the anvil. The whole combination is mounted under the plunger of a hydraulic press by means of which the pistons can be pushed against the anvil with any desired force up to the maximum which the steel will support, which under these conditions is 50,000 kg./cm.^{2} or even more."*
>
> *"At very low pressures on the pistons rotation of the anvil is permitted by simple slip of the material A on the steel, and the turning moment gives at once the coefficient of friction. In the initial range, in which the coefficient of friction is approximately constant, the curve of torque rises linearly with pressure. With most substances a point is soon reached, however, at which the shearing stress applied to the substance by friction becomes equal to the shearing strength of the material itself. When this point is reached, slip at the surface ceases, and from here on rotation is accompanied by internal plastic flow of the material. This point is manifested on the curves of "normal" substances by a more or less pronounced knee."*
>
> *"Beyond the knee the curve of torque against pressure determines the shearing strength (i.e., the maximum shearing stress that the material will support without plastic yield) as a function of average pressure."*

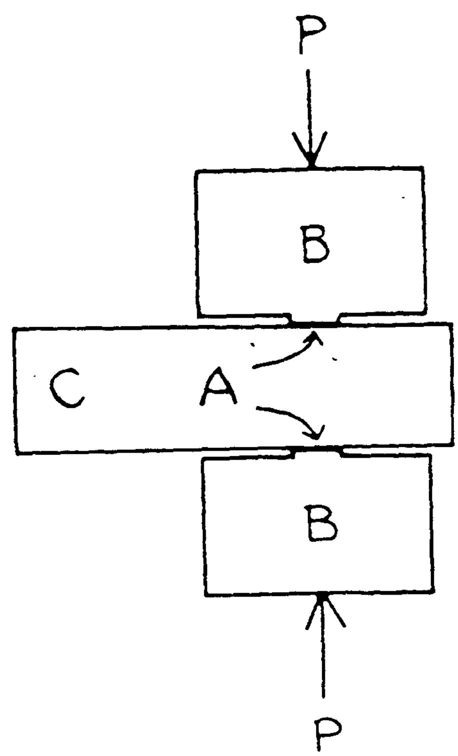

Figure 1. Schematic of Bridgman's Test Fixture

(Reference 3)

Figure 2 shows typically how shearing stress varies with applied pressure for the substances tested by Professor Bridgman. Slippage occurs at the interface between the test material and steel surface up to point "a." Also over this range shearing deformation within the test material are elastic. The coefficient of friction can be determined from the data at any point. The portion of the curve beyond point "b" shows how yield strength varies with applied pressure. Beyond point "b" plastic deformations occur within the test material when slippage does occur.

> *"The knee between "a" and "b" is often rounded instead of sharp, because the pressure is not uniform across the surface of the pistons."*

Professor Bridgman does not give a shear stress/pressure curve for graphite, but does report a shear strength of 10,000 kg/cm^2 at a pressure of 50,000 kg/cm^2. These numbers are represented by point "c" in Figure 2. Note that the effective coefficient of friction at this load level is 0.2 and that slippage took place internally and not at the graphite/steel surface interface.

Coefficient of Friction: Boyd and Robertson (6) used a test rig patterned after the one by Bridgman (3) to determine the coefficient of friction of liquids, semi-solids, and solid materials, including graphite, at applied pressures up to 2760 MPa (400,000 psi). Test results indicate that graphite powder lubricants compacted to a pressure level of 2760 MPa have coefficients of friction between 0.036 and 0.058. Bridgman's discussion of this paper suggested that at the 2760 MPa pressure level slippage probably occurred internally to the test specimen due to plastic flow and not at the interface with the anvil. Peterson and Johnson (8) report coefficients of friction for graphite of 0.06 and 0.11.

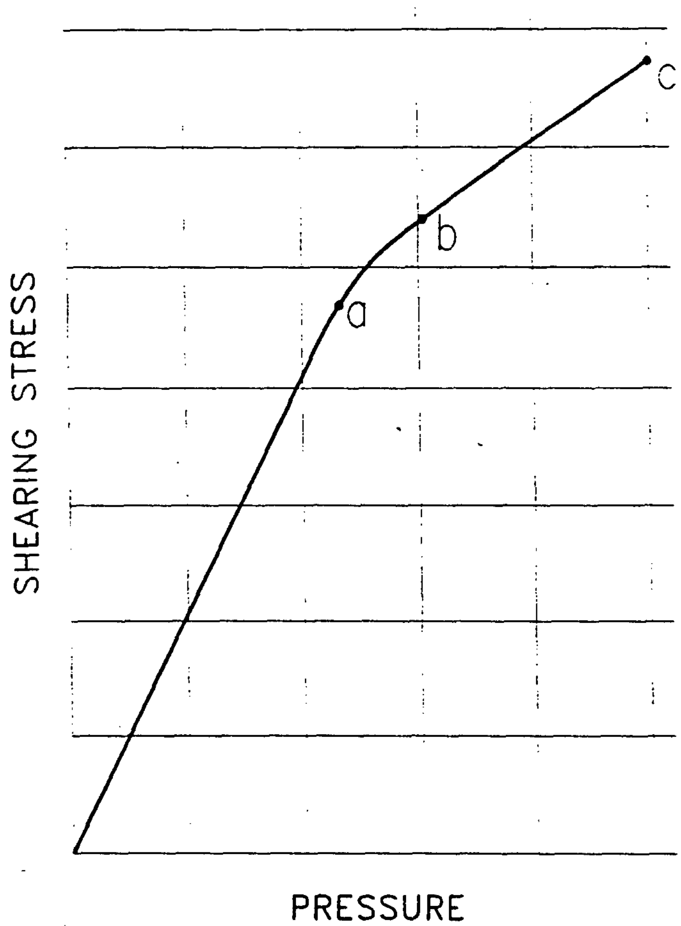

Figure 2. Typical Test Results of Shearing Stress Versus Applied Pressure

Bulk Modulus of Compacted Graphite Powder: Bulk Modulus is defined as the ratio of incremental change in average stress to the corresponding unit volume compression. Bulk modulus (K_m) relates to modulus of elasticity (E) through (see Timoshenko and Goodier (9))

$$K_m = \frac{E}{3(1 - 2v)} \tag{1}$$

where (v) is Poisson's ratio. This formula applies strictly to an isotropic, linearly elastic solid and is used later to extract the modulus of elasticity from experimentally determined values of bulk modulus for highly compressed graphite. Bulk modulus is also used in the paper to predict the minimum film thickness in Hertzian contact regions. Both E and h are used in predicting traction coefficient curves. Bulk modulus is not a constant for compacted graphite powder but varies with compaction pressure (also see Atluri (10)).

Bulk modulus was determined during this study by compressing graphite powder within a cylinder by means of a solid ram (see Figure 3). The compressive force was generated by a materials testing machine which has the capacity to apply up to 889.64 kN (200,000 lbs) force. Applied loads up to 222.41 kN (50,000 lbs) were applied giving 690 MPa (100,000 psi) compressive stress on the graphite sample. The maximum compressive stress was limited by the strength of the cylinder material, which was high tensile steel (HS420) having a yield strength of 1449 MPa (210 ksi).

The axial stress on the graphite plug generated lateral pressure on the inside wall of the cylinder. The magnitude of this pressure was determined by use of tangential strain measurements at the outside surface of the cylinder (Figure 3). Strain gages were positioned at two locations on the outer surface for this purpose. These strain measurements were also used to determine volume changes of the graphite plug associated with radial expansion.

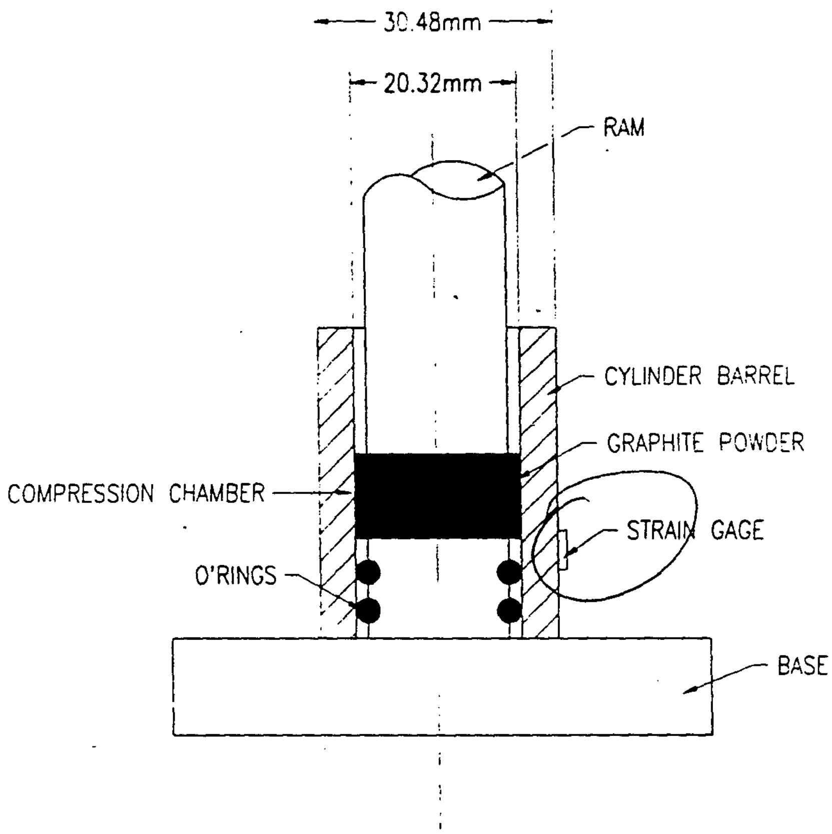

Figure 3. Test Fixture Used in Compressing Graphite Powder (reference 10)

The experiments were conducted at room temperature. Dry graphite powder was placed inside the cylinder barrel in small volume increments until a height of 50.8 mm (2 inches) of the sample was reached. Initially the graphite powder settled essentially from its own weight. A positive axial load on the graphite powder could not be measured until a certain degree of compaction was reached, i.e., when most of the air in the sample was removed. From that point, the load was applied in steps of 8900 N (2000 lbs) and the corresponding displacement of the ram was measured. Load on the ram reached a maximum level of 222.41 kN (50,000 lbs), developing an axial compressive stress of 690 MPa (100,000 psi) (cross sectional area of the ram was 322.58 mm^2 (0.5 in^2).

A typical test included measurements of axial force applied to the ram, axial travel of the ram, and circumferential strain measurements at the outside surface of the test cylinder. At the beginning of each test, the ram moved a considerable distance with little required force until the air within the sample was removed; for more details of the test set-up and procedure, see Atluri (10).

Mathematically, bulk modulus is defined as

$$K_m = -\frac{d\,\sigma_{avg}}{\frac{dv}{v}} \tag{2}$$

where

dv	-	change in volume due to applied $d\sigma_{avg}$
v	-	volume corresponding to σ_{avg}
$d\sigma_{avg}$	-	incremental change in average stress
σ_{avg}	-	$(\sigma_1 + \sigma_2 + \sigma_3) / 3$

In the test procedure described above,

$\sigma_1 = \sigma_a$ (axial compressive stress)

$\sigma_2 = \sigma_r = P_1$

$\sigma_3 = \sigma_\theta = P_1$

so

$$\sigma_{avg} = \frac{[\sigma_a + 2P_i]}{3} \tag{3}$$

The change in volume, dv, includes the effects of axial displacement of the ram and radial ballooning of the cylinder. Axial displacements of the ram were measured directly. Radial displacements (δr_1) of the inside surface of the cylinder and internal pressure (P_1) were calculated from the tangential strain measurements on the outside surface of the cylinder using Lame's thickwall cylinder equations and the constitutive equations for elastic materials.

The volume of graphite inside the cylinder corresponding to a given axial stress condition was determined from,

$$v = \pi \left(r_i + \delta r_i\right)^2 l_i \tag{4}$$

where (l_i) is the length of the sample inside the cylinder. This length is determined by subtracting ram displacement from the initial height of graphite powder in the test cylinder.

The above equations were then used to calculate bulk modulus of compacted graphite powder at the various compaction loads.

In finite difference form, the bulk modulus equation becomes,

$$K_m = -\frac{\Delta\left(\frac{\sigma_a + 2P_i}{3}\right)}{\frac{\Delta v}{v}} \tag{5}$$

where (σ_a) and (v) are measured directly and (P_i) and (Δv) are calculated from measured data as explained above.

Typical test data generated from the test rig and the above formulations are given in Table I. One of the first observations from testing was the similarity of the magnitudes of the applied axial stress and the radial stress (or pressure) at the inside surface of the test cylinder; notice the similarity between the stress levels in the fourth and fifth columns. These data show that the graphite plugs generated high radial pressures within confined boundaries. This feature was manifested in all of the testing on several different high quality, graphite powder lubricants. This radial stress on the test cylinder, along with tangential stress, combined to produce high von Mises stress levels and caused failure in early test cylinder designs.

The total volume (second column, Table I) of the graphite plug within the test cylinder includes the radial expansion of the inside surface of the test cylinder due to the radial stress (or pressure).

A plot of the average stress on the graphite plug versus volume is given in Figure 4. The bulk modulus can be determined either numerically according to equation 5 or analytically using equation 2 (after curve fitting the data). The curve fitting approach produces a more uniform determination of bulk modulus and was applied here. The curve in Figure 4 is developed from

$$\sigma_{avg} = 1.6^{14} \quad v_{avg}^{-14.766} \tag{6}$$

which gives a reasonable representation of the data. The bulk modulus in the last column of Table I was determined by applying equation (2) to the above curve fit equation.

The curve in Figure 5 shows how bulk modulus changes with average stresses up to 690 MPa using the curve fitting approach.

Table II gives Bridgman's (4, 5) compression data for Ceylon graphite. Note that bulk modulus at 25,000 kg/cm^2 is:

$$K_m = \frac{30{,}000 - 25{,}000}{(0.007)} \times 0.947$$

$$K_m = 676{,}428 \text{ kg/cm}^2$$

or

$$K_m = 132.6 \text{ GPa}$$

at a pressure of 4900 MPa.

Table I.

Compaction Test Results at Room Temperature
(Premium Graphite Grade)

Length (cm)	Volume (cu. cm.)	Stress in Theta Dir. (MPa)	Radial Stress (MPa)	Axial Stress (MPa)	Average Stress (MPa)	Bulk Modulus (GPa)
5.0800	16.3983	0.00	0.00	0.00	0.00	
2.1252	6.8639	35.72	64.64	107.64	78.97	1.10
2.0790	6.7158	48.76	88.22	140.07	105.51	1.52
2.0469	6.6130	56.00	101.33	165.60	122.75	1.91
2.0184	6.5220	66.14	119.67	193.20	144.18	2.34
2.0028	6.4724	77.49	140.20	222.18	167.53	2.61
1.9828	6.4092	88.90	162.48	250.47	191.81	3.02
1.9650	6.3528	101.62	183.88	276.00	214.58	3.43
1.9544	6.3194	113.94	206.16	307.74	240.02	3.71
1.9472	6.2972	122.63	221.88	333.27	259.01	3.90
1.9401	6.2754	136.63	247.21	358.80	284.41	4.11
1.9223	6.2188	146.29	264.68	389.57	306.31	4.69
1.9188	6.2084	158.36	286.52	415.38	329.48	4.81
1.9131	6.1913	173.56	314.04	444.36	357.48	5.01
1.9081	6.1762	183.70	332.39	467.82	377.53	5.19
1.8988	6.1473	195.29	353.35	499.56	402.08	5.56
1.8903	6.1206	206.39	373.44	528.44	425.14	5.93
1.8796	6.0870	217.49	393.53	552.00	446.35	6.43
1.8739	6.0697	229.57	415.37	581.67	470.81	6.70
1.8646	6.0409	242.60	438.96	609.27	495.73	7.18
1.8582	6.0214	257.09	465.16	636.18	522.17	7.53
1.8525	6.0041	269.40	487.44	660.61	545.16	7.86
1.8362	5.9519	279.06	504.91	670.68	560.17	8.93

NOTE: Initial height of graphite sample = 5.08 cm.
Area of the compression chamber = 3.2258 sq.cm.

Table II.
Compressibility of Ceylon Graphite
Bridgman (4, 5)

Pressure kg/cm^2	Volume
1	1.000
25,000	.947
30,000	.940
40,000	.929
50,000	.919
60,000	.911
70,000	.903
80,000	.896
90,000	.890
100,000	.885

FILM THICKNESS OF GRAPHITE POWDER IN HERTZIAN CONTACT

This section gives a procedure for predicting the rate of flow of graphite powder required to establish and maintain a given film thickness between rolling/sliding discs commonly used in traction tests. The procedure is based on simple compaction of dry powder within the Hertzian contact region using bulk modulus data. Compaction pressure is assumed to be constant throughout the film and equal to the average of the Hertzian pressure distribution. This approach is different from Heshmat (11) who postulates that the behavior of powder lubricants in rolling contact bearings is akin to that of liquid lubricants.

Side leakage from the contact region will affect the prediction to some extent. Bridgman (4) (5) ignored this effect in his measurements of compressibility by reasoning that friction forces at the interface oppose side leakage. Side leakage was apparently not a concern, although film thickness was 0.0025 cm and greater... "the dimensions of the apparatus were such that the film thickness was very seldom reduced below 0.0025 cm and for most substances the thickness was several times as great as this." The thickness of solid films in rolling contact applications is typically smaller than 0.0025 cm; usually in the neighborhood of 0.00254 mm.

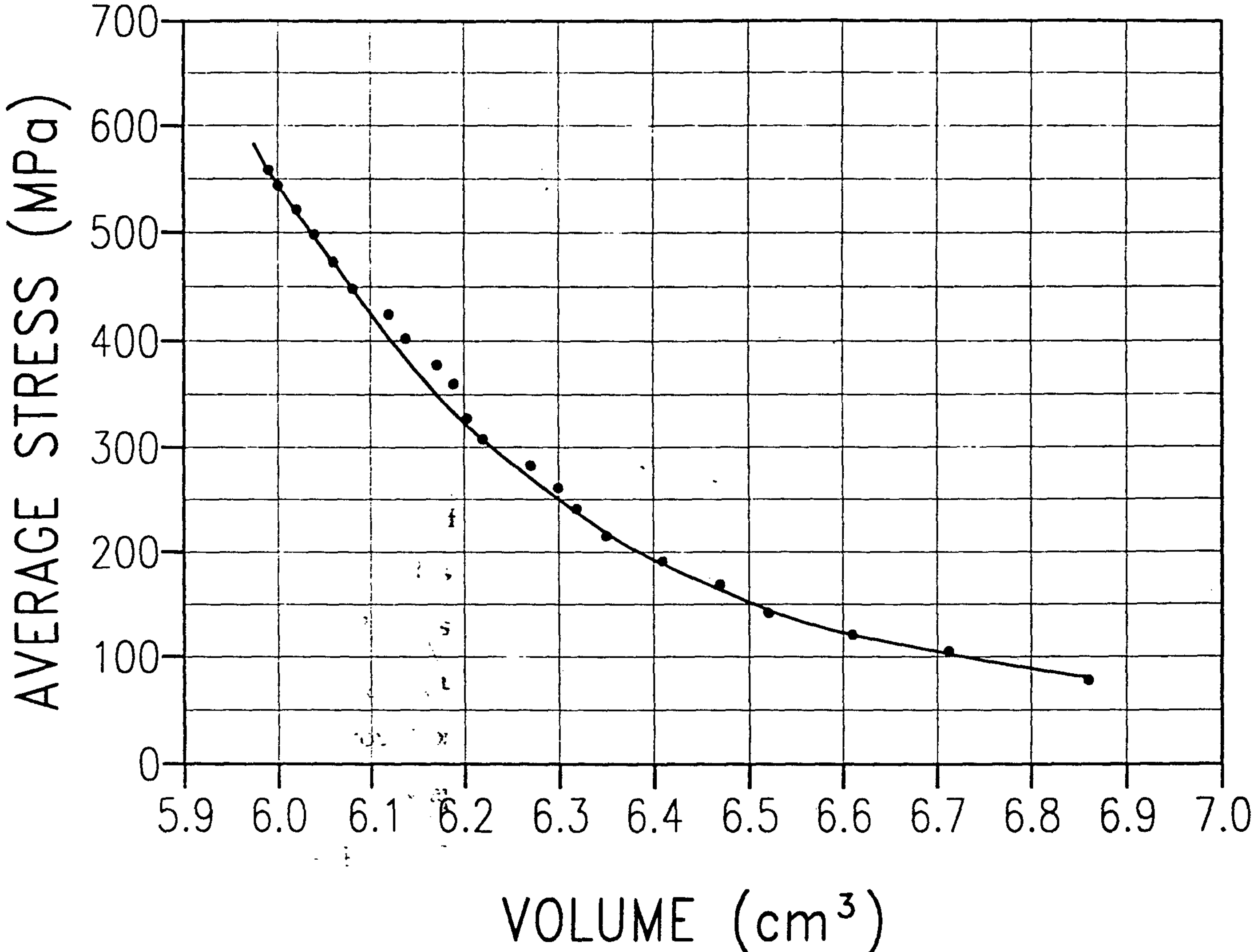

Figure 4. Average Stress versus Volume (Premium Graphite Grade)

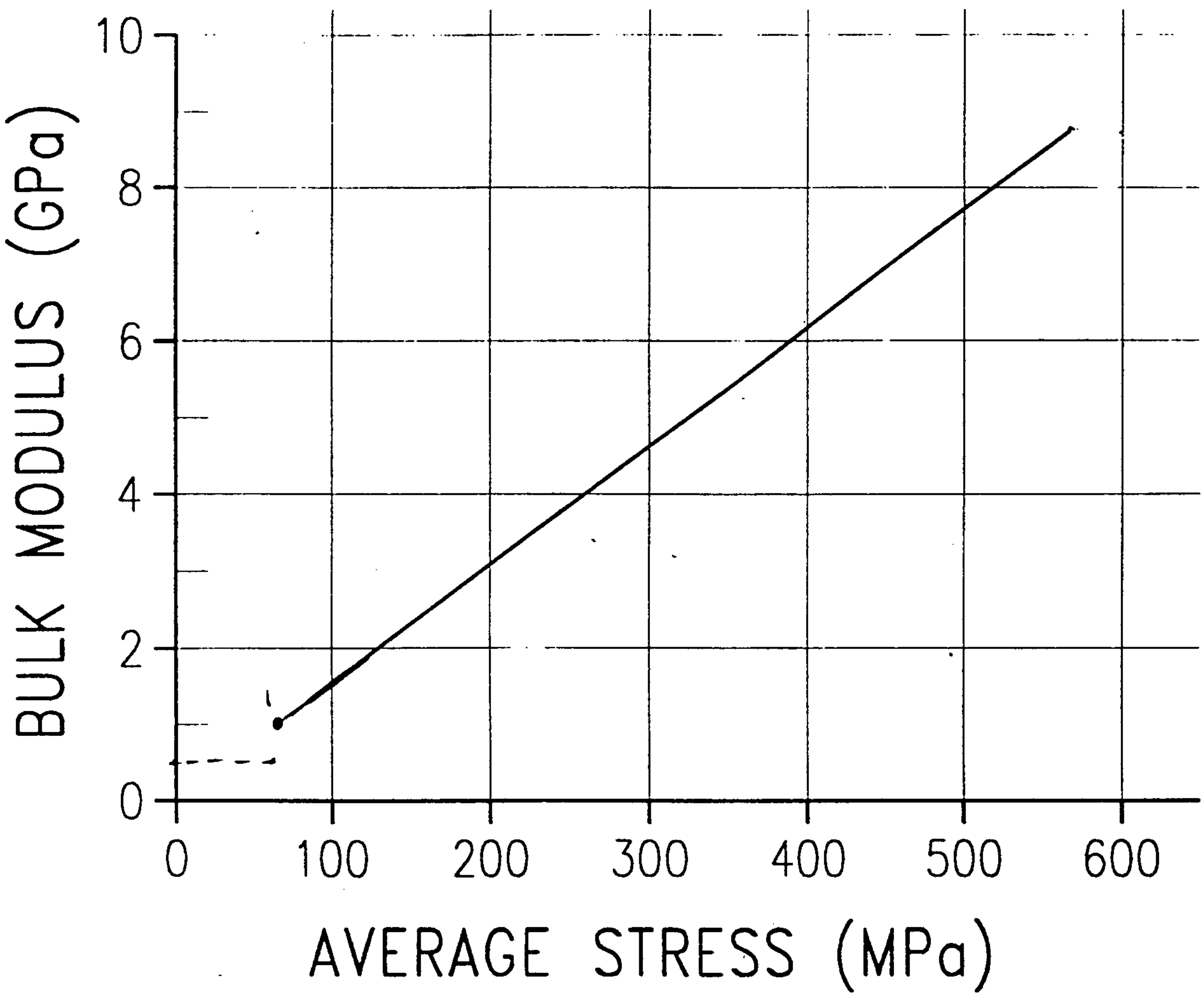

Figure 5. Average Stress versus Bulk Modulus
(Premium Graphite Grade)

Consider a volume between two contacting surfaces defined by height (H), width (2a) and depth (B). Assume that this volume is filled with unconsolidated graphite powder at atmospheric pressure (Figure 6). Next, assume that the volume is compacted to a new height of (h) as a result of a uniform pressure, p, defined by the average of the Hertzian pressure distribution. The relation between average pressure and film thickness (h) can be determined through the use of bulk modulus data as explained below.

The graph of bulk modulus versus average stress (Figure 5) can be approximated by a straight line represented by the following equation:

$$K_m = mp \tag{7}$$

where (m) is the slope of the line, (m = 14.635 for the line in Figure 5) and (p) is average Hertzian pressure in the contact area.

Pressure-volume data at average applied pressures near zero were not recorded. More data over the low pressure range is needed for bulk modulus determination. For film thickness calculation purposes in this paper, bulk modulus is assumed to be constant and equal to 1/2 of the bulk modulus at the lowest measured average stress or 1/2 (1.10) = 0.55 GPa (see Figure 5) at pressures near zero.

Integration of equation 2 gives

$$\int_0^1 \frac{dp}{K_{mo}} + \int_1^2 \frac{dp}{m\,p} = ln\left(\frac{v_0}{v_2}\right) \tag{8}$$

or

$$\frac{1}{K_{mo}}(p_1 - p_0) + \frac{1}{m}\,ln\,\frac{p_2}{p_1} = ln\,\frac{v_0}{v_1} + ln\,\frac{v_1}{v_0} \tag{9}$$

Separating the compression over 0-1 limits from 1-2 limits gives

$$\frac{1}{K_{mo}}p_1 = ln\,\frac{v_0}{v_1} \tag{10}$$

and

$$\frac{p_2}{p_1} = \left(\frac{v_1}{v_2}\right)^m \tag{11}$$

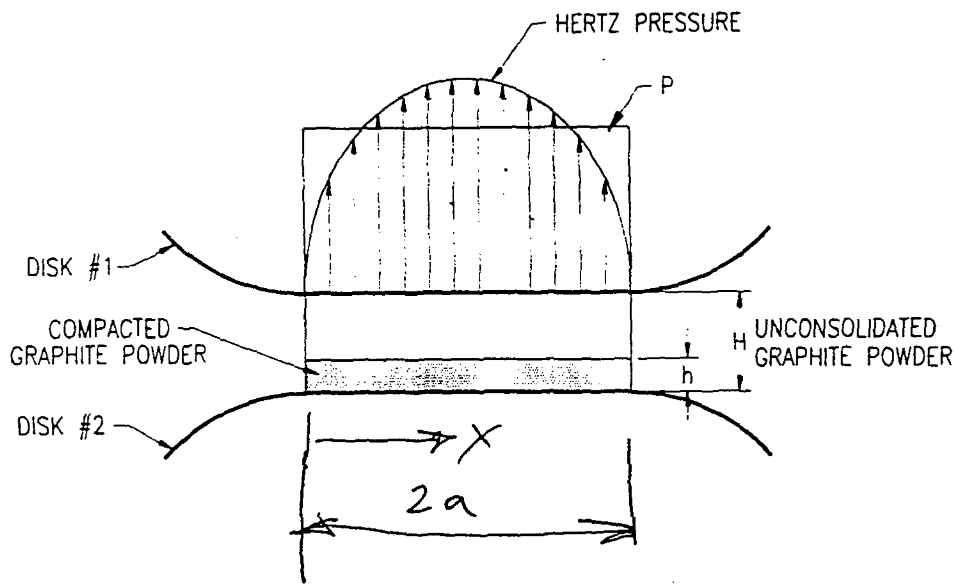

Figure 6. Compaction of Graphite Powder Lubricants in Hertzian Contact Region

where

$$v_0 = H\,2a\,B$$

$$v_2 = h\,2a\,B$$

and v_1 is an intermedia volume.

For the data in Table I

$$p_1 = 78.97 \text{ MPa}$$

$$K_{mo} = 0.55 \text{ GPa}$$

$$m = 14.635$$

Equations (10) and (11) are solved together to determine the relation between v_0 and v_2.

The volumetric flow rate of unconsolidated graphite powder (Q_g) is given by,

$$Q_g = v_0 / \Delta t \tag{12}$$

and

$$U = 2a / \Delta t \tag{13}$$

where (U) is average tangential velocity of the discs. Therefore,

$$Q_g = (v_0\, U) / 2a \tag{14}$$

Combining equations 10, 11 and 14 gives the volumetric flow rate of unconsolidated graphite powder required to establish a given film thickness (h) corresponding to an average Hertzian pressure level of (p_{avg}).

The corresponding weight rate of flow of unconsolidated graphite powder is determined by,

$$Q_{\gamma g} = Q_g\, \gamma_g \tag{15}$$

The above equation represents the weight rate of flow of unconsolidated graphite powder that has to be supplied to the Hertz contact region to establish a film of thickness (h) for a given load level.

PREDICTING TRACTION COEFFICIENTS FOR GRAPHITE FILMS

This section gives a procedure for predicting traction coefficients for dry powder lubricants compressed by Hertzian contact. The method treats the compacted film as a solid having perfectly elastic properties and requires the knowledge of the physical properties mentioned earlier.

The method of solution for predicting traction coefficients for graphite powder follows the method developed by Dareing (12) for predicting traction coefficients for solid lubricants (Teflon) working against soft metal coatings. Other methods of solution are given by Kannel and Dow (13) and Barber and Kannel (14).

What is unknown in this case is the plane at which the graphite will slip or fail. Slippage could occur at the substrate/graphite interface or within the graphite film itself. The total shear force can be determined only after the plane of slippage or failure has been established.

If the shear strength of the compacted graphite is greater than the product of the contact stress and the coefficient of friction at the substrate/graphite interface, slippage will occur at the interface with no failure within the film. On the other hand, if the shear strength of the compacted graphite is less than the limiting value (f x p) at the interface, slippage will occur internal to the film.

The location of the slippage plane in the latter case can be determined by dividing the film thickness into two films separated by an assumed plane. If the corresponding shear stress along this assumed plane is greater than the shear strength of graphite, failure along this plane is possible. The weakest plane can be determined by repeating this exercise at different planes in the film. This calculation requires shear stress-pressure data which is not available in the literature and is therefore beyond the scope of this paper.

The data provided by Professor Bridgman shows that internal slippage occurs under extreme pressures while slippage at the substrate/graphite interface occurs at the lower pressures (see Figure 2).

Example Calculation:

Calculations presented here are based on two 15.24 cm (6 inch) diameter discs of 25.4 mm width pressed together at three different force levels. Physical responses within the contact region corresponding to these loads are given in Table II. Because of the low level of Hertzian pressure (p_{max} is less than 690 MPa (100,000 psi) in all three cases), slippage is assumed to occur at the graphite/surface interface where the coefficient of friction is assumed to be 0.10. Furthermore, bulk modulus information given in Figure 5 apply. The modulus of rigidity, G, of compacted graphite is calculated at the different load levels assuming a Poisson ratio of 0.25. Film thickness in each case is assumed to be 0.00254 mm.

Table III
Physical Responses Within the Contact Region

Normal Force W N	Contact Width 2a cm	Maximum Pressure p_{max} MPa	Average Pressure p_{avg} MPa	Bulk Modulus K_m GPa	Modulus of Elasticity E_g GPa
4,450	0.0546	408.48	317.40	4.658	6.983
8,900	0.0772	577.53	453.33	6.728	10.088
13,350	0.0947	707.25	555.45	8.280	12.420

The traction shear stress distribution for this set of numbers and a slip velocity ratio of 0.0005 is calculated according to the preceding theory.

Calculated data corresponding to a load of 4.45 kN show that graphite sticks to the substrate over the initial contact zone from x = 0 to x = 0.36424 mm. Beyond this point the graphite film slides on the substrate surface. The traction coefficient under the 4.45 kN load and the slip velocity ratio of 0.0005 is equal to 0.0725. This point is identified in Figure 7 as a dot on the 4.45 K_m curve.

The three traction curves in Figure 7 correspond to the three normal forces in Table III. All three traction coefficient curves (Figure 7) approach the assumed value of the coefficient of friction (f = 0.1) for graphite on steel at high slip velocity ratios.

The volumetric flow of unconsolidated graphite powder to maintain a film thickness of 0.00254 mm under, say, the 4,450 N normal contact force is determined as follows:

$$U = 3989.83 \text{ mm/sec (100 rpm)}$$

$$h = 0.00254 \text{ mm}$$

$$B = 25.4 \text{ mm}$$

$$p_{avg} = 317.4 \text{ MPa}$$

$$m = 14.635 \text{ (dimensionless)}$$

$$p_1 = 78.97 \text{ MPa}$$

$$K_{mo} = 0.55 \text{ GPa}$$

From equation (11)

$$\frac{317.4}{78.97} = \left(\frac{h_1}{0.00254}\right)^{14.635}$$

$$h_1 = 0.00279 \text{ mm}$$

From equation (10)

$$\frac{78.97}{550} = \ln\left(\frac{H}{h_1}\right)$$

$$H = 0.002932 \text{ mm}$$

From equation (14)

$$Q_g = \frac{(H\,2a\,B)\,U}{2a}$$

$$Q_g = H\,B\,U$$

$$Q_g = (0.002932)(25.4)(3989)$$

$$Q_g = 297.1 \; mm^3/sec$$

The required volumetric flow is therefore 0.297 cm^3/sec.

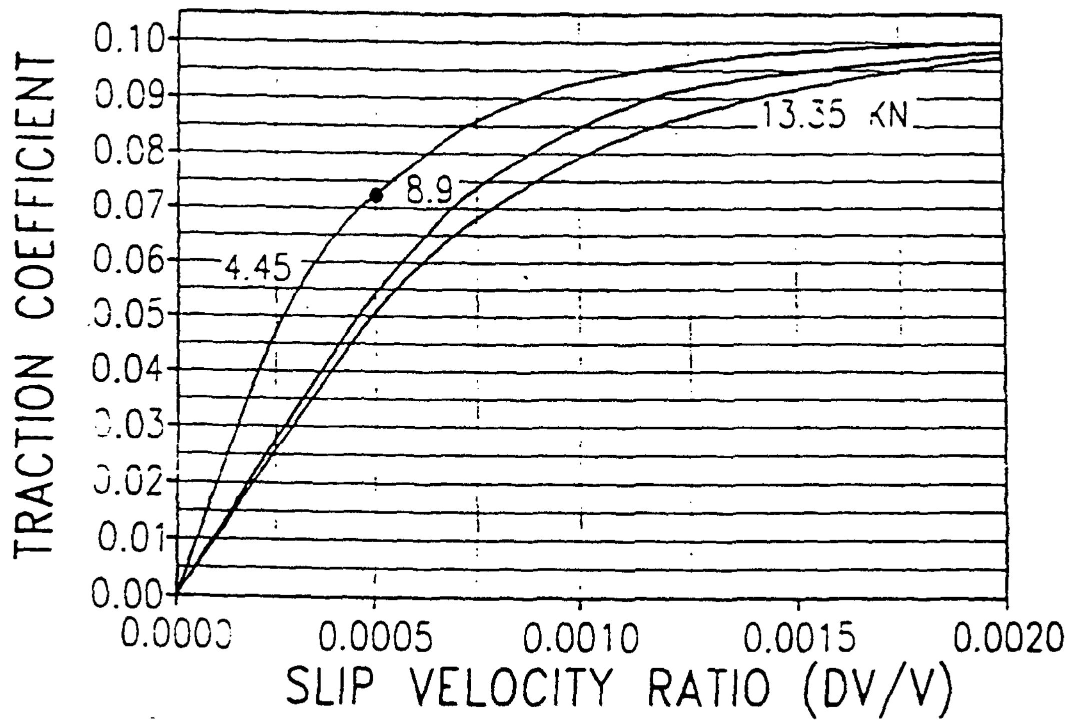

Figure 7. Traction Coefficients

(15.24 cm diameter; 0.00254 mm Graphite Film)

This assumes fresh graphite powder is continuously fed into the contact region and the compressed graphite is discarded after leaving the contact region.

CONCLUSIONS

The paper gives a procedure for predicting traction coefficients for powder lubricants compressed to Hertzian contact pressures. The method of analysis requires prior knowledge of physical properties of the powder lubricant under extreme pressures. Relevant physical properties are: bulk modulus, shear strength, coefficient of friction, modulus of elasticity/rigidity and Poisson's ratio. Each of these physical properties depend on the magnitude of applied compressive stress. Expected minimum film thickness of powder lubricants in Hertzian contact is also predicted using bulk modulus/pressure data.

The data given in this paper were obtained at atmospheric temperatures and at compressive stress levels up to 690 MPa (100,000 psi). Powder lubricants being considered for high temperature applications can be analyzed with this method but would require the above physical properties at the specified temperature.

NOMENCLATURE

K_m	Bulk Modulus of Elasticity (GPa)
E	Modulus of Elasticity (GPa)
ν	Poisson's ratio
σ_{avg}	Average Stress (MPa)
$\sigma_1, \sigma_2, \sigma_3$	Principal Stresses (MPa)
σ_a	Axial Compressive Stress (MPa)
σ_r	Radial Stress (MPa)
σ_θ	Tangential Stress (MPa)
v, v_1, v_2	Volume (cm^3)
$dv, \Delta v$	Change in Volume (cm^3)
P_1	Internal Pressure $P_1 = \sigma_r = \sigma_\theta$ (MPa)
p, p_{avg}	Average Hertzian contact pressure (MPa)
$(\delta r)_1$	Radial Strain Inside the Cylinder
l_1	Length of Compacted Graphite Powder (cm)
2a	Hertzian Contact Width (mm)
H	Height of Uncompacted Graphite Powder (cm)
h, h_{min}	Film Thickness (mm)
Q_g	Volumetric Flow Rate of Unconsolidated Graphite Powder (cm^3/sec)
$Q_{\gamma g}$	Weight Flow Rate of Unconsolidated Graphite Powder (N/sec)
γ_g	Specific Weight of Unconsolidated Graphite Powder (N/cm^3)
B	Depth of Hertzian Contact (cm)

ACKNOWLEDGMENT

The authors gratefully acknowledge the support of this work by the

Aero Propulsion and Power Directorate
Wright Laboratory
Air Force Systems Command (ASD)
United States Air Force
Wright-Patterson AFB, Ohio 45433-6563

under contract No. F33615-92-C-2214

The authors are indebted to Dr. G. J. Piermarini, Research Scientist at the National Institute of Standards and Technology (Gaithersburg, Maryland), for identifying and locating the classic papers of Professor P. W. Bridgman.

LIST OF REFERENCES

(1) Bridgman, P. W.; "Effects of High Shearing Stress Combined with High Hydrostatic Pressure," Phys. Rev. 48, 827-847 (1935); also see Collection of Experimental Papers of P. W. Bridgman, Vol. V, paper 112-2929.

(2) Bridgman, P. W.; "Shearing Phenomena at High Pressure of Possible Importance for Geology," J. Geol. 44, 653-669; University of Chicago Press (1936); also see Collection of Experimental Papers of P. W. Bridgman, Vol. V, paper 115-3001.

(3) Bridgman, P. W.; "Flow Phenomena in Heavily Stressed Metals," J. Appl. Phys. So, 328-336 (1937); also see Collection of Experimental Papers of P. W. Bridgman, Vol. V, paper 116-3018.

(4) Bridgman, P. W., "The Compression of Sixty-One Solid Substances to 25,000 kg/cm^2, Determined by a New Rapid Method," Proc. Am. Acad. Arts. Sci. 76, 9-24 (1945); also see Collection of Experimental Papers of P. W. Bridgman, Vol. V, paper 148-3609.

(5) Bridgman, P. W., "The Compression of 39 Substances to 100,000 kg/cm^2," Proc. Am. Acad. Arts Sci. 76, 55-70 (1948); also see Collection of Experimental Papers of P. W. Bridgman, Vol. V, paper 160-3819.

(6) Boyd, J. and B. P. Robertson, "The Friction Properties of Various Lubricants at High Pressures," Trans. Amer. Soc. Mech. Engrs., Vol. 67, pp. 51-56, 1945.

(7) UNCAR Carbon Company, The Industrial Graphite Engineering Handbook, UCAR Carbon Company, Inc., Parma, Ohio (1970).

(8) Peterson, Marshall B. and Johnson, Robert L.: "Friction of Possible Solid Lubricants with Various Crystal Structures," NACA TN 3334, 1954.

(9) Timoshenko, S. and J. N. Goodier, "Theory of Elasticity," Second Edition, McGraw-Hill Book Company, 1951.

(10) Atluri, S., "Traction Behavior and Physical Properties of Powder Graphite Lubricants Compacted to Hertzian Pressure Levels," Master's Thesis, University of Southwestern Louisiana, July 1994.

(11) Heshmat Hooshang, "Solid-Lubricated Roller Bearing Development Static and Dynamic Characterization of High-Temperature, Powder-Lubricated Materials," Wright Laboratories Report WL-TR-92-2050, June 1992.

(12) Dareing, D. W., "Traction Coefficients for Coated Bearing Races Lubricated with Teflon Transfer Films," ASME Journal of Tribology, Vol. 113, pp. 343-348, April 1991.

(13) Kannel, S. W. and T. A. Dow, "Analysis of Traction Forces in a Precision Traction Drive," ASME Journal of Tribology, Vol. 108, pp. 403-410, July 1986.

(14) Barber, S. A. and J. W. Kannel, "Evaluation of Slip-Traction Characteristics of Polymeric Transfer Films," ASME Journal of Tribology, Vol. 110, pp. 670-673, October 1988.

APPENDIX 21, P. Cento and D. W. Dareing, "Evaluation of Ceramic Materials in Hybrid Ball Bearings," submitted for publication.

Evaluation of Ceramic Materials in Hybrid Ball Bearings

by

Pete Cento
and
Don W. Dareing

Mechanical and AeroSpace Engineering
and Engineering Science

University of Tennessee
Knoxville, Tennessee

September 1997

ABSTRACT

Modern ball bearings used under high speed applications (50,000 to 100,000 RPM or more) can be subject to very high rates of wear, heat generation, and torque input requirements. A major contribution to these frictional losses is the slip and deformation at the ball/race contact points. This study was conducted to evaluate the above parameters of radial ball bearings for micro-slippage and elastic deformation mechanisms and also to accomplish performance predictions of ceramic balls in hybrid radial ball bearings and compare them to the performance of conventional bearings with steel roller balls. This study is part of a broader research effort to establish probable modes of failure of ceramic material used in aerospace applications. Performance predictions are based on the mechanism of micro slippage within Hertzian contact regions. As part of the study, software was developed to predict micro slippage between bearing races and roller balls, tractive forces, and traction coefficients. Energy losses (heat generation and torque) and wear rate are predicted for various combinations of bearing geometry, material properties, loads, surface conditions, and rotational speeds. Example calculations predict that a Si_3N_4 ceramic ball bearing would have much lower losses than the steel ball bearing and also that at rotational speeds above 50,000 RPM heat generation, wear rate, and torque rise dramatically for both materials as angular velocity increases.

INTRODUCTION

The bearings considered are radial roller ball bearings designed for radial loads only (no axial loads). A mathematical model was derived and a computer program developed specifically for this study. The program is designed to calculate slip velocities and tractive coefficients due to micro-slippage, and tangential and normal forces on differential elements of the contact area between ball and race. Then, these quantities are used to calculate energy losses and wear rate. The experimental evaluation of ceramic wear characteristics was conducted by researchers at the University of Florida [Ref. 7] and is covered in their reports.

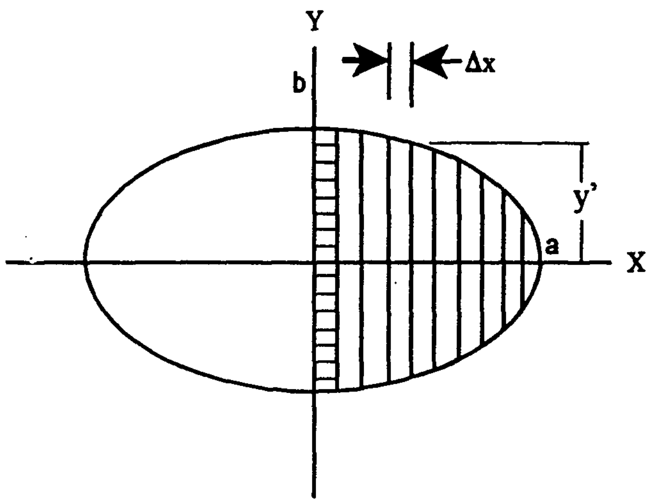

Figure 1 - Discretization of Hertzian Contact Patch

The contact area is calculated using Hertzian theory for contact between solid bodies. Normal loads exist between the spherical rolling elements and the races that produce a Hertzian contact area for two curved solid bodies in contact at a point [Ref 3; Sect. 2.3; Eschmann et. al]. The assumed Hertzian contact patch is an elliptically shaped area with length 2a and width 2b (figure 1) for which the overall dimensions and the contact force at a given location can be predicted using Hertzian theory. For the method used the Hertzian contact patch is discretized as shown into differential strips along the semi-major (X) axis. The Slip velocity ratio [(v2-v1)/v1) ; see figure 2] due to the micro-slippage varies continuously along the semi-major axis of the patch and is approximated by the

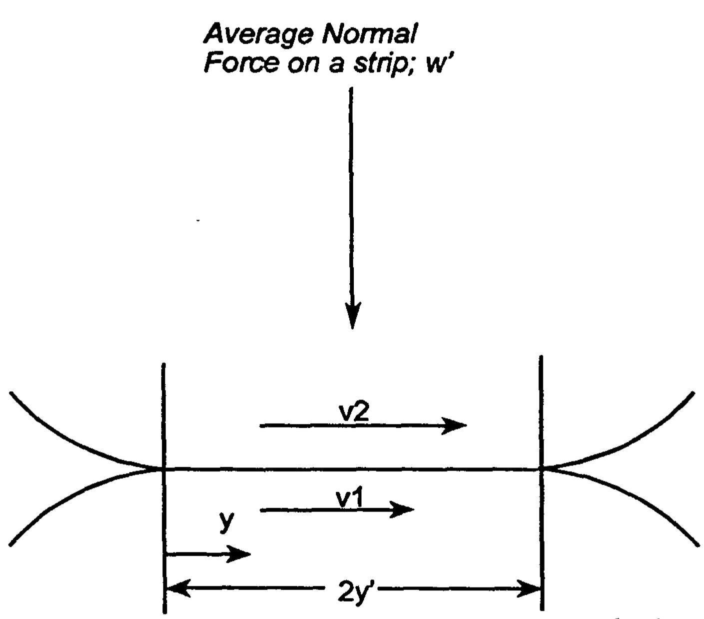

Figure 2-Tangential Rolling Velocities at Differential Strips

strips that each represent a width of constant slip velocity. The normal force on each strip is approximated in a similar manner as the average normal force on each strip. Each differential strip is an area of contact between the ball and the race that can be thought of as contact between two discs that are in engaged in tractive rolling with a particular normal load and slip velocity ratio, with the length of engagement equal to the length of the strip. The coefficient of traction and tractive forces are calculated using the method developed by Dareing [Ref. 1]. Each strip is meshed into elements and nodes along their length (figure 1). The tractive force on a strip is the sum of the differential traction forces along the length of the strip. The slip velocity ratio, tractive forces, and normal forces on the strips are used to calculate energy losses and wear on each strip. The sum of these quantities for all strips result in predicting heat generation, wear rate, and torque on the entire Hertzian contact area.

MATHEMATICAL MODEL & METHOD DESCRIPTION

Tractive Forces and Coefficients

As previously mentioned and shown in figure 1, the Hertzian patch at the ball/race interface is discretized into differential strips, each strip Δx units wide approximates a constant slip velocity for that strip width. The slip velocity and slip velocity ratio models the micro-slippage mechanism. A slip velocity implies that the velocity v2 is slightly higher than velocity v1 (figure 2). Each of the differential strips on the Hertzian contact patch in figure 1 models a cylinder in contact as depicted in figure 2 with length 2y'. This micro-slippage is a combination of slipping and sticking along the length of each strip [Ref. 2 Section 13.3; Harris]. The differential strips are themselves discretized into elements and nodes along their length, parallel to the y-axis (figure 1). At the initial point of contact and for some distance x along the length of the strip, sticking occurs which produces elastic shear micro-strains and displacements on the surfaces, tangent to the plane of the surface in the contact region. Along this length the tractive force is less than the friction force. At the point of impending slip and in the remainder of the strip length, the traction coefficient becomes equal to the friction coefficient and the tractive force equals the frictional force. The displacements in the stick region are calculated as the product of the slip velocity ratio and the 'y'coordinate at the nodes [((v2-v1)/v1)*y ; y=0 is at -y' for this calculation]. The displacements are used to find the tractive force at the nodes along the length of the strip in the stick region based on these surface displacements, using concepts from the finite element method. This method is presented in detail by Dareing [Ref. 1]. Tractive forces in the slip region are calculated using the dynamic coefficient of friction and the normal force [$T_f = f \times N$] at a given node. The slip region begins at the node for which the calculated tractive force based on displacement exceeds the frictional force at that location. The total tractive force [designated dF_t] on a strip is the sum of all the forces at the nodes for that strip. Typically traction data as shown in figure 3 is used to obtain the total tractive force between two discs, for instance interpolating the traction coefficient for a given slip velocity and using the traction coefficient along with the normal force to obtain the tractive force. In this case the computer program was used to calculate the actual tractive curves [like that in figure 12] for each differential strip for greater accuracy, summing the nodal forces as described above. The normal forces are calculated using the Hertzian load distribution [Ref 3; Sect. 2.3; Eschmann et. al] as described below. The effect of the normal force on tractive forces in the stick region is in it's effect on Hertzian contact region size and the slip velocity (equations 3, 4, and 5 respectively).

Slip Velocity

The method for calculation of the slip velocity is based on geometry (curvatures of the roller ball and bearing race groove), normal load between ball and race, and angular velocity ω_i of the inner race. The assumption here is that only the inner race rotates. A spherical ball (radius R_b) loaded against a race groove (radius R_g) causes deformation such that the ball and the race groove have the same effective radius along the semi-major axis transverse to rolling motion [Ref. 2 Section 13.3; Harris], calculated using Equation (1).

$$R_c = \frac{2R_g R_b}{R_g + R_b} \qquad (1)$$

Figure 4 shows the ball and race in contact along the semi-major axis of the region, the semi-major axis being transverse to the direction of rolling motion. There are two positions at $x = \pm$ ca along the *x* axis where the slip velocity is zero. A no slip condition exists at these locations and there is pure rolling and no transmission of tractive forces. The parameter 'c' has been typically shown to be approximately 0.35 by Jones [Ref 10]. As shown in figure 4 the horizontal line connecting the two points {at x=±ca} is the instantaneous axis of rotation of the ball. Points on

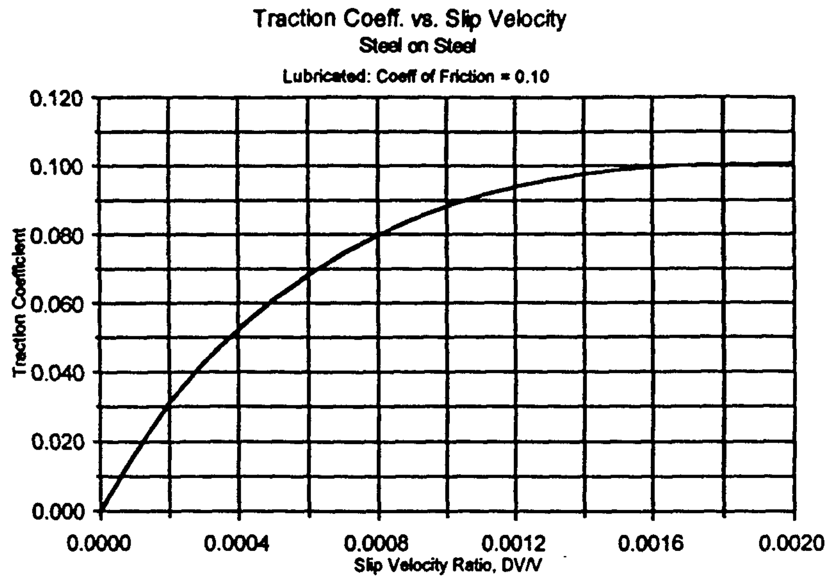

Figure 3

the ball not at the no slip positions experience slip $V_s(x)$ [v2-v1] calculated with equation 2, a function of x. Thus the slip velocity and slip velocity ratio on a given differential strip can be calculated based on the coordinate x. Delta (Δ) is the length from the point on the surface of the ball to the instantaneous axis of rotation and calculated with equation (3) from the geometry in figure 4. $\omega_{b/i}$ is the angular velocity of the ball with respect to the inner race calculated using conventional kinematic principles as explained briefly in the following sections. Slipping in between the x = ± ca positions is against the direction of race rotation and with the direction of race rotation at points outside of the no slip positions [Ref. 2 Section 13.3; Harris] (against and with meaning the shear traction of the race on the rolling elements). This change in slippage direction is evident in Figure 6; a plot of Slip Velocity vs. 'x' for a number of angular velocities.

$$V_s(x) = \Delta\,(\omega_{b/i}) \qquad (2)$$

$$\Delta = R_c\sqrt{1-(x/R_c)^2} - \sqrt{R_c^2-(ca)^2} \qquad (3)$$

The rolling radius of curvature R' is used in calculating Δ, it's length being the second radical term in equation (3). Apparent in equation (3), the contact load influences delta by effecting the size of the Hertzian contact area and thereby the length of 'a'.

Hertzian Contact Area & Pressure Distribution and Normal Loads Computation

As mentioned previously, when two curved solid bodies are in contact at a point deformation is produced resulting in an elliptically shaped contact patch that can be calculated using Hertzian theory. The length and width of the ellipse are calculated using Hertzian equations (4) and (5) respectively from Ref 3 [Eschmann et. al]. W is the normal load between the bodies and E & μ are the average of the moduli of elasticity and Poisson's ratio respectively for the ball and race materials. Forces within the elliptical contact region are based on the x and y

$$2a=(2\zeta)*\sqrt[3]{\frac{3(1-\mu^2)W}{E(\Sigma\rho)}} \tag{4}$$

$$2b=(2\xi)*\sqrt[3]{\frac{3(1-\mu^2)W}{E(\Sigma\rho)}} \tag{5}$$

coordinates of the ellipse and also are calculated from Hertzian theory. Equation (6) [Ref. 8; Johnson] calculates the maximum Hertzian pressure P_o, occurring at x = y = 0. Then equation (7) [Ref 8] is used to calculate the Hertzian pressure on each strip element using the x & y element coordinates. Then the force (pressure*element area) on a differential strip or element could be calculated as a function of x & y. The normal force at each node of a strip was necessary so the friction force could be calculated at each node, for comparison to the calculated tractive forces, to insure the displacement based tractive forces at each node does not exceed the friction force (as explained above). Equation (7) was also used to find the average normal force (dN_i) on each differential strip by integrating it over the length of the strip from -y' to +y' using the x coordinate at the middle of the strip width. This resulted in equation (8), the average Hertzian pressure (P_{avg}) on the strip. Then an average normal force on a strip could be calculated using [$dNi = P_{avg} \times 2y'(\Delta x)$].

$$P_o=\frac{3Q}{2\pi ab} \tag{6}$$

$$P(x,y)=P_o\sqrt{1-(\frac{x}{a})^2-(\frac{y}{b})^2} \tag{7}$$

$$p_{avg}=\frac{\pi}{4}p_o\sqrt{1-\frac{x^2}{a}} \tag{8}$$

The normal load between a roller ball and each race at any given time depends on the angular position of the ball with respect to the direction of the shaft's transverse load,W. In addition, there is also a load for centripetal acceleration on the outer race, which is independent of angular position. The method used to calculate the load based on angular position is from Houghton [Ref.

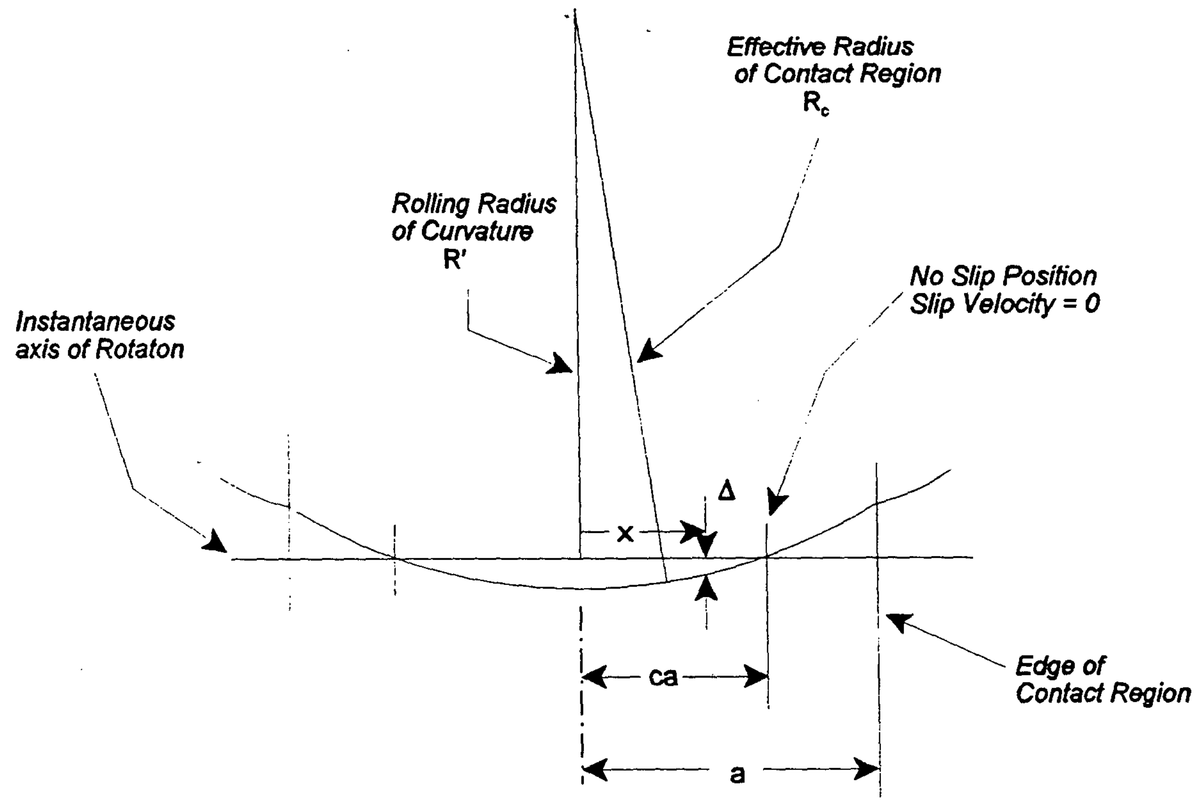

Figure 4 - Geometry of Rolling

4; P.S. Houghton, chap. 9]. He uses an equilibrium expression [equation (9)] and experimental data from Stribeck [Ref. 5] to calculate the normal load magnitudes (p_i) at each angular position. Gamma (γ) is the angular interval between each rolling element. The procedure used here is derived in detail in Reference 11.

$$W = p_o + 2p_1\cos\gamma + 2p_2\cos 2\gamma + 2p_3\cos 3\gamma + \ldots + 2p_n\cos n\gamma \qquad (9)$$

The inertia load on the outer race was calculated from Newton's second law and conventional kinematics assuming the roller bearing is kinematically similar to planetary gear system, using the angular velocity of a imaginary arm. The percentage of time a ball is under each load P_i from the shaft load W was calculated by assuming the load is constant (p_i) at specific positions over an angular interval of γ [gamma]. For a steady state shaft angular velocity ω_i, the percentage of time at a given load was calculated as $2^*(\gamma/2\pi)$, one in each of the lower quadrants. For the upper half, it was assumed that the load due to the shaft load W, is zero for 50% of the time. Summing the percentages for all race angular intervals yields 100%. The inertial load on the outer race is added to each ball in all intervals (100% of the time). For a given number of roller balls, the computer program calculates the correct number of intervals and correct interval angles.

Kinematic Methods

In calculating the slip velocity and slip velocity ratio, it is necessary to relate the roller ball angular velocity with the angular velocity of the inner and outer races [such as $\omega_{b/i}$ in equation (2)]. Equation (10) is the corresponding equation for the outer race slip velocity ($\omega_{b/o}$ being the angular velocity of the ball with respect to the outer race). The method used assumed the radial bearing is behaving like a planetary gear system [Ref. 6; Mabie & Ocvirk]. The inner race for this study has an angular velocity ω_i, while the outer race is stationary. Even though some slippage occurs between balls and races, wherein there is no slip in planetary gears, it is assumed that the slippage is negligible in comparison to the angular velocities of the inner race and balls. For the slip velocity ratio [$\Delta v/v1$], the overall velocity (v1 is typically used) at the ball/race point of contact is also needed. Equations (11) and (12) are the equations for the overall velocity at the point of contact of the ball with the inner race and outer race respectively. $\omega_{i/a}$ and $\omega_{o/a}$ are the angular velocity of the inner race and outer race respectively with respect to the imaginary planet arm.

$$V_s(x) = \Delta\,(\omega_{b/i}) \quad (2) \qquad V_s(x) = \Delta\,(\omega_{b/o}) \quad (10)$$

$$Vel_i = R_i\,(\omega_{i/a}) \quad (11) \qquad Vel_o = R_o\,(\omega_{o/a}) \quad (12)$$

The angular velocity terms below (ω's) were derived using the tabulation method [not shown; Ref. 11]. The inner race has angular velocity ω_i with a stationary outer race.

R_o : radius of the outer race

R_o : radius of the outer race

R_b : radius of the roller ball

$$\omega_{b/i} = \omega_i * [\,(1-R_o/R_b)/(1+R_o/R_i) - 1] \quad (13)$$

$$\omega_{i/a} = \omega_i\,[1 - R_i/(R_i+R_o)] \quad (14)$$

$$\omega_{o/a} = -\omega_i\,R_i/(R_i + R_o) \quad (15)$$

$$\omega_{b/o} = \omega_i(1-R_o/R_b)/(1+R_o/R_i) \quad (16)$$

Slip velocity ratios for the inner and outer race can now be expressed using these equations as shown below:

Inner Race

$$(Vs_i(x)/V) = \Delta\omega_{b/i}/(Ri\ {}^*\omega_{i/a}) = \frac{\Delta^*((1-R_o/R_b)/(1+R_o/R_i) - 1)}{Ri\ {}^*[1 - Ri/(Ri+Ro)]} \quad (17)$$

Outer Race

$$(Vs_o(x)/V) = \Delta\omega_{b/o}/(Ro\ {}^*\omega_{o/a}) = \frac{\Delta^*(1-R_o/R_b)/(1+R_o/R_i)}{(R_i\ R_o)/(R_i + R_o)} \quad (18)$$

Note that in equations 17 and 18 the ω_i term divides out. Therefore the slip velocity ratios are not dependent on the inner race angular velocity, but on the radii of the races and balls, material properties, and the location within the Hertzian patch.

Heat Generation and Friction Torque

The heat generation calculation on the contact region simply uses the definition of work for tangential forces acting over the contact area [$W = \int F\,dx$]. For each differential strip a tractive force dF_i is calculated as previously discussed. The distance Δx each force does work over is the product of the slip velocity [$V_s(x)$] on a given strip and a finite period of time Δt. The power or heat generation [Q(in-lbf./sec)] produced is the work per unit time. Then heat generation is summed over all strips in a contact patch. The final form for the heat generation for all strips on the entire contact area is shown in equation (19). The factor of two accounts for left and right halves (-a to +a), taking advantage of the symmetry of the contact area.

$$Q = 2^*\int V_s(x)\,dF = 2^*\sum(\Delta v_i)(dF_i) \quad (19)$$

The torque input at the inner shaft is calculated using an energy balance with the heat generation [equation (20)], the standard relation for power based on shaft speed and torque.

$$Q = T\omega_i \quad (20)$$

Wear

The wear rate of the roller balls is calculated based on the sliding distance at points within the contact region per unit time and the normal force between ball and race in the contact region.

$$\frac{dh}{dt}=K\frac{F}{A}\left(\frac{dy}{dt}\right) \tag{21}$$

The wear rate dh/dt in equation (21) is the thickness of material removed Δh for a time Δt on the area of contact for a given sliding velocity dy/dt. dh/dt is the wear rate on a differential strip with area A with the average normal force dNi on a strip substituted for F and slip velocity Δv_i substituted for dy/dt. Then equation (21) becomes equation (22). Then equation (22) is converted into a volume removed per second by multiplying both sides by the area of the strip. Then set this equal to a volume wear rate over the surface of the ball ($[dh_{sph}/dt)*A_{sph}]$; equation 23). Uniform wear over the entire spherical surface of the ball is supposed, assuming an equal statistical chance for each point on the ball to contact the race. Dividing by A_{sph} results in the wear rate $(dh_{sph}/dt)_i$ from each *ith* strip over the whole surface of the ball [equation (24)].

$$\frac{dh_i}{dt}=\frac{K(dN_i)}{A_{strip}}(\Delta v_i) \tag{22}$$

$$Q=\frac{dh_{sph}}{dt}(A_{sph})=\frac{dh_i}{dt}(A_{strip})=\frac{K(dN_i)}{A_{strip}}(\Delta v_i)A_{stri} \tag{23}$$

$$\frac{\Delta r}{\sec}=\frac{dh_{sph}}{dt}=\frac{K(dN_i(\Delta v_i))}{A_{sph}} \tag{24}$$

Summing for each strip of the Hertzian contact patch gives equation (25), the wear rate over the entire roller ball due to rolling contact with one race.

$$\frac{\Delta R}{sec.} = 2 * \sum \frac{K[(dN_i)(V_s(x))]}{A_s} \qquad (25)$$

Then a wear rate is calculated for each normal load according to the position of a ball with respect to the shaft load with the addition of the inertial load also. The coefficient K is a wear coefficient calculated from wear data provided by Adair et. al. [Ref. 7; University of Florida]. The data provided is from a plot (figure 5) in Adair's report for the wear of silicon nitride against M-50 steel. In addition, the coefficient of friction for silicon nitride against M-50 steel was obtained from the University of Florida report. The conditions for the University of Florida tests included lubrication using MIL-L-23699 gas turbine lubricant at different stages of environmental duress (schedules 1, 2 and, 3 in the graphs). The wear data from these tests were measured and reported as [mass loss/sliding distance]. This data enabled the calculation of the wear coefficient 'K' in equations (21) - (25). At this time, wear data for steel components against silicon nitride is not available, so a wear coefficient for the wear of the races could not be computed. Therefore race wear could not be predicted. This is also the case for a steel ball against a steel race at the time of this writing as well. With experimental wear data for any combination of materials, appropriate wear coefficients and therefore wear rates (using the computer program) could be calculated. In this case the wear data was presented in picograms/meter and then converted to units appropriate for the wear coefficient.

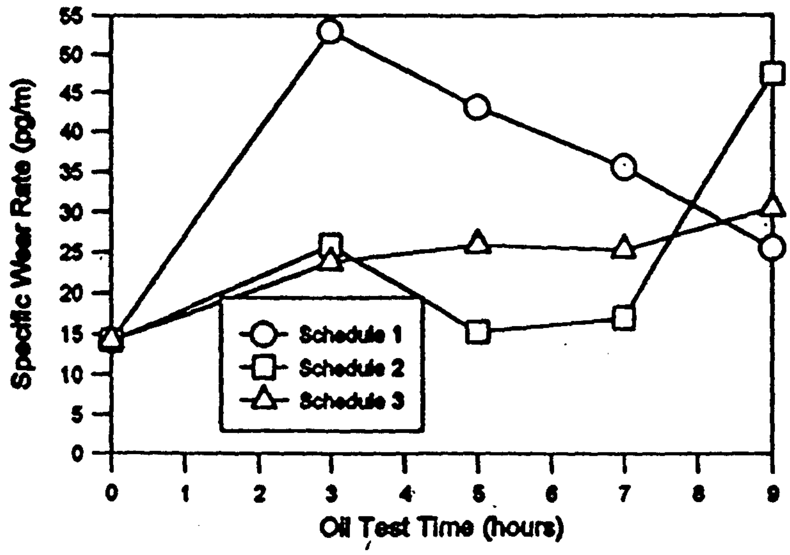

Figure 5 - Rate of Wear Data for Pin Surfaces [Ref. 7, Univ. of FL]

PERFORMANCE PREDICTIONS & COMPARISONS
M50 STEEL vs. SILICON NITRIDE ROLLER BALL

Bearing Parameters and Configuration for Example Calculations

Computations were made to predict and make comparisons of heat generation, roller ball wear, and bearing torque for radial roller bearings using an M50 steel ball vs. a Si3N4 ceramic ball . These quantities are calculated for the tractive rolling mechanism occurring at the ball/race contact region. This includes Hertzian contact of each roller ball with both inner and outer race. The bearing design characteristics used in the computer program are those typical for bearings used for the main turbine/compressor shaft of aircraft jet engines. A radial roller ball bearing with eighteen roller balls is assumed with radial loads but no axial loads. The bearing outer race is stationary and the inner race rotates at the specified RPM. A radial shaft load is imposed through the inner race. On the outer race, the inertial load is added to shaft loads. Table 1 lists the bearing dimensions used for this study. For this comparison bearing speed, race groove radii, and friction coefficient were varied independently to observe the effects of each on predicted performance results. The results are plotted in the following figures. Overall, it can be seen from the plots that the ceramic ball generates less frictional heat and torque losses than the steel ball.

Table 1 - Bearing Dimensions & Geometry (inches)

1.00	Groove radius of the inner race
1.00	Groove radius of the outer race
0.5	Radius of the roller balls
2.5	Radius of the bearing inner race
3.5	Radius of the bearing outer race
18	Number of balls in the bearing
500	Total radial bearing load from the shaft (pounds).
3.8098E-15	Wear coefficient for Si3N4 ceramic against M-50 Steel (in^2 / lbf)

The race materials were assumed to be M-50 steel. For performance comparisons between steel and ceramic roller balls, properties of M-50 steel and silicon nitride ceramic (Si3N4) respectively were utilized for the balls in separate computations. Table 2 lists the properties for these materials as provided by the University of Florida [Ref. 7]. Also, it was assumed that neither the races or ball materials had any special friction reducing coating. As previously mentioned, wear data for steel on steel was not available at this time, so wear rate predictions could not be made for this comparison study.

Table 2:

Material Properties used for the steel and ceramic roller balls as provided by the Department of Material Science and Engineering of the University of Florida.

Material Property	M-50 Steel	MgO-Si3N4	Y2O3-Al2O3-Si3N4
Density (g/cc)	7.8	3.16	3.23
Poisson's Ratio	0.3	0.26	0.29
Elastic Modulus (GPa)	207	320	308
Vickers Hardness (GPa)	8-10	16.6	14-16
Coeff of Therm. Expan (x10-6/K)	12	2.9	2.9-3.2
Specific Heat (J/kg(K)	450	800	800
Thermal Conductivity W/(m-K)	30	29.3	18-25
High Temperature use (K)	600	1300	1300
Fracture Toughness (Mpa($m^{1/2}$))	16	4.1	6-8

Calculated wear coefficient for Si3N4 ceramic against M-50 Steel :
3.8098E-15 in^2/lbf. [ref. 7]

Coefficient of friction for Si3N4 ceramic against M-50 Steel :
approx. 0.1 [ref. 7] (lubricated with MIL-L-23699 gas turbine lubricant).

Coefficient of friction for hard steel on hard steel (lubricated w/ turbine oil): 0.108 [Ref. 9].

Results of Example Calculations

Variable Angular Velocity (RPM)

Calculations were done for angular velocities from 10,000 RPM to 100,000 RPM in increments of 10,000. Both heat generation and wear rate increase with increasing RPM due to a number of factors and are significantly higher above 50,000 RPM. Most apparent is the increasing slip velocity, which causes both heat generation and wear rate to increase [see equations (19) & (25)]. Figure 6 is a plot of slip velocity vs. position within the Hertzian region for several angular velocities, clearly showing the much higher slip velocities for higher RPM. From figure 7 it is clear that the ceramic ball has a lower heat generation, especially at the higher shaft speeds (RPM). Heat generation predicted for the steel ball is about 4 times that predicted for the ceramic ball. Since torque due to micro-slippage is directly related to heat generation, torque input curves are the same as the heat generation with a maximum of 71 and 19 inch-pounds for the steel ball and ceramic ball respectively at 100,000 RPM. For an increasing RPM, a significant contribution to the higher energy loss in the steel was due to the higher inertial loading of the ball against the outer race as shown in figure 8. The density of steel is

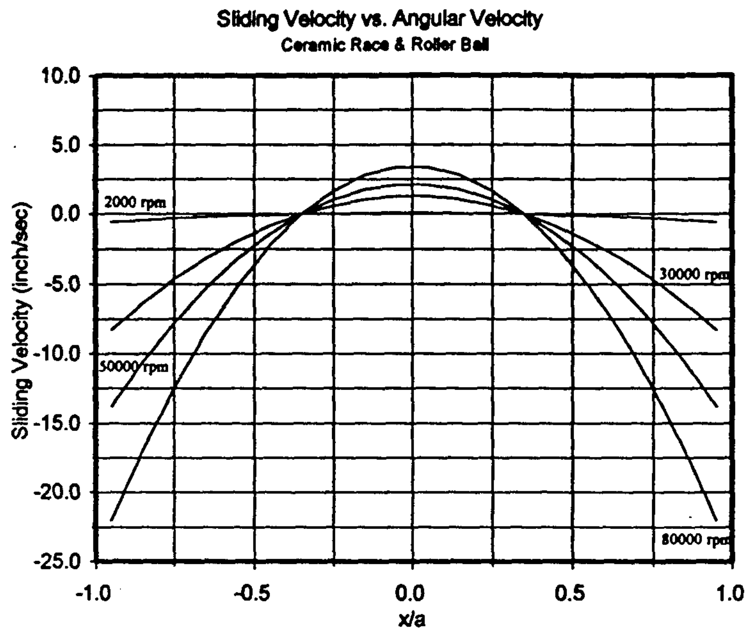

Figure 6

approximately 2.4 times that of the ceramic material. This results in a rapidly increasing inertial load with increasing angular velocity, especially for the heavier steel ball. This higher load in addition to a lower Young's Modulus causes a larger Hertzian contact region (higher degree of deformation) for the steel ball at a given RPM. This results in increased slip velocity and slip velocity ratios on the differential strips and also longer strips (y' in figure 1), both these factors yielding higher tractive forces as discussed in the section describing traction (also see Dareing's paper ref. 1). The larger 'a' dimension also increases tractive forces with wider differential strips that are stiffer and require higher forces to enforce the displacements of the slip velocities (or uses more strips of the same width, still causing a higher tractive force on the whole contact region). In addition the parameter Δ (Delta) in equations (2) & (3) increases with a larger 'a' dimension (the half-length of the semi-major axis of the Hertzian contact region), also contributing to higher slip velocities with larger contact regions. Wear also increases with higher slip velocities and normal forces as evident from equation (25).

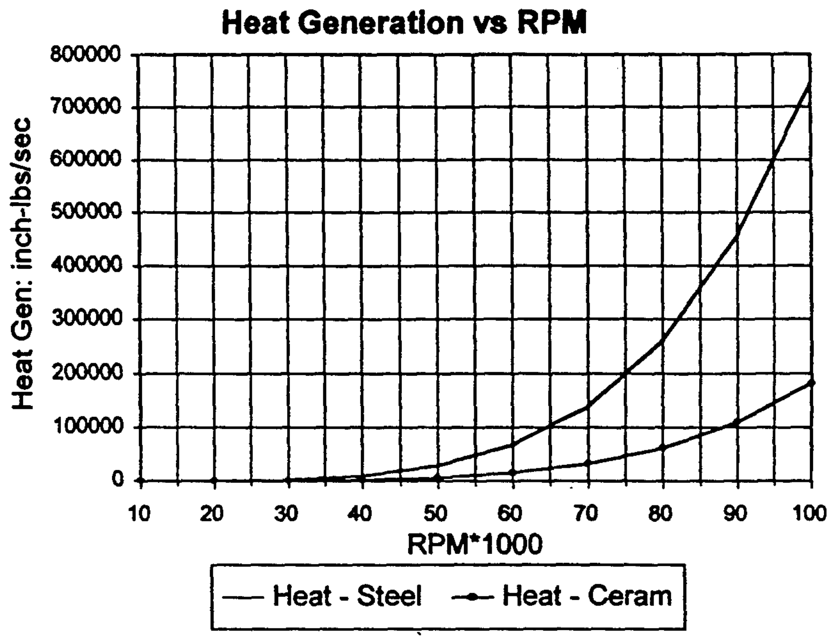

Figure 7

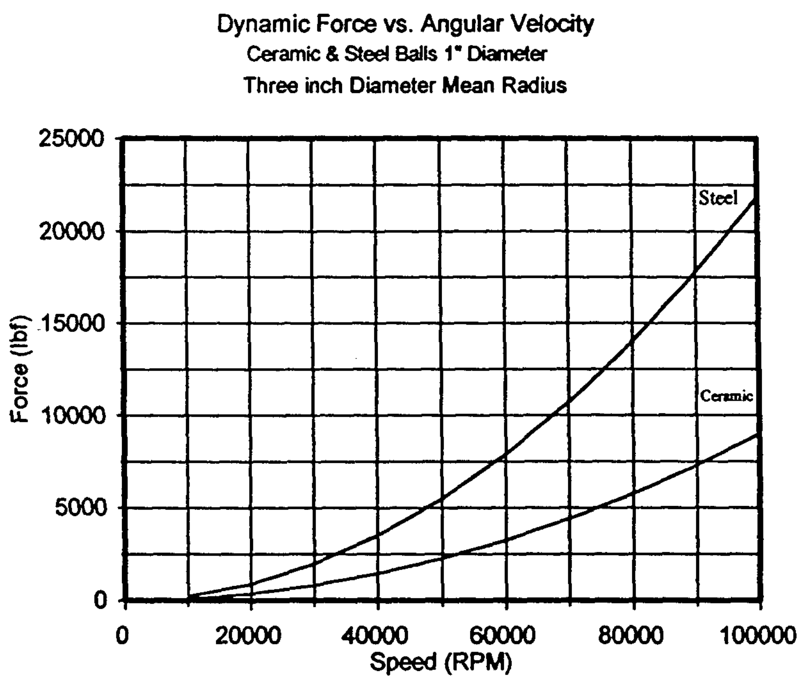

Figure 8

Variable Race Groove Radius

The second set of calculations were done for variations in the race groove radii, ranging from 0.8 inches to 1.25 inches in increments of 0.05 inches. The radius of a race groove is the radius transverse to the direction of rolling. The groove radii for the inner and outer race were varied identically. Plots in figures 9 & 10 show the wear and torque respectively, plotted vs. the race groove radii. Angular velocity for these calculations was at 25,000 RPM (steel & ceramic). The dotted lines show the predicted values of wear and torque for the baseline bearing groove radii (1.0 inch) listed in table 1. Heat generation values for these example calculations were a maximum of 2100 and 500 in-lb/sec. for the steel and ceramic ball respectively. Again, the predicted energy losses for the steel are higher, by about a factor of four. This is due to the same fundamental reasons stated above that cause the larger Hertzian contact region for the steel ball for a given load and geometry. Also, the plots definitively show a decrease in energy loss and wear for increasing groove radius for both steel and ceramic roller balls. This is due to a number of factors. The contact radius R_c decreases with decreasing race groove radii R_g and vice versa. A smaller contact radius increases the length of Δ (Delta) in figure 4 thereby increasing slip velocity and tractive forces at any given '**x**' coordinate. Another contributing factor to the higher slip velocities for smaller race groove radii is the longer Hertzian region (larger 'a' dimension) at smaller radii. As previously stated, a longer Hertzian region increases slip velocities and tractive forces, even for constant race groove radii. Figure 11 shows the 'a' & 'b' dimensions (using equations 4 and 5) plotted vs. radii. The 'b' dimension is slightly less at smaller radii, which in itself reduces the tractive force df_i on a given strip and would tend to reduce heat generation [equation (19)], but the amount is very small compared to the increase

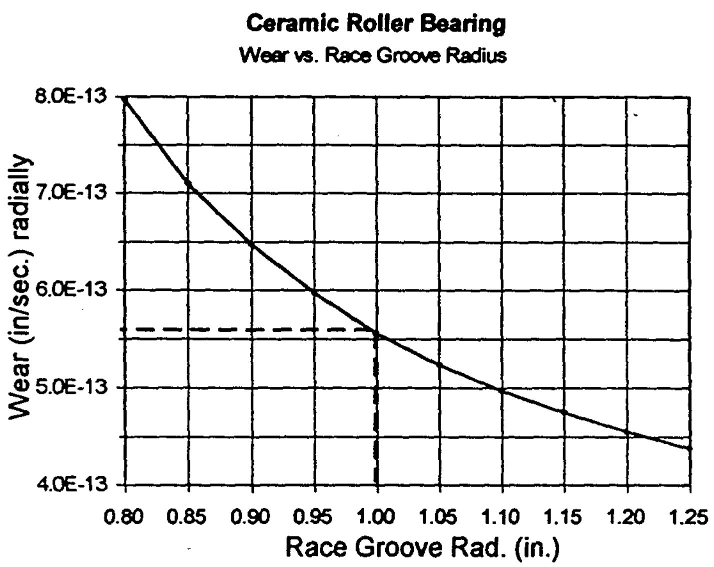

Figure 9

caused by higher slip velocities.

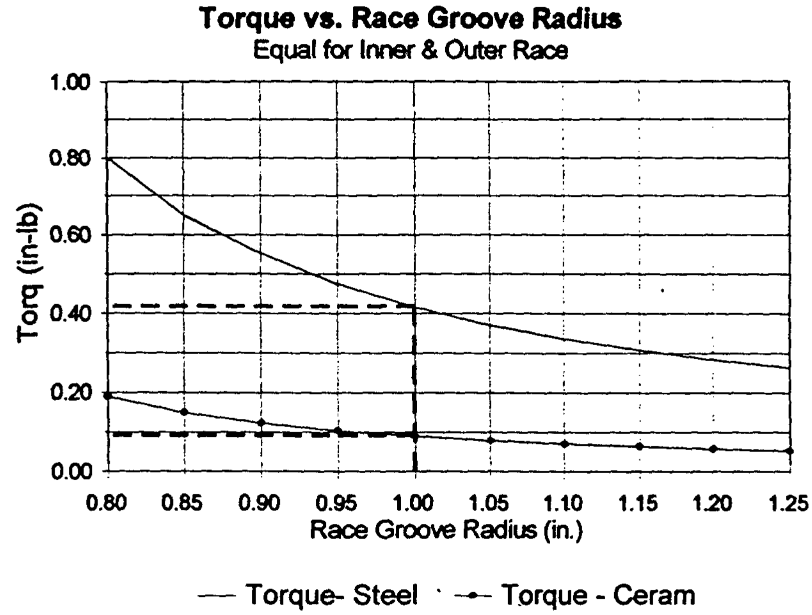

Figure 10

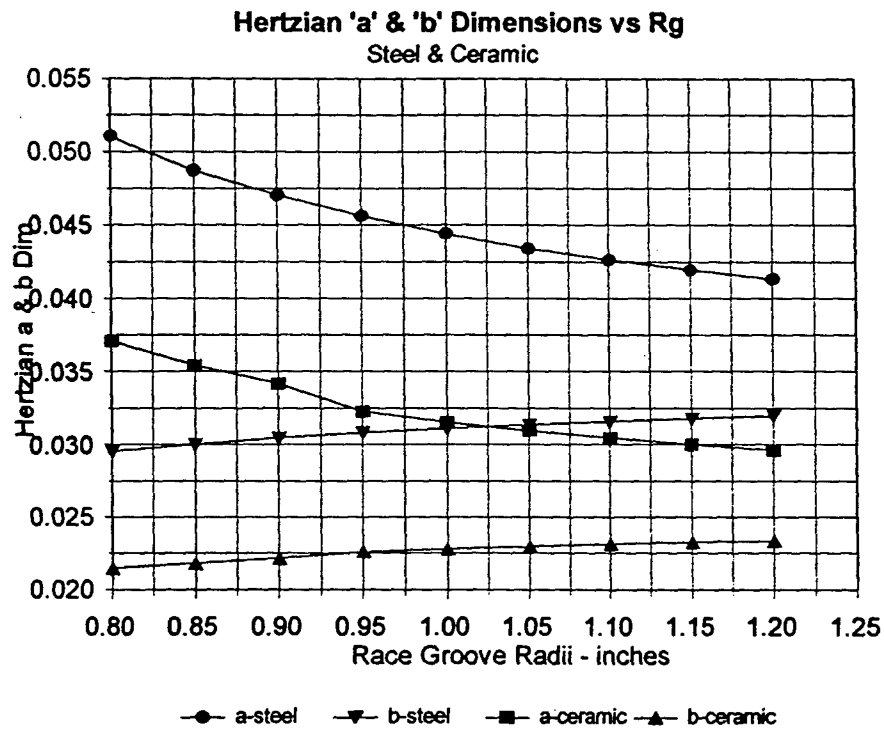

Figure 11 - [Equ. 4 & 5, Ref. 3: Eschmann]

Variable Coefficient of Friction

The coefficient of friction was varied through a range of values for the steel ball and ceramic ball. This was done for 80,000 RPM and standard race groove radii of 1.0 inches. The coefficient of friction *f*, was varied through a range around the published or average value. For steel, the value of 0.1 was obtained from Marks Handbook [ref 9]. For the ceramic material an average value for *f* of 0.1 was obtained from the University of Florida report [ref. 7]. Heat generation for both the steel ball and ceramic ball increased almost linearly with an increasing coefficient of friction. Predictions showed this is a direct result of the tractive force increasing with an identical curve as the heat generation. The tractive force increases with increasing '*f*' because the tractive force in the slip region on a differential strip is equivalent to the average

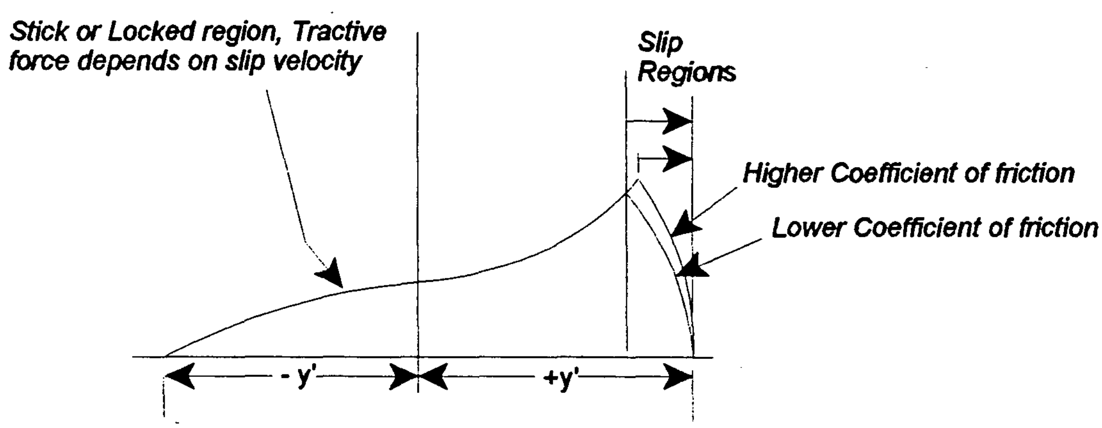

Figure 12 - Traction Curve for two friction coefficients.

normal force on that strip times the friction coefficient '*f*' as discussed previously. Figure 12 depicts the larger area under the traction curve in the slip region due to the higher coefficient of friction. It should be noted that for configurations where the tractive force was much lower than the friction force (high friction coefficient with low normal loads and/or low slip velocity ratio's), there would be no slip region in the tractive curve, and therefore the traction force would not change as the coefficient of friction varied. It should also be noted that the method used to calculate wear rate is independent of friction coefficient. Computationally, this is because the terms used in calculating wear rate [average normal force dN_i and slip velocity $V_s(x)$] in equation(25) are independent of friction coefficient. Physically, it is believed that the coefficient of friction is based on conditions during the wear test and the experimental wear rate data is a result of these same conditions. Therefore it would be invalid to predict wear rates computationally at other coefficients of friction.

CONCLUSIONS

A comparison study of the ceramic and steel ball materials was accomplished for three parameters that were varied independently to evaluate variations in heat generation, torque, and wear rate for variations of each parameter. The three parameters were bearing speed (RPM), race groove radii, and coefficient of friction between ball and race. Heat generation, torque, and wear rate due to the micro-slippage mechanism were calculated in a computer program using the methods presented. These quantities were shown to be about five times lower for the ceramic Si_3N_4 rolling element over the M50 steel ball under similar conditions. The methods utilized principles to calculate slip velocities, tractive forces, and normal forces within the Hertzian contact region and use these quantities to calculate the frictional losses and wear rate.

The results are summarized below:

- The rate of heat generation is significantly higher for both the ceramic and steel balls at angular velocities higher than 50,000 RPM due to:
  - higher slip velocities
  - higher inertial loads on the outer race

- Steel balls generate heat much faster than ceramic balls. Since heat generation rate and torque are related the same conclusion applies to friction torque. The reason is the Hertzian contact region is larger for steel due to the higher inertial load on the outer race and lower Young's modulus. This results in:
  - higher slip velocities for the steel ball
  - higher tractive forces and coefficients due to larger contact area

- The wear rate also increases with higher slip velocities and tractive coefficients but since experimental wear data was available only for the ceramic ball against the steel race at the time of this writing a comparison could not be made.

- Heat generation, torque, and wear rate are greater for smaller race groove radii due to a number of characteristics.
    - greater contact area between ball and race
    - smaller contact radius in the Hertzian region
    - wider Hertzian contact region along the semi major axis
    - higher slip velocities

- Heat generation and torque increase with increasing coefficient of friction due to higher tractive forces in the slip region of the tractive force curve and higher peak tractive forces in the no slip region.

Acknowledging Government Rights as Sponsorship

Research sponsored by the Air Force Office of Scientific Research, Air Force Systems Command, USAF, under grant or cooperative agreement number, AFOSR F49620-93-1-0349DEF. The US Government is authorized to reproduce and distribute reprints for governmental purposes notwithstanding any copyright notation thereon.

This manuscript is submitted for publication with the understanding that the US Government is authorized to reproduce and distribute reprints for governmental purposes.

References:

1. Dareing, D.W., April 1991, "Traction Coefficients for Coated Bearing Races Lubricated with Teflon Transfer Films." Vol. 113, Journal of Tribology, Transactions of the ASME.

2. Harris, Tedric A., "Rolling Bearing Analysis", John Wiley & Sons, Inc., USA, 1984.

3. Eschmann, Hasbargen, Weigand, "Ball and Roller Bearings Theory, Design, and Application", John Wiley & Sons, Inc., USA, 1985.

4. Houghton, P.S., "Ball and Roller Bearings", Applied Science Publishers LTD., Essex, England, 1976.

5. Stribeck, R., "Ball Bearings", J. Mech. Sci. Eng., Vol 12, 1970.

6 Mabie, H.H. & Ocvirk, F.W., "Mechanisms and Dynamics of Machinery", John Wiley & Sons, Inc., USA, 1975.

7. Adair, James H, Sabia, Robert, and Whitney, E. D., Dept of Materials Science and Engineering, University of Florida, "Effects of Oil Degradation on the Friction and Wear Behavior of Hybrid Sliding Couples", 1996.

8. Johnson, K.L., "Contact Mechanics", Cambridge.

9. Avallone, Eugene A., Baumeister, T., "Mark's Standard Handbook for Mechanical Engineers", McGraw-Hill.

10. A. B. Jones, "Ball Motion and Sliding Friction in Ball Bearings", Journal of Basic Engineering March, 1959.

11. Dareing, D.W. & Cento, P.F. "A Focused, Fundamental Study on Predicting Materials Degradation and Fatigue in Aerospace Structures", sub-contract report, AFOSR Grant F49620-93-1-0349DEF, May 1997.

Nomenclature

a	Half Hertzian area length
A_s [A_{sph}]	Ball surface area
b	Half Hertzian area height
dF_i	Tractive Force on a Strip
dN_i	Average strip normal force
E	Young's Modulus
f	Coefficient of friction
F_a	Inertial Force on outer race
K	Wear rate coefficient
P_i	ith ball normal load
P_{avg}	Average strip pressure
P_o	Max Hertzian pressure
Q	Heat generation
R_i	Inner Race radius
R_o	Outer Race radius
R_b	Roller ball radius
R_g	Race groove radius
R_c	Contact radius
ΔR	Radial wear
R'	Rolling radius of curvature
T	Torque
T_f	Friction tractive force
v1	Velocity
Vel_i, Vel_o	Tangential Velocity (races)
Δv [$V_s(x)$]	Slip velocity (v2-v1)
$\Delta v/v1$	Slip velocity ratio
W	Shaft Load
x	Hertzian area major coord.
y, y'	Hertzian area minor coord.
ω_i	Angular Velocity - Inner race
Δ(Delta)	Dist from rotation axis
δ_i	ith ball/race deflection

Task 3

APPENDIX 22, Z. Chen, "Wear Mechanisms of Silicon Nitride Bearing Materials Under Contact Fatigue Stresses," Abstract of Ph.D. Dissertation presented to the Graduate School, University of Florida, May 1995. Dissertation copy available upon request. J.J. Mecholsky, advisor.

APPENDIX 23, Z. Chen, J. C. Cuneo, J. J. Mecholsky, Jr., and S. Hu, "Damage Processes in Si_3N_4 Bearing Material Under Contact Loading," *Wear* 198, (1996) 197-207.

APPENDIX 24, S. Hu, Z. Chen and J. J. Mecholsky, Jr., "On the Hertzian Fatigue Cone Crack Propagation in Ceramics," accepted for publication in *International Journal of Fracture.*

APPENDIX 25, Z. Chen, J. J. Mecholsky, Jr., T. Joseph and C. L. Beatty, "Application of Fractal Fracture to Advanced Engine Material," in *Ceramic Materials and Components for Engines*, D.S. Yan, X.R. Fu and S.X. Shi, eds., World Scientific, Singapore, 1995, pp. 506-509.

APPENDIX 22, Z. Chen, "Wear Mechanisms of Silicon Nitride Bearing Materials Under Contact Fatigue Stresses," Abstract of Ph.D. Dissertation presented to the Graduate School, University of Florida, May 1995. Dissertation copy available upon request. J.J. Mecholsky, advisor.

Abstract of Dissertation Presented to the Graduate School of the University of Florida in Partial Fulfillment of the Requirements for the Degree of Doctor of Philosophy

WEAR MECHANISMS OF SILICON NITRIDE BEARING MATERIALS UNDER CONTACT FATIGUE STRESSES

By

Zheng Chen

May 1995

Chairman: Dr. John J. Mecholsky, Jr.
Major Department: Materials Science and Engineering

The objective of this research was to investigate wear mechanisms of silicon nitride as bearing elements. The study is focused on two questions: (1) How does Si_3N_4 wear initiate and develop in the hybrid ball bearing system? (2) What materials and mechanical factors control wear initiation and development? The properties and fracture behavior of advanced silicon nitride bearing material, such as toughness, crack initiation and propagation, R-curve behavior, cyclic fatigue resistance, subcritical crack growth, and fractography, have been studied. The ball-on-disc cyclic-fatigue testing method has been successfully designed and applied to simulate loading

conditions in a hybrid ball-bearing operation. The diametral compression test has been used to study crack growth mechanisms and environmental influence on crack growth. The AFM, SEM, and XPS are the primary techniques that were used to study the topography and chemistry of the fracture and wear surfaces. From this research, wear mechanism models for Si_3N_4 bearing materials have been established. The causes of the wear have been determined to be directly related to a mode I brittle fracture process. The results of this research will lead to improvement in silicon nitride wear resistance by adjustment of the microstructure.

APPENDIX 23, Z. Chen, J. C. Cuneo, J. J. Mecholsky, Jr., and S. Hu, "Damage Processes in Si_3N_4 Bearing Material Under Contact Loading," *Wear* 198, (1996) 197-207.

ELSEVIER

Wear 198 (1996) 197–207

WEAR

Damage processes in Si_3N_4 bearing material under contact loading

Zheng Chen [a,*], Jacques C. Cuneo [a], John J. Mecholsky, Jr [a], Shoufeng Hu [b]

[a] Department of Materials Science and Engineering, University of Florida, Gainesville, FL 32611-2066, USA

[b] NRC Associate, Air Force Materials Directorate, WPAFB, OH 45433, USA

Received 18 October 1995; accepted 22 February 1996

Abstract

High quality silicon nitride ceramics have excellent high temperature strength, low density and excellent wear resistance due to their low friction. The combination of these properties makes silicon nitride an attractive material for rolling element bearing applications. The low density of the silicon nitride material has particular advantages when applied to the rolling elements of high-speed air turbine bearings. Much work has been done to improve Si_3N_4 mechanical properties. However, wear in Si_3N_4 bearing balls still is a major problem that limits the lifetime of hybrid Si_3N_4 bearings. The wear mechanisms of Si_3N_4 bearing balls in hybrid bearings have not been substantially characterized even though many experimental observations have been recorded. This paper describes Si_3N_4 bearing ball wear as a microcrack initiation and propagation process due to fatigue contact stresses. Experimental results agree with a proposed fracture model to describe the major cause of silicon nitride wear and the major factors affecting the lifetime of bearing balls.

Keywords: Damage; Nitrides; Ceramics; Bearing materials; Contact load

1. Introduction

High quality silicon nitride (Si_3N_4) ceramics have low densities, low friction coefficients, low thermal expansions, high strengths, and high temperature and chemical stability, and are non-magnetic. The combination of these properties makes Si_3N_4 an attractive material for rolling element bearing applications to withstand high loads, severe environments, and high speeds [1]. Many investigators have devoted their time to processing and evaluating Si_3N_4 bearing materials [2–10]. Since Si_3N_4 has a covalently bonded (hexagonal crystalline) structure, difficulty in sintering became a major barrier to its manufacture. Machining was also extremely difficult because of the high hardness of Si_3N_4. The difficulties in both sintering and machining resulted in the fact that it was impossible to limit all defects, such as porosity, large inclusions, surface damage, and sintering flaws, in Si_3N_4 products. The various types of defects resulted in an uncertainty in the Si_3N_4 failure mode for many products. Even though many investigators explored damage mechanisms in Si_3N_4 under contact loading and have documented their attempts [11–15], the damage mechanisms of Si_3N_4 have not been precisely explained. This is because most of the failures resulted from random, external factors (such as defects caused by manufacturing and machining or improper preparation and improper selection of tests) rather than from aspects of material structure.

Numerous investigators have described Si_3N_4 damage mechanisms under contact loading as cracking, spalling, subsurface damage, and tribochemical reaction mechanisms [16–21]. Another investigator suggested that plastic deformation was also involved [22]. The basic experiments currently used are rolling contact fatigue (three balls with one rod, or four- or five-ball contact rolling) [18–20,22,23], pin-on-disc [12], and rolling and sliding contact fatigue [11,13]. These experiments had success in evaluating quantitative volume loss with loading time. However, they lacked control of the damage process and, as a result, were unable to monitor the different stages in damage initiation and development. Notably, a large surface area was tested in these experiments and it was unavoidable that random defects due to specimen preparation could be present in the tests. The defects enhance the material degradation during the tests and may result in a change in the damage mechanism. Therefore, the artificial factors due to specimen preparation could confuse the final results.

With increasing demand for Si_3N_4 hybrid bearing applications, a mechanism which can precisely describe the Si_3N_4 damage process such as initiation and development under a contact load is needed. The understanding of aspects of mate-

* Correspondence address: Space Power Institute, Auburn, AL 36849, USA.

0043-1648/96/$15.00
PII 0043-1648(96)06970-0

rial structure (not random defects) which cause Si_3N_4 damage could be gauged by considering the following two factors: first, the damage process in the material structure is assumed defect-free, to study the damage resulting from material aspects under contact loading; second, the damage process in the material is assumed to have well-defined defects, to study the damage affected by the defects. The objective of this paper is to describe the detail of the damage process in Si_3N_4 bearing materials under contact loading.

2. Experimental procedures

Two types of commercial Si_3N_4 bearing material which are currently widely used in industry were selected as the test materials. They were designated as type A and type B. Both materials have fine microstructures (less than 5 μm) and high density.

Disc-shaped specimens of Si_3N_4 materials were cut from 10 mm diameter rods in 3–5 mm thick sections. The specimens then were ground down to a 15 μm finish using diamond polishing plates in order to remove any visible scratches or pits. An automatic polishing machine was used to further polish these samples until the surface roughness was less than 6 nm.

Surface roughness was calculated from a surface image using the computer software which comes with the NanoScape III atomic force microscope (AFM). The surface roughness value, RMS, is the standard deviation of the Z values (the vertical range of a point in the surface) in the given area and is calculated using the following expression:

$$\mathrm{RMS}=\sqrt{\frac{\Sigma(Z_i-Z_{\mathrm{ave}})^2}{N}} \tag{1}$$

where Z_{ave} is the average of the Z values within the given area, Z_i is the current Z value, and N is the number of points within the given area.

A 4.76 mm (3/16 in) tungsten carbide (WC) ball with surface roughness of about 10 nm was used as a rigid indenter. The ball was used to create a Hertzian stress in the Si_3N_4 discs. Cyclic loading in the form of a half sine wave was used in the experiment. The number of cycles, which varied from 1 to 7 000 000, was chosen to examine the wear initiation and development in Si_3N_4. The maximum compressive contact stress, which is in the central point of the contact area, was calculated using the following expression [24]:

$$\sigma_{\max}=\left(\frac{6P(E^*)^2}{\pi^3R^2}\right)^{1/3} \tag{2}$$

where

$$\frac{1}{E^*}=\frac{1-\nu_1^2}{E_1}+\frac{1-\nu_2^2}{E_2} \tag{3}$$

and P is the applied load, R is the radius of the indenter, $E_{1,2}$ and $\nu_{1,2}$ are the Young's modulii and Poisson's ratios of the disc and the indenter, respectively. Six different maximum compressive stresses (3.2, 7, 10, 15, 17, and 20 GPa) were applied to the specimens, respectively.

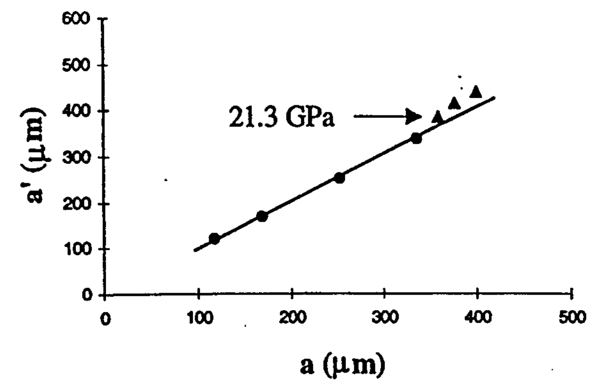

Fig. 1. Measured radius a' of the contact area vs. calculated radius a. Some inelastic deformation occurred in the contact area after the contact stress exceeded 20 GPa (labeled with solid triangles).

The strain in the Si_3N_4 due to contact loading was within the elastic range. This was verified using the following experiment. A fine surface finished Si_3N_4 disc was coated with about 15 nm thick gold–palladium (Au-Pd). The reason for using Au-Pd coating is that this type of coating can record the real contact area after a Hertzian loading is applied to the sample. Therefore, we were able to examine whether the load which was applied to the sample caused any inelastic deformation by comparing the real contact area with the area calculated using the analytical solution. The coated specimens were loaded at different contact stresses. The Au-Pd coating recorded the contact area corresponding to each loading level. The measured radius a' of the contact area was plotted against the calculated radius a of the contact area (Fig. 1). The calculated radius a is given by an elastic equation [24]:

$$a=\left(\frac{3PR}{4E^*}\right)^{1/3} \tag{4}$$

When a load starts to cause the measured area to deviate from the calculated area, the load is a transition load. Loading above this value will result in inelastic strain occurring in the Si_3N_4. All the loads which were used in the contact fatigue experiments were below the transition load. Considering the advantage of lower test times, contact stresses higher than the stresses used in actual bearing operations were used most of the time in this experiment. The Hertzian stress distributions within the Si_3N_4 material were calculated using the finite element analysis (FEA) method. The detail of this analysis is described in Appendix A.

The contact fatigue test was designed to simulate loading conditions in the Si_3N_4 hybrid ball bearing system under the assumption that there was no external tangential traction force on the contact surface. This was assumed because very low friction between Si_3N_4 and M50 steel was observed [25]. Hertzian contact stresses were applied to the Si_3N_4 specimens using a WC ball. The tests were conducted in a Materials Test Systems (MTS) machine using the load control mode. Exxon

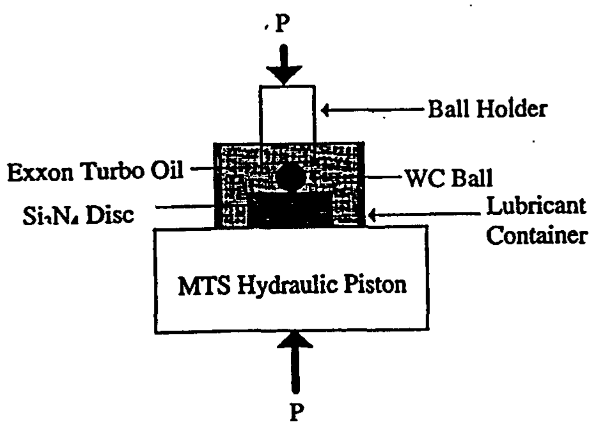

Fig. 2. Schematic of the ball-on-disc contact fatigue test.

turbo oil 2380, which has 26.28 cSt viscosity at 38 °C, 249 °C flash point, and 50.67 kg mm^{-1} Ryder gear test [34], was used at the contact surfaces as a lubricant. A schematic of the test method is shown in Fig. 2.

Two important physical regions of the test specimens were investigated using scanning electron microscopy (SEM) and atomic force microscopy (AFM). The first was the contact area where initial wear occurred. It was possible to examine the whole wear process in this area. The other was the tensile region just outside the contact area. From this region, the cone-crack initiation, propagation, and path were examined afterwards. This test method provides total control over stress level, cyclic frequency, and the number of cycles. The stress state in the contact region was also well defined. Therefore, the damage process (or wear process) under the contact stress region could be closely monitored.

3. Results and discussion

Both type A and type B Si_3N_4 showed a similar wear process. The differences in their degree of wear will be discussed in a separate paper [26]. A typical Si_3N_4 bearing ball wear pattern caused by a bearing test is shown in Fig. 3(a). In Fig. 3(b), an SEM photo shows the Si_3N_4 wear pattern that was caused by the ball-on-disc fatigue test. The wear pattern in Fig. 3(a) was caused by multiple contact fatigue damage, whereas the wear pattern in Fig. 3(b) was caused by single contact fatigue damage. If the damage in regions 1, 2 and 3 of Fig. 3(a) are examined closely, it becomes apparent that the damage is similar to the Hertzian cone type fracture that is shown in region 4 of Fig. 3(b). It is concluded, therefore, that the ball-on-disc contact fatigue testing method is appropriate for use in studying Si_3N_4 material wear mechanisms in hybrid bearing systems.

The ball-on-disc contact fatigue test data are listed in Table 1. The wear process observed in these tests consisted of three different stages (Fig. 4): roughening of the contact surface (stage I), cone-crack initiation and propagation (stage II), and large volume material removal from outside

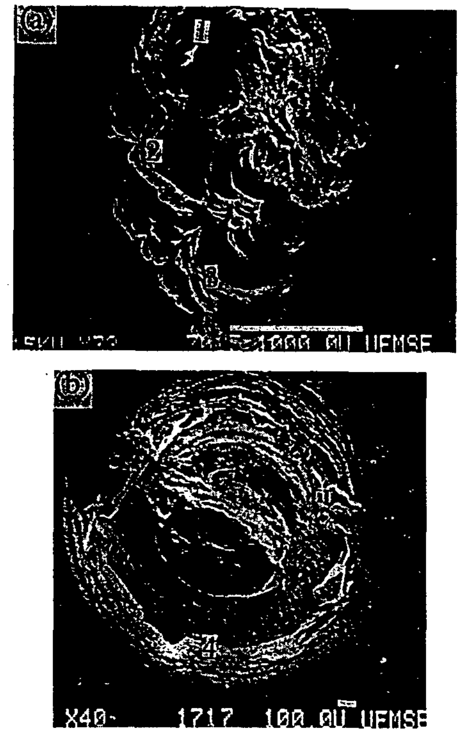

Fig. 3. (a) Type A hybrid bearing ball failure pattern and (b) a Hertzian contact failure pattern from the ball-on-disc contact fatigue test. Both show some similarity in the regions labeled 1, 2, 3, and 4.

Table 1
Data from the ball-on-disc contact fatigue test

Si_3N_4 type	σ_{max} (GPa)	Hz	No. of cycles (k)	Damage description
A	10	10	1500	few grains pull out, cone-crack
A	15	10	600–1500	few grains pull out, cone-crack
A	15	10	2000	cone-crack, chip-out
A	15	10	3000	large volume loss
A	17	10	20	few grains pull out, cone-crack
A	17	10	1700	large volume loss
A	20	10	1	cone-crack, chip-out
A	15	7	700	cone-crack
A	15	5	500	cone-crack
A	7	10	5000	grain pull-out, cone-crack
A	3.2	10	7000	grain pull-out, cone-crack

the contact area (stage III). In the following sections, each stage of wear will be discussed and the mechanisms of wear will be proposed.

3.1. *Stage I wear—roughening on the contact surface*

The type A specimen was tested under a 3.2 GPa maximum stress at 10 Hz frequency. Fig. 5(a) is the wear pattern after 7 000 000 loading cycles. The plot of roughness vs. its corresponding location on the contact surface is shown in Fig. 5(b). Each location is represented by a letter A, B, C or

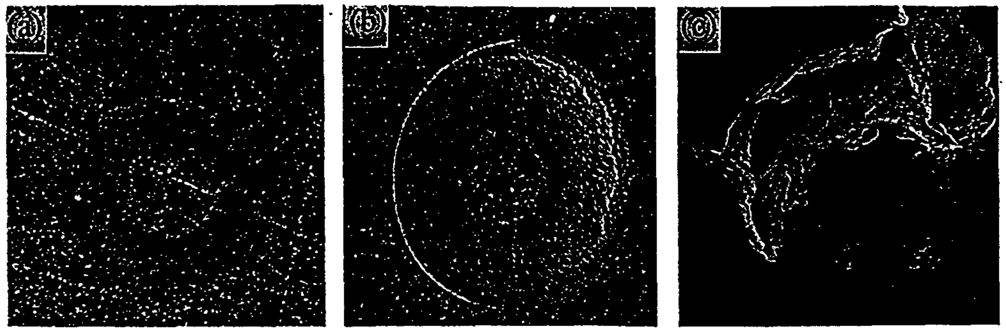

Fig. 4. Wear on the type B Si_3N_4 due to the ball-on-disc contact fatigue test consists of three different stages: (a) stage I (under σ_{max} = 15 GPa after 50 000 cycles), (b) stage II (under σ_{max} = 15 GPa after 1 000 000 cycles), and (c) stage III (under σ_{max} = 15 GPa after 3 000 000 cycles).

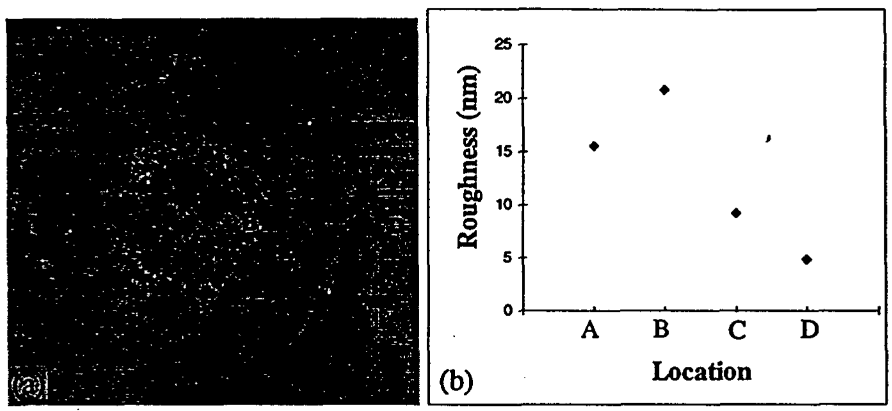

Fig. 5. (a) AFM image resulting from a wear surface of type A Si_3N_4 under σ_{max} = 3.2 GPa after 7 000 000 cycles. (b) Surface roughness at different locations on the contact surface, as labeled in (a).

D, corresponding to the location shown in Fig. 5(a). An increase in the contact surface roughness indicates that wear has occurred. For convenience in later discussion, the middle of the contact surface (labeled A in Fig. 5(a)) was designated as the central region. The roughest area just outside the middle contact area was named the outside central region (labeled B). The contact area was examined under high magnification SEM. In the central region (Fig. 6(a)), most of the grain boundaries were damaged and a few grains were pulled out from the surface. Away from the central region, many more grains were lifted up, as shown in Fig. 6(b).

Theoretically dense brittle materials with covalent or ionic bonds are difficult to fracture under hydrostatic compression at room temperature. This is because none of the three fracture modes in fracture mechanics can explain fracture under hydrostatic compression. The questions raised here are: why are the grain boundaries damaged under a compressive stress and why are fewer grains pulled out in the central contact region than in the area outside the central region?

First, damage of the grain boundaries under the compressively loaded region was observed. The existing grain boundary phase is recognized as a glass phase which was used to improve Si_3N_4 densification during the sintering process [26]. The boundary phases in type A and type B Si_3N_4 are mainly composed of Al_2O_3, Y_2O_3, and SiO_2, and of MgO and SiO_2, respectively. The glassy or amorphous materials are susceptible to structural rearrangement under high stresses because of their long-range disordered structure or disordered network structure [27]. Therefore, there is a delayed elastic deformation of the glass phase in response to a load due to disentangling of structural elements, such as rings of atoms [28]; this is viscoelastic behavior. The delayed elastic component can be represented by a generalized Kelvin–Voigt model. The schematic curves in Fig. 7(a) show the relationship between loading and deformation for both glassy material and polycrystalline materials, respectively. The glass mechanical behavior is represented by springs and dashpots; Si_3N_4, a polycrystalline material, is represented by a spring. Si_3N_4 deformation responds to the loading immediately, whereas the glass deformation shows an immediate response (elastic) and a delayed response (viscous) to the loading. The delayed response results from the glassy structural units gradually undergoing a relaxation process during unloading. This "relaxation action" causes a time-dependent change in volume manifested as the delayed deformation. Therefore, when a highly compressive load $P(t)$ on a Si_3N_4 grain is released (Fig. 7(b)), the grain is immediately back in its original position; whereas the glass phase along the boundary is gradually returned to its original position due to the relaxation action happening among its glassy structural units. A tensile stress is built up in the glass phase due to the delayed deformation during the unloading cycle. The cyclic tensile

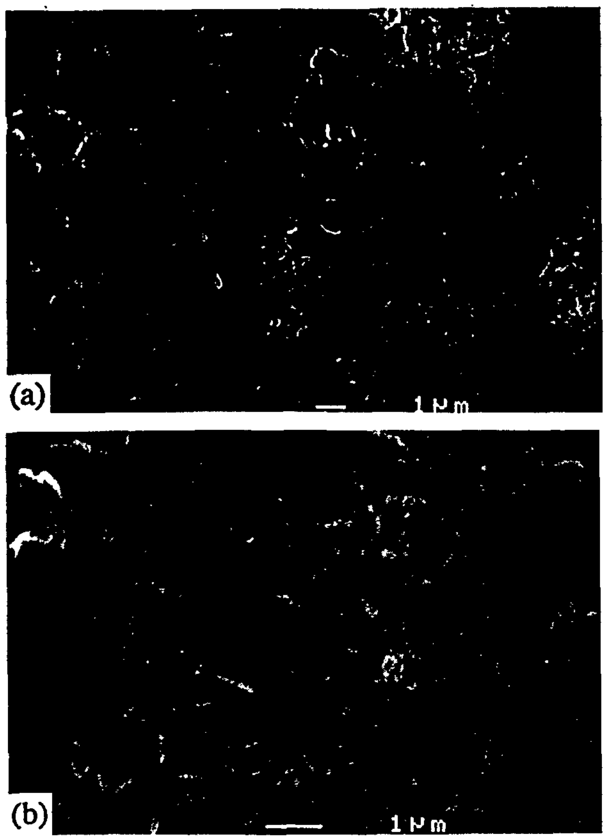

Fig. 6. Wear surface topography: (a) wear at the central region and (b) wear at the outside central region.

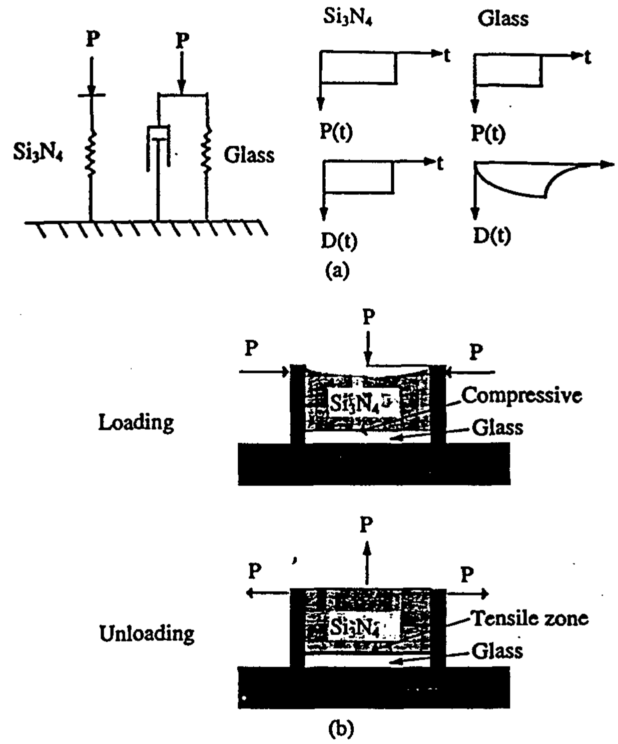

Fig. 7. (a) Kelvin–Voigt solid model and its load-deformation curve. (b) Schematic showing tensile stress built along the grain boundary due to delayed deformation in the grain boundary phase.

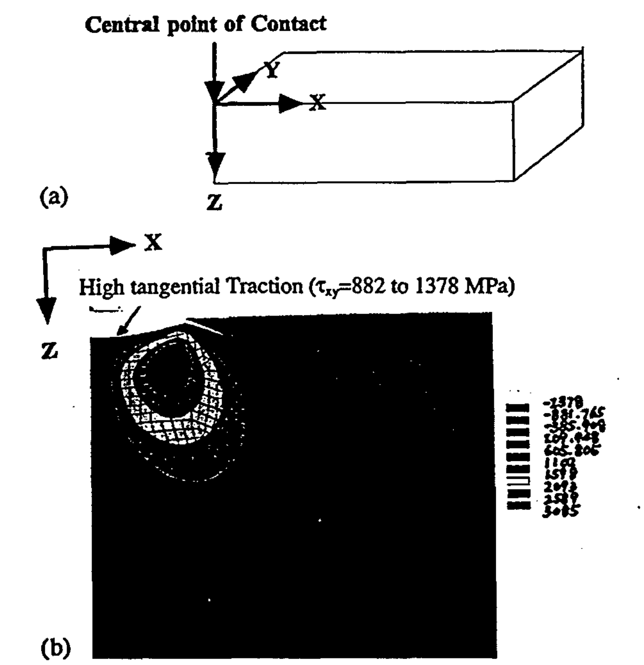

Fig. 8. Hertzian shear stress distribution, τ_{xy} (resulting from the Hertzian load, $P = 1998$ N), within a range of $x = 1000$ mm and $z = 865$ mm. Notice that a high tangential traction exists at the outside central region.

stress in the glass phase eventually causes grain boundary fracture. However, if there is no tangential traction to lift up the damaged grains from the contact surface, the grains will still remain in their position due to the grain boundary mechanical interlock.

Now, why are fewer grains pulled out in the central contact region than outside the central region? To answer this question, it is first necessary to examine the shear stress distribution to see if there is any stress difference between these areas. The shear stress, τ_{xy}, distribution (the xy plane is denoted on the sample surface) is shown in Fig. 8. A higher surface shear stress was found on the outside central region. This shear stress is primarily due to Young's modulus and Poisson's ratio mismatch between the ball and the disc during the contact loading. So, the traction lifts up the grains whose boundaries have been damaged. In the central region, most of the grains still remain in their position because of the lower shear stress.

Stage I wear, therefore, can be described using the model shown in Fig. 9. There is a different deformation response to the loading and unloading cycles between the grain and grain boundary phase. In addition, the constraint force on the surface is decreased due to the free surface. Both of these factors cause fatigue damage along the grain boundaries near the surface. Then the grains whose boundaries have been damaged are pulled out by the shear stress. The wear initiation is due to heterogeneous mechanical behavior between the grain and grain boundaries (elastic behavior vs. elastic and viscoelastic behavior). Wear development is attributed to the shear

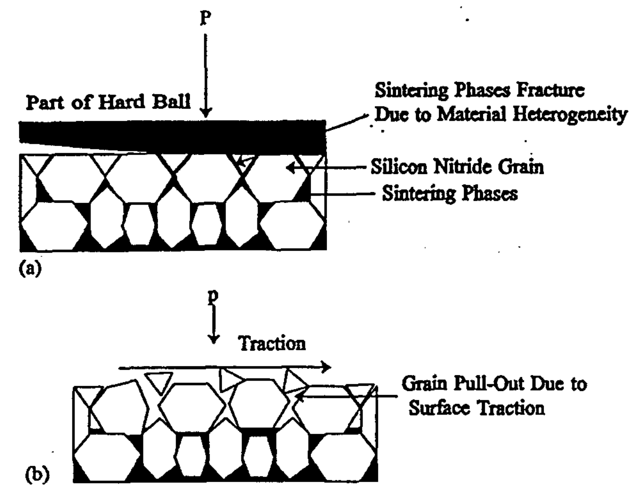

Fig. 9. Schematic showing a cross-sectional view of the mechanisms of wear in stage I. The section is from the high tangential traction region indicated in Fig. 8. (a) Grain boundary phase damaged due to its delayed deformation under cyclic loading, and (b) grain pull-out caused by the higher surface tangential traction.

stress on the contact surface which lifts up grains from the surface.

To verify this explanation, a contact fatigue load was applied to a homogeneous material, borosilicate glass, and single crystal sapphire, respectively, to investigate if any damage occurred in the contact areas [26]. The contact areas of both specimens remained intact after the number of loading cycles. The result clearly demonstrates that a homogeneous structure can eliminate stage I wear on the contact surface. In other words, this experiment confirms that the heterogeneous nature in the Si_3N_4 material and the grain boundary phase is the cause of stage I wear.

3.2. *Stage II wear—cone-crack initiation and propagation*

Considering the bond structure of brittle materials, i.e. covalent or ionic bonding, mode I stress is a basic stress mode that causes brittle material fracture. From the contact stress distribution in the lateral direction (Fig. 10), there is a maximum tensile stress, σ_x, just outside the circumference of the contact area. The surface of the specimens has been carefully polished down to a surface roughness less than 6 nm. We assume that there are no pre-existing cracks in the surface (or at least, we can assume there are no pre-existing sharp cracks). For crack growth, the first step is to initiate a sharp crack. The following discussion will be focused on crack initiation in the tensile region.

The SEM photos taken from a wear area are shown in Fig. 11. There appears to be a cone-crack near the maximum tensile region in Fig. 11(a). However, under high magnification, it was identified as a loose grain region (Fig. 11(b)). After grains loosen and are pulled out from the surface, a crack initiates from the pulled-out grain region. The crack then propagates under a cyclic stress in mode I. The model in Fig. 12 is used to explain the cone-crack initiation and propagation in the maximum tensile stress region under cyclic contact fatigue. The material just outside the contact area circle experiences a maximum (cyclic) tensile stress. The cyclic stress causes fatigue damage in the grain boundary phase near the surface due to its weak mechanical properties, i.e. low strength, low toughness, and environmental sensitivity. The loose grains near the surface at the maximum tensile region, which are caused by boundary phase fatigue, result

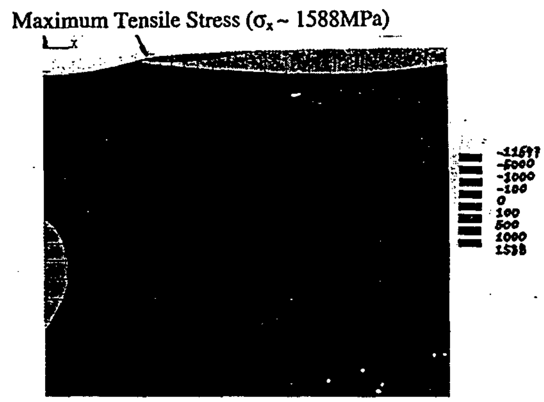

Fig. 10. Hertzian stress distribution, σ_x (resulting from the Hertzian load, $P=1998$ N), in x direction within a range of $x=1000$ mm and $z=865$ mm. Notice that the largest tensile stress field is just outside the contact area (axis notation is the same as that in Fig. 8).

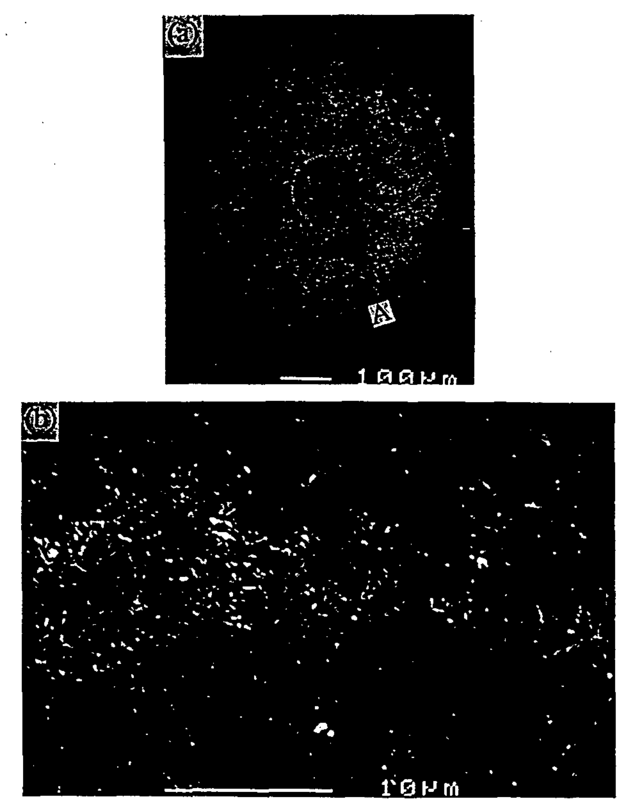

Fig. 11. (a) The cone-crack seems to be initiated near the maximum tensile stress region of the type A Si_3N_4 under $s_{max}=15$ GPa after 1 000 000 cycles. (b) High magnification from point A shows the cone-crack is a loose grain region.

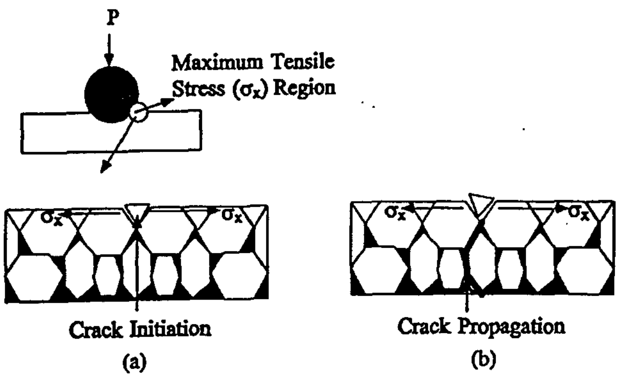

Fig. 12. Schematic showing a cross-sectional view of the mechanism of wear in stage II. (a) A loose grain caused by cyclic fatigue stress and (b) crack propagation under local tensile stress.

in cone-crack initiation. The crack then propagates stably along the grain boundary under a cyclic mode I stress. Again, the weakness of the grain boundary phase and the existence of the tensile stress outside the contact area are two major factors which results in stage II wear: stage II wear is a process of cone-crack initiation and propagation from the surface outside the contact area. The wear process is governed by a cyclic tensile stress from contact loading on the surface.

3.3. Stage III wear—material removal from outside the contact area

During stage III wear, a large volume of material removal was observed outside the contact area (Fig. 4(c)). To investigate the causes of this stage of wear, the wear specimens were sectioned across their contact areas. From the pictures of the cross-section in Fig. 13, the cone-crack starts to curve up to the surface after the crack propagates down into the bulk of the specimen.

Fig. 14 shows a specimen fractured at 27.8 GPa maximum contact stress under monotonic loading (at 900 kg sec^{-1} loading rate). The cone-crack propagates following a cone-shaped path all the way down to the bottom of the sample and then the propagation results in fracture from the bottom

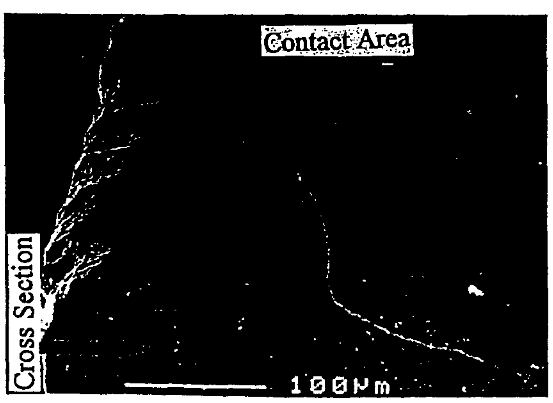

Fig. 13. SEM photo from the cross-section showing the cone-crack curving up to the surface after growing a certain depth into the specimen.

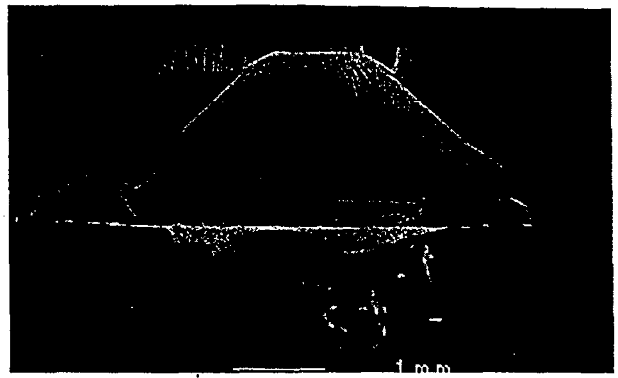

Fig. 14. SEM picture from the cross-section showing a monotonic fracture path.

to the top of the specimen. However, for cyclic loading, the crack only grows downwards a short distance and then starts curving up to the free surface.

Singh and Shetty have demonstrated that a pre-existing crack in a brittle material will propagate towards a direction with a pure mode I stress even though the crack starts with mixed mode stresses [29]. Hu et al. also indicated that a microcracking path in brittle laminated composites under complicated (mixed-mode) local stresses follows the local mode I stress path [30].

The cone-crack paths predicted by the mode I stress path are shown in Fig. 15. Comparing the predicted path with a crack path measured from the specimen which was fractured under monotonic loading shows that there is good agreement of the experimental and theoretical paths. This result clearly

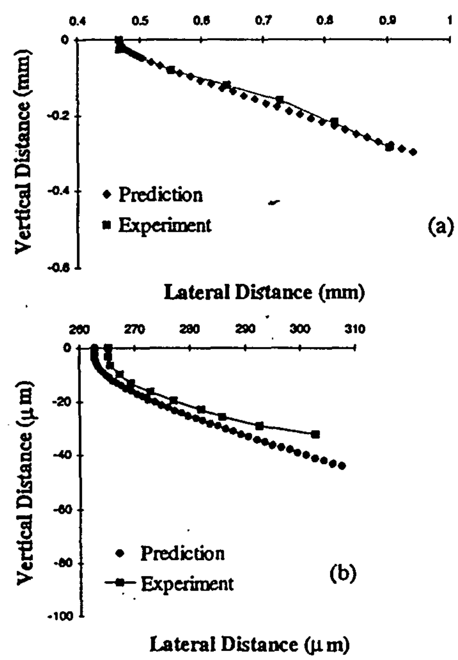

Fig. 15. A measured monotonic fracture path (a) follows the predicted mode I stress path. A cyclic fatigue fracture path (b) follows the predicted path (mode I stress path) for a certain distance then deviates toward the free surface.

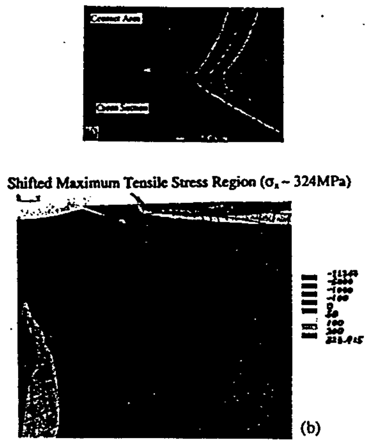

Fig. 16. (a) SEM photo showing multiple cone-cracks outside contact area. (b) Hertzian stress, σ_x (resulting from the Hertzian load, $P = 1998$ N), is redistributed due to existing cracks (axis notation is the same as that in Fig. 8).

demonstrates that crack propagation in brittle material is governed by mode I stress (tensile stress). However, under cyclic loading conditions, the crack path only follows the mode I stress path to a certain distance and then starts to deviate from the predicted path.

Another phenomenon which occurred during stage III wear is the initiation of multiple cone-cracks outside the contact area, as illustrated by the SEM photo in Fig. 16(a). From this cross-section, it can be seen that the first cone-crack, which is closest to the contact circumference has the longest length. The length of other cone-cracks decreases with an increase in distance between the cone-crack and the circumference.

An FEA program was used to analyze the stress distribution after the first cone-crack was initiated (Appendix A. The stress distribution along the lateral direction (Fig. 16(b)) shows that there is a higher tensile stress around the crack tip region. In addition, the maximum tensile region on the surface is shifted from next to the contact circumference to a distance away from it. The shifted tensile stress, σ_x, is the cause of the second cone-crack initiation. The third and the fourth cone-cracks follow for the same reason.

Therefore, the curved-up primary crack joins the second or the third cone-cracks to form a pocket in the outside contact area. This results in material removal as a chip from the pocket bounded by these multiple cone-cracks and the free surface of the specimen. The initiation of the first cone-crack determines stage II wear, and the following cone-cracks contribute to stage III wear.

There is no precise explanation for the crack to curve up at this stage. We speculate that the reflected stress wave or multiple cone-crack formation may redistribute the stress field around the first cone-crack tip and force the crack to propagate up to the free surface. In fact, the crack does not have strong motivation to continuously propagate downwards after having grown a few hundred micrometers based on our stress analysis.

Three wear patterns and their mechanisms under contact fatigue loading have been demonstrated. However, there are still some primary concerns in hybrid ball bearing applications which will be addressed in the following section.

3.4. The effect of defects on Si_3N_4 wear behavior

An additional concern is the existence of defects such as surface scratches and subsurface flaws or pores on Si_3N_4 wear behavior. In order to study the influence of the defects on wear behavior, indentation techniques were used to artifi-

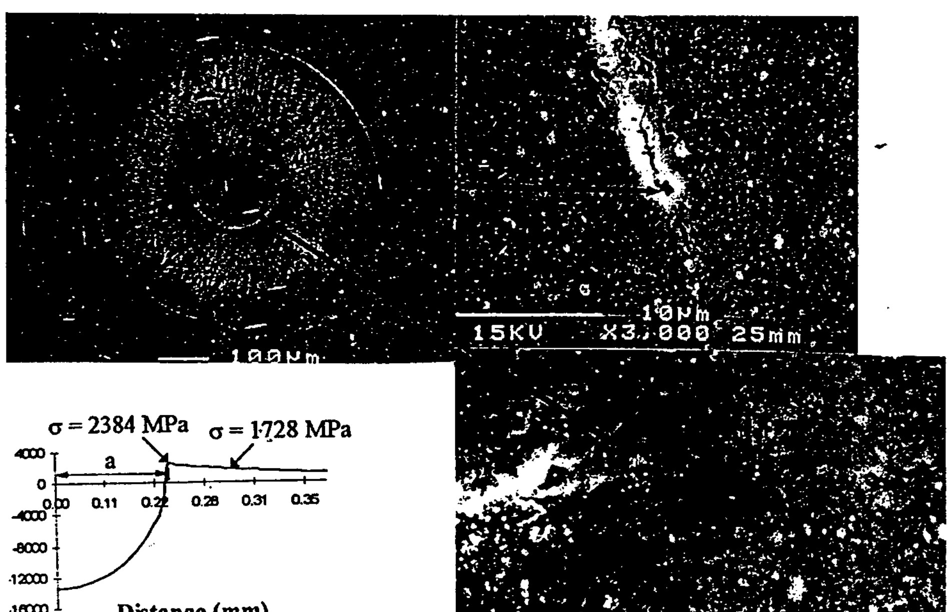

Fig. 17. SEM photos indicating that the defects in the contact area caused little wear in type A Si_3N_4. The defect outside the contact area resulted in a cone-crack initiation at low stress level. The stress curve shows the stress at the crack to be almost 600 MPa lower than the maximum stress.

cially create these defects. First, a Knoop indentation was employed to create 5 μm wide and 40 μm long Knoop impressions to simulate scratches. The indentations were placed at different locations within an area where a contact load would be applied. A 200 g Knoop indent load was chosen to avoid creation of a large local inelastic zone and initiation of cracks at the corners of the impressions. SEM examination was used to verify that no cracks were found around the indentation. A cyclic contact load then was applied to the area. The results indicate that, in the contact area, scratch defects (Knoop impressions) have little effect on wear. No crack initiation and no extra wear damage were found near the indentations after 80 000 cycles under 15 GPa contact stress (Fig. 17). However, the scratch (Knoop indentation) in the outside contact area promoted a cone-crack initiation. The cone-crack initiated from one of the indentation sites rather than from the maximum tensile stress region, even though the stress at the location of the indentation was almost 600 MPa lower. Thus, defects such as scratches can promote crack initiation and increase wear in Si_3N_4 at a lower stress level.

A Vickers indentation technique was also employed to create a large local inelastic deformation zone, near which a subsurface lateral crack can be initiated. The indentations from 1 kg load were created both inside and outside the contact area. Spallation occurred from one of the indentations after 300 000 cycles under 15 GPa stress (Fig. 18(b)). The spalling pattern is very similar to those observed from the failed Si_3N_4 balls due to subsurface defects. The spallation initiated from the region between two radial cracks of the indentation (Fig. 18(a)) where a shallow subsurface crack has potential to initiate due to the inelastic zone of the indentation. The pictures in Fig. 18 display the process of the lateral crack growing to the surface under contact fatigue loading. This experiment indicates that spallation only occurs when there are pre-existing defects underneath the surface. These defects, most likely, are lateral cracks due to large local inelastic deformation caused by sharp indenters or due to the sintering process. The lateral crack develops quickly to result in spallation under contact fatigue stress.

One important thing needs to be clarified: the difference between spallation and Hertzian cone-cracking. Spallation is initiated from lateral defects which are mostly associated with local inelastic deformations caused by sharp indenters or pre-existing subsurface defects due to an improper sintering process. The crack initiates underneath the surface and then propagates towards the material surface under loading. Hertzian cone-cracking is due to a mode I stress created by contact loading within an elastic strain region. The crack initiates at the surface and then propagates into the material. The different appearances are clearly shown in Fig. 3 and Fig. 18(b).

The defects near the surface can significantly reduce the lifetime of Si_3N_4 under contact fatigue loading. Greater attention to limit scratches and subsurface defects may result in greater improvement in Si_3N_4 bearing ball wear resistance.

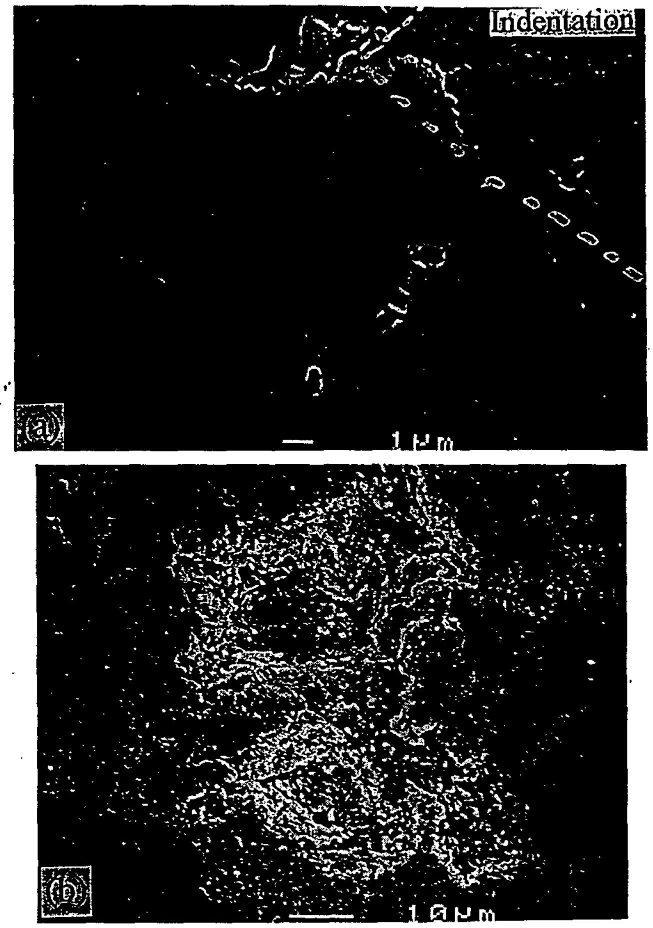

Fig. 18. (a) SEM picture showing that spalling initiates in type A Si_3N_4 at the area near the indentation. (b) A high magnification photo displaying the spalling pattern, which is similar to those observed in failure bearing balls.

4. Conclusions

Problems in studying wear always exist due to the large number of variables involved in the wear process. Any change in the variables will potentially lead to a wear rate change, perhaps even a wear mechanism change [31]. Wear problems in a Si_3N_4 hybrid ball bearing system are also very complicated, and involve many wear mechanisms. However, careful consideration of the primary bearing ball wear patterns can help find the primary causes of wear.

In this study, contact stress fatigue was considered a primary wear mechanism. After extensive experimental investigation in Si_3N_4 wear, it is proposed that the wear process in the hybrid ball bearing system occurs in the following manner. Wear in the Si_3N_4 bearing ball is initiated by contact fatigue stresses. Each wear stage described in the previous sections can cause Si_3N_4 debris, e.g. a grain or a conglomerate of many grains, which subsequently deposit in the lubricant. The debris in the lubricant creates a second wear mechanism that is essentially three-body abrasive wear; i.e. scratching or cutting in both Si_3N_4 and M50 steel race surfaces. Furthermore, the large pieces of debris in the lubricant act as sharp

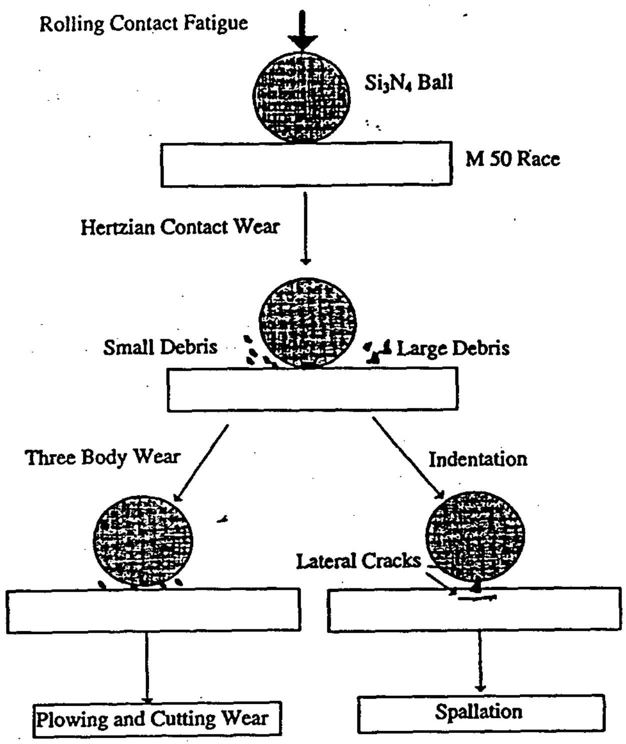

Fig. 19. Schematic of the wear process in Si_3N_4 hybrid ball bearing system.

indenters and create larger local inelastic deformation regions in the ball or race surface due to their indentation. The lateral cracks from this process could be initiated underneath the free surface due to local inelastic deformation. Therefore, the third wear mechanism starts to join in the wear process, i.e. spallation. The wear process is shown schematically in Fig. 19.

Wear in Si_3N_4 hybrid ball bearing systems involves multiple wear mechanisms, but contact stress fatigue is the primary mechanism, and this mechanism determines the entire wear or degradation process. Consequently, an increase in contact stress fatigue resistance in Si_3N_4 can lead to significant reduction of overall wear in the system.

Acknowledgements

The authors gratefully acknowledge the support of Air Force Office of Scientific Research Grant Number F49620-93-0349DEF and the Major Analytical Instrumentation Center at the University of Florida for partial support of this work.

Appendix A

The finite element analysis (FEA) method is one of the most popular numerical analysis techniques widely used by engineers and scientists. It is used to obtain approximate solutions to a wide variety of engineering and scientific problems, one of which is the stress distribution in solids.

For the problem of Hertzian contact we can use the model of axi-symmetric analysis which is considered two-dimensional to replace the three-dimensional analysis. The indenter is spherical and the sample dimension is sufficiently large compared with the contact area. It is obviously preferable to model the problem using a two-dimensional analysis to reduce an enormous amount of computational effort without sacrificing accuracy. Therefore, two-dimensional elements are used; but all three-dimensional nonzero stress components are obtained.

Commercially available FEA software ANSYS was used for all finite element analyses. This software provides a wide variety of element types and analysis capabilities.

In the beginning, we used two-dimensional elements for both the spherical indenter and the sample ceramics, and point-to-surface contact elements to join the nodes between the elements of sample and indenter at the potential contact area. The dimensionless contact elements used present a bilinear stress/strain relationship under loading [32]. When under no contact stress, the contact elements do not function, which allows for the physical separation between the sample and the indenter. When under contact stress, the elements function like stiff springs which permit the continuity of contact stress and displacement by allowing minimum penetration of the indenter into the sample. The spring constant is chosen an order of magnitude greater than the stiffness of the adjacent material with higher stiffness [32] and the zero friction coefficient was set according to the experimental conditions. Ideally, the spring constant should be infinite to prevent any unrealistic physical penetration. However, in reality a large spring constant will introduce extensive error in the numerical process leading to a very slow convergence or even failure to convergence.

We then considered a Hertzian distributed pressure applied on the sample to simulate the contact between two frictionless elastic solids of revolution. The purpose of this was to compare the results from both analyses—real contact (RC) which is discussed above and simulated contact (SC) under which the Hertzian distributed pressure is used as the loading boundary condition. If the agreement between the two methods is acceptable, the operation of nonlinear and computing time consuming real contact analyses will not be necessary. The comparison shows that the discrepancy resulted in no significant difference. Take the example of glass under a load of 124.58 N which was run as a test. The maximum σ_r which occurs at the edge of the contact zone was found to be 260 MPa (RC) and 261 MPa (SC). The minimum σ_Z which occurs at the center of the contact was obtained as -2140.0 MPa (RC) and -2154.0 MPa (SC). The errors for both components are considered negligible due to the nature of computational analysis. We conclude, therefore, that it is sufficient to use a Hertzian distributed pressure to simulate the real contact situation.

Finally, an FEA was performed for the ceramic sample containing a Hertzian cone-crack (HCC) due to the fatigue contact loading. FEA has a long history of being used to simulate crack propagation. The general tactic is as follows. First we arrange the FEA mesh line in coincidence with the predicted crack propagation path. Next we examine the crack tip strain energy release rate numerically. If the strain energy release rate obtained is greater than or equal to its critical value, the crack will be allowed to propagate. The crack tip node will then be relaxed into two nodes and crack extension will be one element length in the predicted direction. Nonetheless, if we do not know the crack propagation path beforehand, the prediction will be rather difficult. It is well known that for monolithic materials like the ceramic being tested, any crack will tend to follow a path for which the stress intensity at the crack tip is purely mode I (crack opening). The crack propagation direction, accordingly, will be the direction at which the strain energy release rate for mode II fracture vanishes. If the determination of the crack propagation direction is achievable, the determination of the crack path will not be considered achievable, especially if the crack has a high curvature path such as the initial stage of HCC. The analysis becomes an element size dependent problem. In other words, different FEA meshes will result in different crack paths. For the case of HCC, the crack is initiated somewhere outside of the contact edge and propagates perpendicular to the surface. The crack gradually alters its direction within a few dozen microns and later propagates asymptotically toward a constant angle. We do not intend to simulate the initial HCC path which has already been done using an analytical prediction. Since at a later stage HCC propagates almost with a constant angle with the surface, we can consider the HCC as a straight line initiating from the contact edge. We believe that the curvature at its initiation will not affect the late-stage HCC propagation.

The next task is to determine the angle of propagation. According to the concept described above, we obtained the angle with respect to the surface as 24.4° for a crack length of 0.160 mm. Several stress contour plots for the ceramic sample with HCC are given in the text and compared with the stress plots without HCC. It has been shown in a parametric FEM study that the effect of crack length variation on the angle is small. There are many FEA techniques available for calculating the crack tip strain energy release rate. The one which was employed used the crack closure integral method. The detail of this technique can be found in Ref. [33]. In the analysis it was assumed that the creation and propagation of Hertzian cone-cracks do not affect the given Hertzian distributed pressure.

References

[1] J. Hannoosh, *Design News, 11*(21) (1988) 224–231.
[2] H.K. Zu, L. Wei, N.P. Padture, B.R. Lawn and R.L. Yeckley, *J. Mater. Sci., 30* (4) (1995) 869–878.
[3] K. Jack, The crystal chemistry of the sialons and related nitrogen ceramics, in F. Riley (ed.), *Nitrogen Ceramics*, Noordhoff, Leyden, Netherlands, 1977, pp. 109–128.
[4] F. Riley, Nitridation and reaction bonding, in F. Riley (ed.), *Nitrogen Ceramics*, Noordhoff, Leyden, Netherlands, 1977, pp. 265–288.
[5] D. Richerson, *Am. Ceram. Soc. Bull., 52* (7) (1973) 560–569.
[6] L. Gauckler, L. Boskovic, G. Petzow and T. Tien, Desification β-Si_3N_4 solid solutions containing AlN:Al_2O_3 during chemical reaction, in F. Riley (ed.), *Nitrogen Ceramics*, Noordhoff, Leyden, Netherlands, 1977, pp. 41–62.
[7] C. Greskovich and C. O'Clair, *Am. Ceram. Soc. Bull., 57* (11) (1978) 1055–1056.
[8] A.G. Evans, The fracture of brittle materials, in F. Riley (ed.), *Nitrogen Ceramics*, Noordhoff, Leyden, Netherlands, 1977, pp. 451–475.
[9] D. Clark and G. Thomas, *J. Am. Ceram. Soc., 61* (3–4) (1977) 114–118.
[10] A. Tsuge and K. Nishida, *Am. Ceram. Soc. Bull., 57* (4) (197?) 424–431.
[11] M. Akazawa, *Wear, 124* (1988), 123–132.
[12] T.E. Fischer and H. Tomizawa, *Wear, 105* (1985) 29–45.
[13] J.F. Braza and H.S. Cheng, *Tribology Transactions, 32* (1989) 4439–4446.
[14] B.C. Bunting, *Lubrication Engineering, 46* (11), pp. 745–751.
[15] A.T. Galbato, R.T. Cundill and T.A. Harris, *Lubrication Engineering, 46* (11), pp. 886–894.
[16] R. Rice, K. McKinney, C. Wu, S. Freiman and W. McDonough, *J. Mater. Sci., 20* (1985) 1392–1406.
[17] P.J. Kennedy, A.A. Conte, Whitenton, L.K. Ives and M.B. Pertson, in S. Jahanmir (ed.), *Friction and Wear of Ceramics*, pp. 79–98.
[18] R. Gates and S. Hsu, *Tribology Transactions, 34* (3) (1991) 417–425.
[19] X. Dong and S. Jahanmir, *Wear, 165* (1993) 169–180.
[20] J. Lucek, *Gas Turbine and Aeroengine Congress and Exposition*, Brussels, 1990, ASME Paper no. 90-GT-165.
[21] S. Danyluk, M. McNallan and D. Park, in S. Jahanmir (ed.), *Friction and Wear of Ceramics*, pp. 61–77.
[22] O. Adewoye, *Wear, 70* (1981) 37–51.
[23] D. Scott, J. Blackwell and P. McCullagh, *Wear, 17* (1971) 73–82.
[24] K.L. Johnson, *Contact Mechanics*, Cambridge University Press, Cambridge, 1985.
[25] B. Bhushan and L.B. Sibley, *ASLE Transactions, 25* (4), pp. 417–428.
[26] Z. Chen, A. Morrone, J.J. Mecholsky and S. Hu, Effect of amorphous grain boundaries in Si_3N_4 on the damage in a Hertzian contact area, in preparation.
[27] D. Kulawansa, L. Jensen, S. Langford and J. Dickinson, *J. Mater. Res.*, 9(2) (1994) 476–484.
[28] J. Zarzycki, *Glasses and the Vitreous State*, Cambridge University Press, Cambridge, 1991.
[29] D. Singh and D. Shetty, *J. Am. Ceram. Soc.*, 72(1) (1989) 78–84.
[30] S. Hu, J.S. Bark, J.A. Nairn, *Composites Sci. and Technol., 47* (1993) 321.
[31] D. Rigney, *Scripta Metallurgica et Materialia, 24* (1990) 799–803.
[32] *ANSYS User's Manual for Revision 5.0*, Swanson Analysis Systems, Inc.
[33] E.F. Rybicki and M.F. Kanninen, *Engineering Fracture Mechanics, 9* (1977) 931–938.
[34] *Exxon Products Summary*, USA, November, 1992.

International Journal of Fracture, ~~submitted~~ – October 1995 Accepted

On the Hertzian Fatigue Cone Crack Propagation in Ceramics

Shoufeng Hu

WL/MLLP, Materials Directorate, Air Force Wright Laboratory,

Wright-Patterson AFB, OH 45433

Zheng Chen and John J. Mecholsky, Jr.

Department of Materials Science and Engineering, University of Florida

Gainesville, Florida 32611

Abstract

The Hertzian cone crack initiation and propagation in ceramics under cyclic fatigue loading with a spherical indenter is studied. Unlike the so-called quasi-static Hertzian cone crack, the fatigue Hertzian cone crack propagation eliminates the dynamic effect on unstable crack propagation. As such, the crack is found to propagate following the path of pure Mode I type. We use an elasticity approach, a finite element analysis, and a empirical analysis to investigate the Hertzian cone crack in three stages: crack initiation, crack propagation, and crack kinking. The mechanism of the multiple concentric cone cracks is also explained. The purpose is to understand and predict the behavior of the formation of the Hertzian fatigue cone crack using available modeling tools.

Introduction

More than one hundred years ago, Hertz first published his work about the contact behavior between two elastic bodies [1]. Decades later, investigators were able to define the stress state in a semi-infinite solid under a spherical indentation [2,3]. It shows that the stress underneath the indenter is highly hydrostatic compressive. However, tensile stresses exist outside of the contact area with the maximum value at the rim of the contact area in the radial direction. The Hertzian cone crack formation is primarily due to this tensile stress [4-6].

The Hertzian cone cracks produced in brittle materials have been reported decades ago [4-6]. In general, people use this indentation-induced fracture as a technique to measure the material fracture surface energy and fracture toughness for brittle materials like glasses and structural ceramics. The significance of the research, however, has not been manifested until the recent application of the structural ceramics in the bearing of aircraft turbine engines under high temperature, high corrosive environment conditions [7,8]. For these high temperature, high stiffness and strength, high corrosive and wear resistance, and low density materials, damage related to the Hertzian fatigue cone crack has been the only primary damage form reported [7,8].

A typical Hertzian fatigue cone crack has these characteristics (see Figs. 1): it is initiated slightly outside the contact area; it is near-symmetric about the loading axis; initially it is perpendicular to the top surface and propagates downward, and after a number of loading cycles it gradually propagates outward away from the loading axis to form a curve in the axisymmetric plane (Fig. 2); at a late stage of crack propagation it may kink (Figs. 2a and 2b) or it may form a secondary concentric cone crack outside of the existing major crack (Figs. 2a and 2c). In this study we focus on using available analytical and numerical modeling tools to explain and predict all listed characteristics.

There have been many research activities for the investigation of the Hertzian cone crack. The interested reader is referred to Ref. [9] for detailed literature survey on this topic. However, most work in this area investigates the so-called quasi-static indentation fracture. These are the studies in which the Hertzian cone crack may propagate instantly under an increased applied load and the entire crack may form under different loads. The intention of this study is to investigate the behavior of the Hertzian cone crack initiation and propagation under a cyclic fatigue loading. Since the fatigue crack propagation is stable and the fatigue loading pattern remains the same, it is more appropriate to use modeling tools to study this phenomenon than the crack propagation under a static or quasi-static loading.

Experimental Study

Disc-shaped silicon nitride (Si_3N_4) specimens were used in this experiment. They were cut from a rod and polished by diamond polishing plates to remove any visible scratches and pits. The material is manufactured by Toshiba Corporation with the brand name TSN-03H. The sample dimensions are 10 mm in diameter and 3 mm in thickness.

All the tests were conducted at an MTS machine using a load control mode (see Fig. 3). A radius 4.76 mm (3/16") tungsten carbide ball was used as the rigid indenter. The cyclic load, applied on the ball to create the Hertzian contact, was in the form of half sine wave with a frequency of 10 Hz and maximum and minimum loads of 2016 N (453 lb.) and 0 respectively. The corresponding maximum contact pressure is 15.01 GPa. Tests were also run under a maximum load of 2936 N (660 lb.) with a corresponding maximum contact pressure of 17.02 GPa.

The contact behavior between the indenter and the sample is assumed as compressive only with no tangential traction involved. This is because very low friction exists between the silicon nitride disc and the rigid ball when Exxon turbo oil 2380 is used at the contact surface [10].

In general, after its initiation the Hertzian cone crack propagates circumferentially. After about one million loading cycles, a ring on the top surface can be seen. In order to examine the crack propagation inside the sample, it was necessary to section the sample, which was done after each fatigue test. The samples were sectioned through the contact area using a diamond saw and then the sectioned surface was polished down to 1 μm. By doing so, the crack path and pattern can be clearly observed (Fig. 2). For all the samples sectioned the observed asymptotic crack angle with respect to the loading axis ranged from 58.3° to 65.3° with an average of 62.9°.

The Hertzian cone crack is initiated at the weakest spot in the neighborhood of the rim of the contact area and gradually propagates circumferentially and symmetrically about the loading axis. Under the view of SEM the crack path is not smooth, but zigzags in the boundary of the grain structure. On the macroscopic scale, the material is homogeneous. But on the microscopic scale, it is a highly heterogeneous polycrystalline ceramics. The grain boundary is a glassy phase rich region and has a significantly lower strength than the grain structure itself. The crack propagation in silicon nitride material, as such, proceeds intergranularly. For fine grain structure ceramics like silicon nitride the grain size is about a few microns. The localized heterogeneity will not invalidate the assumption of global homogeneity used in analysis.

Another primary concern in the bearing application is the possible subsurface damage of the material under indentation. The stress analysis for the Hertzian contact illustrates a high hydrostatic compressive stress underneath the indenter. For brittle ceramic materials such as the silicon nitride samples used in experiments are highly resistant to compressive fatigue. The fatigue tests which had been conducted using different dense materials such as fine grain ceramics, coarse grain ceramics, and amorphous glasses showed no subsurface damage induced by the Hertzian fatigue indentation [7] (e.g., see Fig. 2). The reported "shear fault" damage underneath the indentation [11] may be attributed to the construction of the bonded interface in the sample and not the material itself. The detailed explanation of the damage mechanism is offered in [12].

Analysis

In this study we analyzed the problem with three steps, namely crack initiation, crack propagation and crack kinking. For crack initiation we used the elasticity solution as a tool. For crack propagation we employ both the elasticity approach and the finite element analysis. For crack kinking which occurs at the late stage of crack propagation, our investigation is limited to a qualitative description.

The material constants used in the analysis are as follows:

Indenter:	$E_i = 625$ GPa	$\nu_i = 0.24$
Sample:	$E_s = 309$ GPa	$\nu_s = 0.27$

Both materials are assumed to be homogeneous, isotropic, and present a linear strain/stress relationship. Axisymmetry is assumed in the analysis. The cylindrical coordinate system is used and the symmetric axis (z-axis) coincides with the loading axis as shown in Fig. 1. $z = 0$ delineates the boundary of the assumed semi-infinite solid for the elasticity solution. In the finite element analysis actual sample dimensions were used. The peak fatigue load was used as the loading boundary condition in all analyses.

1. Elasticity approach for crack initiation and propagation

Ever since Hertzian indentation fracture in brittle materials was first observed, investigators have reportedly claimed that the Hertzian cone crack is straight, forming a cone shape axisymmetric crack [9,13]. Based upon this claim, mixed mode fracture behavior was investigated [9,13]. However, repeated fatigue experiments performed in this study showed that the cracks always have a curvature and never propagate straight.

In a homogeneous material, any crack will tend to follow a path for which the crack tip energy release rate is purely Mode I [14]. The so-called quasi-static tests which many investigators conducted may have dynamic contributions during the unstable crack propagation. It is possible that with the inclusion of dynamic effects the straight crack propagates in a pure Mode I crack path. We claim that for the fatigue cone crack propagation, the Mode I crack path is not straight. It is initiated at the top surface slightly outside the periphery of the circle of contact and propagates downward from the top surface. As the number of the fatigue cycles increases, the crack gradually changes direction and propagates outward away from the loading axis. The crack path in the axisymmetric plane asymptotically makes a material property and loading dependent angle with the symmetric axis.

In order to predict the crack path especially for the stage of crack initiation, we proposed an approximation that the cracking proceeds orthogonally to the greatest tensile stress, thus following a surface delineated by the trajectories of the other two principal stresses, one in-plane (the axisymmetric plane) and the other out-of-plane in the hoop direction. Here we define the principal stress in the hoop direction as the third principal stress, disregarding its magnitude. The first in-plane principal stress is the one which is greater in magnitude than the second one at the location of the global maximum principal stress. In the neighborhood of this location the crack is expected to be initiated. In the axisymmetric plane, the above mentioned approximation is accomplished by the trajectory of the second in-plane principal stress starting from the very location. In fact, this approximation involves two assumptions, i.e., both the crack initiation and propagation are controlled by the maximum principal stress. The first assumption that the crack is initiated in the neighborhood of the location of the maximum principal stress is generally acceptable. However, the second assumption needs careful scrutiny. It is noted that at each increment of crack propagation, a new stress field is formed. At the crack tip, the maximum principal stress may change its direction due to the new stress field. Consequently the path maximizing the strain energy release rate for crack propagation may change accordingly. An excellent agreement between the trajectory of the second in-plane principal stress and the experimentally observed crack path (Fig. 4), however, indicates that the formation of the crack does not significantly change the principal stress trajectories. A satisfactory agreement between the trajectory of the second principal stress and the experimentally observed curved microcrack was also observed for brittle composites in a similar approach [15]. Thus the reduction of the system energy due to crack formation and propagation sometimes has minimum effect on the principal stress trajectories prior to any fracture.

The expressions for the stress components in a semi-infinite solid under a concentrated load was originally proposed by Boussinesq and is referred to as the Boussinesq Equation [16]. The stress state of the solid under the distributed Hertzian contact pressure was first derived by Huber [2] and later by Love using a potential method [3]. Many other workers also derived the stress state for more complicated loading boundary conditions (e.g. see [17]).

Upon the availability of the stress components, the crack path which follows the trajectory of the second in-plane principal stress is obtained by this first order differential equation:

$$\frac{dz}{dr} = \frac{\tau_{rz}}{\sigma_1 - \sigma_r} = -\frac{\sigma_z - \sigma_r}{2\tau_{rz}} + \sqrt{\left(\frac{\sigma_z - \sigma_r}{2\tau_{rz}}\right)^2 + 1} \qquad (1)$$

where σ_1, σ_r, σ_z, and τ_{rz} are the first principal stress, radial stress, axial stress and in-plane shear stress, respectively. This equation can be solved numerically using a fourth-order

Runge-Kutta method [18]. The step size for numerical integration is 1 μm. An example of the comparison between the trajectory of the second in-plane principal stress and the experimentally observed crack path is shown in Fig. 4.

The agreement of the Hertzian cone crack path with the principal stress trajectory was first proposed by Frank and Lawn [19]. They found that the angle of the asymptotical trajectory of the second in-plane principal stress is in a remarkable agreement with that of the crack path. The experimental data they used were from the quasi-static indentation. The crack propagates under an increased load and contact area. It is therefore not possible to have a good match between the experimental crack path and the trajectory of the second in-plane principal stress for the crack in its entirety, especially at its initiation and the early stage propagation. In this study since the fatigue loading is applied and the load pattern remains the same throughout the entire experiment, the agreement is not limited to the principal stress at its asymptotical part but along the entire curve (see Fig. 4). It is as such more meaningful to use the elasticity approach for a problem with a constant maximum load (fatigue loading) than that for a problem with an increased load (quasi-static loading).

The elasticity solution indicates that the maximum tensile stress always occurs at the contact periphery. However, experimentally the crack is initiated outside the contact area by approximately 10% to 20 % of the radius of the contact area. This is because directly underneath the contact periphery the radial stress changes to compressive. For this particular problem the radial stress decreases from the maximum at the contact periphery to zero at 4.2 μm below the periphery and further becomes compressive in z direction. The detailed explanation was given on the physical basis of Auerbach's law [20]. This phenomenon may also depend on the grain size of the material or the localized material heterogeneity. As such, if the initiation site for the trajectory of the second in-plane principal stress and that for the crack is the same, the agreement between experimental and elasticity results is excellent as shown in Fig. 4.

2. Finite element analysis for crack propagation

For the finite element analysis (FEA) of Hertzian contact behavior we used the axisymmetric analysis, which is a two dimensional model in nature. Therefore, two dimensional elements were used, but axisymmetric three dimensional stress components were obtained. A commercially available finite element analysis software ANSYS was used for all finite element analyses.

For the first set of modeling, we used two dimensional elements for both the spherical indenter and the ceramic sample, and point-to-surface contact elements in between the indenter and the sample to simulate the contact behavior (see Fig. 5). These three noded contact elements were used to represent a bi-linear stress/strain relationship under loading [21]. When under no contact stress, the elements do not function, which allows for the physical separation between the sample and the indenter. When under contact stress, the elements function like stiff springs which permits the continuity of contact stress and displacement by allowing minimum penetration of the indenter into the sample. The spring constant is chosen an order of magnitude greater than the stiffness of the adjacent material with a higher stiffness [21] and a zero friction coefficient was used based on the experimental results. Ideally the spring constant should be infinite to prevent any unrealistic physical penetration. In reality an unreasonably large spring constant may introduce extensive numerical error in the numerical process leading to a very slow, or even failure in, convergence.

Next, a Hertzian distributed pressure [3,22] was applied on the sample as the loading boundary condition to simulate the contact between two frictionless elastic solids of revolution. The purpose of doing this is to compare the stresses from both analyses — the real contact analysis using contact elements and the simulated contact analysis using the given Hertzian distributed pressure. If the agreement is acceptable, we will not need to perform nonlinear, complex and computing time consuming real contact analyses. The resulting comparison shows that the discrepancy is not significant. An example was given using borosilicate glass as a candidate [23]. The results show that the discrepancy for both the maximum radial normal stress and maximum axial normal stress is less than one percent. These errors are considered negligible due to the nature of computational analysis.

We conclude, therefore, that it is sufficient to use the Hertzian distributed pressure to simulate contact behavior.

Finally, finite element analyses were performed for the ceramic sample with and without a Hertzian cone crack. FEA has a long history of being used to simulate crack propagation. The general tactic is as follows. First we arrange the FEA mesh line coincident with the possible crack propagation path. Next we examine the crack tip strain energy release rate numerically; this will be discussed later. If we do not know the crack propagation path *a priori*, the prediction will be rather difficult. As mentioned earlier, for homogeneous materials like the ceramic sample being tested, any crack will tend to follow a path for which the energy release rate at the crack tip is purely Mode I (crack opening). The crack propagation direction, accordingly, will be the direction at which the Mode II type strain energy release rate vanishes. The determination of the direction for a straight crack is achievable though tedious. The determination of the path of a curved crack is not considered achievable, especially if the crack has a high curvature path such as the initial stage of the Hertzian cone crack. It becomes an element size dependent problem. In other words, different FEA meshes will result in different crack paths. However, in the finite element analysis we do not intend to simulate the initial stage of the Hertzian cone crack path which had been simulated using the elasticity approach. Since at its late stage, the Hertzian cone crack propagates almost at a constant angle with respect to the symmetric axis, we can approximate the crack as a straight line initiated from the rim of the contact area. The crack curvature itself at the initiation stage is assumed not to affect the later stage of crack propagation.

The crack closure integral method used in FEA for the calculation of the crack tip strain energy release rate was originally proposed by Rice [24] and later modified by Rybicki and Kanninen [25]. The theory simply states that if the crack extends by an increment Δa, the energy absorbed in the process is equal to the work required to close the crack to its original geometry. In finite element analysis, the stresses over the crack extension Δa are replaced by the nodal forces of a whole element which is of the same size as the unit crack extension Δa. Consequently, the crack closure integral method states that the energy release rate is equal to the work required to close two nodes at the crack tip. If Δa

is small enough and $x_{i+1} - x_i = x_i - x_{i-1}$, the forces required to close the crack can be replaced by the forces of the crack tip node i, and the displacements at the nodes $i+1$ can be considered as the displacements through which the forces do the work (see Fig. 6).The expressions for the Mode I and the Mode II energy release rates G_I and G_{II} using crack closure integral method are:

$$G_I = \frac{1}{2\Delta A}(F_i^n \Delta u_{i+1}) \quad (2)$$

$$G_{II} = \frac{1}{2\Delta A}(F_i^s \Delta v_{i+1}) \quad (3)$$

where $\Delta A = 2\pi r \Delta a$ is the surface area created by the increment of crack extension and r is the crack tip radius; F_i^n and F_i^s are the nodal forces in normal and shear directions with respect to the local crack coordinates, which are circumferentially based for axisymmetric problems; Δu_{i+1} and Δv_{i+1} are the relative displacements in normal and shear directions for nodes at the position $i+1$. A similar approach was employed in [9]. In the analysis it was assumed that the initiation and propagation of the Hertzian cone crack do not change the given Hertzian distributed pressure. In [9] the interaction between the contact pressure distribution and the cone crack was studied. The conclusion was that if the radius of the contact area is smaller than the cone crack radius at the surface, which is always true for the present investigation using fatigue loading, the cone crack initiation and propagation will not affect the contact pressure distribution.

Using FEA we are able to not only predict the formation of the Hertzian cone crack but also explain the phenomenon of multiple cracking mentioned earlier. For FEA without a crack, the maximum tensile stress is located in the neighborhood of the rim of the contact area (Fig. 7a); this result was also found by analytical solution [3,22]. If a crack exists in FEA mesh as described above, the maximum tensile stress shifts away from the original position (Fig. 7b) and provides the possibility to form a new crack. After the formation of two cracks, the maximum tensile stress will shift again. The formation of three crack has been observed experimentally (see Fig. 2c).

In finite element analysis, the crack was straight, and initiated at the rim of the contact area. The applied load was 2016 N. The crack tip element size, which is

APPENDIX 24, S. Hu, Z. Chen and J. J. Mecholsky, Jr., "On the Hertzian Fatigue Cone Crack Propagation in Ceramics," accepted for publication in *International Journal of Fracture.*

APPENDIX 25, Z. Chen, J. J. Mecholsky, Jr., T. Joseph and C. L. Beatty, "Application of Fractal Fracture to Advanced Engine Material," in *Ceramic Materials and Components for Engines*, D.S. Yan, X.R. Fu and S.X. Shi, eds., World Scientific, Singapore, 1995, pp. 506-509.

APPLICATION OF FRACTAL FRACTURE TO ADVANCED ENGINE MATERIAL

Z. Chen, J.J. Mecholsky,Jr, T. Joseph, and C.L. Beatty
Dept. of Materials Science and Engineering, University of Florida, Gainesville Florida 32611, USA

ABSTRACT

High intrinsic mechanical properties and good chemical compatibility at high temperature make silicon nitride a good candidate as an advanced engine material. Much research has been done to characterize the mechanical strength and resistance of crack propagation of the material. In this paper, the authors use a unique technique, fractal analysis, to study the fracture behavior of Si_3N_4. We found that this technique is useful in correlating the fractal dimension to the material properties and fracture-surface topography.

Introduction

The fracture process in brittle materials leave characteristic markings on the fracture surface. Shand[1] and Poncelet[2] both recognized the importance of these markings on the fracture surface of brittle materials in terms of quantitatively identifying characteristic phenomena such as stress at fracture and velocity of the crack front. An idealized fracture surface presents an origin with surrounding topography showing the mirror, mist, and hackle regions. A relationship between the size of the crack at fracture, c, and the inverse of the square of the stress at fracture was also being developed by Irwin as he introduced fracture mechanics. We generally evaluate the critical stress intensity factor, K_{Ic}, one of the presentations of fracture toughness, i.e., the resistance to fracture, as:

$$K_{Ic} = Y\sigma\sqrt{c} \qquad (1)$$

where Y is a "constant" dependent on the geometry and location of the crack as well as the loading configuration; σ and c are the stress and crack size at fracture, respectively.

However, not all fracture surfaces show the idealized features. In figure 1, three Si_3N_4 fracture surfaces show different features, but they are from an identical material. The fracture surface features are determined not only by material properties but also by initial flaw/defect sizes and stress states. Since fracture is an atomic bond breaking process, we can ask if there exists a relationship between bond breaking and fracture surface topography. Recent developments in fractal geometry has presented the possibility of enhancing the field of fractography to this level.

Many people have already pointed out that the nature of the fracture surface can be described using fractal geometry[3-5]. Fractal geometry is a non-Euclidean geometry that allows for non-integer dimensions and has been used to describe a variety of natural processes[4]. The fractal dimension of a line, for example, will reside between 1 and 2. A relatively "smooth" line would have a dimension of 1 (Euclidean). A tortuous line could have a dimension greater than one. The tortuosity increases as the dimension increases. The fractal dimension of a surface lies between 2 and 3, etc.. Mecholsky et al.[5-7], experimentally determined a relationship between fracture toughness (K_{Ic}) and fractal dimension (D). They found that

$$K_{Ic} = AD^{*1/2} + K_o \qquad (2)$$

where A is a family parameter and D* is the fractal dimensional increment. K_o accommodates the possibility of perfectly plane fracture, i.e. D=2. Although not totally defined, there is some evidence that "families" would be composed of either single crystals and large-grained materials, glass ceramics and fine-grained polycrystalline materials. Within a family, an increase in fractal dimension corresponds to an increase in fracture toughness. Another relation was also found[8]:

$$c/r_I = D^* \qquad (3)$$

where r_I is the mirror-mist radius. This equation then provides a link between fractal geometry and fractography.

Silicon nitride has high intrinsic mechanical properties and good chemical compatibility at high temperature. These properties make silicon nitride a candidate for advanced engine material. Much research has been done to characterize the mechanical strength and resistance to crack propagation and fracture. In this study, we use fractal analysis to study the nature of the fracture of silicon nitride and the appearance of the fracture surface.

Experiment

HIP silicon nitride ball bearing material was used for this study. Three types of fracture surfaces (Fig.1) are analyzed in this study. A and B were fractured in four-point flexure at different stresses. C was fractured during a rotating cantilever beam fatigue test. The fractal dimensions of the fracture surfaces were determined using slit island and the Richardson method on portions of contours[9]. Two different techniques were used to experimentally measure the fractal dimension. One technique used dental impression material to create a negative replica of the fracture surface. After the replica dries, a positive of the fracture surface is made by filling with epoxy to the cavity formed in the impression material. After the epoxy is cured, the positive impression is coated with an electroless nickel plating and then the coated sample is covered by epoxy. The replica is now treated in the usual manner to produce slit island contours by polishing approximately parallel to the fracture surface. The detail of this process was described by Plaia and Mecholsky[10]. Another technique is using the atomic force microscope (AFM) [TopoMetrix, 1505 Wyatt Dr., Santa Clara, CA 95054, USA] to create 3-D images directly from the silicon nitride fracture surfaces. Then, a packaged software is able to slit the 3-D fracture surface image parallel to the fracture surface. This sectioning results in slit islands, which further results in the calculation of the fractal dimension.

Results and Discussion

The slit island contours obtained from both polishing the replica sample and slitting AFM image are shown in Fig.2, respectively. The fractal dimensions obtained from the experiments are listed in Table I. The three fracture surfaces have similar fractal dimensions regardless of their different fracture surface appearances. Moreover, the fractal dimensions measured using both techniques show their consistency. In the AFM method, we varied the scanning area from 10 μm^2 to 20 μm^2 and the fractal dimensions obtained are given in the Table I. Comparing both experimental methods, we observe that the measured D* values appear the same regardless of scale. These results imply that the fractal dimension can be related to material characteristics regardless of the fracture stress states. We plot the toughness vs. the fractal dimensional increment $D^{*1/2}$ with other polycrystal data, where K_{Ic} was obtained by the strength indentation technique. The K_{Ic}-$D^{*1/2}$ values lie on a straight line with a correlation coefficient of 0.93. This indicates the relationship between K_{IC} and D* (eq. 2), which was proposed by Mecholsky et al.[5], also applies to silicon nitride. Thus, as the fractal dimension increases, fracture toughness increases. The relationship between D* and the material constants further implies that fracture is a fractal process. The fracture surface has a characteristic fractal dimension regardless of stress state and location on the fracture surface. This experiment also shows $c/r_1 = .34 \approx D^* = .33$, which is the relationship shown in equation 3.

In summary, we were able to correlate the appearance, i.e., topography of silicon nitride fracture surface through the fractal dimensional increment, D*, to material fracture constants, i.e., K_{Ic} and c/r_1. This correlation is consistence with previous findings. We interpret these relations to mean that silicon nitride fracture is a fractal process. Thus, the reason that the fractal approach is appealing is that it not only provides a means of characterizing the material, but also suggests a means for generation of the fracture surface, and potentially will lead to an understanding of atomic fracture and wear processes.

Acknowledgment:

The authors gratefully acknowledge the support of Air Force Office of Scientific Research Grant Number F49620-93-10349DEF and the Major analytical Instrumentation Center (MAIC) at the University of Florida in partial support of this work.

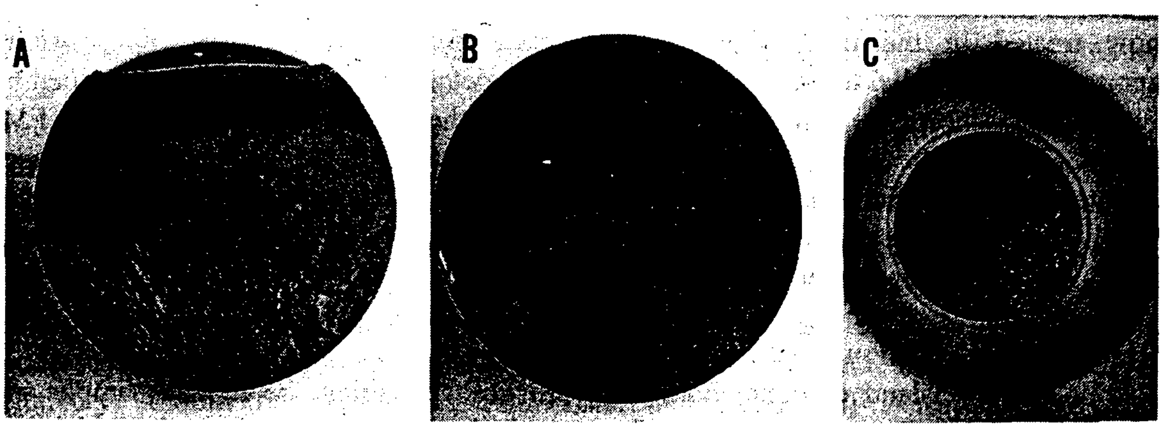

Fig.1 A, B and C are from an identical material (Si_3N_4). A and B were fractured in bending at different stresses. C was fractured during rotating fatigue. Each gave their own characteristic markings on the fracture surfaces.

Table I

Sample	D_1*	D_2*	D*	c/r_1	K_{Ic} (MPa)
A	0.32	0.33	0.33	0.34	5.1
B	0.33	0.34			
C	0.33	0.31			

D_1* and D_2* are obtained from polishing method and AFM method, respectively. D* is an average value.

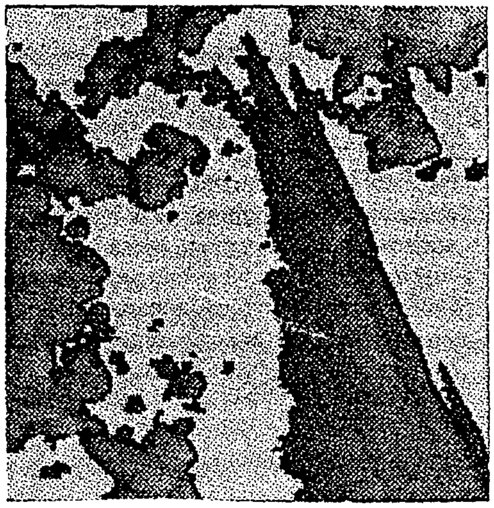

Fig.2 Slit island contours are shown in these photos. The left photo is from the polishing method at X100. The right one is from AFM at X3,200. Both photos show similarity regardless of the different scale.

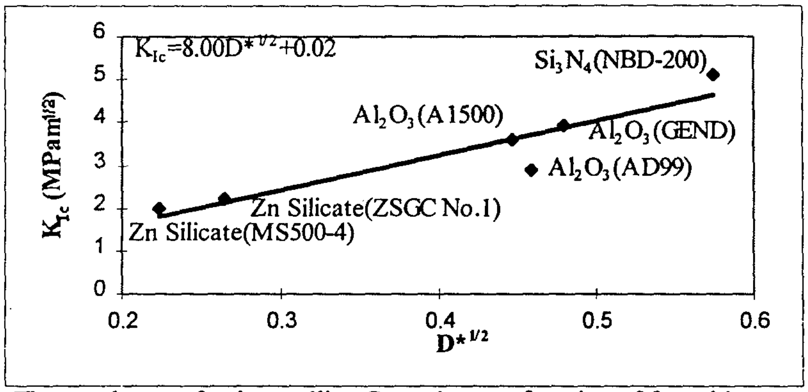

Fig.3 The toughness of polycrstalline Ceramics as a function of fractal increment, D*

References

[1]E. B. Shand, *J. Am. Ceram. Soc.*, **42**[10](474-77)1959.

[2]E. F. Poncelet, "*The Markings on Fracture Surfaces,*" Trans. Soc. Glass Tech., **52**(279-88)1958.

[3]B.B. Mandelbrot, D. E. Passoja, and A. J. Paullay, *Nature*, **308** (1984) 721.

[4]B.B. Mandelbrot, "*The Fractal Geometry of Nature,*" Freeman, San Francisco, 1982.

[5]J.J. Mecholsky, D.E. Passoja and K.S. Feinberg-Ringel, *J. Am. Ceram. Soc.,* **72**(1) 60-65 (1989).

[6]J.J. Mecholsky, *J.Am. Ceram. Soc.*, **74**[12]3136-38(1991).

7Y.L. Tsai and J.J. Mecholsky, *J. Mater. Res.*, **6**[6]1991.

[8]J.J. Mecholsky and S.W. Frieiman, *J. Am. Ceram. Soc.*, **74**[12]3136-38 (1991).

[9]T.J.Mackin,"*Fractal and Fracture,*" Ph.D. Thesis, The Pennsylvania State University.

[10]J.J. Mecholsky and J.R. Plaia, *J. Non-crystalline Solids*, **146**(1992)249-255.